UNIVERSIDAD SAN FRANCISCO DE QUITO USFQ

Colegio de Posgrados

Nonlinear finite element simulations for Embedded Based Plate Connection.

Proyecto de Investigación y Desarrollo

Nicolás Mora Bowen Pérez

Pablo Torres Rodas, Doctor of Philosophy.
Director de Trabajo de Titulación

Trabajo de titulación de posgrado presentado como requisito
para la obtención del título de Magíster en Ingeniería Civil, Mención Diseño y Construcción
de Estructuras Sismo Resistentes

Quito, 22 de marzo de 2021

UNIVERSIDAD SAN FRANCISCO DE QUITO USFQ

COLEGIO DE POSGRADOS

HOJA DE APROBACIÓN DE TRABAJO DE TITULACIÓN

Nonlinear finite element simulations for Embedded Based Plate Connection.

Nicolás Mora Bowen Pérez

Nombre del Director del Programa:	Fernando Romo
Título académico:	Master of Science
Director del programa de:	Maestría en Ingeniería Civil

Nombre del Decano del colegio Académico:	Eduardo Alba
Título académico:	Doctor of Philosophy
Decano del Colegio:	Colegio de Ciencias e Ingenierías

Nombre del Decano del Colegio de Posgrados:	Hugo Burgos
Título académico:	Doctor of Philosophy

Quito, 22 de marzo de 2021

© DERECHOS DE AUTOR

Nombre del estudiante: Nicolás Mora Bowen Pérez

Código de estudiante: 00215835

C.I.:   171975777-3

Lugar y fecha: Quito, 22 de marzo de 2021.

ACLARACIÓN PARA PUBLICACIÓN

Nota: El presente trabajo, en su totalidad o cualquiera de sus partes, no debe ser considerado como una publicación, incluso a pesar de estar disponible sin restricciones a través de un repositorio institucional. Esta declaración se alinea con las prácticas y recomendaciones presentadas por el Committee on Publication Ethics COPE descritas por Barbour et al. (2017) Discussion document on best practice for issues around theses publishing, disponible en http://bit.ly/COPETheses.

UNPUBLISHED DOCUMENT

Note: The following graduation project is available through Universidad San Francisco de Quito USFQ institutional repository. Nonetheless, this project – in whole or in part – should not be considered a publication. This statement follows the recommendations presented by the Committee on Publication Ethics COPE described by Barbour et al. (2017) Discussion document on best practice for issues around theses publishing available on http://bit.ly/COPETheses.

DEDICATORIA

Dedicado a mi esposa Verónica y a mis padres Agustín y Elba.

AGRADECIMIENTOS

ABSTRACT

Column base connections are one of the most critical components in Steel Moment Frames (SMFs) since these connections transfer the loads (i.e., gravity, seismic, wind) from the entire superstructure into the concrete-foundation, being an interface between them.

Embedded Base Connections (EBC) consist of a column welded to a bottom base plate and embedded into a concrete foundation. The applied forces, are resisted by a combination of the bearing stresses developed by the contact between the column flange and the foundation and by the vertical stresses at the bottom base plate. Grilli and Kanvinde conducted a large-scale experimental program to study the seismic response of EBC. This program's focus was the flexural capacity of these connections and the development of a strength method based on the insights gained from the tests. A total of five tests were evaluated. The difference among them was the embedded length (510 and 760mm), column size, and axial load level.

This paper presents a series of nonlinear finite element models developed to provide insights into the behavior of embedded base connections for SMFs. The analytical models were calibrated and evaluated against experimental results from full scales tests. These models incorporate the essential aspects that control the connection behavior, including constitutive material modeling and contacts among the connection components. Possible design implications are discussed, while the limitations of the current work and future lines of research are outlined.

Key words: Column Base Connections, Embedded Base Connections, Finite Element Models, Nonlinear Finite Element Models, ABAQUS, Concrete Damage Plasticity Model

TABLA DE CONTENIDO

ÍNDICE DE TABLAS

ÍNDICE DE FIGURAS

1. Introduction

Embeded Base Conections (EBC) consist of a column welded to a bottom base plate (Refer to Fig. 1) and embedded into a concrete foundation. The applied forces, i.e., Axial Load, Bending Moment, and Shear, are resisted by a combination of the bearing stresses developed by the contact between the column flange and the foundation and by the vertical stresses at the bottom base plate. Grilli and Kanvinde conducted a large-scale experimental program to study the seismic response of EBC. This program's focus was the flexural capacity of these connections and the development of a strength method based on the insights gained from the tests. A total of five tests were evaluated. The difference among them was the embedded length (510 and 760mm), column size, and axial load level.

Figure 1: EBC detail (from [7,12])

The aim of this study is to replicate, using analytical technics (nonlinear finite element method using plain concrete constitutive models), the hysteretic behavior of the embedded base plate connections for full scale specimens presented in the doctoral dissertation of David Grilli "Seismic Response of embedded Column Bases Connections and Anchorages."

In order to characterize the connection response, a tridimensional mathematical model was developed using "ABAQUS" a commercial multipurpose FEA software developed by "Dassault Systemes".

The mathematical model of the connections seeks to replicate the hysteretic response of the connection, the maximum strength developed, and the stiffness and stiffness degradation during the cyclic response.

To achieve this, the model must capture the nonlinearity generated by the materials, the contacts interactions, and the geometrics effects.

The material nonlinearity is incorporated in the model using plain concrete constitutive modes that adequately take into account the tension and compression behavior of the material. The stiffness and strength degradation are considered using material damage parameters incorporated in the software material model

.

1.1 Backgound

Base plate connections are essential components in any type of structure. Moment resisting connections are of special importance in special moment frames, where the lateral resisting system stiffness and system collapse probability, is highly dependent of the system boundary conditions. Typically, exposed base plates are preferred for low-, and mid-rise buildings, while for tall buildings, embedded base connections are the norm. The response of this latter base configuration is controlled by complex interactions between the column flange and the bottom base plate with the concrete foundation, where the mechanisms to transfer, internal forces are idealized to underpin the current strength design methods. These mechanisms include horizontal bearing stresses between the column flange and the surrounding concrete, and vertical bearing stresses of the base plate and the concrete foundation. Current methods to estimate the strength of these connections are validated against a limited number of experimental tests complicating their generalization for the different configurations that have not been tested.

Although the results from these methods show good agreement with test data, the assumptions that underpin these methods have not been verified through sophisticated nonlinear finite element models. Motivated by this issue, this dissertation presents a series of nonlinear finite element models developed to provide insights on the behavior of embedded base connections for SMFs. These models incorporate the essential aspects that control the connection behavior, including constitutive material modeling, and contacts among the connection components. Possible design implications are discussed, while the limitations of the current work and future lines of research are outlined.

1.2 Objectives

In contrast with exposed based connections, where the behavior is well understood and there exist ample research and experimental essays that validate the connection; there are only a few studies that deals with embedded based connections and its seismic behavior is not well characterized.

The aim of this work is to calibrate analytical models to characterize the seismic behavior of the embedded based connection using results obtained from full scales tests of the embedded base connection. Once the mathematical model is calibrated, virtual prototypes of the connection can be modeled and its possible to run different alternatives of the propose connection to evaluate it sensitivity.

Taking into account that there exists limited information to understand the behaviour of embedded based connections, the aim of this work is to calibrate analytical models with experimental results. Virtual prototypes are an inexpensive to theorize possible design alternatives and evaluate their behavior prior to laboratory testing.

1.3 Experimental Program

Four real world size specimens test results are used to calibrate the analytical model. The specimens where subject to constant axial loading and then subject to a lateral load using cyclic loading protocol. The variables studied in the essays where embedment depth, axial load, and column size.

The real-world specimens' results are obtained from the doctor dissertation "Seismic Response of Embedded Column Base Connections and Anchorage" by David Grilli. The tested specimens consist in five real world scale connections:

Table 1: Test Matrix Geometry and Loads

Test Matrix Geometry and Loads

Test #	Column Size	P	$d_{embeded}$	Base Plate			
				t_p	N	B	Z
		[N]	[mm]	[mm]	[mm]	[mm]	[mm]
1	W14x370	445000 [C]	510	50	760	760	2850
2	W18x311	445000 [C]	510	50	865	710	2850
3	W14x370	0	760	50	760	760	3100
4	W14x370	445000 [C]	760	50	760	760	3100
5	W14x370	667000 [T]	760	50	760	760	3100

Test #5 is not talked into account in the analytical model calibration due to issues presented during the laboratory test.

In the reference dissertation, the author states that the test matrix may be considered a fractional factorial, such that pairs (or trios) of test may be used to examine the effects of isolated test variables. Test #1 and #2 examine the effect of column flange width, and test #1 and #4 examine the effect of embedment depth.

For the experimental test the columns were made artificially strong, the author states that this was done to force damage into the concrete foundation and study the force resisting mechanisms of the connection.

For the analytical model virtual replicas of the test setup were model, considering test #1 through #4; contact interaction, and material constitutive relationships were used in plasticity and damage material models to try to replicate the hysteretic cycle of the connection subject to the test loading protocol.

Taking into the account the fact that due to the way that the experimental essay is conceived, and recognizing that most of the damage was concentrated in the concrete foundation, priority was given in the analytical model to the concrete materials. The material model used is "Concrete Damage Plasticity Model", this is a continuum model based in plasticity and damage. The material model assumes that the two primary damage mechanisms are tension

crocking and compression crushing. The evolution of the yield (or failure) surface is controlled by two hardening variables.

For the element contact simulation it was used a general contact constrain based on the tangential and frictional interaction of the contact surfaces.

The SAC loading protocol was used for the cyclic loading.

1.4 Finite Element Models

A total of four FE models have been developed to study the seismic behavior of EBCs using the ABAQUS simulation platform. The models are composed of 3D Hex-structured elements. The meshes were refined in places where concentrations of stress are anticipated. As described in the previous section, the strength of the connection may be explained due to the contacts between the column flange and the base plate with the concrete foundation and the frictional interaction of the components. Thus, the contacts are an essential feature of these models. These contacts are simulated with a finite sliding formulation with Normal and Tangential interaction properties. The former property was defined as hard contact, while the latter with a frictional formulation following the penalty method. A friction coefficient of 0.45 is adopted as recommended by Gomez et al. In contrast, welded elements inside the connection are assigned the tie constraint (i.e., steel column and base plate, steel column, and stiffeners) since welds are detailed to resist fracture even at large deformations. Geometric nonlinearities, including large deformations formulations, are included in the models. The steel column and base plate are modeled with the Von-Misses surface with isotropic hardening. On the other hand, for concrete modeling, it is common to assume that this material behaves as an elastoplastic material in compression and brittle in tension. In this investigation, the concrete damaged constitutive plasticity (CDP) model was employed since it provides a general capability for modeling concrete and other quasi-brittle materials. The

CDP model uses concepts of isotropic damaged elasticity in combination with isotropic tensile and compressive plasticity to represent the inelastic behavior of concrete. It assumes that the main two failure mechanisms are tensile cracking and compressive crushing of the concrete material. The material properties are obtained from the ancillary tests reported for the full scale specimens, and true stresses and strains were assumed in the material formulation.

The FE models were subjected to the reported loading protocol based on the SAC load protocol in the Axial Load presence. In order to avoid the interference of P-delta effects in the connection response, the Axial Load was applied strategically at the bottom of the base plate. Thus, the Moment-Rotation response was recorded from the simulations and compared to validate the models with the associate experimental test.

1.5 Research Objective

The embedded base connection bearing mechanism is highly nonlinear it is based on a complex interaction of multiple variables; the ability to develop mathematical models that are able to characterize the load displacement relationship of the connection for cyclic load would enable us study the strength, stiffness, and deformation capacity of multiple design alternatives by which we would be able to evaluate different parameter sensitivity in the connection response before doing more physical essays. Also, a deeper understanding of the connection load resisting mechanisms and modes of failure would help us to understand better which components are critical to the adequate seismic performance of the connection.

The objective of this study is to calibrate analytical models with test data to replicate the hysteretic behavior of the connection.

2. DESARROLLO TEÓRICO

2.1 Experimental Program Description.

2.1.1) Test Specimen Geometry.

The embedded base connection consists of a steel wide flange column embedded in a concrete footing and supported at the base using a standard based plate. Web stiffeners are used in the steel column located near the concrete footing face.

The column height in the connection represents the typical inflection point of traditional moment frames first floor columns. In the test set up the following test and variables were used:
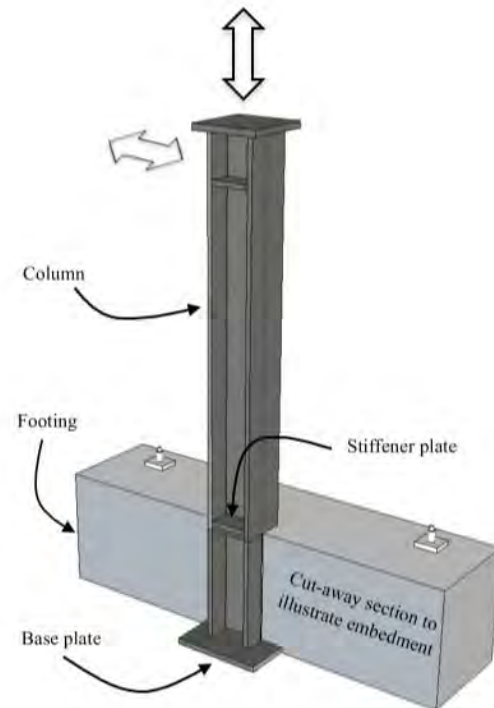
Figure 2: EBC Schematics (from [7,12])

				Base Plate			
Test #	Column Size	P	$d_{embeded}$	t_p	N	B	Z
		[N]	[mm]	[mm]	[mm]	[mm]	[mm]
1	W14x370	445000 [C]	510	50	760	760	2850
2	W18x311	445000 [C]	510	50	865	710	2850
3	W14x370	0	760	50	760	760	3100
4	W14x370	445000 [C]	760	50	760	760	3100
5	W14x370	667000 [T]	760	50	760	760	3100

Test Matrix Geometry and Loads

The embedment depth is defined as the distance between the top of the concrete surface and the top of the embedment base plate.

Tensile and axial loads where selected to be approximately 10-20% of the column yield capacity.

It was decided not to model test #5 due to the fact that there were issues with the test and it was terminated prior to completing the loading protocol due to slippage of the test block along the test floor

2.1.2) Test #1 Geometry

STEEL COLUMN
ASTM A572 Gr50

PLAIN CONCRETE
f'c=30 [MPa]

W14x370 - 20in
Escala: 1 : 25

Section 1-1
Escala: 1 : 50

EMBEDED BASE PLATE

PLAIN CONCRETE
f'c=30 [MPa]

Section 2-2
Escala: 1 : 50

EMBEDED BASE PLATE

PLAIN CONCRETE
f'c=30 [MPa]

Figure 3: Test#1 Set-up

2.1.3) Test #2 Geometry

STEEL COLUMN
ASTM A572 Gr50

PLAIN CONCRETE
f'c=30 [MPa]

W18x311 - 20in
Escala: 1 : 25

Section 3-3
Escala: 1 : 50

EMBEDED BASE PLATE

PLAIN CONCRETE
f'c=30 [MPa]

Section 4-4
Escala: 1 : 50

EMBEDED BASE PLATE

PLAIN CONCRETE
f'c=30 [MPa]

Figure 4:Test#2 Set-up

2.1.4) Test #3 and #4 Geometry

W14x370 - 30in
Escala: 1 : 25

Section 5-5
Escala: 1 : 50

Section 6-6
Escala: 1 : 50
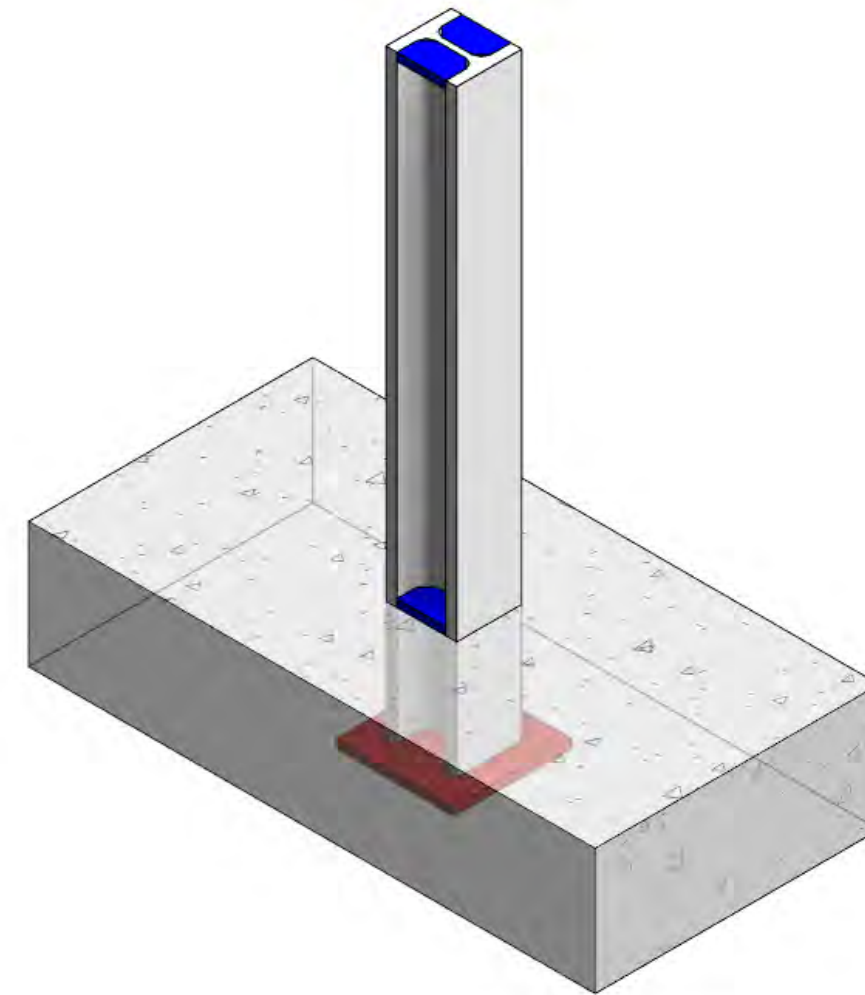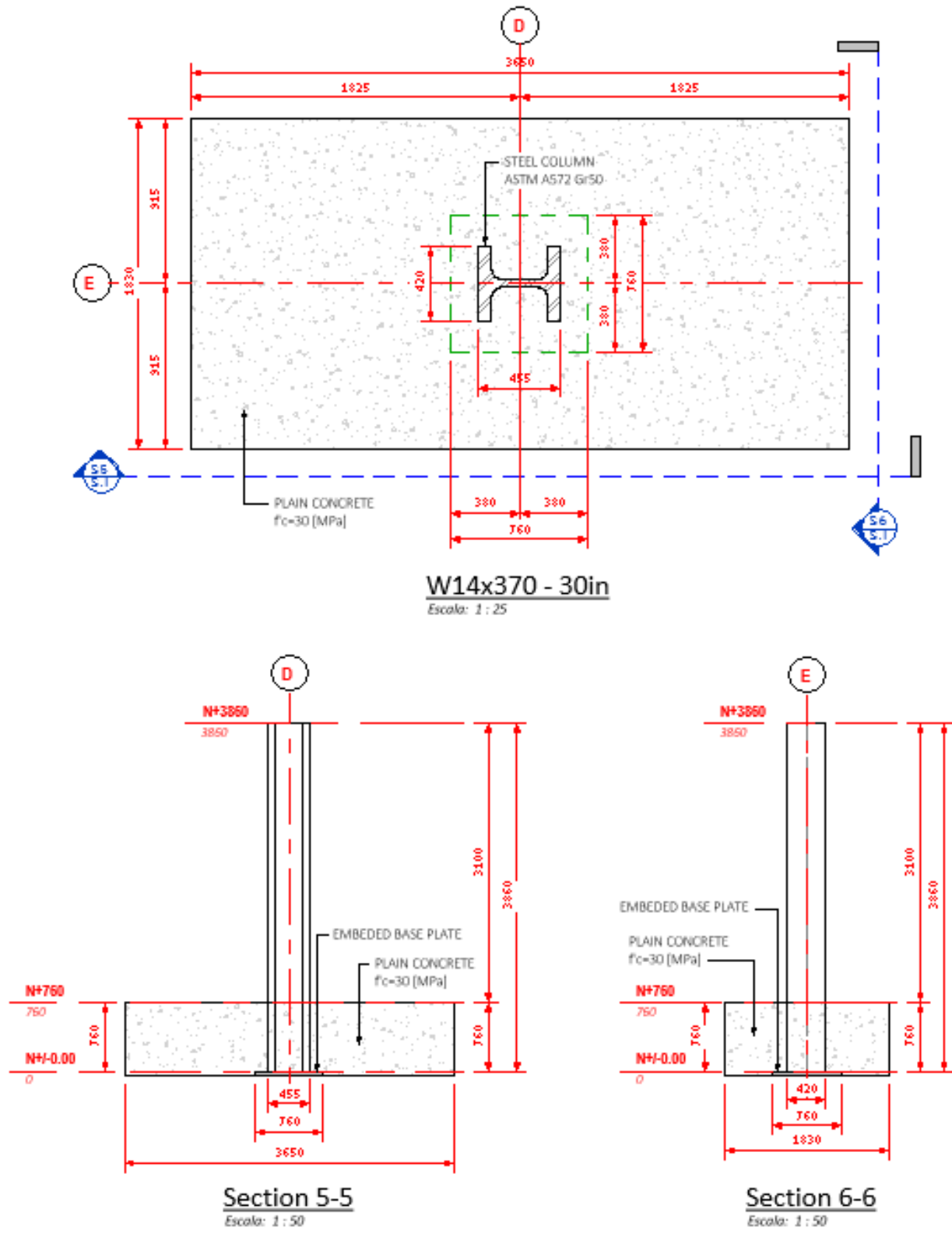
Figure 5:Test#3-4 Set-up

2.1.5) Test Matrix Profiles

The specimens used in the test matrix:
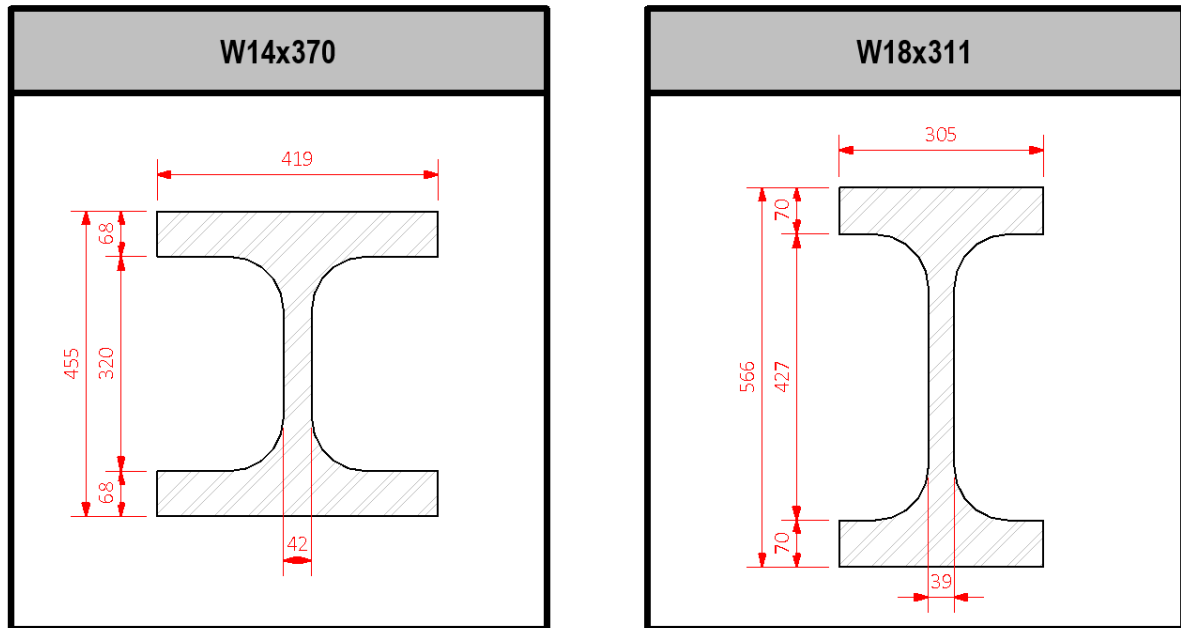
Figure 6: Experimental Test Columns

The dimension used in the mathematical model:
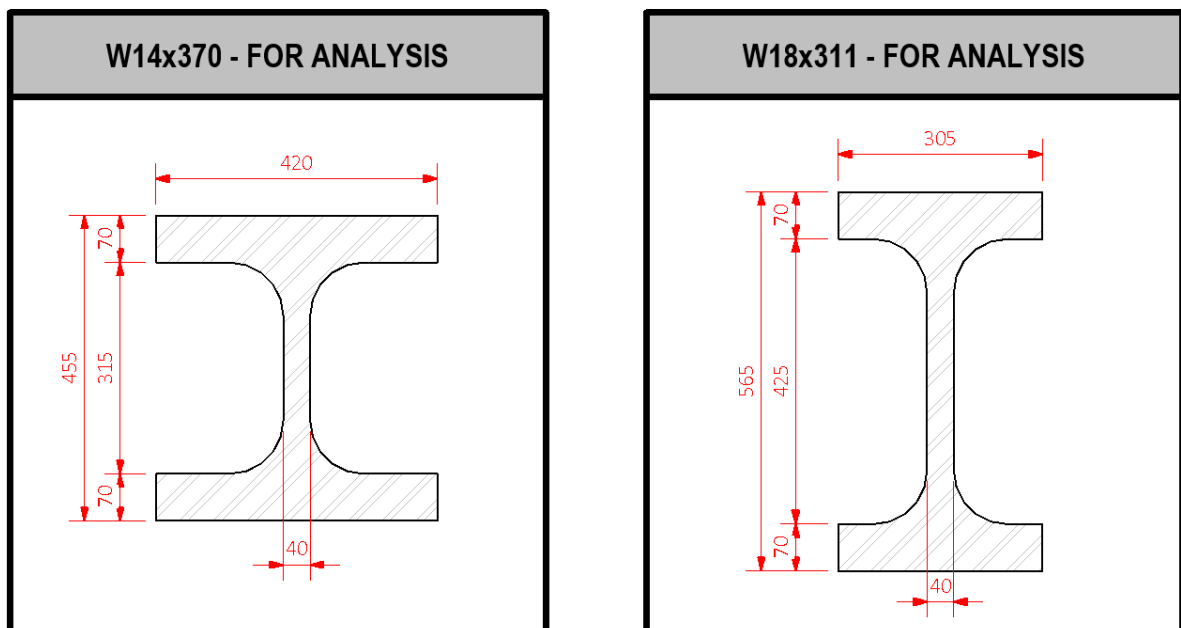
Figure 7: Analytical Model Columns

2.1.6) SAC Loading Protocol.

The loading protocol is based on "SAC Joint Venture Guidelines" (SEAOC, ATC, and

CUREe) and correspond to the loading sequence used in AISC 341-16-chapter K – "Loading

Sequence for Beam-to-Column Moment Connection". Where:

The drift angle, Θ, imposed on the test specimen shall be:

- 6 cycles at $\Theta = 0.00375$ [rad]

- 6 cycles at $\Theta = 0.0050$ [rad]

- 6 cycles at $\Theta = 0.0075$ [rad]

- 4 cycles at $\Theta = 0.01$ [rad]

- 2 cycles at $\Theta = 0.015$ [rad]

- 2 cycles at $\Theta = 0.02$ [rad]

- 2 cycles at $\Theta = 0.03$ [rad]
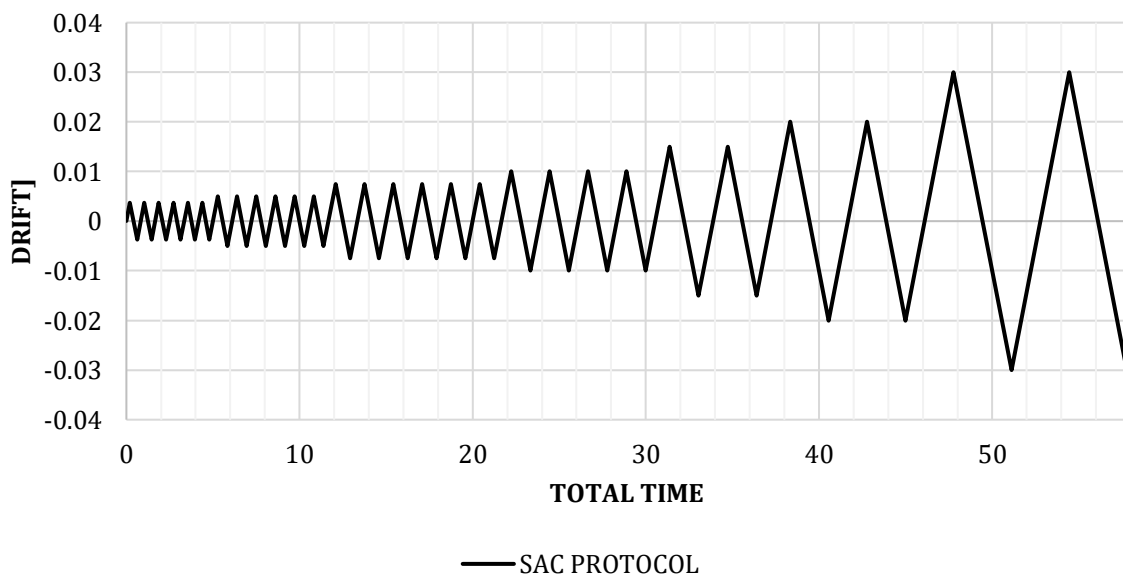
Figure 8:SAC Loading Protocol

To estimate column drift, lateral displacements of the column at the point of application of the

load are divided by the distance between the load and the top of the concrete pedestal.
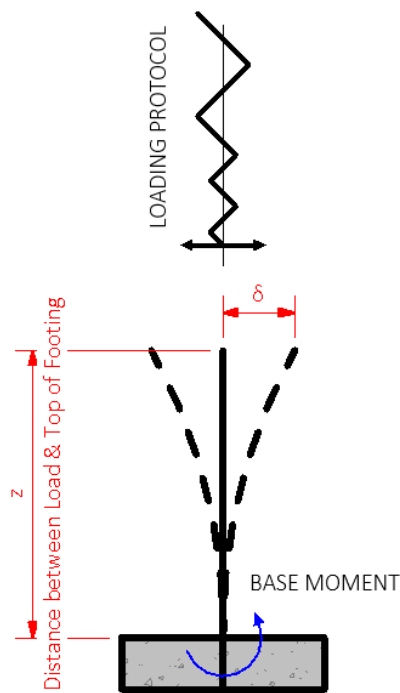
Figure 9: ECB Test Schematics

The load on the experimental test was applied Quasi-Statically, loading speed was less than 1.8% drift per minute, i.e., less than 0.018 radian rotation per minute. Axial load was applied prior to the application of lateral loading, and it was held constant throughout the test. Axial loads did not induce secondary moments in the test.

$$\Delta = \frac{\delta}{z}$$

$$M_{BASE} = F \times z$$

For each test analysis the essay loading protocol was applied to the model

2.1.7) Ancillary tests.

Ancillary test data is reported for the specimen's materials:

Table 2: Ancillary Test Data (from [7,12])

Study	Test # (Refer Table 3.1)	Weight (lbs)	Weight Density (lbs/ft^3)	Compressive Strength (psi)
Embedded Column Base Connections	1,2	X	X	3705
		X	X	3855
	5	28.7	146	4863
		28.9	147	4297
		29	148	3802

Columns, plates	ASTM 572 Gr. 50
Reinforcement	ASTM 615 Gr. 60

2.2 Experimental Results.

2.2.1) Damage Progression.

Linear response was observed until drift of approximately 0.005 radians.

Above 0.005 radians gradual nonlinearity was observed accompanied by the opening of small gaps adjacent to the tension flange.

Nonlinearity was accompanied by strength degradation and pinching response. The pinching response may be a product of the interaction nonlinearity.

Initial spalling of the concrete ahead of the column flange was observed at approximately 0.01 drift.

The increase of embedment depth shows a more gradual decrease in stiffness.

Peak moment was achieved between 1.5 and 5% drifts. After this point strength deteriorated, this may be attributed to the reduction in the moment resisted by the bearing ahead of the column flange as the concrete spalls.

Failure in the footing was defined as the drop of at least 30% of the peak load.

The nonlinear behavior of the connections was observed both in the material and in the contact geometry of the test specimens.

In terms of material nonlinearity, damage was observed in:

- Cracks radiating diagonally from the corners of the column on the top surface of the footing, accompanied by slight upward bulging of the concrete in the bearing zone between these cracks.

- Flexural cracks were observed on the sides the top of the footing on the tension side of the connection. These cracks were parallel to the column flanges, and were produce by bending of the entire block.

- Diagonal shear cracks on the sides of the block appeared as straight cracks parallel to the flange on the top surface.

In terms of contact geometry nonlinearity:

- On the tension side of the column, significant gapping was observed, with widths as large as 40 mm prior failure.

- Cracks opened and closed as the loading direction was reversed, and they grew in width and length as the applied drift was increased.

2.2.2) Trends in the Connection Response.

The specimens with higher embedment depths tend to show greater strength.

The observed failure modes were different based on the embedment depth. For 20in (510mm) the failure was characterized by a failure cone due to uplift. For 30in (760mm) failure occurs due to a gradual strength deterioration as the effective bearing depth of the column decreases due to spalling of the concrete extremities of the embedment region.

Most specimens appear to be stronger in the positive load direction. Damage caused by loading in the positive direction affects the strength in the negative direction.

Connection strength is proportional to the flange width (bearing surface).

2.2.3) Connection Failure Scenarios.

In tests #1 and #2 (shallower embedment), the final failure was accompanied by a sudden uplift of a cone of concrete on the tension side of the connection. As the bearing mechanism became less effective (due to concrete spalling and gapping) a greater fraction of the base moment is resisted by the uplift restrain bearing mechanism of the base plate. When the uplift force due to this moment reaches a critical value, failure occurs.

For tests #3 and #4, failure was more gradual. Increase deformations were accompanied by a steady drop in load, and failure tended to occur between 2.2 and 5%.

Axial loads show a slight increase in the connection capacity.

2.2.4) Connection Resistance Mechanism

Axial loads in the connection area resisted through the base plates, skin friction of the column and footing, and bearing of the stiffener.

The base moment is resisted by a combination of vertical and horizontal bearing, and panel shear.

Horizontal bearing of the column flanges against the concrete footing results in panel shear of the steel column web and a compression strut of the concrete between the column flanges.

Vertical bearing results in a moment pair generated in the base plate, resisted by concrete bearing in the compression zone a failure cone in the tension zone.
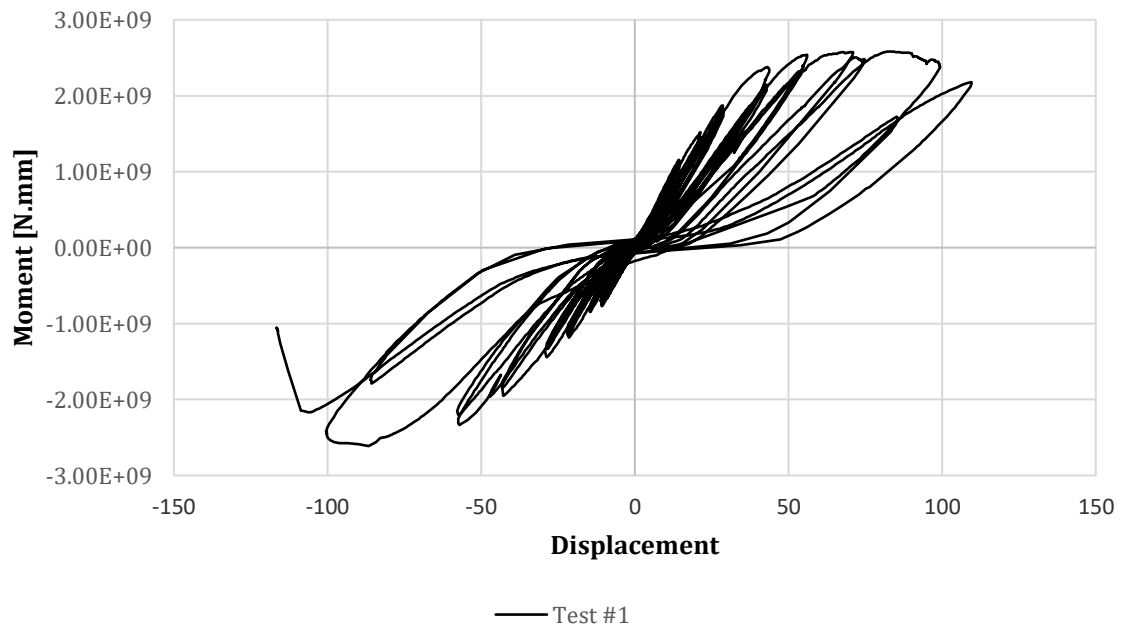
2.2.5) Test Results

2.2.5.1   Test #1

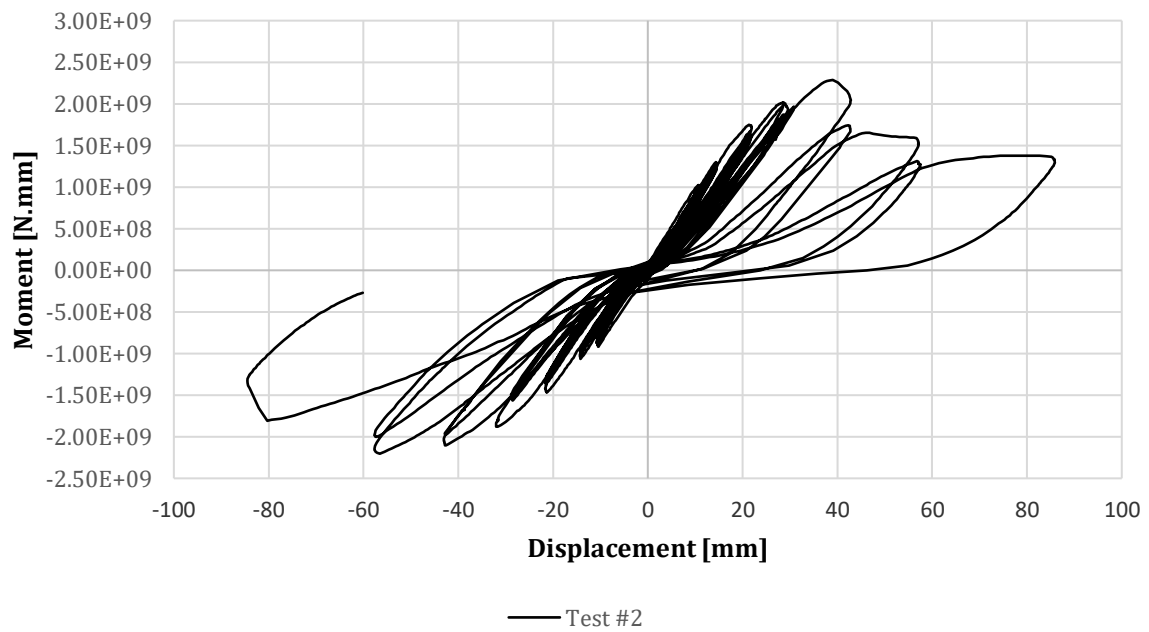Figure 10: Test#1 Results

2.2.5.2   Test #2

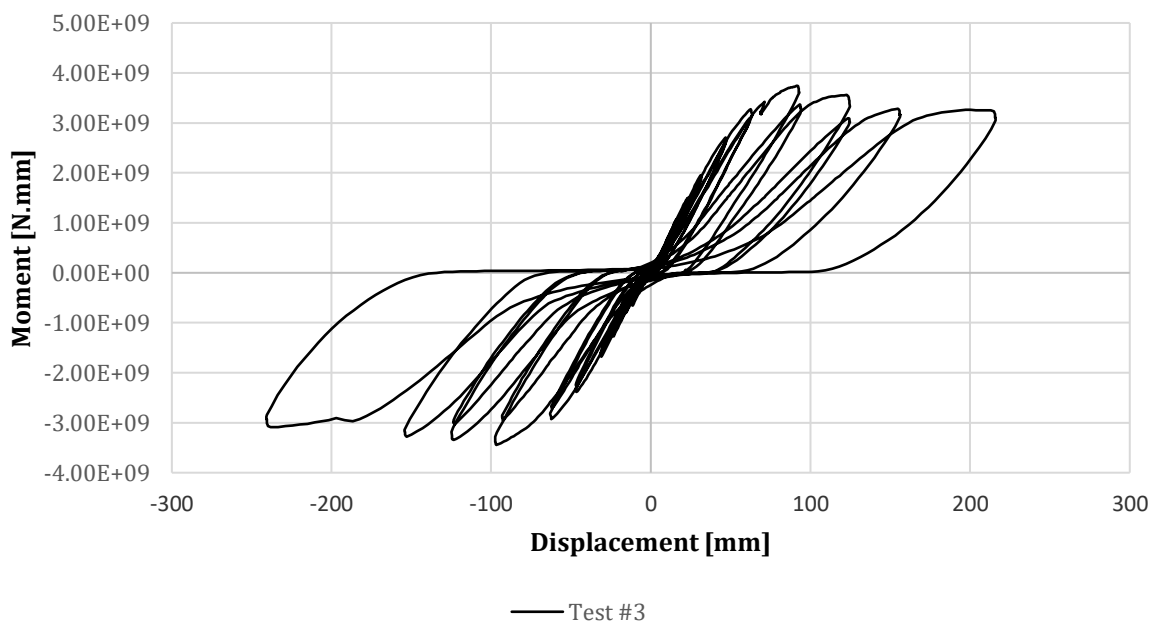Figure 11: Test #2 Results

2.2.5.3   Test #3

Figure 12: Test#3 Results

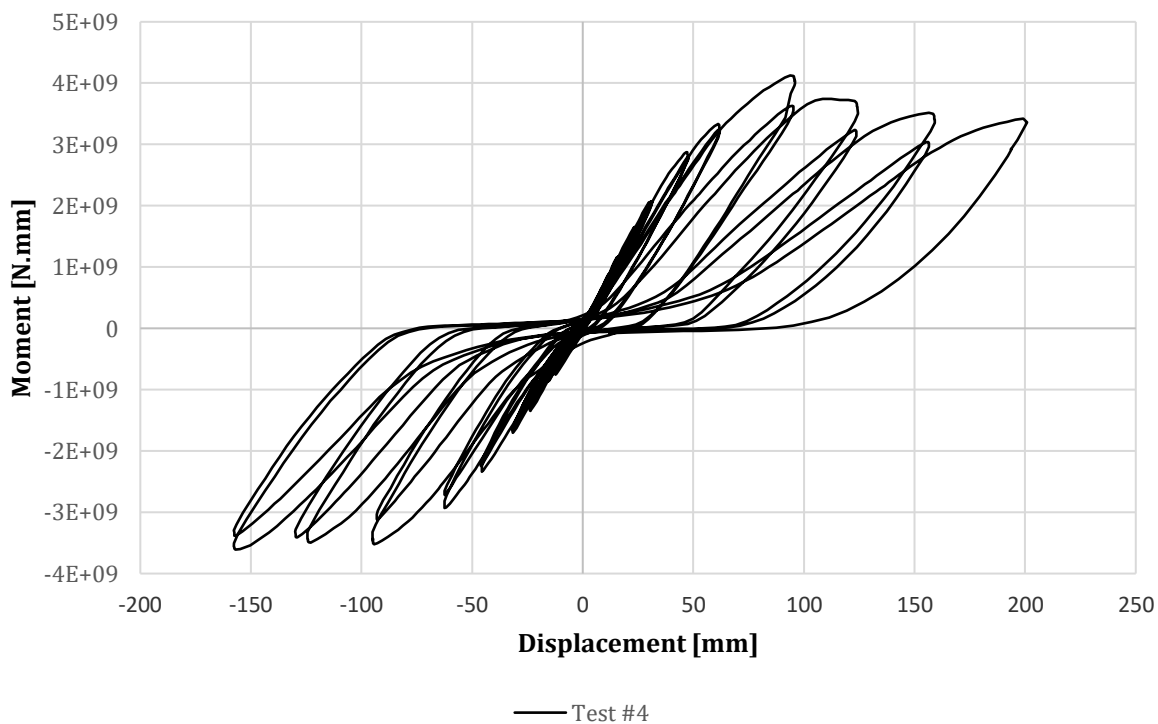### *2.2.5.4   Test #4*

Figure 13: Test#4 Results

2.3 Analytical Parameters.

2.3.1) Overview of Concrete Behaviour.

2.3.1.1   Reinforced concrete characteristic stages.

Typical stages that characterize the behavior of reinforce concrete can be represented using a

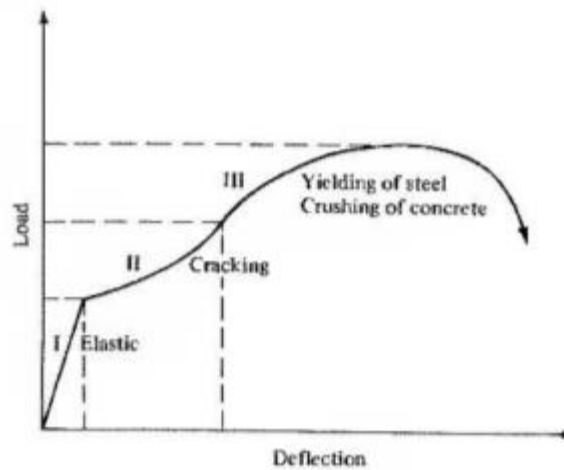load displacement plot, as shown in the figure.

Figure 14: Concrete Load - Deflection Curve (from [20])

Concrete behavior is highly nonlinear, and it can approximately be divided in three stages:

Elastic without cracking, cracking propagation, and plastic stage. The nonlinear behavior is a

consequence of cracking and reinforce steel plasticity.

2.3.1.2   FEA modeling of reinforce concrete.

For nonlinear finite element analysis of concrete, it is common to assume that the concrete

material behaves as an elastoplastic material in compression and a brittle material in tension.

To account for cracking in the material, there are two common approaches:

- To treat cracks as a system of distributed cracks in the continuum element, also known

  as smear crack model.

- By means of discrete crack introduction in the model. These cracks propagate as the

  element topology is changed.

To account for reinforce concrete strain compatibility, it is normal to assume complete adherence, although, it is possible to introduce relationships between both material to account for slippage and loss of adherence.

To model the reinforcement, it is usual to use truss elements represented by it uniaxial stress strain relationships. Flexural rigidity of reinforcement is often neglected.

The interaction between concrete and reinforcement takes into account two mechanisms, tension stiffening and shear dowel action.

2.3.1.3 *Concrete material properties.*

Concrete is made of a large number of micro cracks, specially between the interface of coarser aggregate and mortar. Microcracks propagation contributes to the nonlinear behavior of the material, even at low stress levels, and causes volume expansion of the material near failure.

Microcracks are a product of segregation, shrinkage, or thermal expansion in mortar. Due to these characteristics the size, and texture of the aggregates have a significant effect in the mechanical behaviors of concrete under loading.

2.3.1.3.1 *Uniaxial Compression*

In the typical concrete strain versus stress curve for uniaxial behavior it can be identified the typical behavior of the material. Until 30% of the maximum compressive stress the curve exhibits nearly linear behavior. For stresses above this point the curve shows a gradual increase in curvature un to 75%-90% the maximum compressive stress, beyond this point it bends sharply and approaches peak compressive stress. Past this point the curve has a descending part until crushing failure occurs.
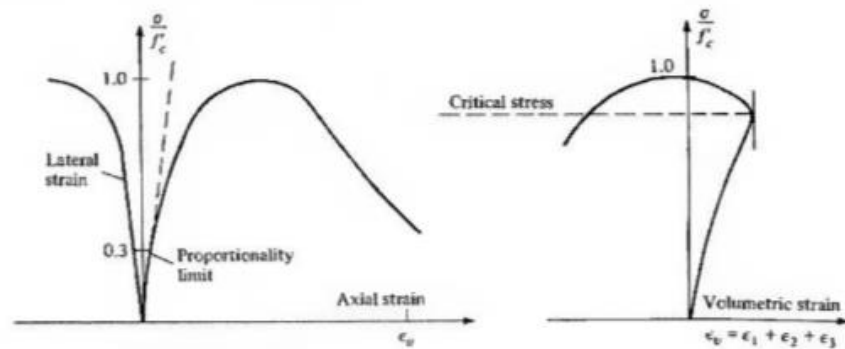
Figure 15: Concrete Volumetric Strain (from [20])

In the stress versus volumetric strain, it can be seen that the change in volume is nearly linear up to 75%-90% of the maximum compressive stress. At this point the direction of the volume change is reversed resulting in a volumetric expansion. The point at which the volumetric strain is at a minimum is called critical stress.

2.3.1.3.2   Uniaxial Tension

From the stress versus strain curve, it can be seen that up to 60% of the maximum tensile stress the behavior is nearly linear. The value of 75% of the maximum tensile stress is considered a reasonable point where the onset of unstable crack propagation tends to occur. The ratios of uniaxial tensile and compressive stress tend to be between 0.05 to 0.10. The modulus od elasticity under tension tend to be slightly higher than the modulus for compression.
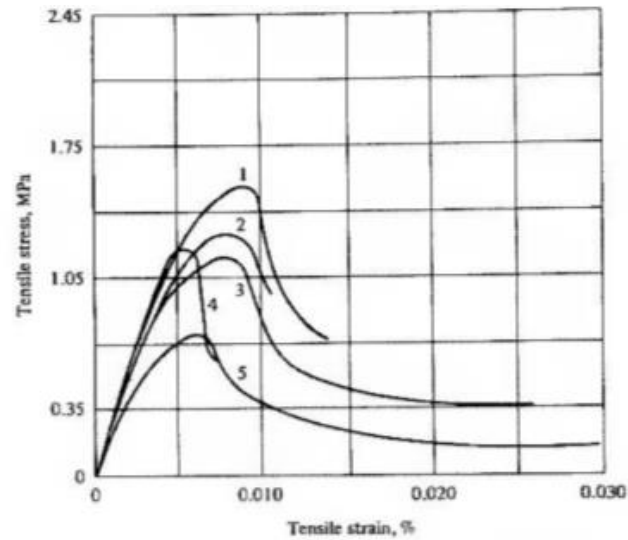
Figure 16: Concrete Tensile Stress vs Strain (from [20])

2.3.1.3.3 Biaxial Behavior

It has been observed that the maximum compressive stress in concrete increases in a biaxial

loading state. An maximum increment up to 25% can be achieved for a stress relationship of

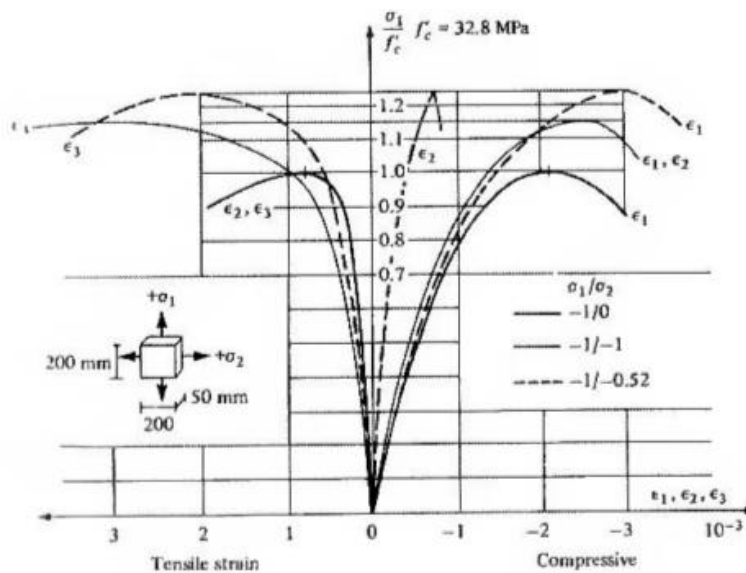σ2/ σ1 of 0.50; and it can decrease up to 16% for a stress relationship σ2/ σ1 of 1.00.

Figure 17: Concrete Biaxial Stress (from [20])

Near the failure point there is a volumetric increment as the compression stress increases. The inelastic volume increment is known as dilatancy, and in general it is attributed to the progressive grow of concrete microcracks.
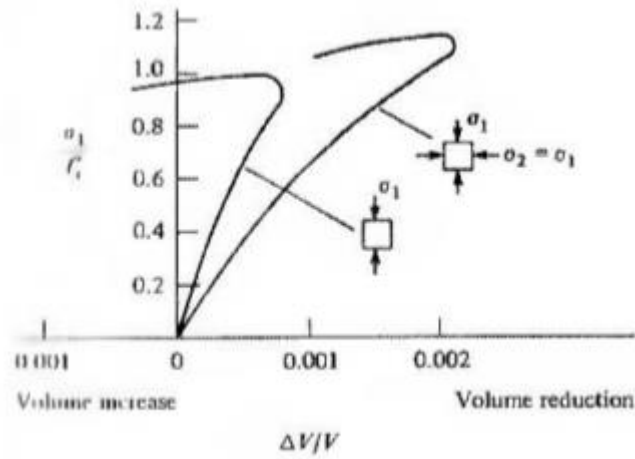

Figure 18: Concrete Biaxial Volumetric Strain (from [20])

2.3.2) Concrete damage plasticity model.

This section is an extract from the "ABAQUS User Manual" for the material model:

"Concrete damaged plasticity"

The concrete damaged plasticity model in ABAQUS:

- provides a general capability for modeling concrete and other quasi-brittle materials in all types of structures (beams, trusses, shells, and solids);

- uses concepts of isotropic damaged elasticity in combination with isotropic tensile and compressive plasticity to represent the inelastic behavior of concrete;

- can be used for plain concrete, even though it is intended primarily for the analysis of reinforced concrete structures;

- can be used with rebar to model concrete reinforcement;

- is designed for applications in which concrete is subjected to monotonic, cyclic, and/or dynamic loading under low confining pressures;

- consists of the combination of nonassociated multi-hardening plasticity and scalar (isotropic) damaged elasticity to describe the irreversible damage that occurs during the fracturing process;

- allows user control of stiffness recovery effects during cyclic load reversals;

2.3.2.1   Mechanical Behavior

The model is a continuum, plasticity-based, damage model for concrete. It assumes that the main two failure mechanisms are tensile cracking and compressive crushing of the concrete material. The evolution of the yield (or failure) surface is controlled by two hardening variables, ϵ_t^{-pl} y ϵ_c^{-pl}, linked to failure mechanisms under tension and compression loading,

respectively. We refer to ϵ_t^{-pl} y ϵ_c^{-pl} as tensile and compressive equivalent plastic strains,

respectively.

2.3.2.1.1 Uniaxial Tension and Compression Stress Behavior

The model assumes that the uniaxial tensile and compressive response of concrete is

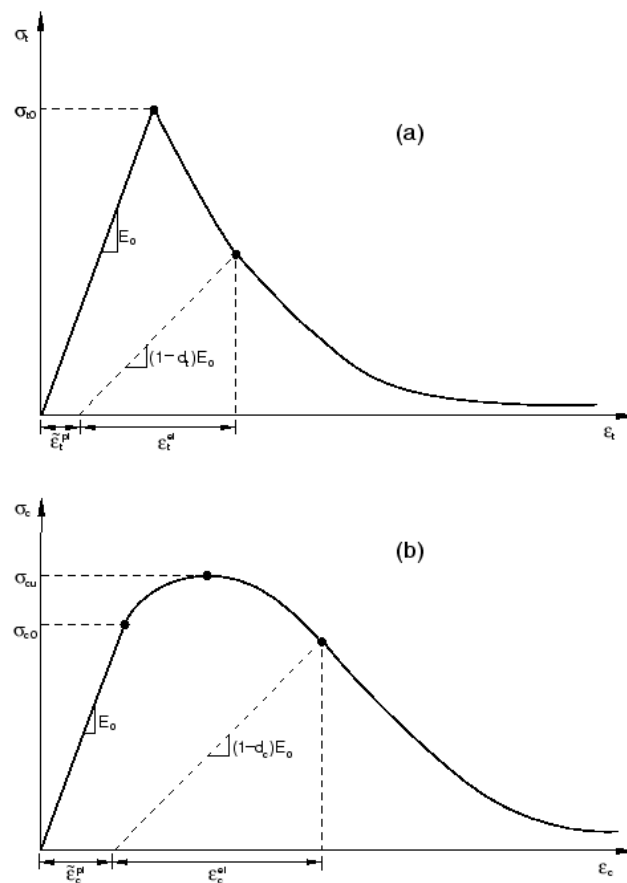characterized by damaged plasticity, as shown in the figure:

Figure 19: CDP Stress vs Strain (from [21])

Under uniaxial tension the stress-strain response follows a linear elastic relationship until the

value of the failure stress, σ_{to}, is reached. The failure stress corresponds to the onset of micro-

cracking in the concrete material. Beyond the failure stress the formation of micro-cracks is

represented macroscopically with a softening stress-strain response, which induces strain

localization in the concrete structure. Under uniaxial compression the response is linear until

the value of initial yield, σ_{co}. In the plastic regime the response is typically characterized by stress hardening followed by strain softening beyond the ultimate stress, σ_{cu}.

It is assumed that the uniaxial stress-strain curves can be converted into stress versus plastic-strain curves. (This conversion is performed automatically by Abaqus from the user-provided stress versus "inelastic" strain data

$$\sigma_t = \sigma_t\left(\epsilon_t^{\tilde{p}l}, \dot{\epsilon}_t^{\tilde{p}l}, \theta, f_i\right)$$

$$\sigma_c = \sigma_c\left(\epsilon_c^{\tilde{p}l}, \dot{\epsilon}_c^{\tilde{p}l}, \theta, f_i\right)$$

where the subscripts t and c refer to tension and compression, respectively; $\epsilon_t^{\tilde{p}l}$ and $\epsilon_c^{\tilde{p}l\sim}$ are the equivalent plastic strains, $\dot{\epsilon}_t^{\tilde{p}l}$ and $\dot{\epsilon}_c^{\tilde{p}l}$ are the equivalent plastic strain rates, θ is the temperature, and fi (i = 1,2,…) are other predefined field variables.

When the concrete specimen is unloaded from any point on the strain softening branch of the stress-strain curves, the unloading response is weakened: the elastic stiffness of the material appears to be damaged (or degraded). The degradation of the elastic stiffness is characterized by two damage variables, d_t and d_c, which are assumed to be functions of the plastic strains, temperature, and field variables:

$$d_t = d_t\left(\epsilon_t^{\tilde{p}l}, \theta, f_i\right); 0 \leq d_t \leq 1$$

$$d_c = d_c\left(\epsilon_c^{\tilde{p}l}, \theta, f_i\right); 0 \leq d_t \leq 1$$

The damage variables can take values from zero, representing the undamaged material, to one, which represents total loss of strength.

If E_0 is the initial (undamaged) elastic stiffness of the material, the stress-strain relations under uniaxial tension and compression loading are, respectively:

$$\sigma_t = (1 - d_t)E_0\left(\epsilon_t - \epsilon_t^{\tilde{p}l}\right)$$

$$\sigma_c = (1 - d_c)E_0\left(\epsilon_c - \epsilon_c^{\tilde{p}l}\right)$$

We define the "effective" tensile and compressive cohesion stresses as

$$\bar{\sigma}_t = \frac{\sigma_t}{(1 - d_t)} = E_0\left(\epsilon_t - \epsilon_t^{-pl}\right)$$

$$\bar{\sigma}_c = \frac{\sigma_c}{(1 - d_c)} = E_0\left(\epsilon_c - \epsilon_c^{-pl}\right)$$

The effective cohesion stresses determine the size of the yield (or failure) surface.

2.3.2.1.2   *Uniaxial Cyclic Behavior*

Under uniaxial cyclic loading conditions the degradation mechanisms are quite complex, involving the opening and closing of previously formed micro-cracks, as well as their interaction. Experimentally, it is observed that there is some recovery of the elastic stiffness as the load changes sign during a uniaxial cyclic test. The stiffness recovery effect, also known as the "unilateral effect," is an important aspect of the concrete behavior under cyclic loading. The effect is usually more pronounced as the load changes from tension to compression, causing tensile cracks to close, which results in the recovery of the compressive stiffness.

The concrete damaged plasticity model assumes that the reduction of the elastic modulus is given in terms of a scalar degradation variable *d* as

$$E = (1 - d)E_0$$

where E_0 is the initial (undamaged) modulus of the material.

This expression holds both in the tensile ($\sigma_{11} > 0$) and the compressive ($\sigma_{11} < 0$) sides of the cycle. The stiffness degradation variable, *d*, is a function of the stress state and the uniaxial damage variables, d_t and d_c. For the uniaxial cyclic conditions Abaqus assumes that

$$(1 - d) = (1 - s_t d_c)(1 - s_c d_t)$$

where st and sc are functions of the stress state that are introduced to model stiffness recovery effects associated with stress reversals. They are defined according to

$$s_t = 1 - w_t r^*(\sigma_{11}) \; ; 0 \leq w_t \leq 1$$

$$s_c = 1 - w_c\big(1 - r^*(\sigma_{11})\big) \; ; 0 \leq w_c \leq 1$$

Where:

$$r^*(\sigma_{11}) = H(\sigma_{11}) = \begin{cases} 1 \; si \; \sigma_{11} > 0 \\ 0 \; si \; \sigma_{11} < 0 \end{cases}$$
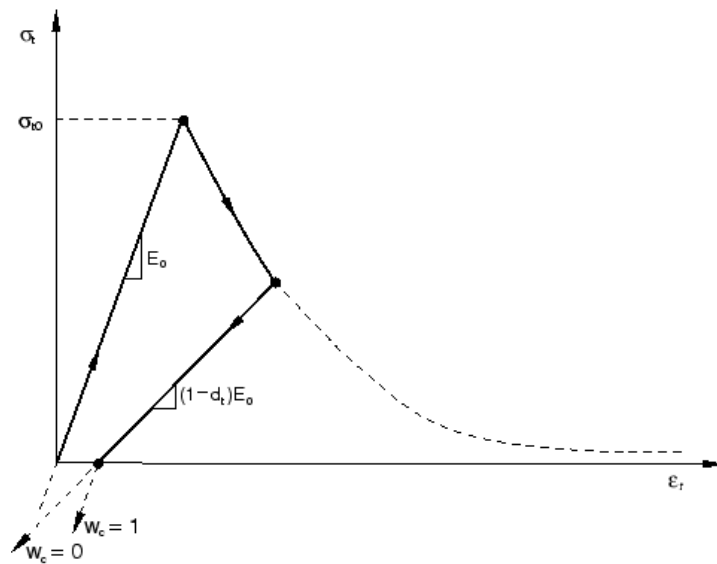
Figure 20: CDP Tensile Stress vs Strain (from [21])

2.3.2.2   *Defining Compresive Behavior*

Compressive stress data are provided as a tabular function of inelastic (or crushing) strain, $\varepsilon_c^{\sim in}$, and, if desired, strain rate, temperature, and field variables. The stress-strain curve can be defined beyond the ultimate stress, into the strain-softening regime.

Hardening data are given in terms of an inelastic strain, $\varepsilon_c^{\sim in}$, instead of plastic strain, $\varepsilon_c^{\sim pl}$. The compressive inelastic strain is defined as the total strain minus the elastic strain corresponding to the undamaged material, as illustrated in:

Figure 21: CDP Compressive Stress vs Strain (from [21])

2.3.2.3   *Visualization of Crack Directions*

Unlike concrete models based on the smeared crack approach, the concrete damaged

plasticity model does not have the notion of cracks developing at the material integration

point. However, it is possible to introduce the concept of an effective crack direction with the

purpose of obtaining a graphical visualization of the cracking patterns in the concrete

structure. Different criteria can be adopted within the framework of scalar-damage plasticity

for the definition of the direction of cracking. Following Lubliner et. al. (1989), we can

assume that cracking initiates at points where the tensile equivalent plastic strain is greater

than zero, $\varepsilon_t^{\sim \mathrm{pl}} > 0$, and the maximum principal plastic strain is positive. The direction of the

vector normal to the crack plane is assumed to be parallel to the direction of the maximum

principal plastic strain.

2.4 Modeling Parameters

2.4.1) Material Models

2.4.1.1   Steel

For the model steel is assumed to behave as a linear elastic material. The mechanical

properties used in the model are:

Table 3: ABAQUS Steel Parameters

Steel	
Mass Density	7.85E-09
Young's Module	200000
Poisson's Ratio	0.3
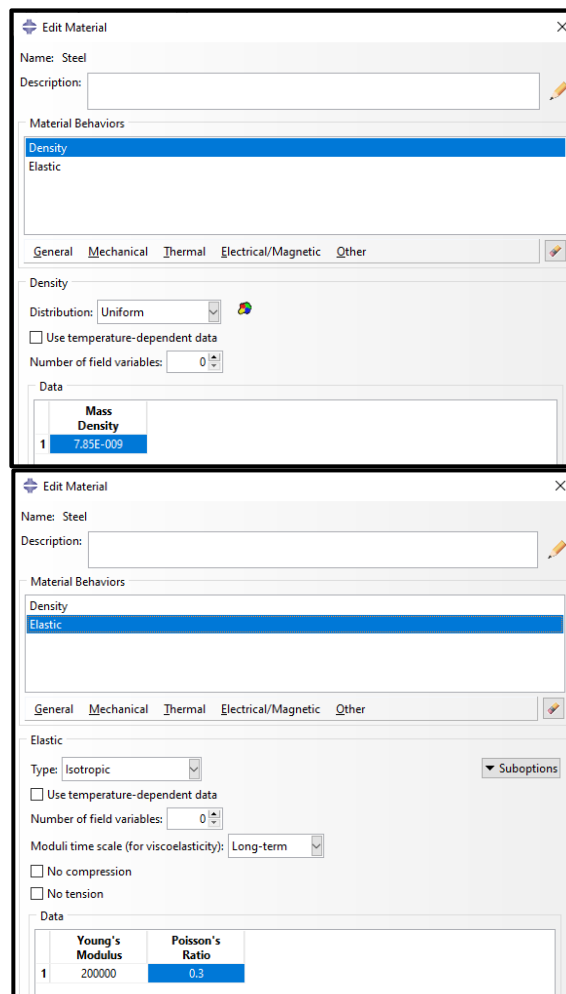
Figure 22: ABAQUS Steel Material Properties

2.4.1.2 Concrete

For the model concrete is assumed to behave as a nonlinear material. It was assumed that the

material model behaves as a plasticity model (damage parameters are not specified).

Table 4:CDP Parameters

Concrete	
Mass Density	2.40E-09
Young's Module	25000
Poisson's Ratio	0.2
Dilatation Angle	31
Eccentricity	0.1
fb0/fc0	1.16
K	0.666
Viscosity Parameter	0.001
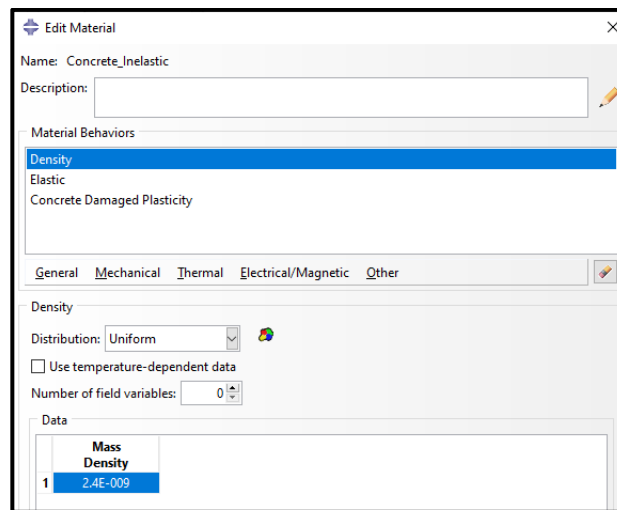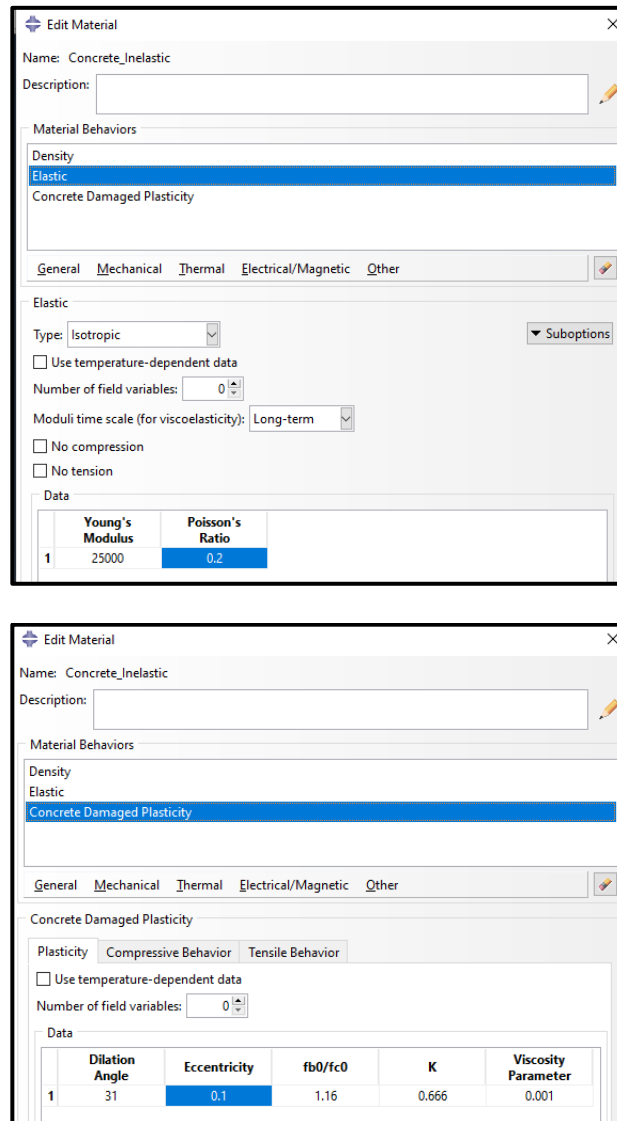
Figure 23: CDP Material Properties

2.4.1.2.1 Concrete Constitutive Model - Compression

For the unconfined concrete stress/strain relationship Popovics (1973) proposed equation was used.

$$\frac{f_c}{f_c'} = \frac{n\left(\frac{\varepsilon_c}{\varepsilon_{co}}\right)}{(n-1) + \left(\frac{\varepsilon_c}{\varepsilon_{co}}\right)^n}$$

$$n = 0.4 \times 10^{-3} f_c' \ [psi] + 1.0$$

$$f_c' = 30 \ [MPa]$$

$\varepsilon_{co} = 0.0020$
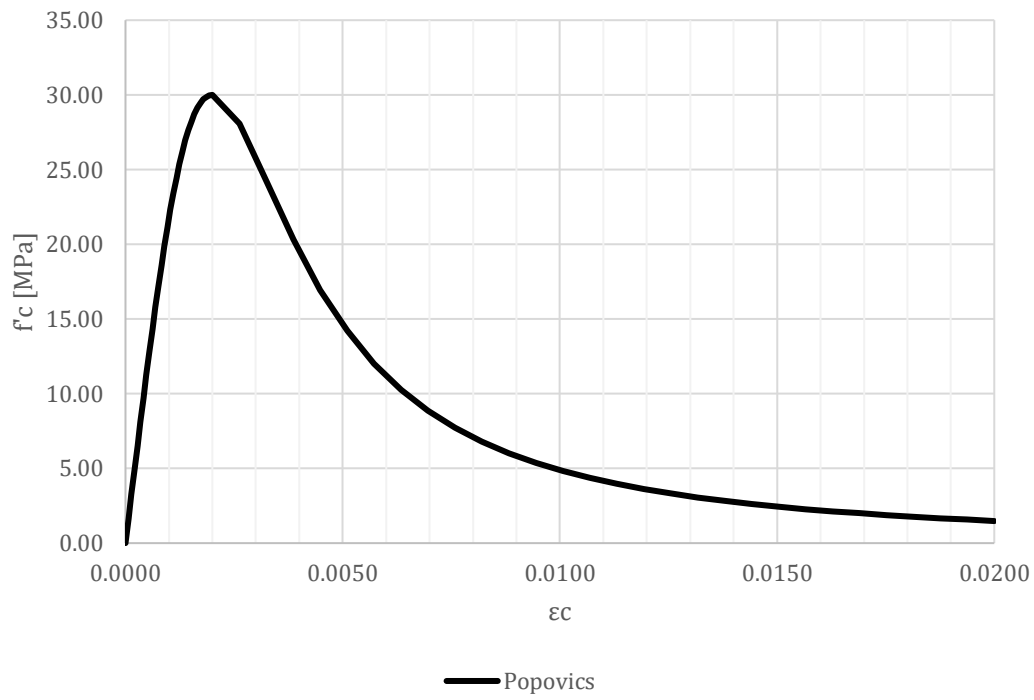
Figure 24: Concrete Compressive Stress vs Strain Relationship

Table 5: CDP Yield Stress vs Inelastic Strain

ABAQUS COMPRESSION	
σ	ε_c^{in}
9.00	0.00000
16.35	0.00002
22.56	0.00009
27.00	0.00023
29.41	0.00046
29.99	0.00077
29.20	0.00113
27.57	0.00154
25.53	0.00196
23.37	0.00238
21.26	0.00280
19.29	0.00322
17.50	0.00363
15.90	0.00403
14.47	0.00442
13.20	0.00481
12.08	0.00519
11.09	0.00556
10.21	0.00593
9.43	0.00630
8.73	0.00666
8.11	0.00702

7.55	0.00738
7.05	0.00773
6.59	0.00808
6.18	0.00843
5.81	0.00878
5.47	0.00913
5.16	0.00947
4.87	0.00982
4.61	0.01016
4.37	0.01050
4.15	0.01085
3.95	0.01119
3.76	0.01153
3.58	0.01187
3.42	0.01221
3.27	0.01255
3.13	0.01288
2.99	0.01322
2.87	0.01356
2.75	0.01390
2.65	0.01424
2.54	0.01457
2.45	0.01491
2.36	0.01524
2.27	0.01558
2.19	0.01592
2.11	0.01625
2.04	0.01659
1.97	0.01692
1.91	0.01726
1.85	0.01759
1.79	0.01793
1.73	0.01826
1.68	0.01860
1.63	0.01893
1.58	0.01927
1.53	0.01960

2.4.1.2.2   Concrete Constitutive Model – Tension

For the stress/strain relationship:

$$f_t' = 0.63\sqrt{f_c'}$$

$$\varepsilon_{ct} = f_t'/E_c$$

$$f_t = f_{ct}\left(\frac{\varepsilon_{ct}}{\varepsilon_t}\right)^{0.4}$$

$$f_c' = 30 \ [MPa]$$
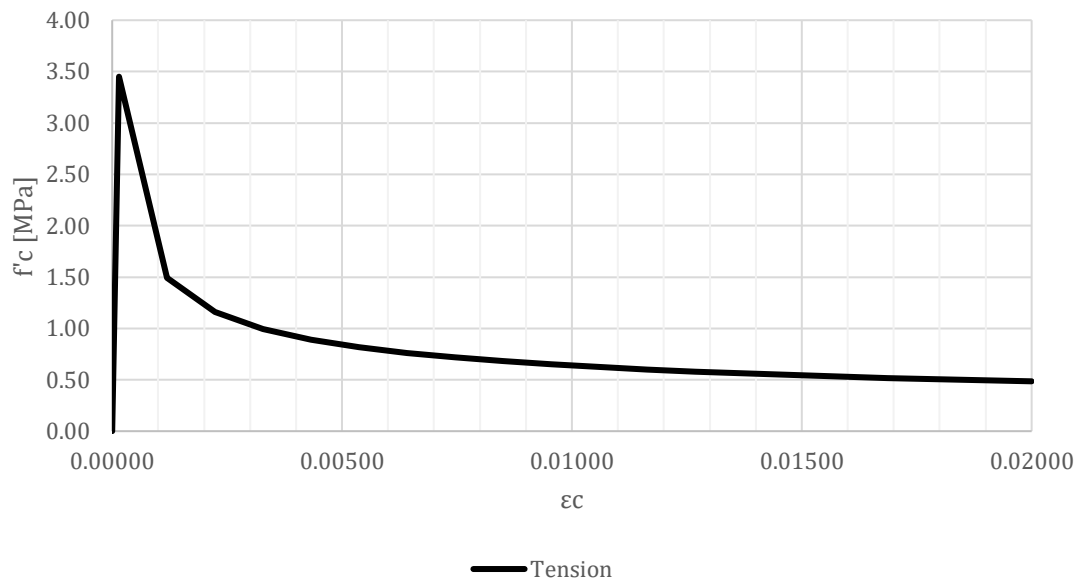
Figure 25: Concrete Tensile Stress vs Strain Relationship

Table 6: CDP Yield Tensile Stress vs Inelastic Strain

ABAQUS TENSION	
σ	ε_t^{in}
3.45	0.00000
1.49	0.00113
1.16	0.00219
1.00	0.00324
0.89	0.00429
0.82	0.00534
0.76	0.00638
0.72	0.00743
0.68	0.00848
0.65	0.00952
0.62	0.01057
0.60	0.01162
0.58	0.01266
0.56	0.01371
0.55	0.01475
0.53	0.01580
0.52	0.01684
0.51	0.01789
0.49	0.01893
0.48	0.01998

2.4.1.2.3   Damage Parameters

The model was assumed as a plasticity model, damage parameters where not specified.

2.4.1.2.4   Stiffness Recovery

Default values for the stiffness recovery factors are used in the model. wc=1 is used assuming fully compressive stiffness recovery as the load changes from tension to compression. wt=0 is used assuming that tension stiffness is non recover as the load changes from compression to tension.

2.4.1.2.5   Rate dependent data

Rate dependent data was not specified as the model was model as Implicit.

2.4.2) Contact Modeling

Contact was model in ABAQUS as "General Contact" between two surfaces. Contact was modeled using tangential and normal interactions.

For the tangential behavior it was assumed a friction coefficient of 0.45.
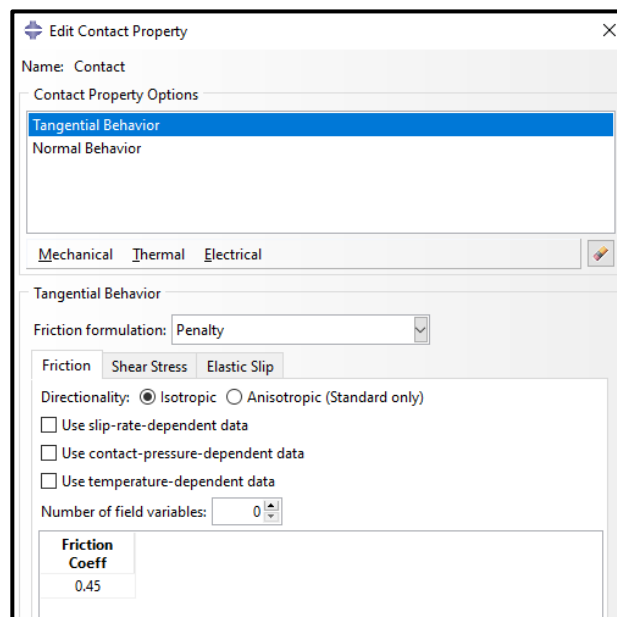
Figure 26: Tangential Contact Interaction

For the normal behavior it was assumed as "Hard Contact"
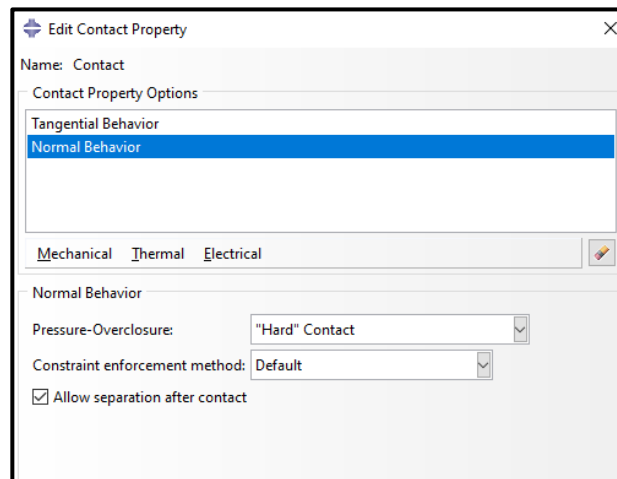
Figure 27: Normal Contact Interaction

2.5 Loading Protocol

For the models it was used the same loading protocol reported in the experimental essays. It was assumed a loading rate of 0.018 [Drift/minute]. In the model the loading rate parameter is only relevant to determine the time step parameters.

2.5.1) Test #1
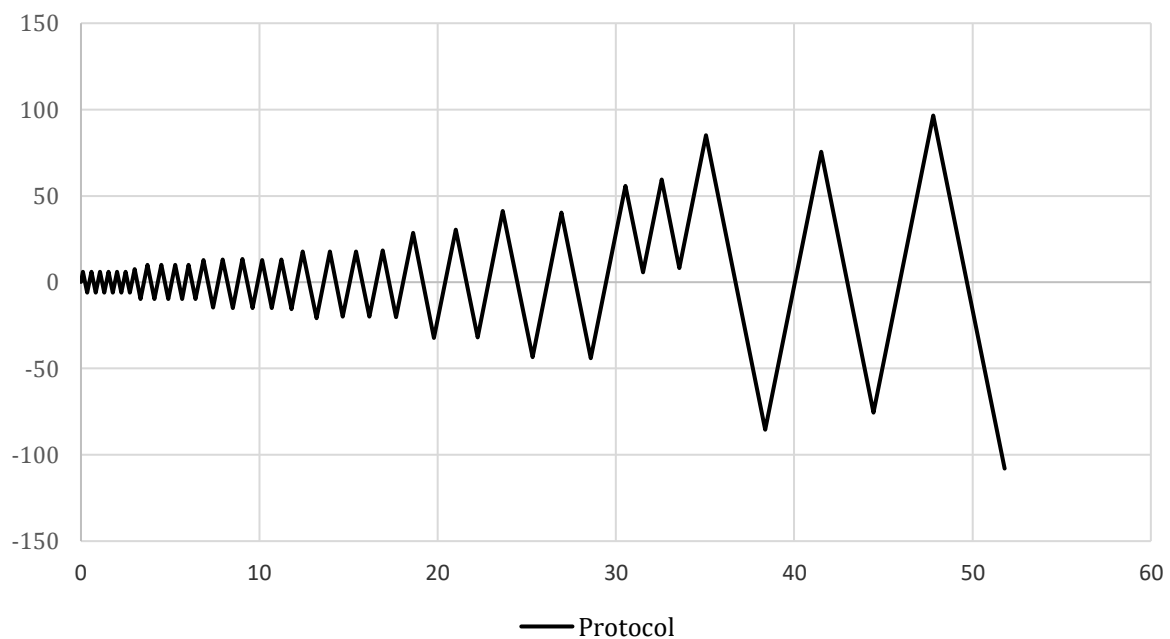
Figure 28: Test#1 Loading Protocol

2.5.2) Test #2
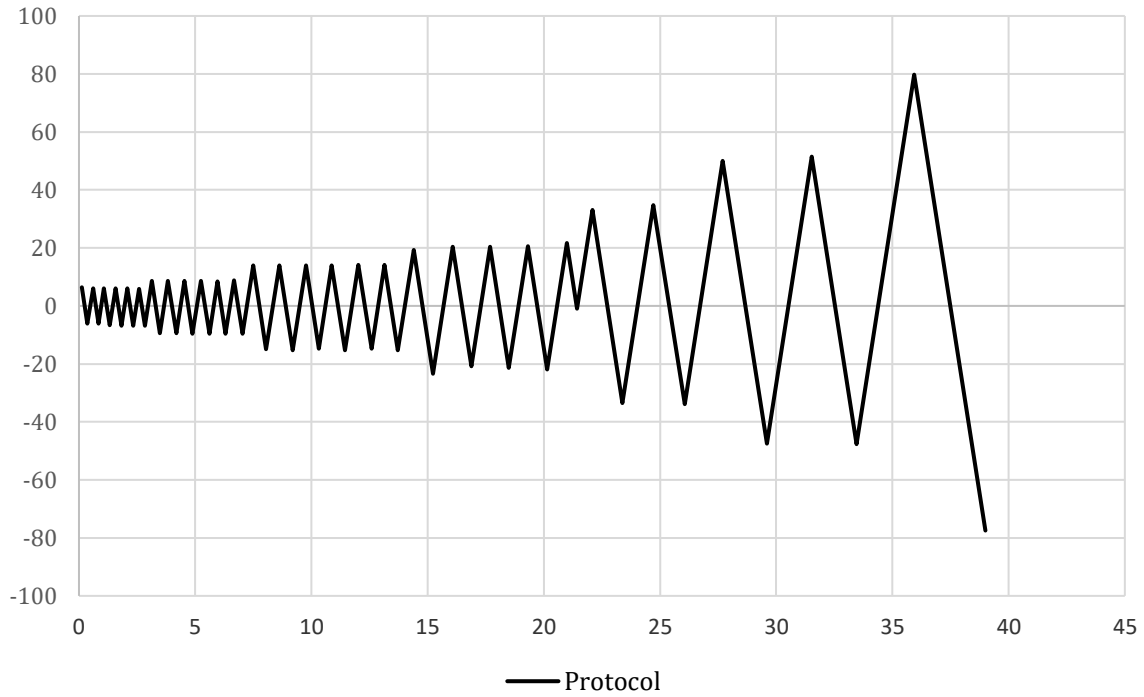
Figure 29: Test#2 Loading Protocol

2.5.3) Test #3
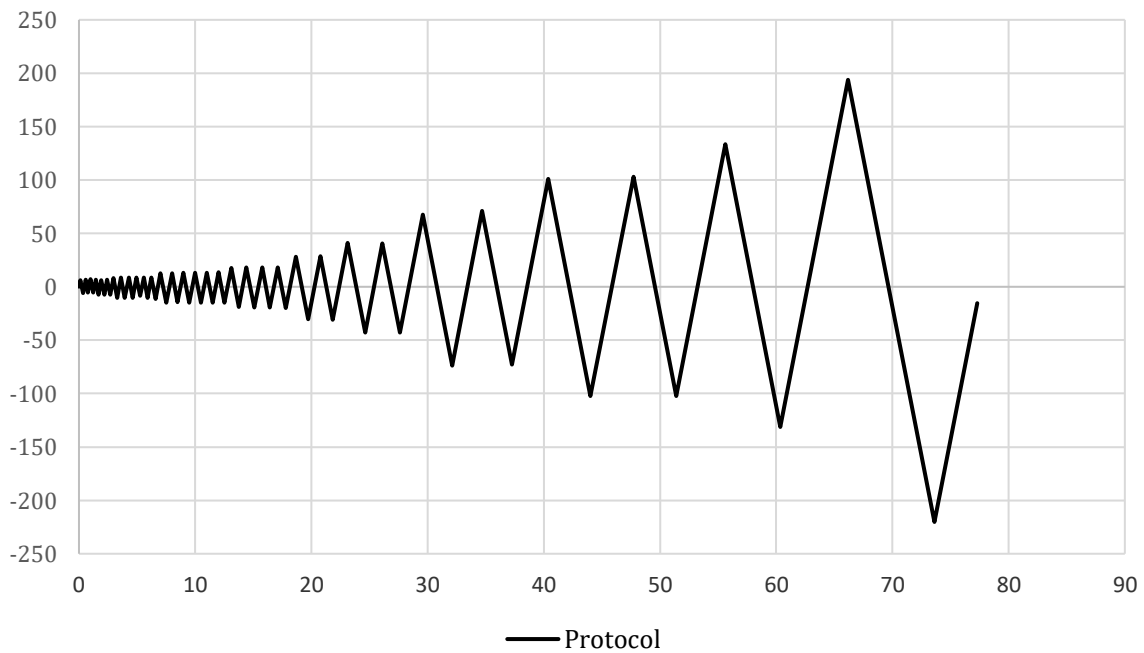
Figure 30: Test#3 Loading Protocol

2.5.4) Test #4
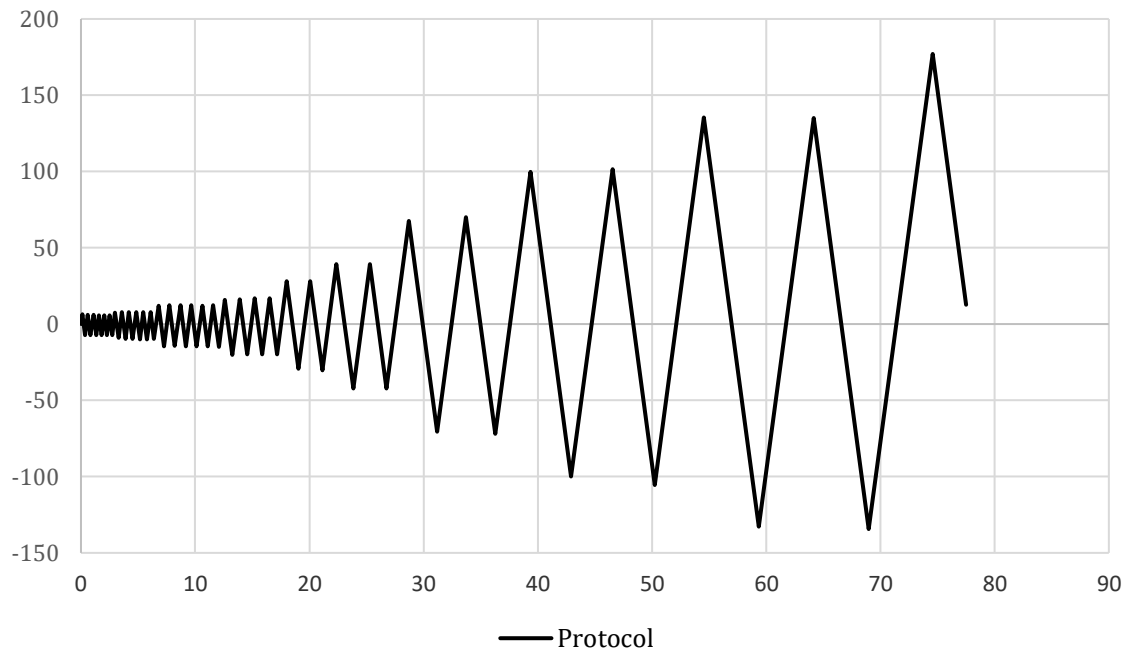
Figure 31: Test#4 Loading Protocol

3. ANALYSIS RESULTS

3.1 Analysis Overview

A mathematical model was constructed from the EBC connection layout. The model incorporates the connection material and contacts nonlinearities and tries to replicate the hysteretic response of the connection.

The essential aspects of the hysteretic response are capture by the numerical results. Specifically, the simulations are able to capture the pinching behavior observed in the tests. Cyclic deterioration of the strength and the unloading stiffness are identified in these connections and well-represented in the simulations. The parameters that define the response's backbone curve are the Moment at First Yield, the Initial Rotational Stiffness, the Peak Moment Strength, and the Rotation Associate to the Peak Strength. A visual inspection of the model results indicates that the differences between the simulations' parameters to the experimental tests' corresponding values are neglectable. Consequently, in the authors' opinion, the FE models are able to capture the key features of the connection response and are appropriate to investigate the behavior of EBC.
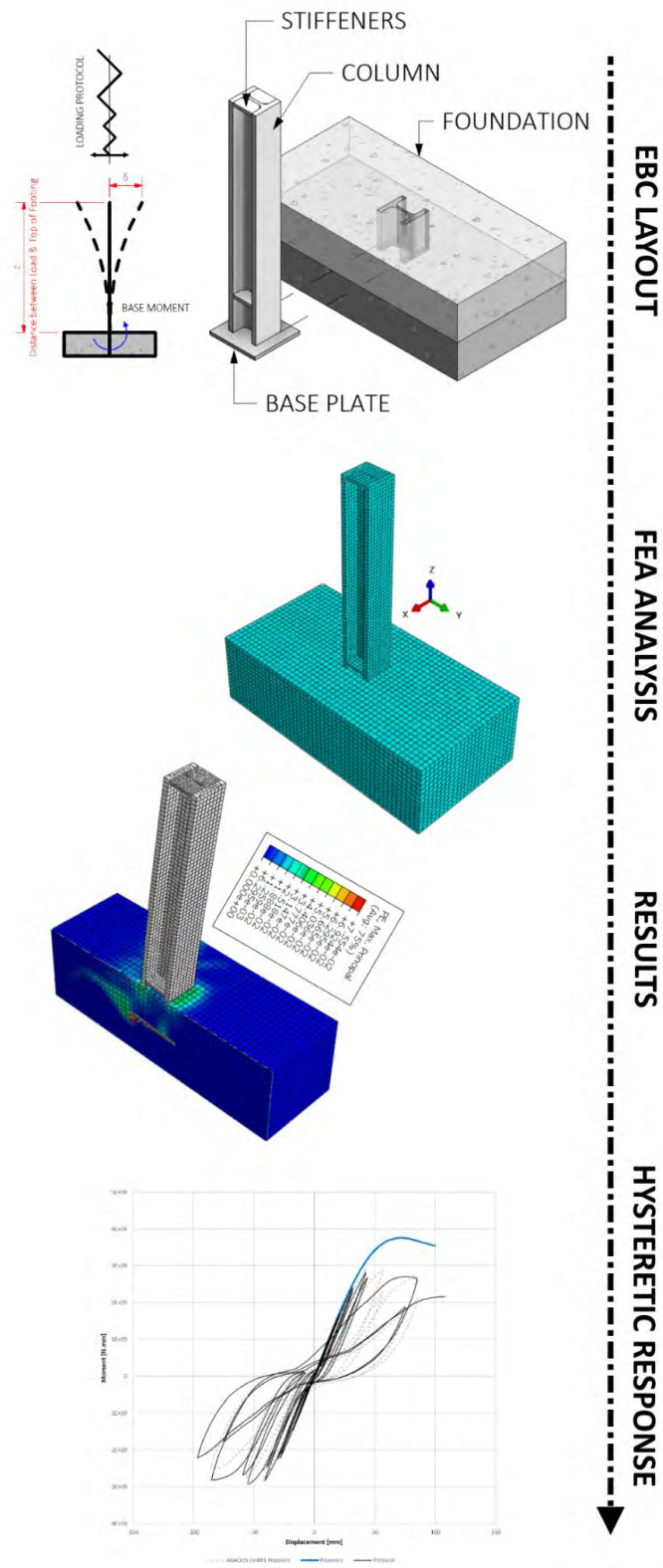
Figure 32: Study Overview

3.2 Test #1

3.2.1) Mathematical Model
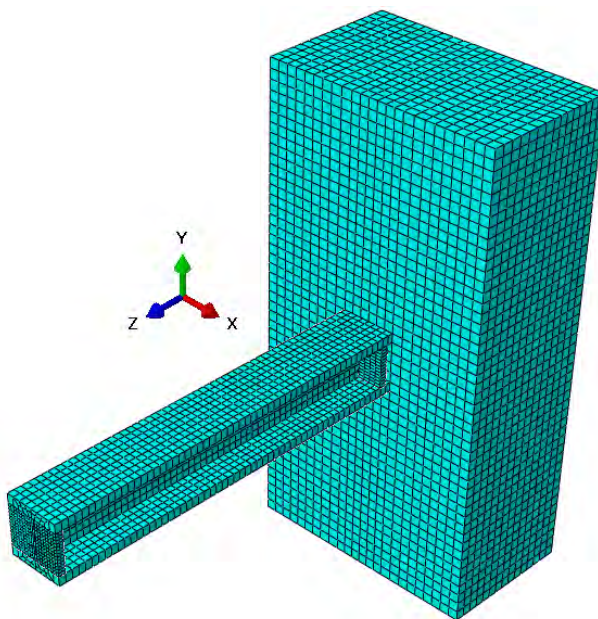
Figure 33:Test#1 Mesh

3.2.2) Monotonic Results at Displacement 100 [mm]
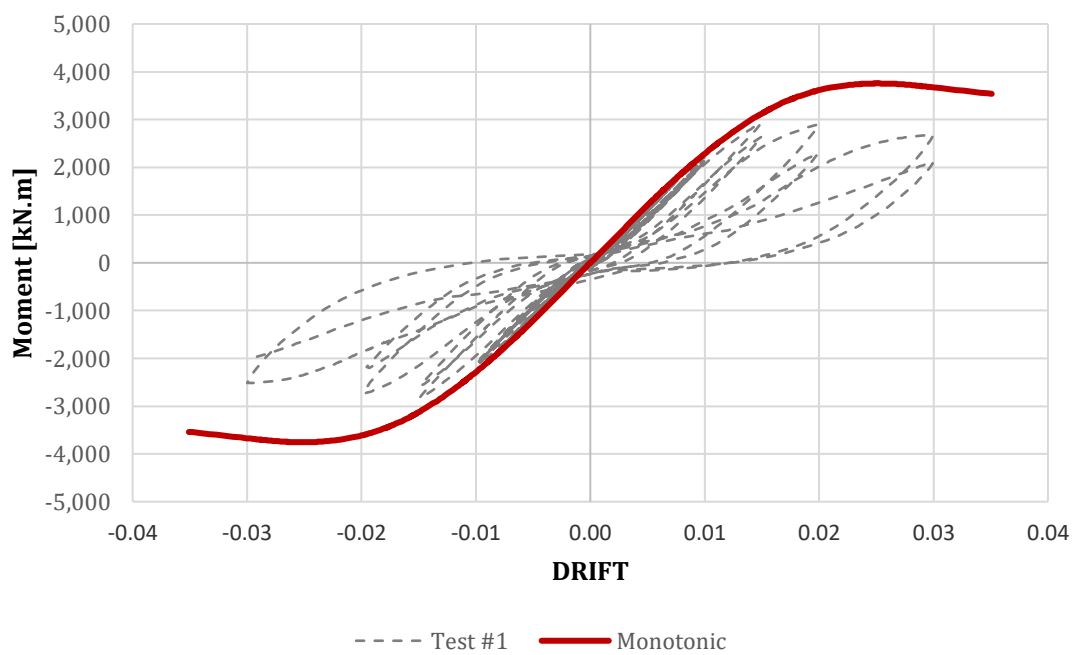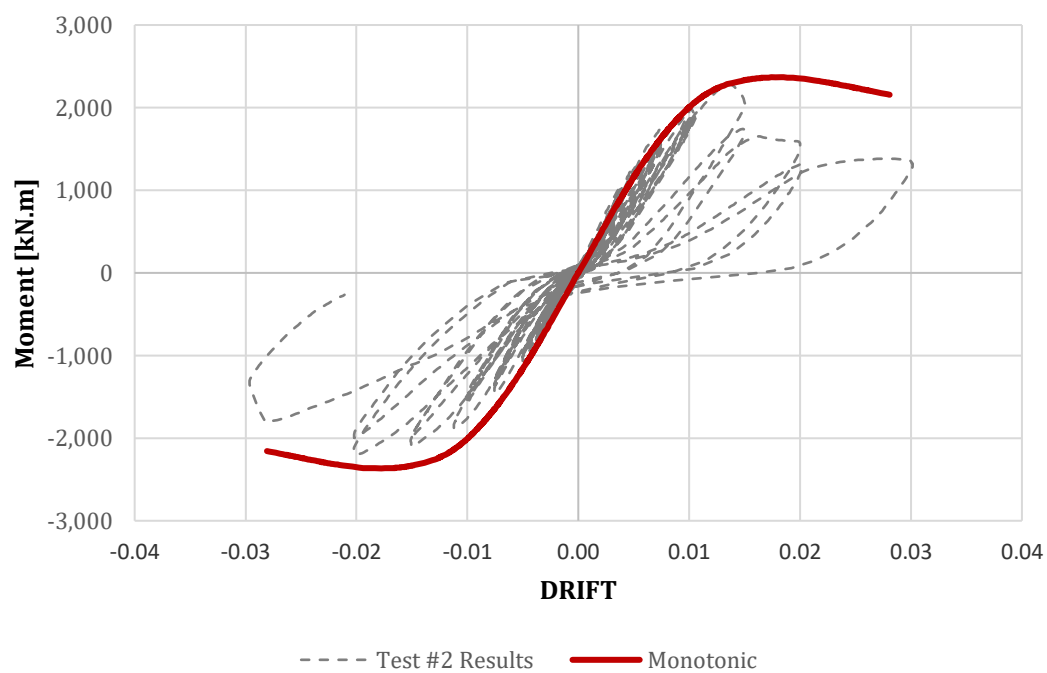

Figure 34: Test#1 Monotonic Results

3.2.3) Cyclic Results
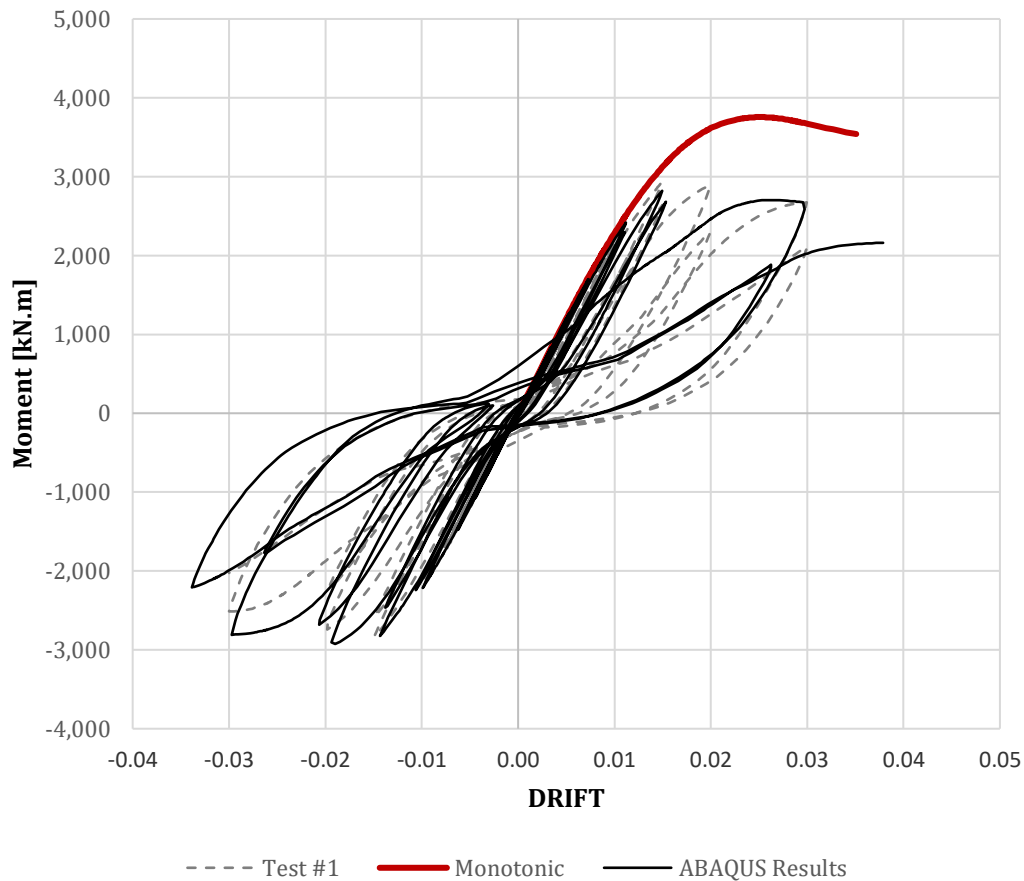
Figure 35:Test#1 Cyclic Results

3.2.4) FEA Results

Table 7: Test/FEA Results Test#1

| Damage Progression				
Drift	Description	Displacement	Step	Time
less than ≈ 1%	Small crack began to form near the corners of the column.	28.5	628	20.55
	Small gap adjacent to the tension flange. Growth of diagonal crack near the corner of the column.	28.5	628	20.55
Drift 1%	Initial spalling of the concrete ahead of the column flanges.			
Drift 3-4%	Cracks radiating diagonally outwards from the corner of the column on the top surface of the pedestal.	114	2737	53.65
	Slight upward bulging of the concreate in the bearing zone between these cracks,			
	Significant gapping in the tension side.			
	Flexural cracks observed on the sides and the top of the pedestal			
	Diagonal shear cracks on the sides of the block, which appeared as straight cracks parallel to the flanges on the top surface.			

Figure 36:Representative Drifts Test#1

Figure 37:Drift 1% Equivalent Plastic Strain - Test#1

PE, Max. Principal
(Avg: 75%)
+2.173e-02
+1.992e-02
+1.811e-02
+1.630e-02
+1.448e-02
+1.267e-02
+1.086e-02
+9.053e-03
+7.242e-03
+5.432e-03
+3.621e-03
+1.811e-03
+0.000e+00

ODB: Test1.odb   Abaqus/Standard 3DEXPERIENCE R2017x   Sun Mar 14 01:39:19 SA Pacific Standard Time 2021
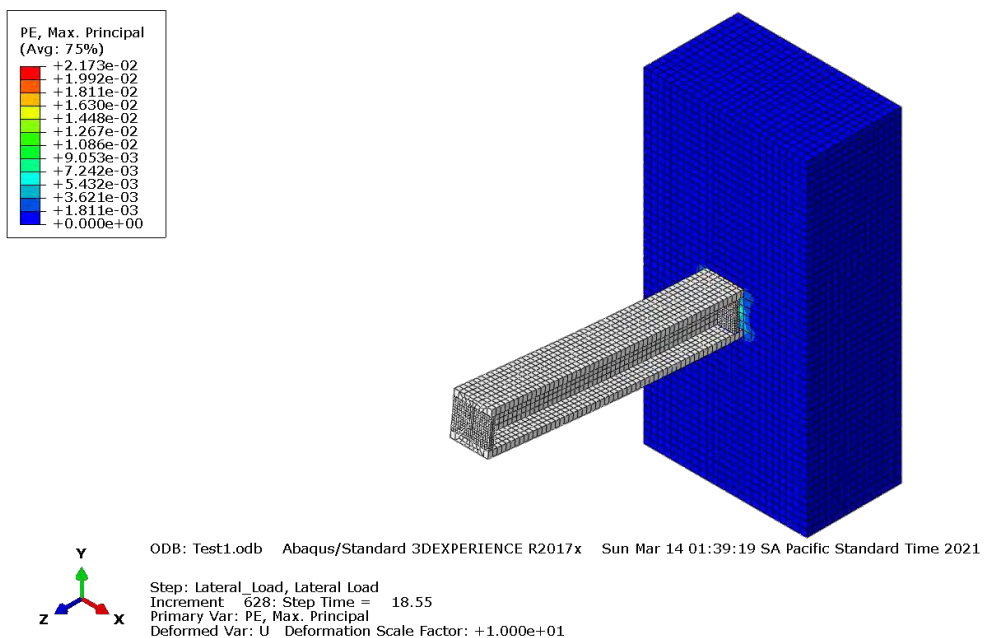
Step: Lateral_Load, Lateral Load
Increment   628: Step Time =   18.55
Primary Var: PE, Max. Principal
Deformed Var: U   Deformation Scale Factor: +1.000e+01

Figure 38: PE Section Cut Drift1%

PE, Max. Principal
(Avg: 75%)
+2.173e-02
+1.992e-02
+1.811e-02
+1.630e-02
+1.448e-02
+1.267e-02
+1.086e-02
+9.053e-03
+7.242e-03
+5.432e-03
+3.621e-03
+1.811e-03
+0.000e+00

ODB: Test1.odb   Abaqus/Standard 3DEXPERIENCE R2017x   Sun Mar 14 01:39:19 SA Pacific Standard Time 2021

Step: Lateral_Load, Lateral Load
Increment   628: Step Time =   18.55
Primary Var: PE, Max. Principal
Deformed Var: U   Deformation Scale Factor: +1.000e+01

Figure 39: PE Joint Drift1%
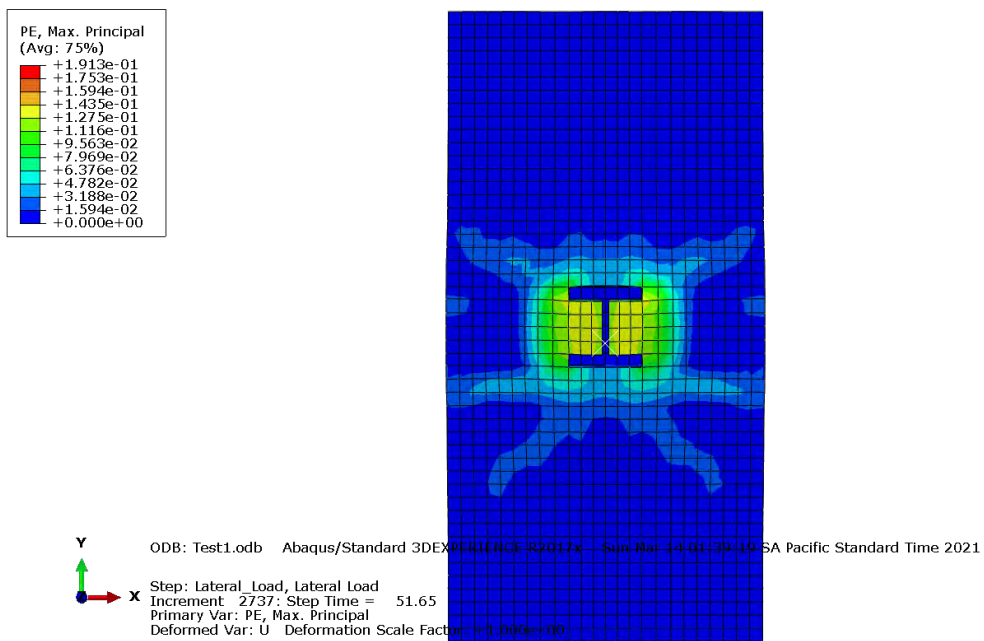
Figure 40:Drift3-4% PE Concrete Block
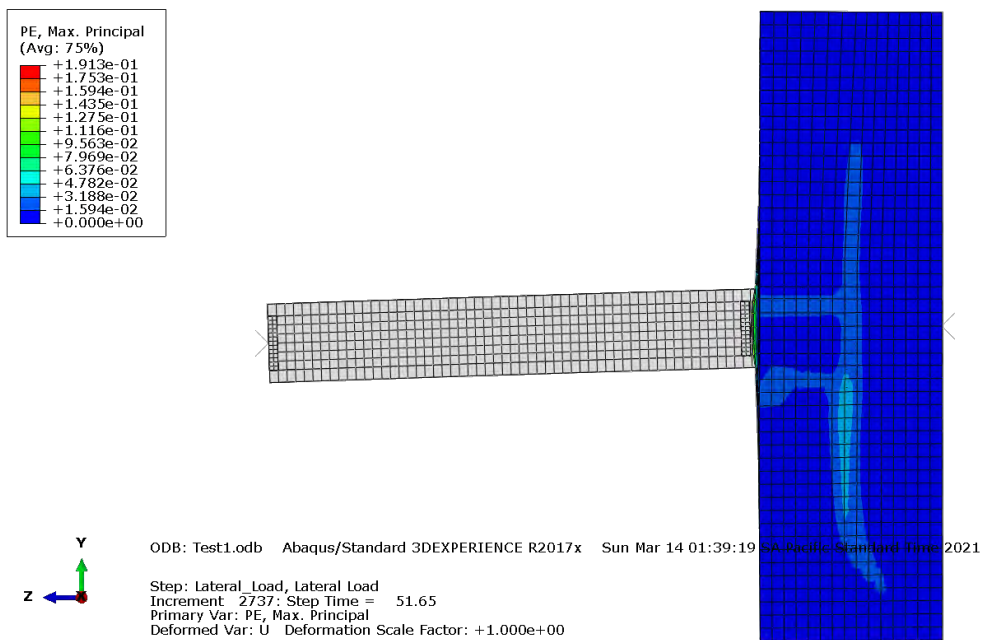

Figure 41: Drift3-4% PE Concrete Block Elevation

PE, Max. Principal
(Avg: 75%)
+1.913e-01
+1.753e-01
+1.594e-01
+1.435e-01
+1.275e-01
+1.116e-01
+9.563e-02
+7.969e-02
+6.376e-02
+4.782e-02
+3.188e-02
+1.594e-02
+0.000e+00

ODB: Test1.odb   Abaqus/Standard 3DEXPERIENCE R2017x   Sun Mar 14 01:39:19 SA Pacific Standard Time 2021

Step: Lateral_Load, Lateral Load
Increment 2737: Step Time =   51.65
Primary Var: PE, Max. Principal
Deformed Var: U   Deformation Scale Factor: +1.000e+00
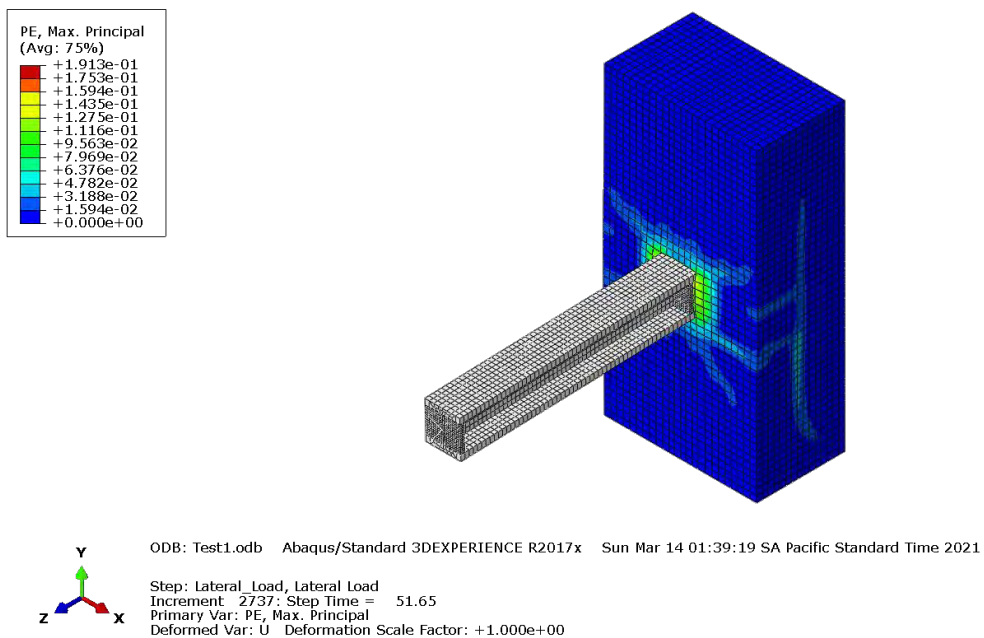
Figure 42: Drift3-4% Plastic Strain

PE, Max. Principal
(Avg: 75%)
+1.913e-01
+1.753e-01
+1.594e-01
+1.435e-01
+1.275e-01
+1.116e-01
+9.563e-02
+7.969e-02
+6.376e-02
+4.782e-02
+3.188e-02
+1.594e-02
+0.000e+00

ODB: Test1.odb   Abaqus/Standard 3DEXPERIENCE R2017x   Sun Mar 14 01:39:19 SA Pacific Standard Time 2021

Step: Lateral_Load, Lateral Load
Increment 2737: Step Time =   51.65
Primary Var: PE, Max. Principal
Deformed Var: U   Deformation Scale Factor: +1.000e+00

Figure 43: Drift3-4% Plastic Strain Section Cut
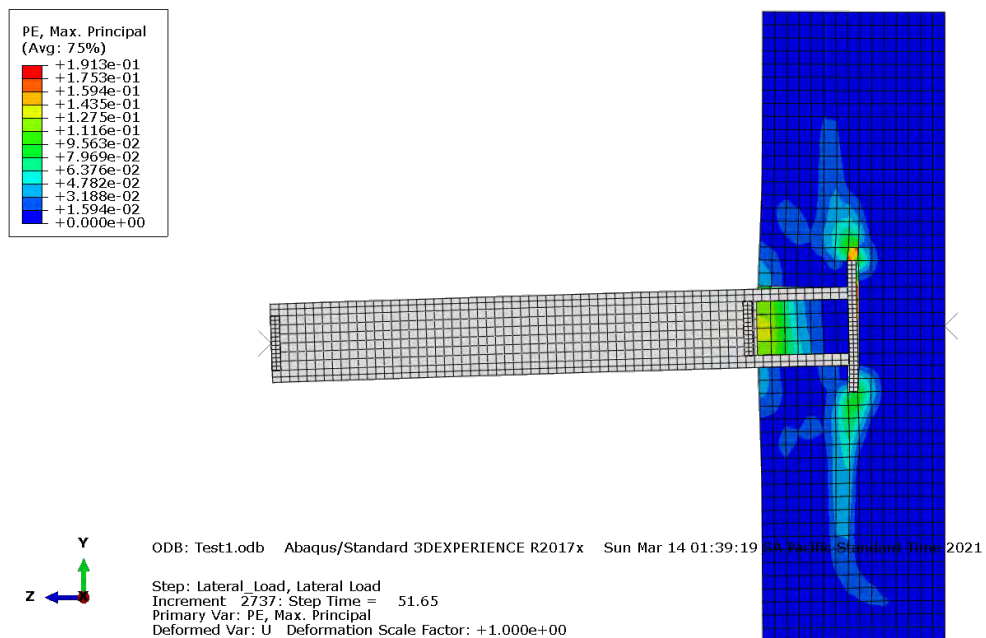
Figure 44: Drift3-4% Plastic Strain Section Cut Elevation
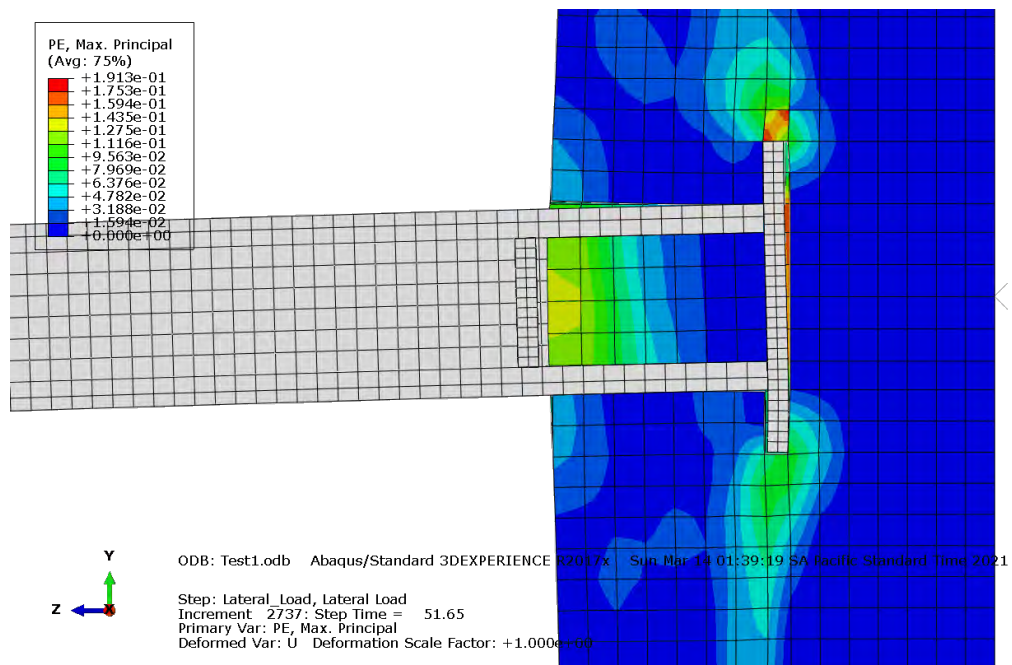
Figure 45: Drift3-4% Plastic Strain Section Cut Joint

S, Mises
(Avg: 75%)
+8.992e+02
+8.243e+02
+7.493e+02
+6.744e+02
+5.995e+02
+5.246e+02
+4.497e+02
+3.748e+02
+2.999e+02
+2.250e+02
+1.501e+02
+7.517e+01
+2.574e-01

ODB: Test1.odb   Abaqus/Standard 3DEXPERIENCE R2017x   Sun Mar 14 01:39:19 SA Pacific Standard Time 2021

Step: Lateral_Load, Lateral Load
Increment   2737: Step Time =   51.65
Primary Var: S, Mises
Deformed Var: U   Deformation Scale Factor: +5.000e+00
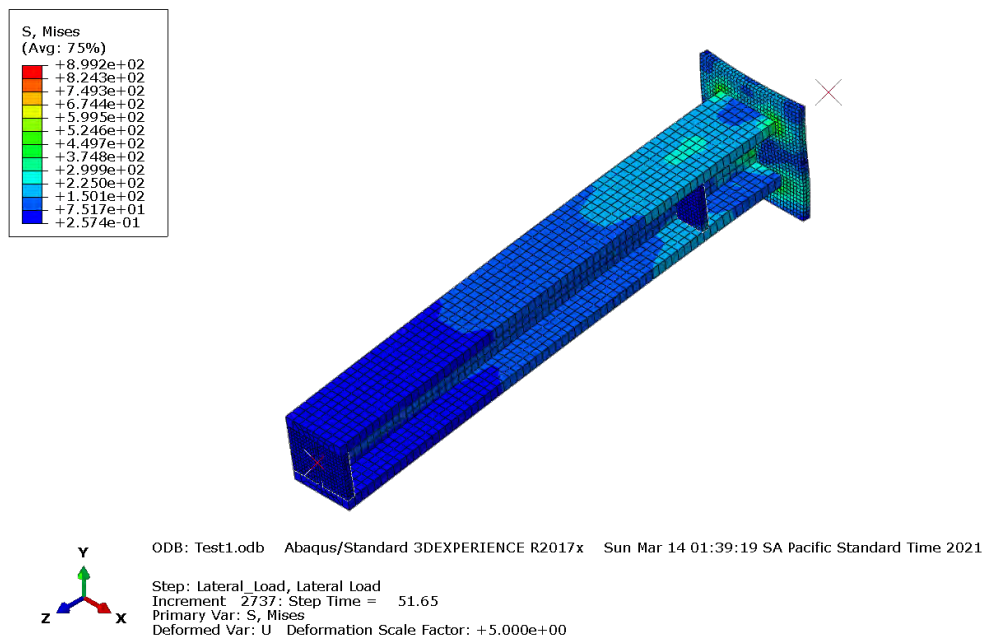
Figure 46: Drift3-4% Von Mises Column

3.3 Test #2

3.3.1) Mathematical Model
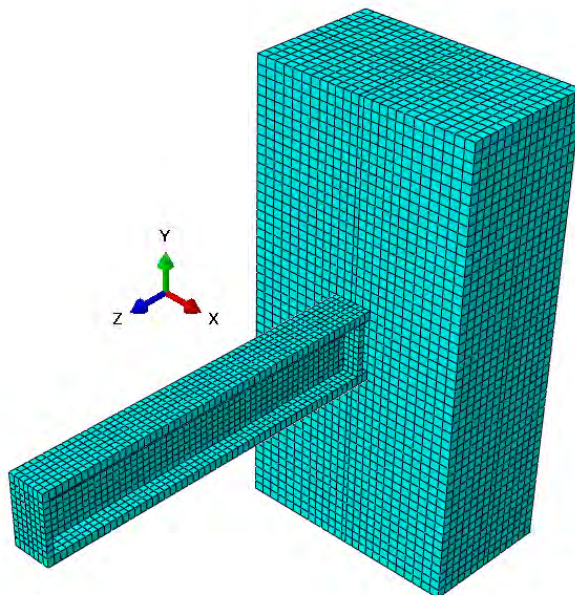
Figure 47: Test#2 Mesh

1.1.1. Monotonic Results at Displacement 80 [mm]

Figure 48: Test#2 Monotonic Results

3.3.2) Cyclic Results
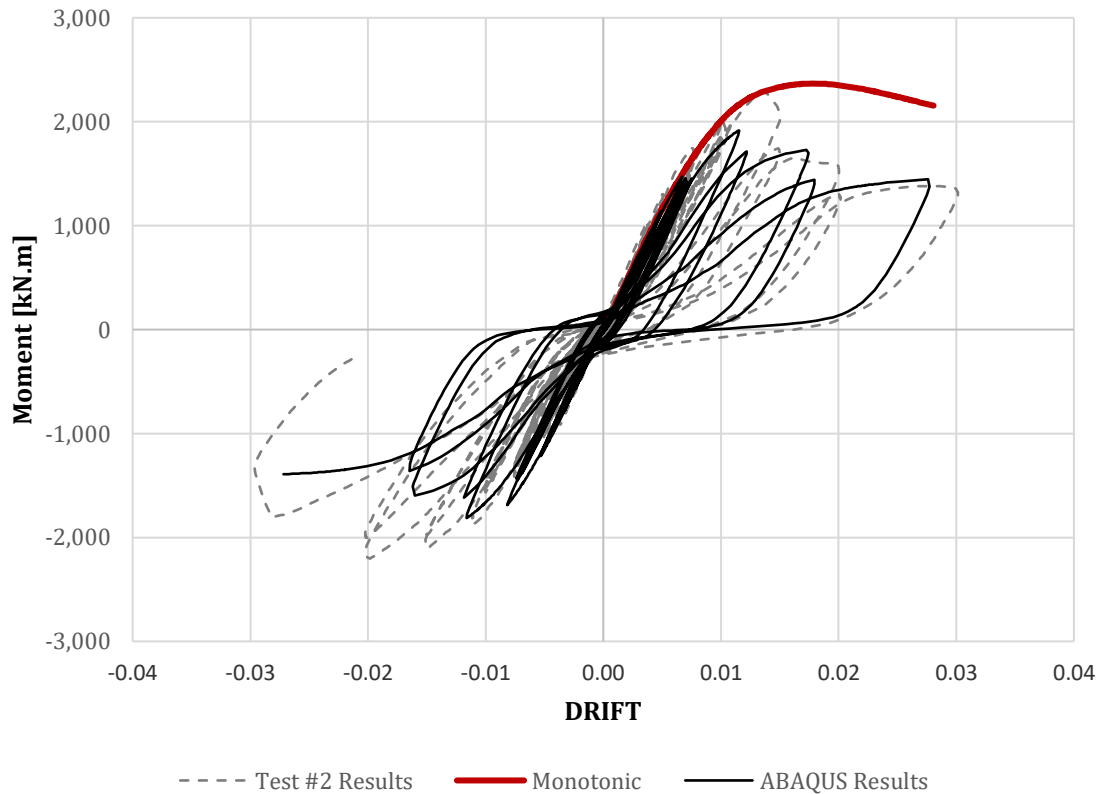
Figure 49:Test#2 Cyclic Results

3.3.3) FEA Results

Table 8: Test/FEA Results Test#2

Drift	Description	Displacement	Step	Time
Damage Progression				
less than ≈ 1%	Small crack began to form near the corners of the column.	28.5	1997	24
	Small gap adjacent to the tension flange. Growth of diagonal crack near the corner of the column.	28.5	1997	24
Drift 1%	Initial spalling of the concrete ahead of the column flanges.			
Drift 3%	Cracks radiating diagonally outwards from the corner of the column on the top surface of the pedestal.	80	3266	77.47
	Slight upward bulging of the concreate in the bearing zone between these cracks,			
	Significant gapping in the tension side.			
	Flexural cracks observed on the sides and the top of the pedestal			
	Diagonal shear cracks on the sides of the block, which appeared as straight cracks parallel to the flanges on the top surface.			

Figure 50:Representative Drifts Test#2
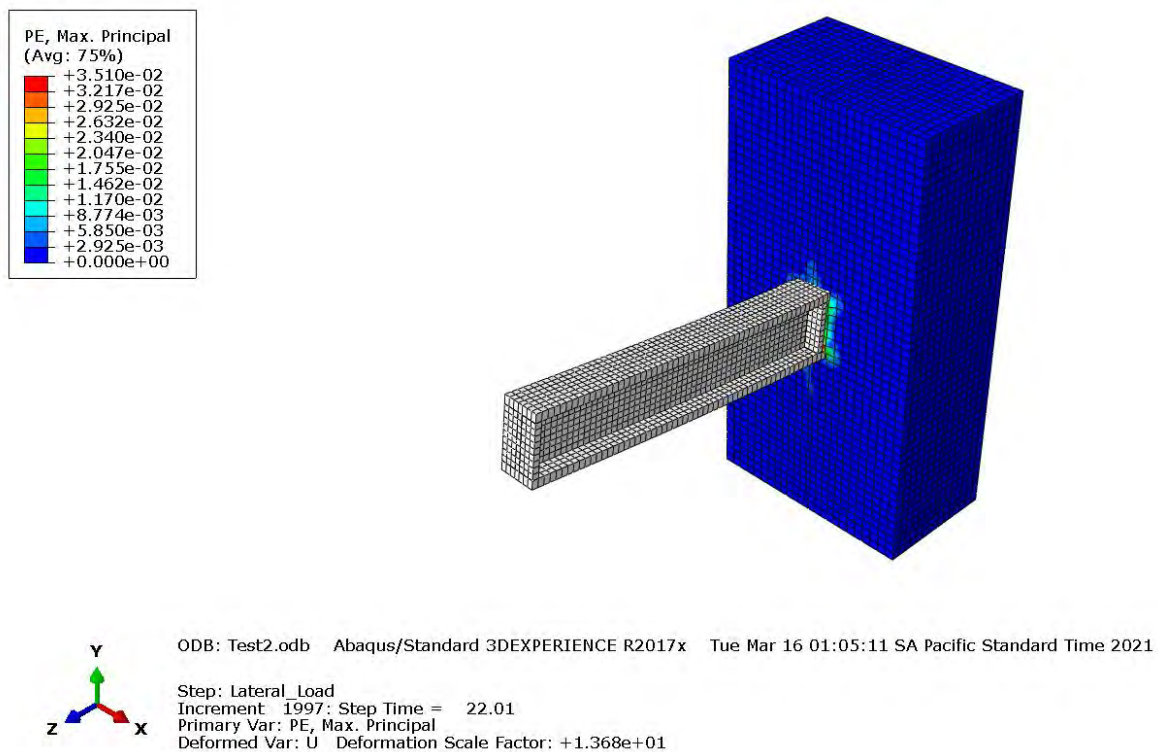
Figure 51:Drift 1% Equivalent Plastic Strain - Test#2
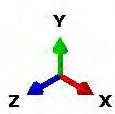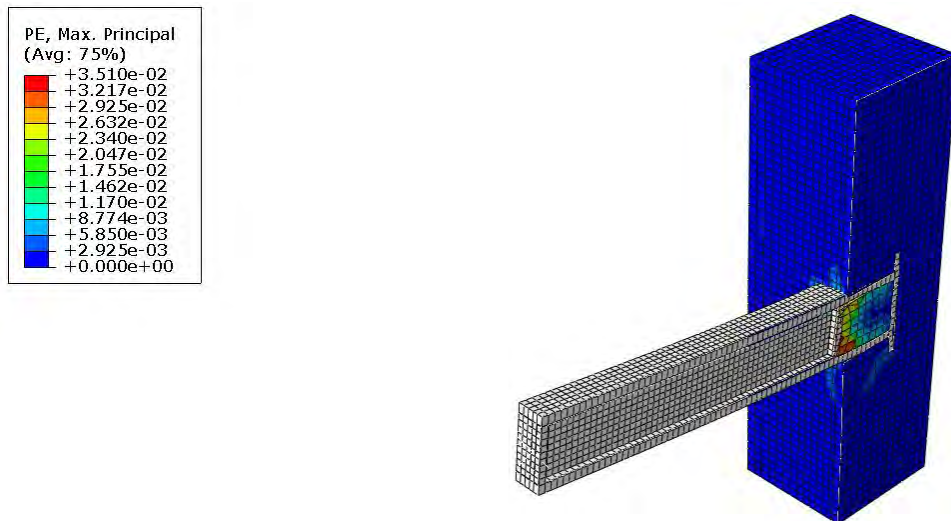
Figure 52: PE Section Cut Drift1%
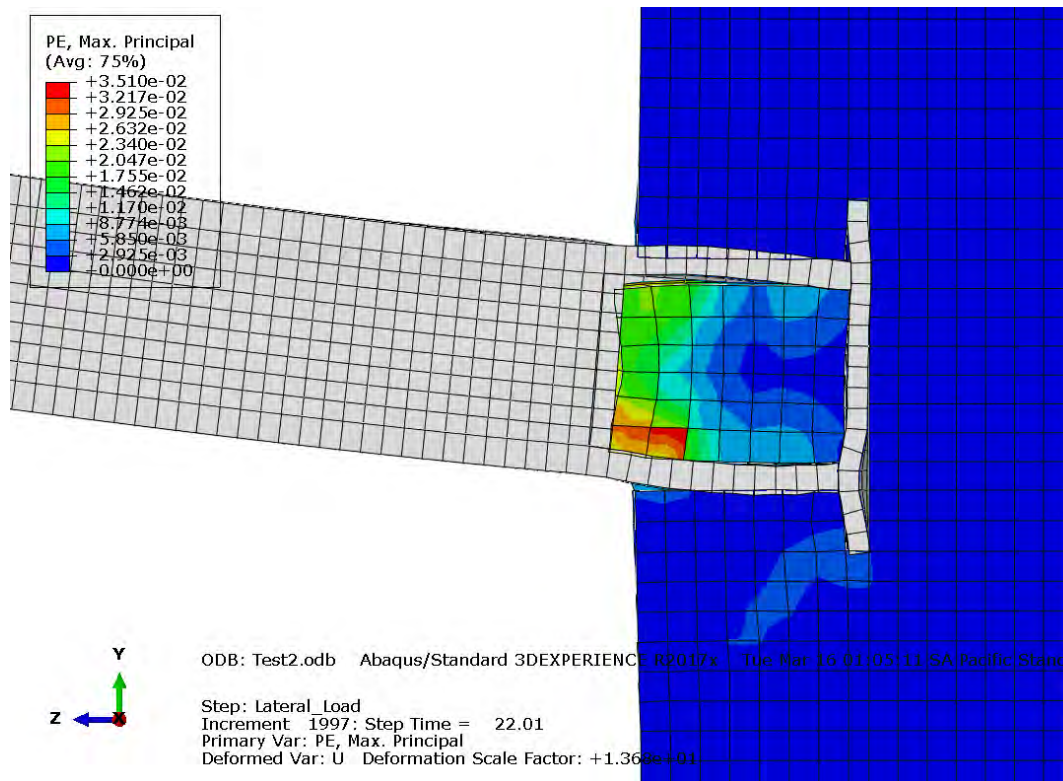
Figure 53: PE Joint Drift1%
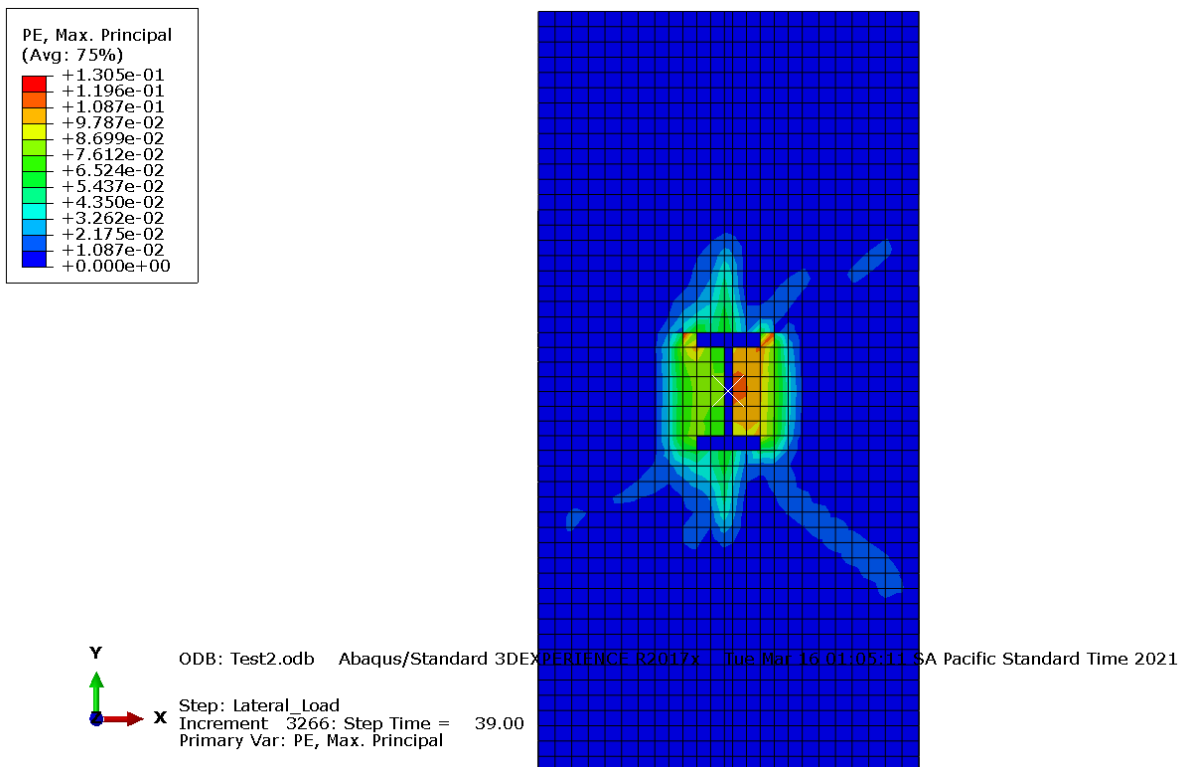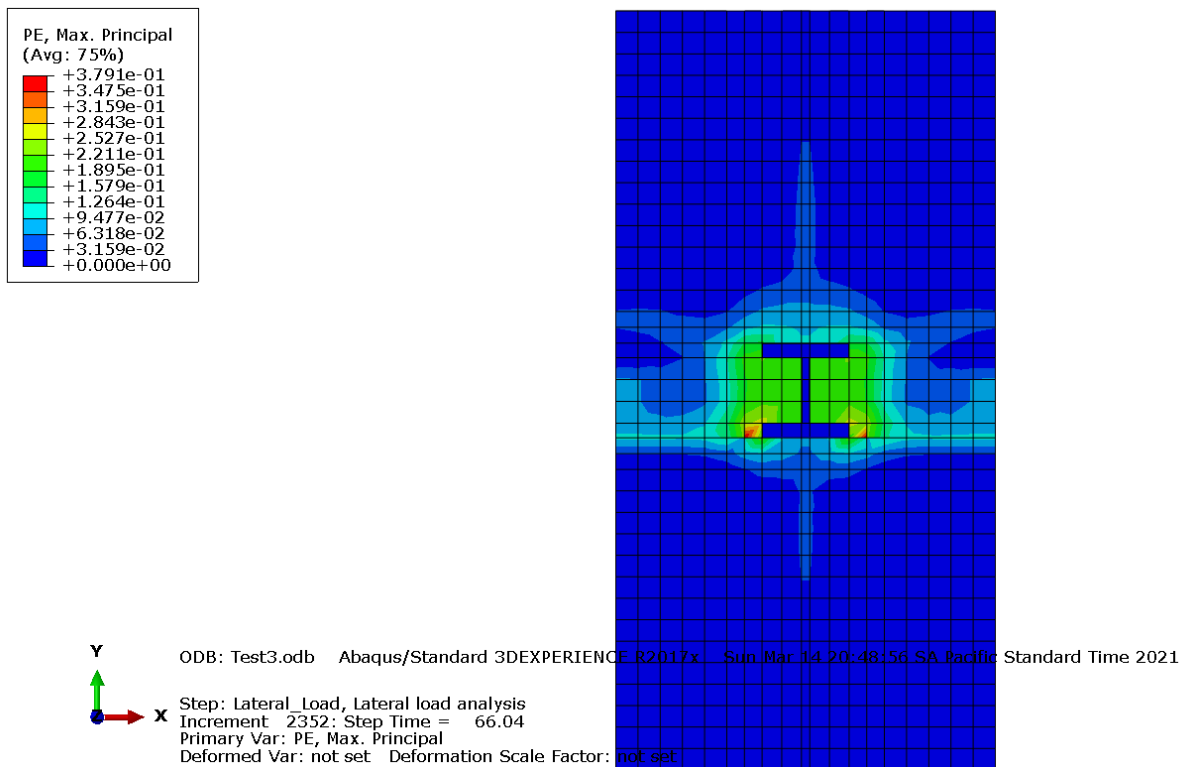
Figure 54:Drift3-4% PE Concrete Block
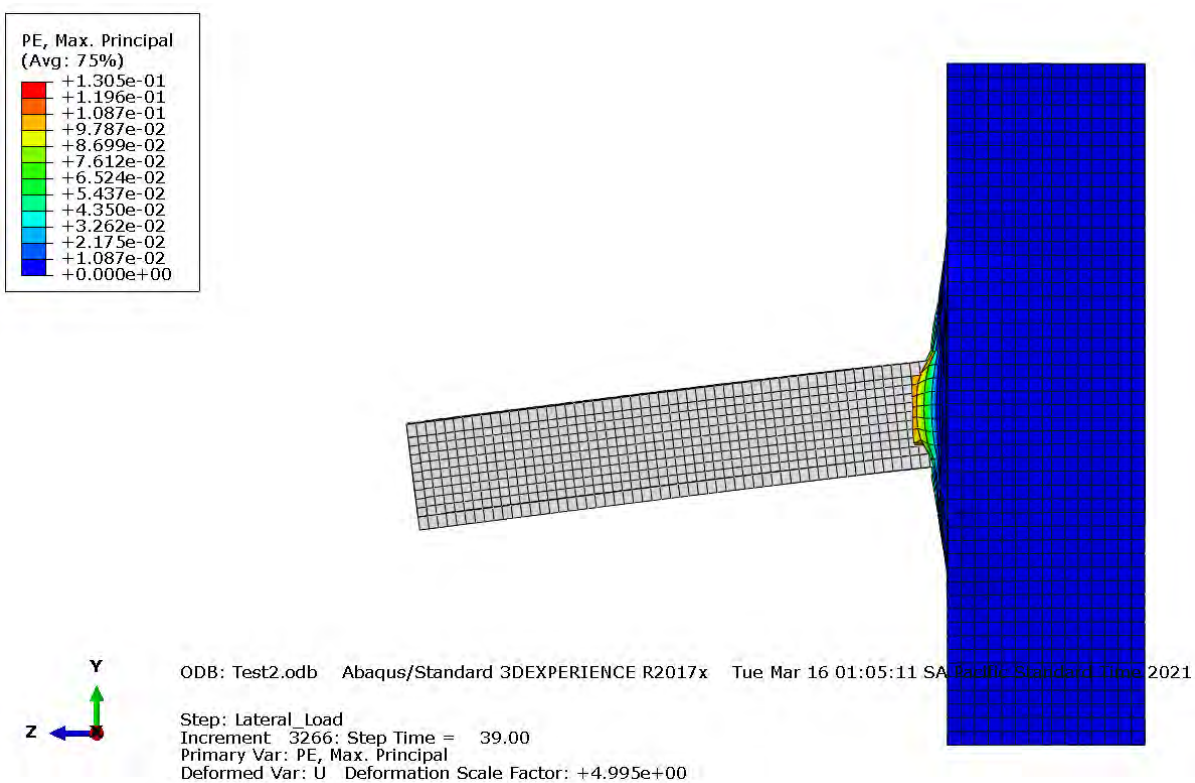
Figure 55: Drift3-4% PE Concrete Block Elevation
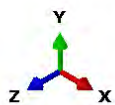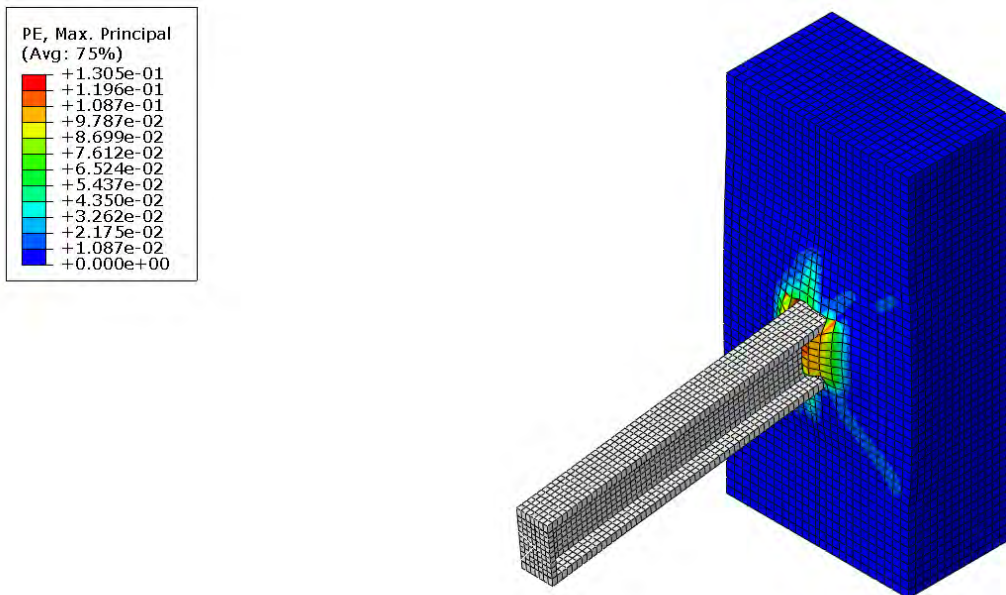
Figure 56: Drift3-4% Plastic Strain
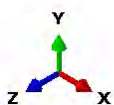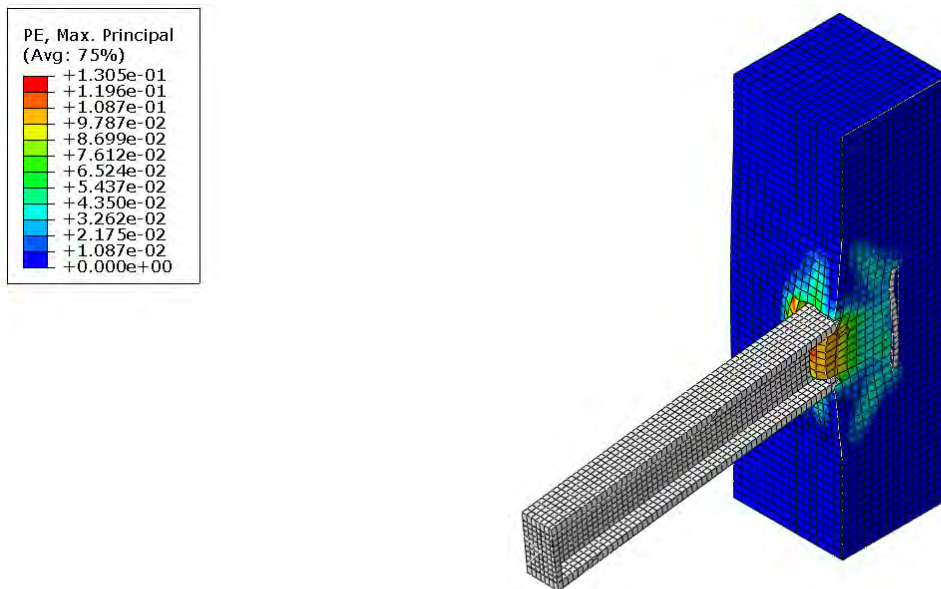

Figure 57: Drift3-4% Plastic Strain Section Cut
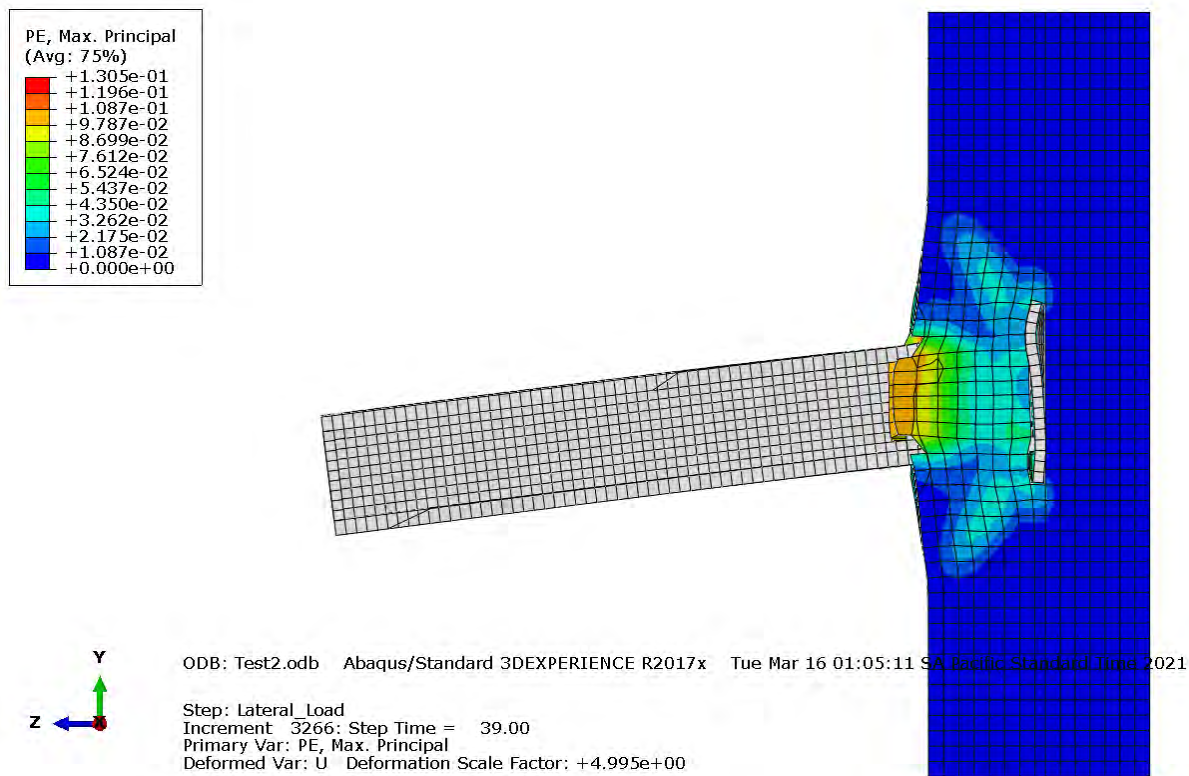
Figure 58: Drift3-4% Plastic Strain Section Cut Elevation
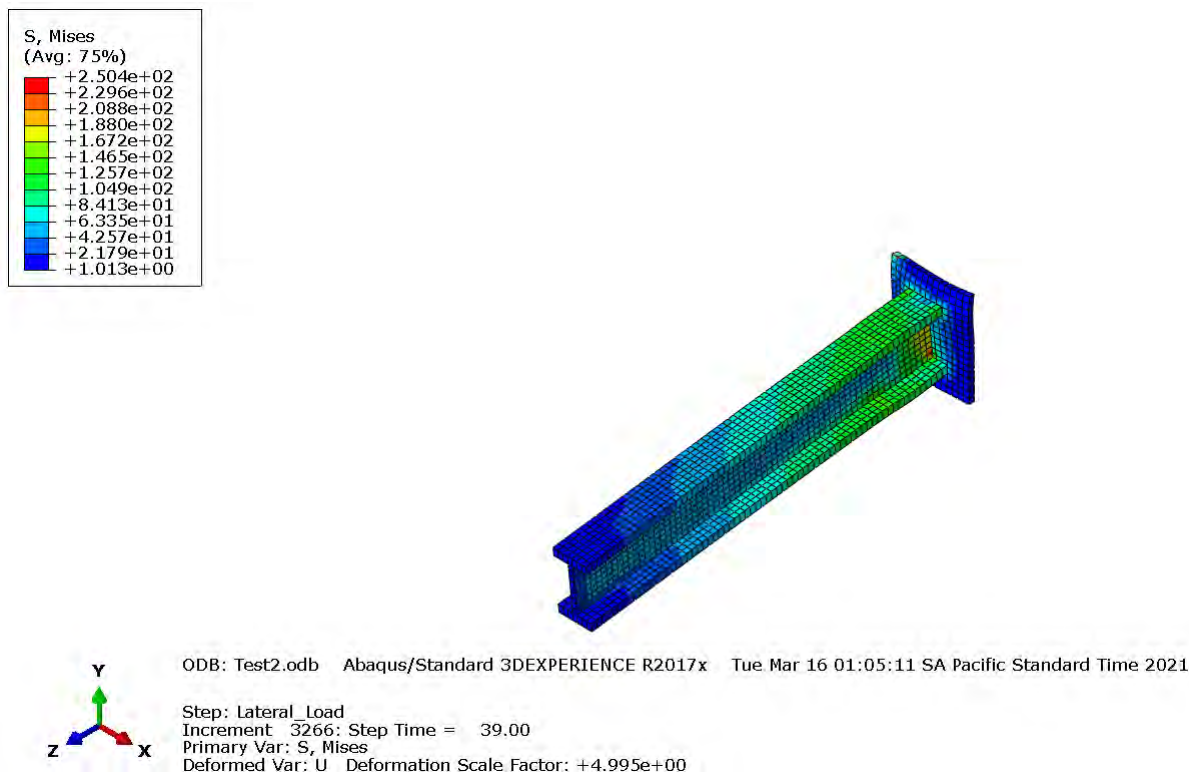
Figure 59: Drift3-4% Von Mises Column

3.4 Test #3

3.4.1) Mathematical Model
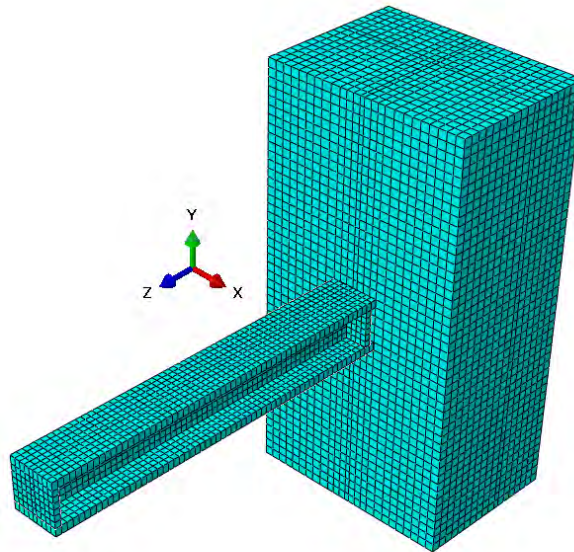
Figure 60:Test #3 Mesh
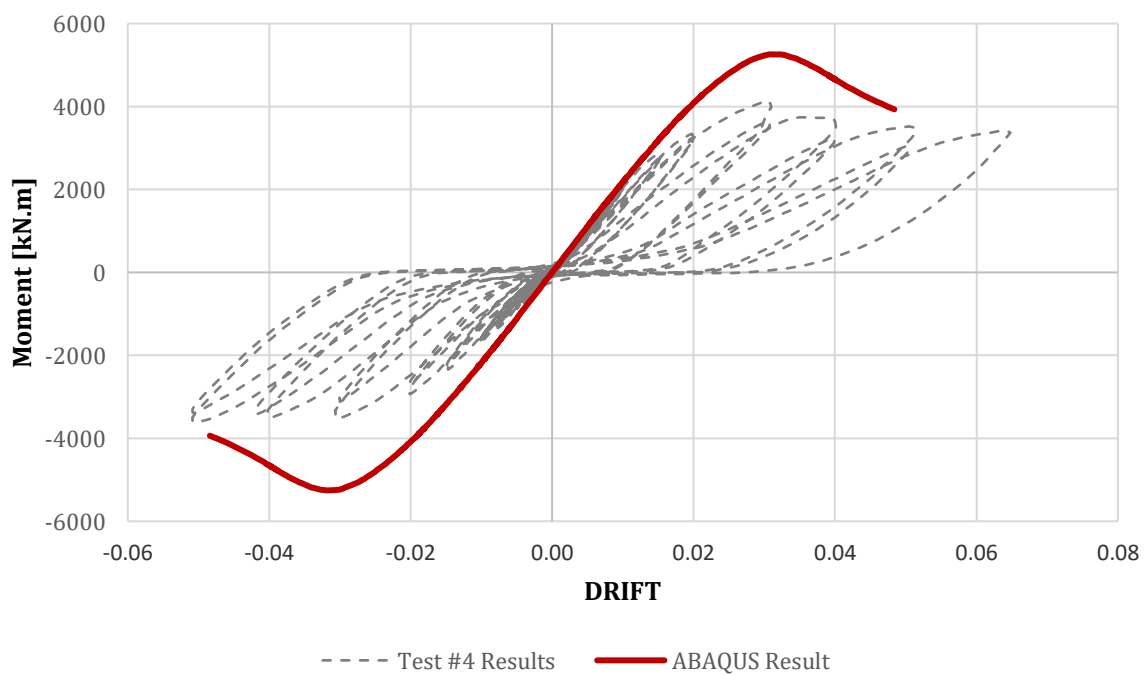
3.4.2) Monotonic Results at Displacement 200 [mm]
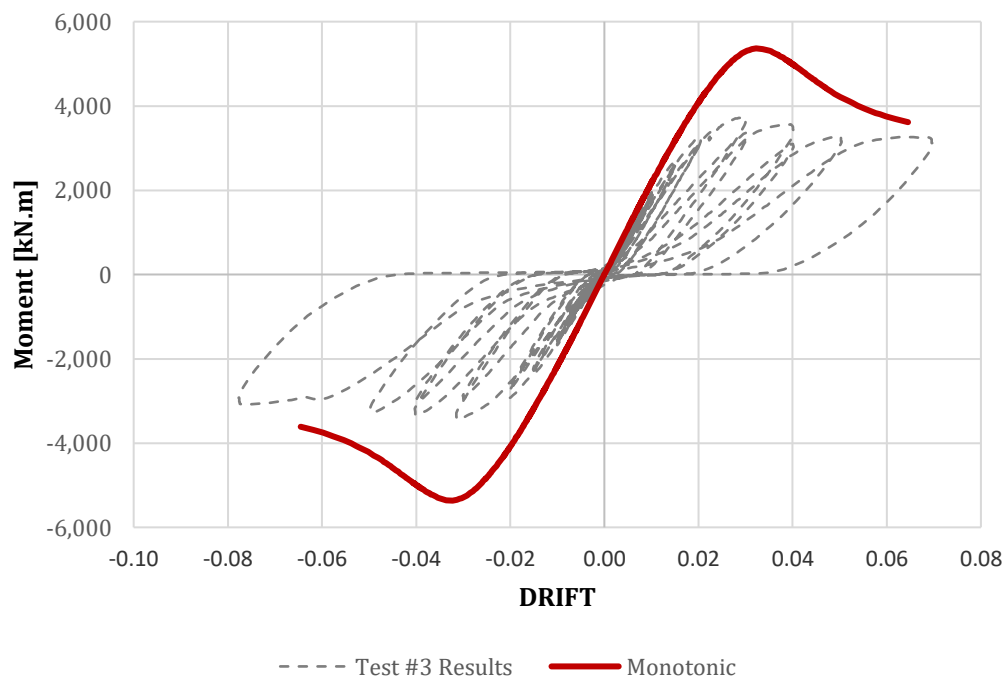
Figure 61: Test#3 Monotonic Results

3.4.3) Cyclic Results
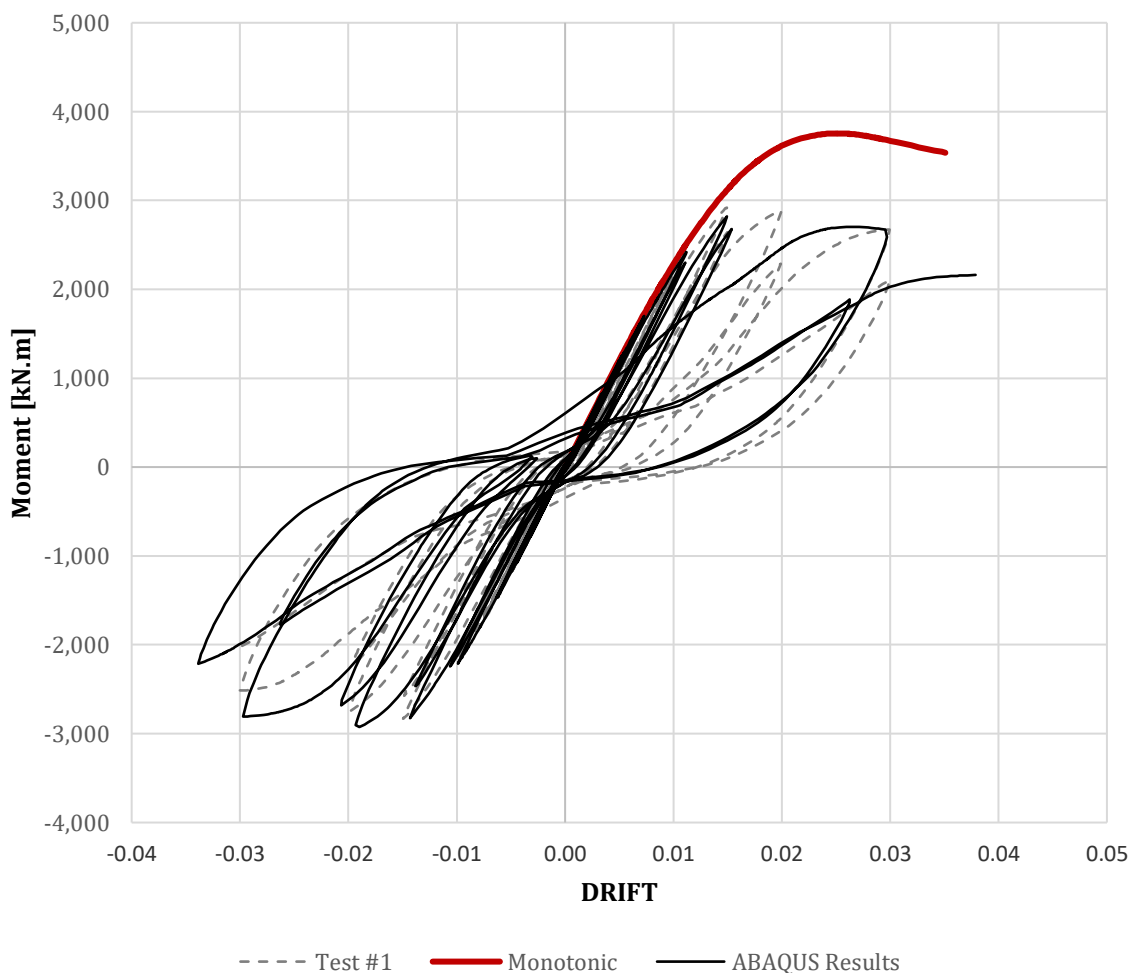
Figure 62:Test#3 Cyclic Results

3.4.4) FEA Results

Table 9: Test/FEA Results Test#3

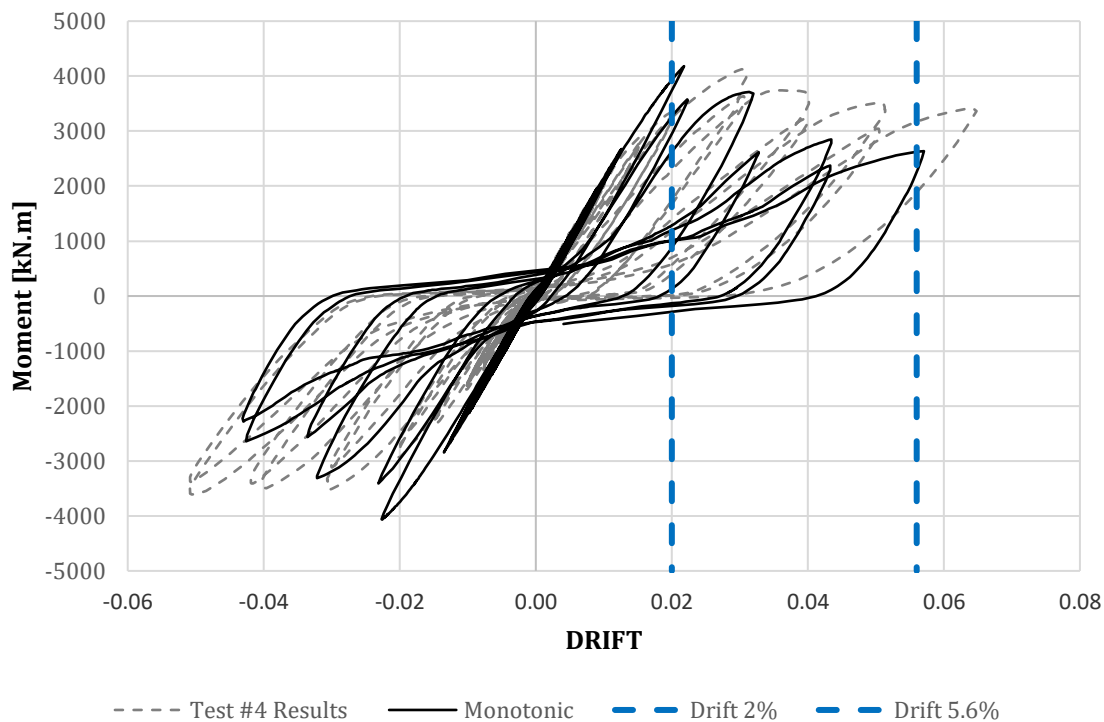| Damage Progression				
Drift	Description	Displacement	Step	Time
less than ≈ 2%	Small crack began to form near the corners of the column.	66	1628	30.5
	Small gap adjacent to the tension flange. Growth of diagonal crack near the corner of the column.	66	1628	30.5
Drift 2%	Initial spalling of the concrete ahead of the column flanges.			
Drift 4-6%	Cracks radiating diagonally outwards from the corner of the column on the top surface of the pedestal.	190	2352	67
	Slight upward bulging of the concreate in the bearing zone between these cracks,			
	Significant gapping in the tension side.			
	Flexural cracks observed on the sides and the top of the pedestal			
	Diagonal shear cracks on the sides of the block, which appeared as straight cracks parallel to the flanges on the top surface.			

Figure 63:Representative Drifts Test#3
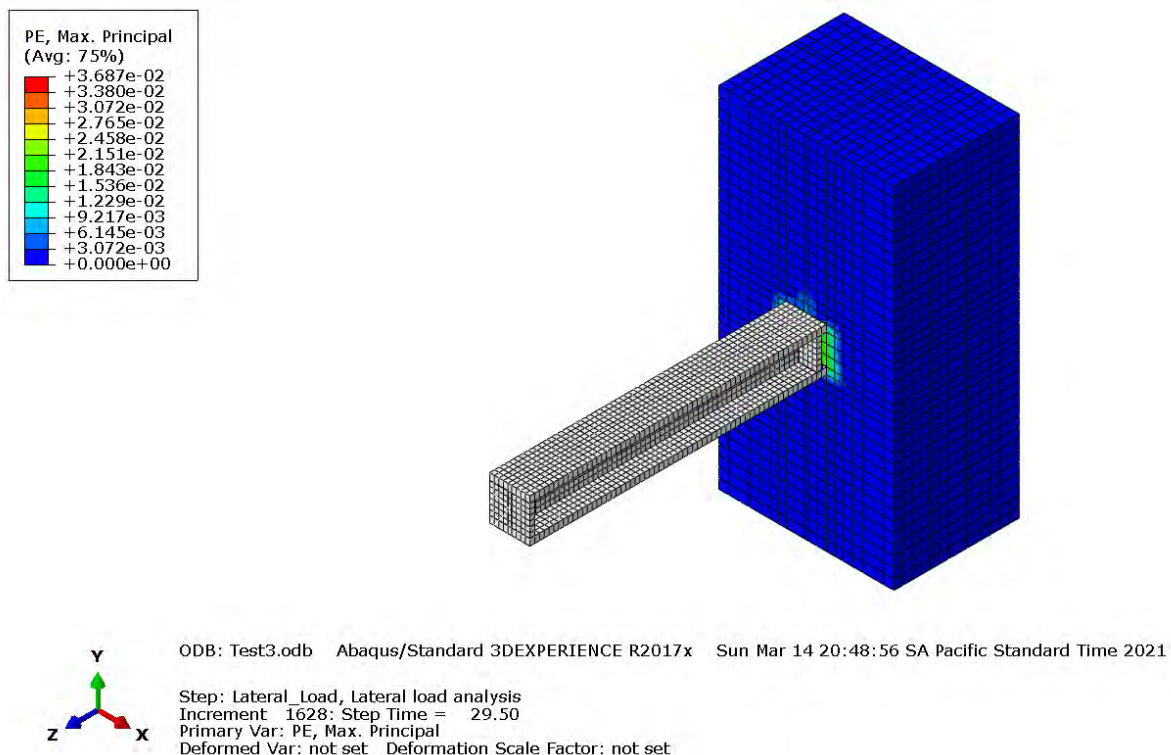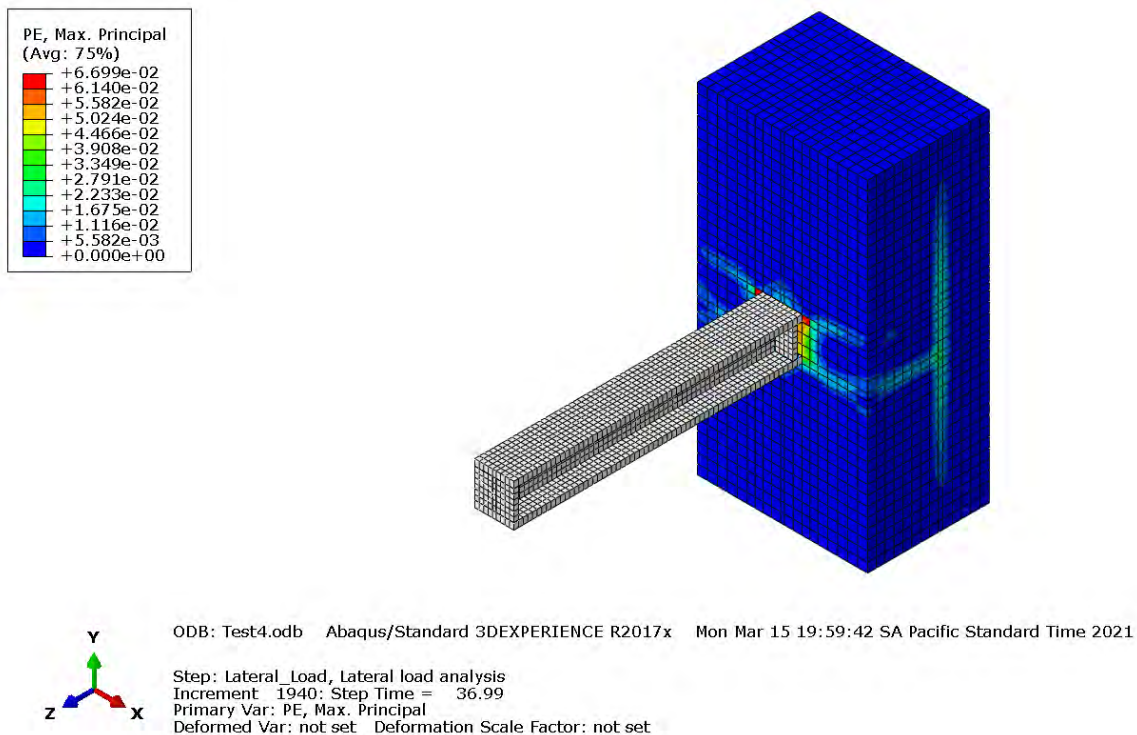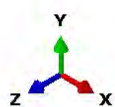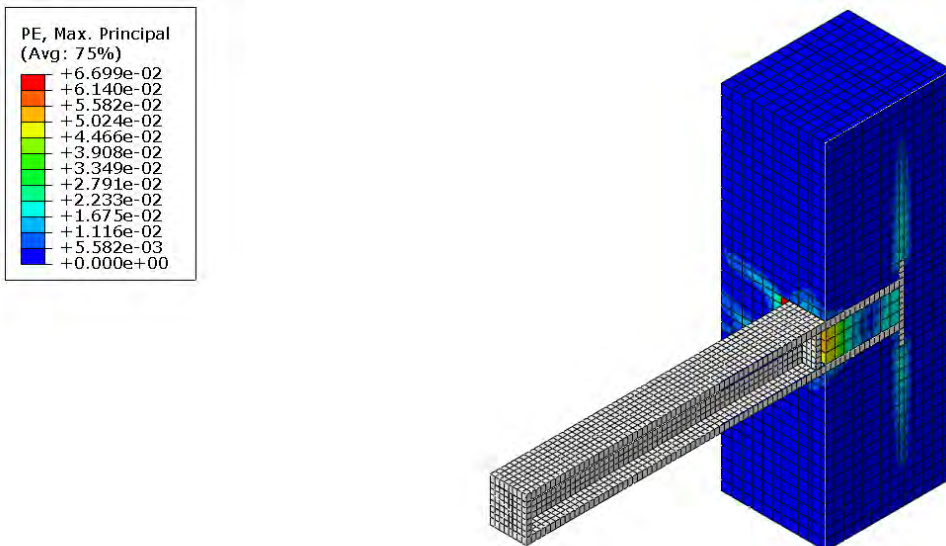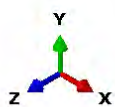

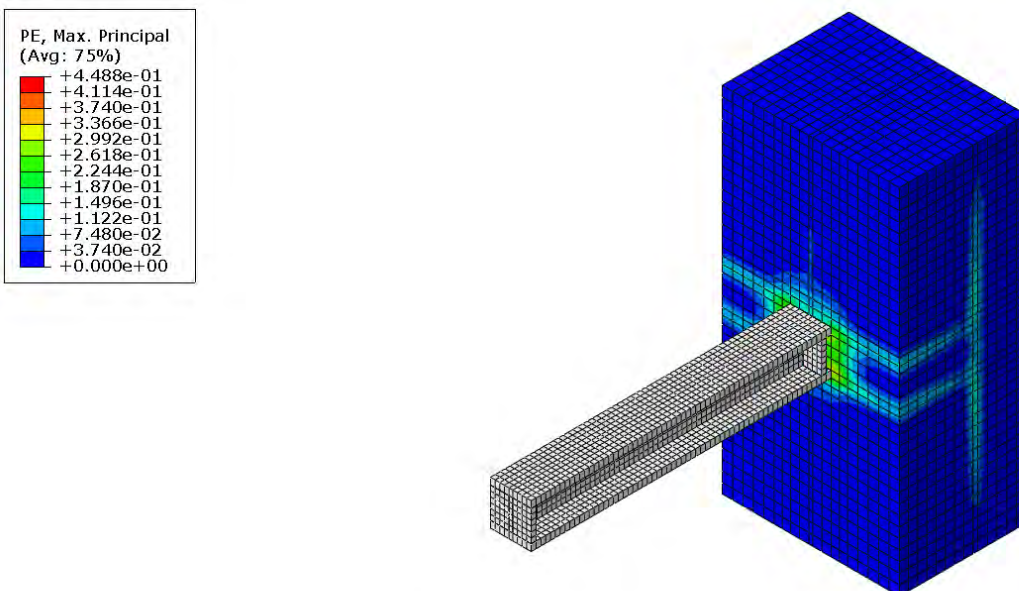Figure 64:Drift 2% Equivalent Plastic Strain - Test#3
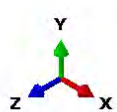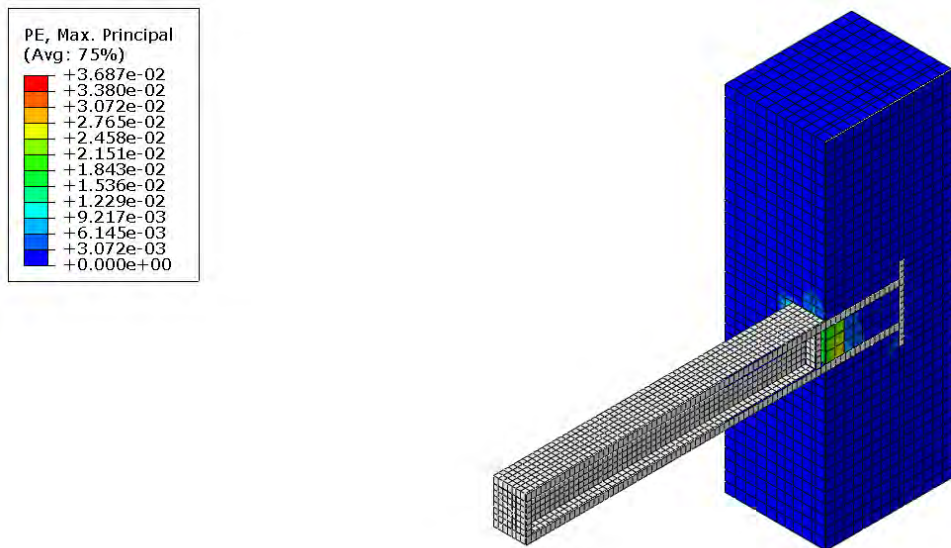
ODB: Test3.odb   Abaqus/Standard 3DEXPERIENCE R2017x   Sun Mar 14 20:48:56 SA Pacific Standard Time 2021

Step: Lateral_Load, Lateral load analysis
Increment   1628: Step Time =   29.50
Primary Var: PE, Max. Principal
Deformed Var: not set   Deformation Scale Factor: not set

Figure 65: PE Section Cut Drift1%
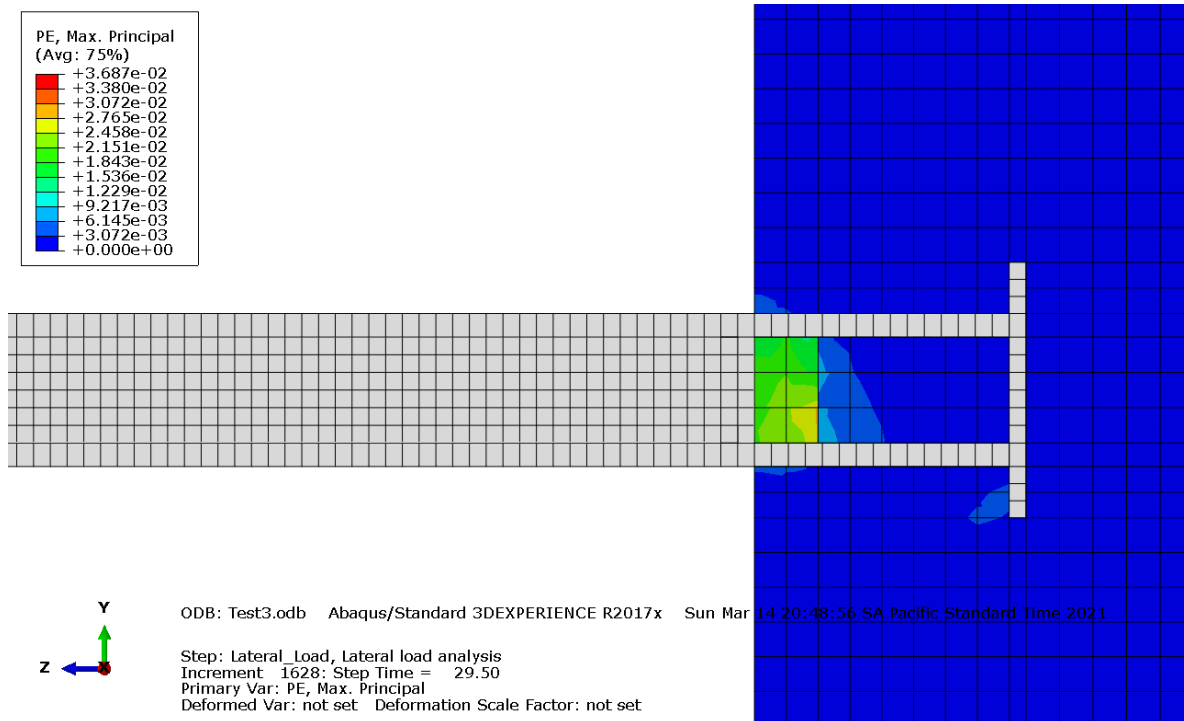
ODB: Test3.odb   Abaqus/Standard 3DEXPERIENCE R2017x   Sun Mar 14 20:48:56 SA Pacific Standard Time 2021

Step: Lateral_Load, Lateral load analysis
Increment   1628: Step Time =   29.50
Primary Var: PE, Max. Principal
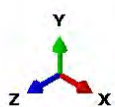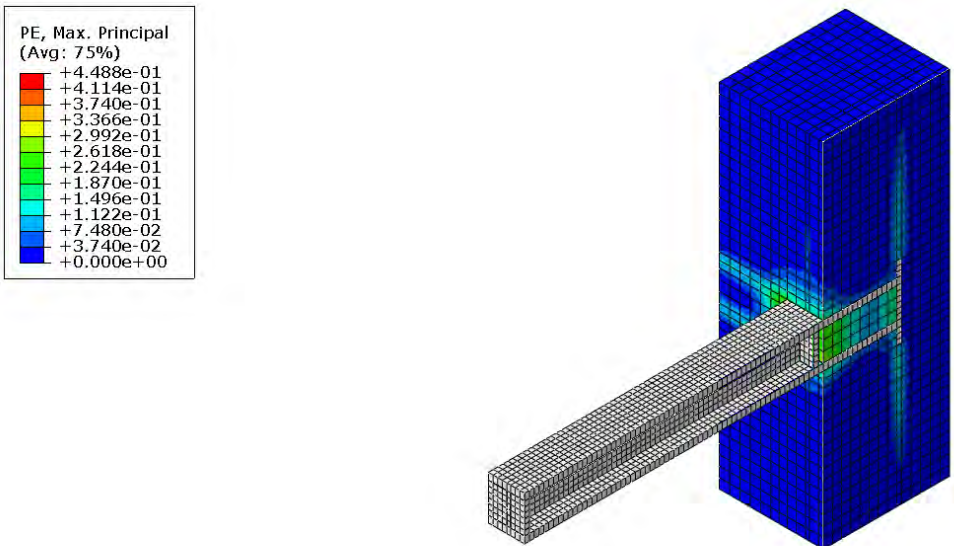Deformed Var: not set   Deformation Scale Factor: not set

Figure 66: PE Joint Drift1%

Figure 67:Drift4-6% PE Concrete Block
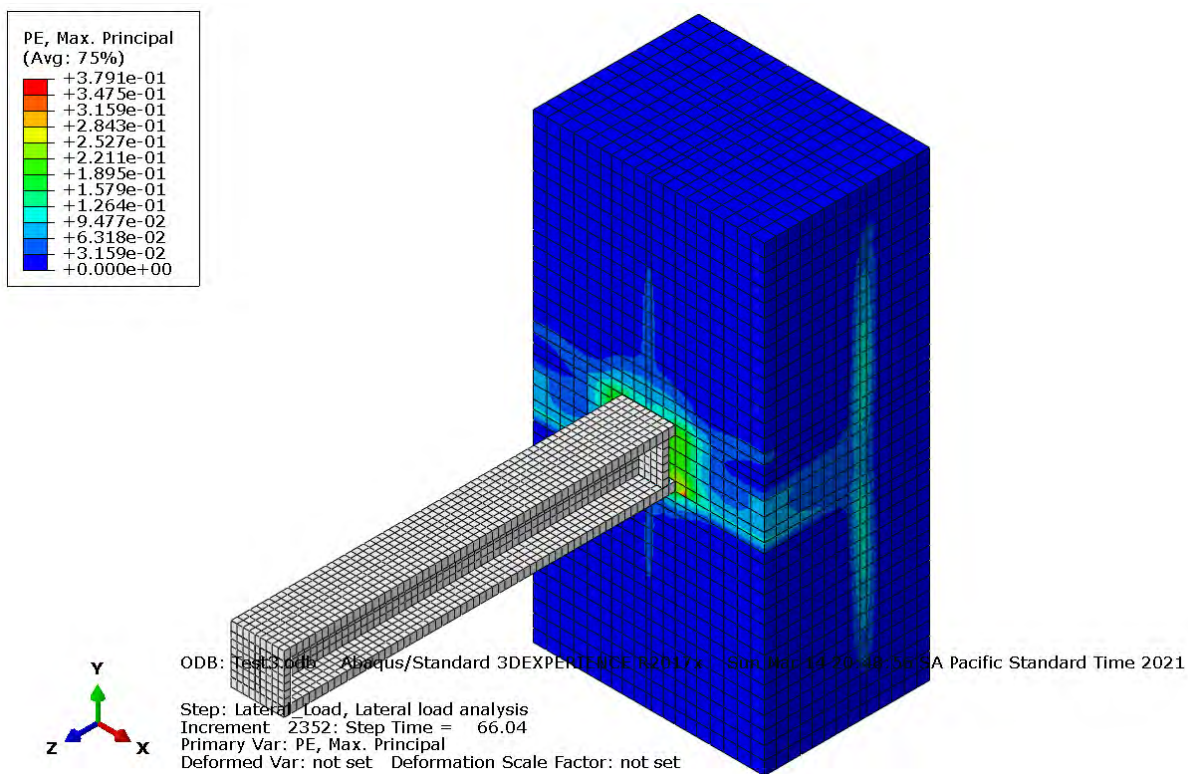
Figure 68: Drift4-6% Plastic Strain

PE, Max. Principal
(Avg: 75%)
+3.791e-01
+3.475e-01
+3.159e-01
+2.843e-01
+2.527e-01
+2.211e-01
+1.895e-01
+1.579e-01
+1.264e-01
+9.477e-02
+6.318e-02
+3.159e-02
+0.000e+00

ODB: Test3.odb   Abaqus/Standard 3DEXPERIENCE R2017x   Sun Mar 14 20:48:56 SA Pacific Standard Time 2021

Step: Lateral_Load, Lateral load analysis
Increment   2352: Step Time =   66.04
Primary Var: PE, Max. Principal
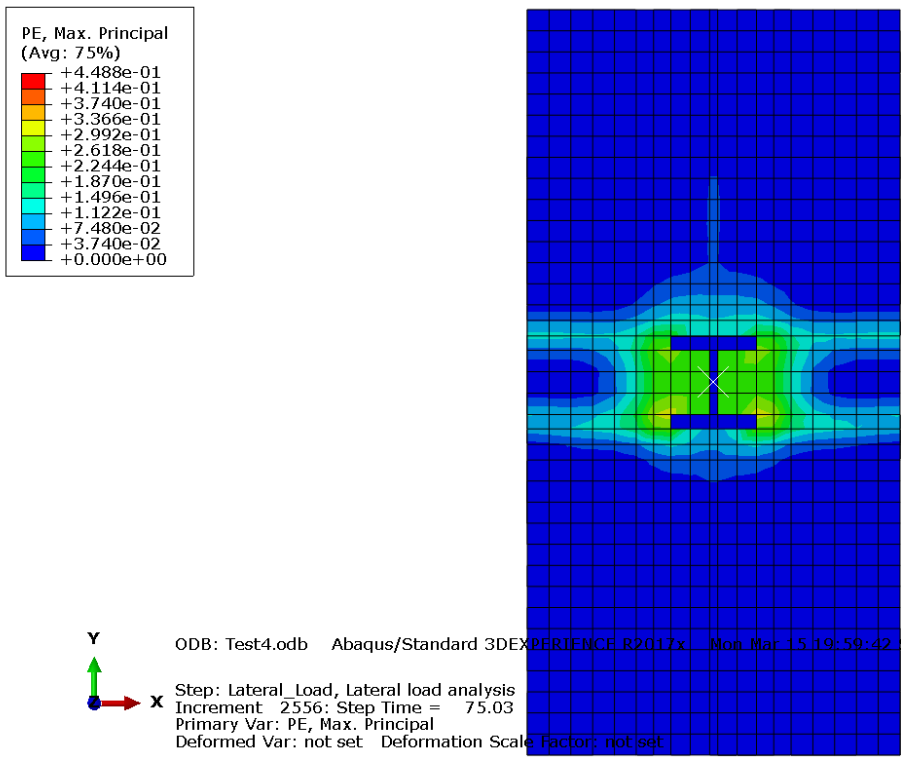Deformed Var: not set   Deformation Scale Factor: not set

Figure 69: Drift3-4% Plastic Strain Section Cut

S, Mises
(Avg: 75%)
+3.694e+02
+3.387e+02
+3.080e+02
+2.773e+02
+2.466e+02
+2.158e+02
+1.851e+02
+1.544e+02
+1.237e+02
+9.296e+01
+6.223e+01
+3.151e+01
+7.937e-01

ODB: Test3.odb   Abaqus/Standard 3DEXPERIENCE R2017x   Sun Mar 14 20:48:56 SA Pacific Standard Time 2021

Step: Lateral_Load, Lateral load analysis
Increment   2352: Step Time =   66.04
Primary Var: S, Mises
Deformed Var: not set   Deformation Scale Factor: not set
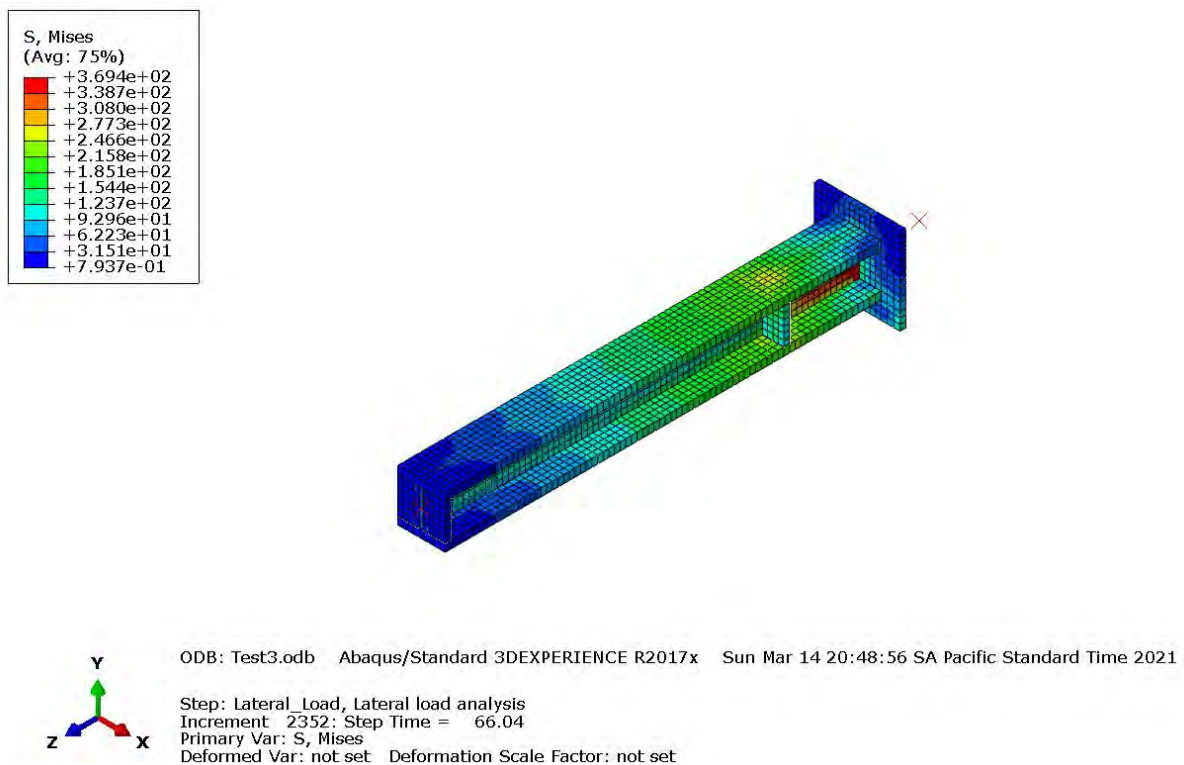
Figure 70: Drift4-6% Von Mises Column

3.5 Test #4

3.5.1) Mathematical Model
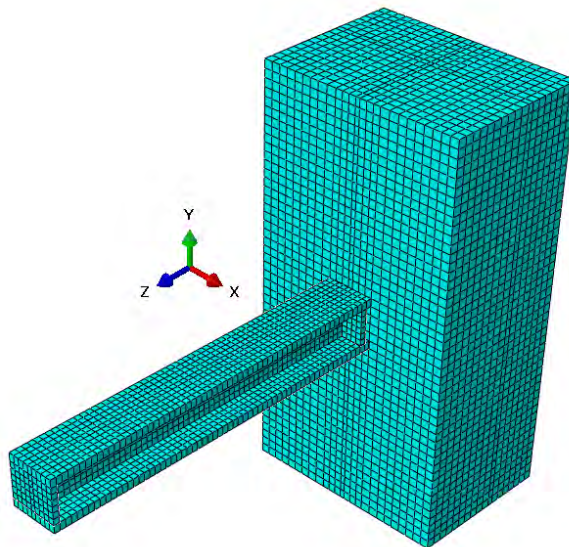
Figure 71:Test#4 Mesh

3.5.2) Monotonic Results at Displacement 150 [mm]

Figure 72: Test#4 Monotonic Results

3.5.3) Cyclic Results
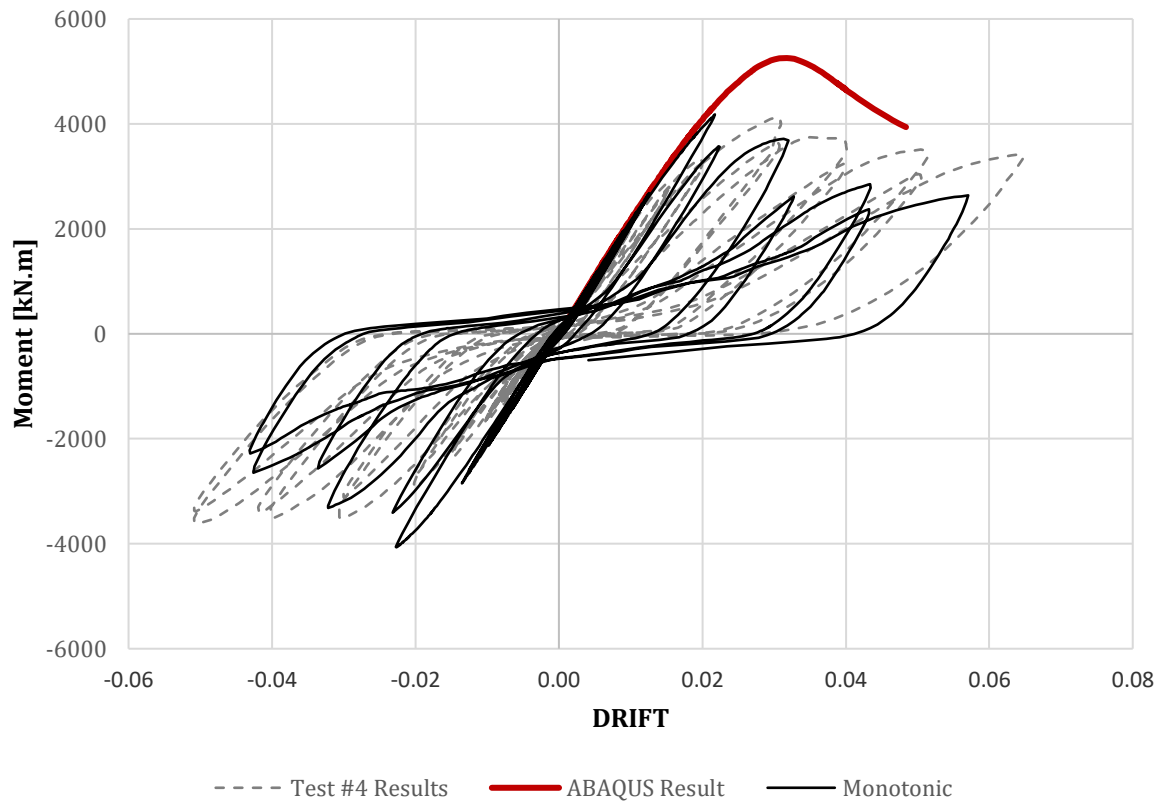
Figure 73:Test#4 Cyclic Results

Table 10: Test/FEA Results Test#4

Damage Progression				
Drift	Description	Displacement	Step	Time
less than ≈ 2%	Small crack began to form near the corners of the column.	66	1940	30.5
	Small gap adjacent to the tension flange. Growth of diagonal crack near the corner of the column.	66	1940	30.5
Drift 2%	Initial spalling of the concrete ahead of the column flanges.			
Drift 4-6%	Cracks radiating diagonally outwards from the corner of the column on the top surface of the pedestal.	176	2556	67
	Slight upward bulging of the concreate in the bearing zone between these cracks,			
	Significant gapping in the tension side.			
	Flexural cracks observed on the sides and the top of the pedestal			
	Diagonal shear cracks on the sides of the block, which appeared as straight cracks parallel to the flanges on the top surface.			

Figure 74:Representative Drifts Test#4

Figure 75:Drift 2% Equivalent Plastic Strain - Test#4

Figure 76: PE Section Cut Drift1%

Figure 77: Drift4-6% Plastic Strain

Figure 78: Drift4-6% Plastic Strain Section Cut

Figure 79:Drift4-6% PE Concrete Block
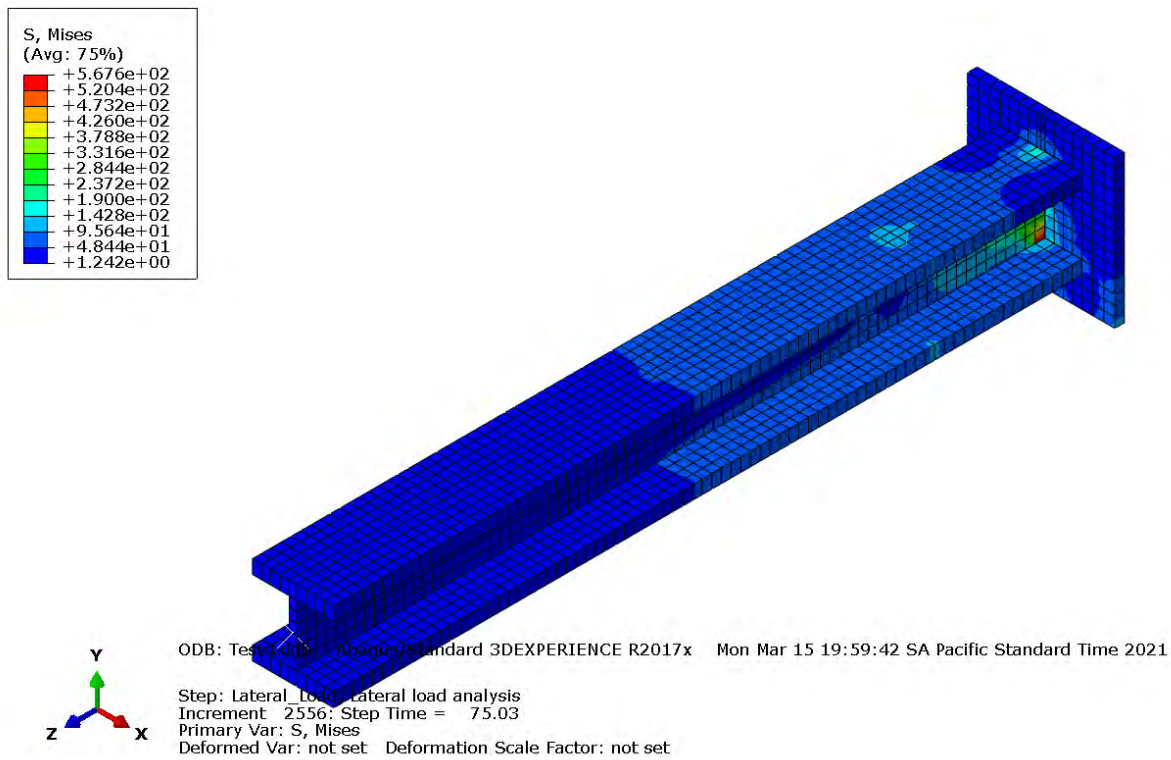
Figure 80: Drift4-6% Von Mises Column

4. Conclusions

All simulations show a well-defined linear-elastic branch up to the point where nonlinear behavior starts, which corresponds to rotations close to 0.005rad. This observation is consistent with the experimental evidence reported that indicates that after 0.005rads, small cracks on the tension column flange start to open, entailing a gradual nonlinear response. These small cracks are accompanied by diagonal cracks, which start to grow near the steel column corners.

As deformation progresses in all simulations, an appreciable loss of stiffness is observed because the concrete reaches its peak strength and the connection start to develop significant gapping. As the gap formed in the foundation in the tension flange side grows, which is consistent with the experimental tests. This gapping is responsible for the pinching behavior observed in all the tests since it causes a relatively unconstrained rotation of the steel column as it moves back to the vertical position and goes in the reverse direction (following the cyclic loading protocol). Tests with higher embedment depths (760mm) present a more gradual stiffness decrease. This phenomenon may be attributed to the fact that higher embedment lengths imply a great fraction of the total Moment carried by the horizontal bearing stresses. Thus, when this latter mechanism starts to deteriorate, the stress decrease seems to be more gradual.

It can be seen from the sensibility analysis presented in Appendix 2 that the strength characterization of the analytical model is highly sensitive to the frictional interaction parameters selected for the model. When frictionless interaction is specified in the model there is a peak strength reduction in the monotonic displacement analysis and an overall strength and post yield strength reduction in the cyclic analysis.

From the parametric analysis presented in appendix 2 it can be seen that the analysis results obtained from a model considering geometric nonlinearity and a model neglecting it are similar. Thus, one can conclude that the hysteretic connection behavior is not susceptible to second order effects in the response.

From the set of analysis presented in Appendix 2 it can be seen that the model strength characterization is sensible to the CDP model parameters, showing the following trends in the response: For higher values of "Dilatation Angle" the model shows an increase in the peak moment strength. Also, for lower "Viscosity Parameters" the model shown a decrease in the connection peak moment strength, for lower values the model requires an increase in the number of iterations required to reach convergence.

It is seen in the analysis results that the stress distribution along the steel column flange for test 1 at first that the "real" stress distribution is closer to a triangular shape. This observation is not surprising since at this level of deformation, the connection starts to incursion in the nonlinear regime, and a triangular shape is consistent with an elastic behavior. In contrast, once the connection has reached its peak, it is observed in the simulations a more uniform stress distribution along a certain length of the flange. This finding is consistent with the rectangular stress block assumed by Grilli and Kanvinde in their strength method.

5.   Future Research

The simulations indicate that at rotation levels close to the "first" yield of the connection, the stresses are not uniform along the column flange; instead, a triangular shape can be assumed. In contrast, at higher rotations, the stresses tend to become relatively uniform. Thus, when the connection reaches its peak strength, it seems that the rectangular block assumption is appropriate. However, this issue deserves a further look.

The paper has several limitations that should be addressed in a new study in order to generalize the conclusions. For example, the number of simulations (four in total) is limited. Moreover, the experimental program is the only testbed used. It is recommended to build more FE models from other experimental programs available to assess different configurations' behavior (e.g., column size, embedment length, the influence of shear studs). Besides, this study does not address issues related to the seismic demands on the EBC, or a reliability analysis to assess if the strength resistance factors adopted are adequate or not. The experimental program research focused in the characterization of the concrete failure modes in the connection, to achieve this the steel column was made artificially strong. The use of nonlinear FE analysis model could aid in evaluating the connection response for standard connection details and aid in the validation of the calculation strength model.

6. Appendix 1 – Modeling Procedure

The following appendix is intended as a step-by-step modeling guideline of the ECB Test #1 in ABAQUS.

ABAQUS assume the use of a consistent unit system. The SI system was selected for this model.

Table 1. Consistent units.

Quantity	SI	SI (mm)	US Unit (ft)	US Unit (inch)
Length	m	mm	ft	in
Force	N	N	lbf	lbf
Mass	kg	tonne (10^3 kg)	slug	lbf s^2/in
Time	s	s	s	s
Stress	Pa (N/m^2)	MPa (N/mm^2)	lbf/ft^2	psi (lbf/in^2)
Energy	J	mJ (10^{-3} J)	ft lbf	in lbf
Density	kg/m^3	tonne/mm^3	slug/ft^3	lbf s^2/in^4

Figure 81: ABAQUS Units (from [22])

6.1 ECB Connection layout

The geometry of the connection was modeled in AUTOCAD. The CAD model didn't include the holes (overlapping space) in the connection, this void space is created in ABAQUS to avoid precision issues.
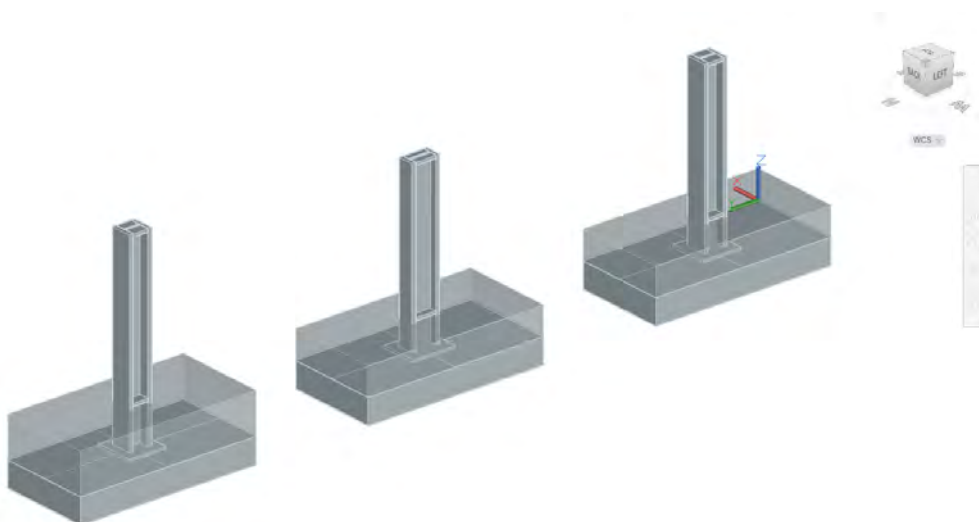
Figure 82:ACAD Layout

The connection parts are later exported using .sat file extension using AUTOCAD export command.
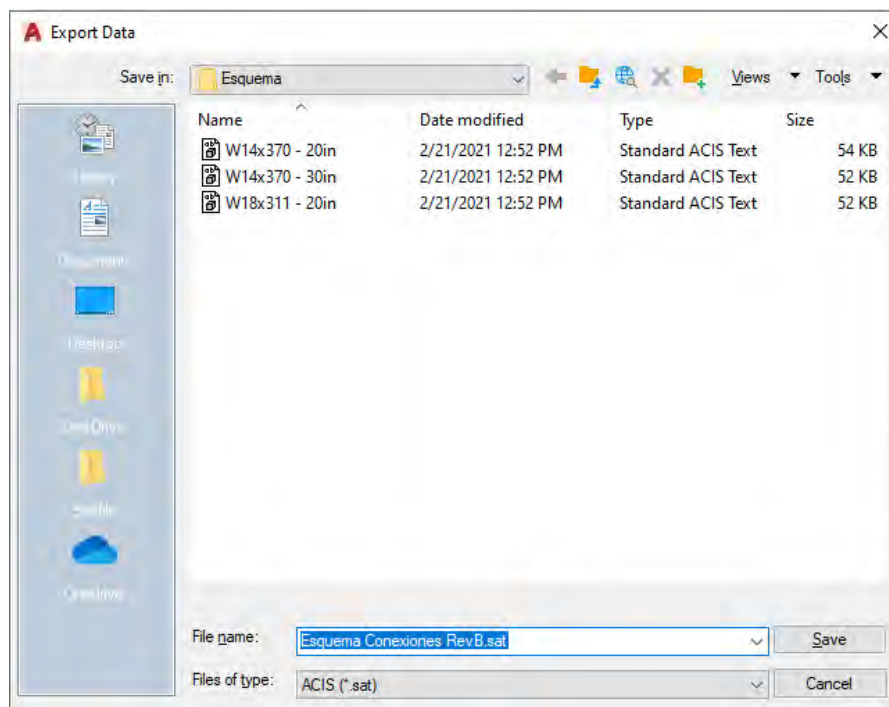
Figure 83:Model Import

6.2 ABAQUS Part import
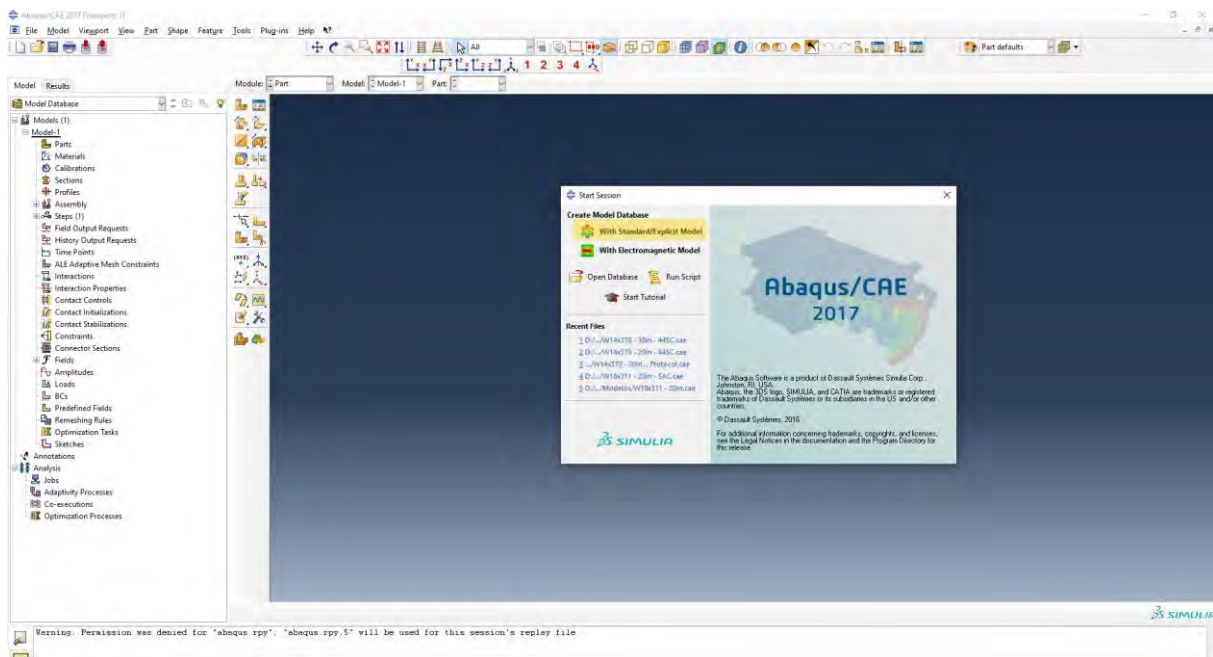
Figure 84: Abaqus import

In ABAQUS the "With Standard/Explicit Model" module is selected.
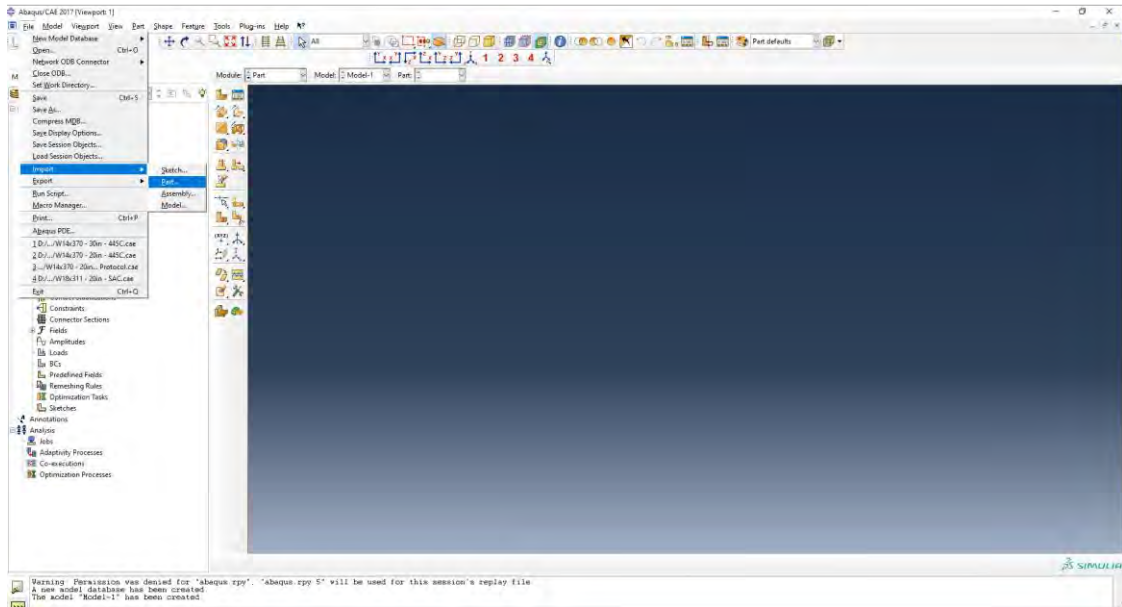
Figure 85:Part Import

The import parts command is selected.
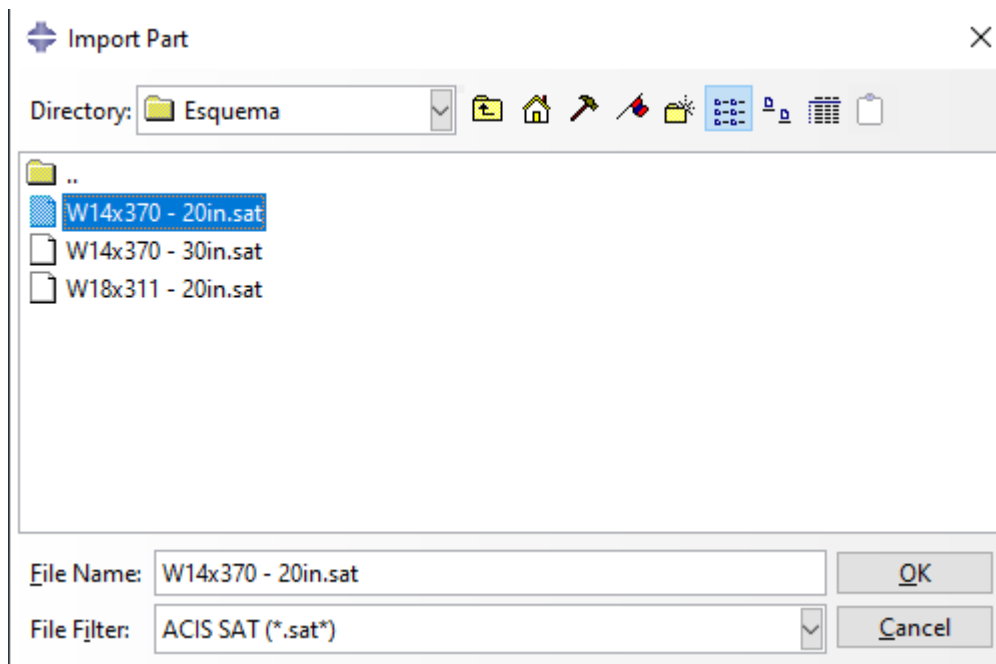
Figure 86: .sat Window

The .sat model is selected.
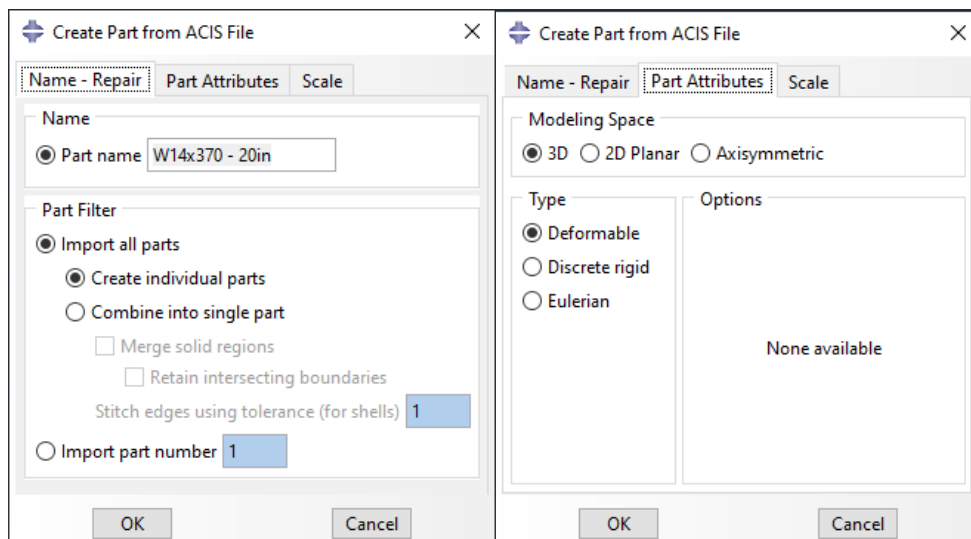
Figure 87: Import Module

Is importian to maintain consisten units between AUTOCAD and ABAQUS.

In the proyect browser the parts are then renamed and only one stiffener is left in the model.
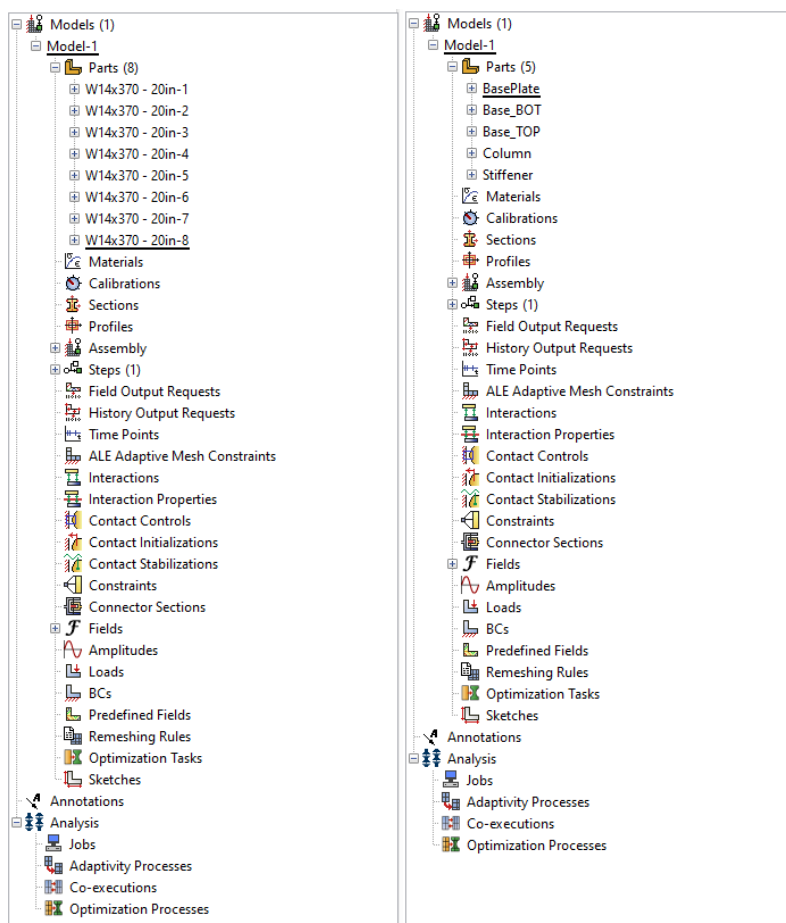
Figure 88:Proyect Browser

The property module is selected, and materials are created.

For steel only Density and Elastic behavior is selected.
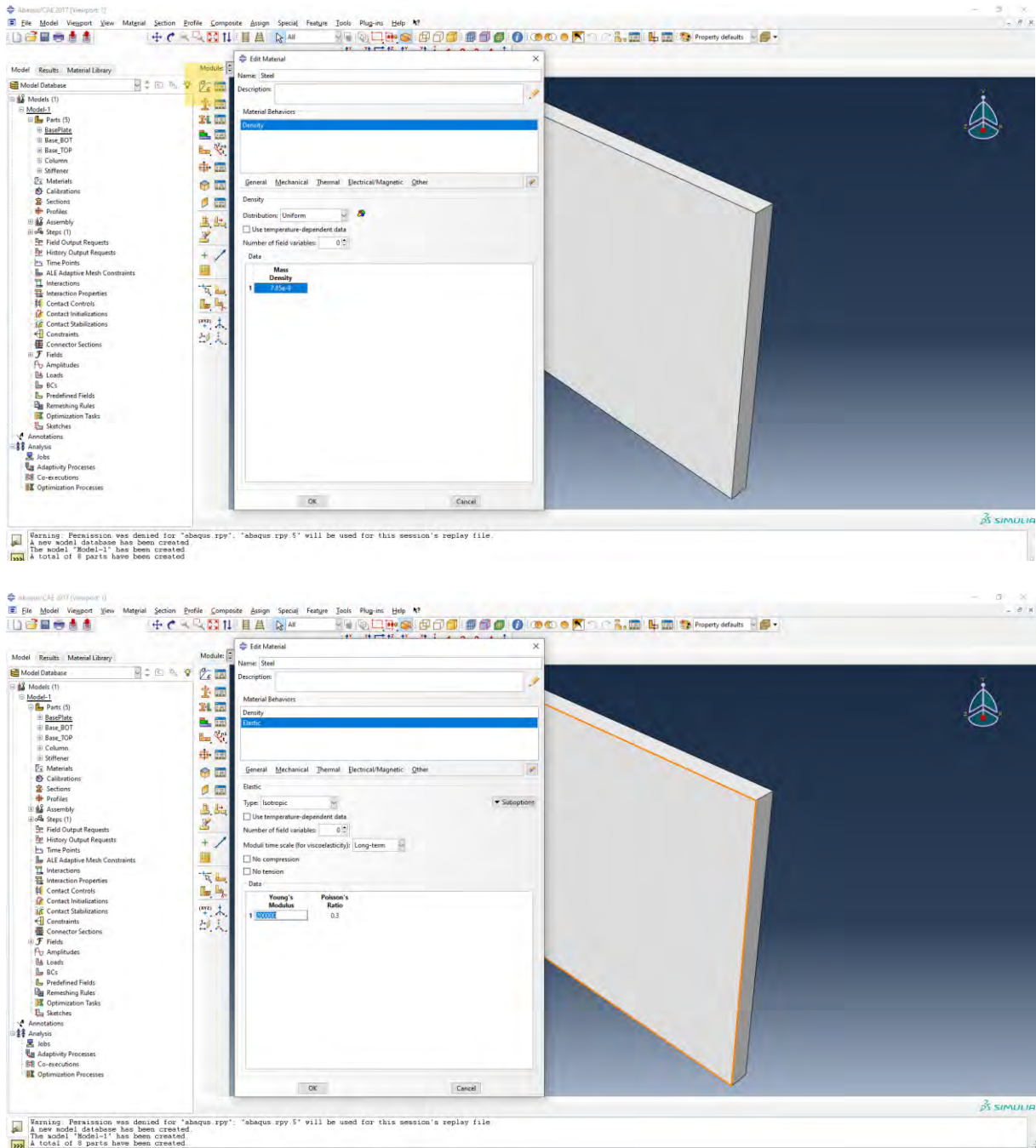
Figure 89: Steel Material

For concrete, Density, Elastic, and Concrete Damage Plasticity behaviors are selected.
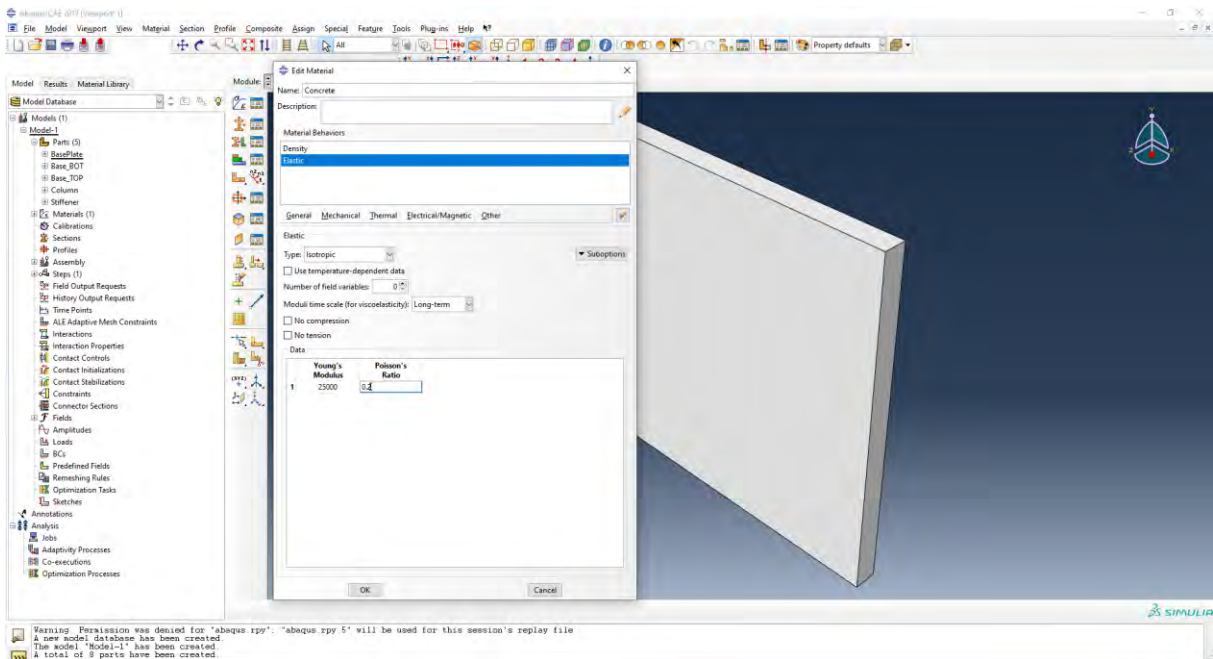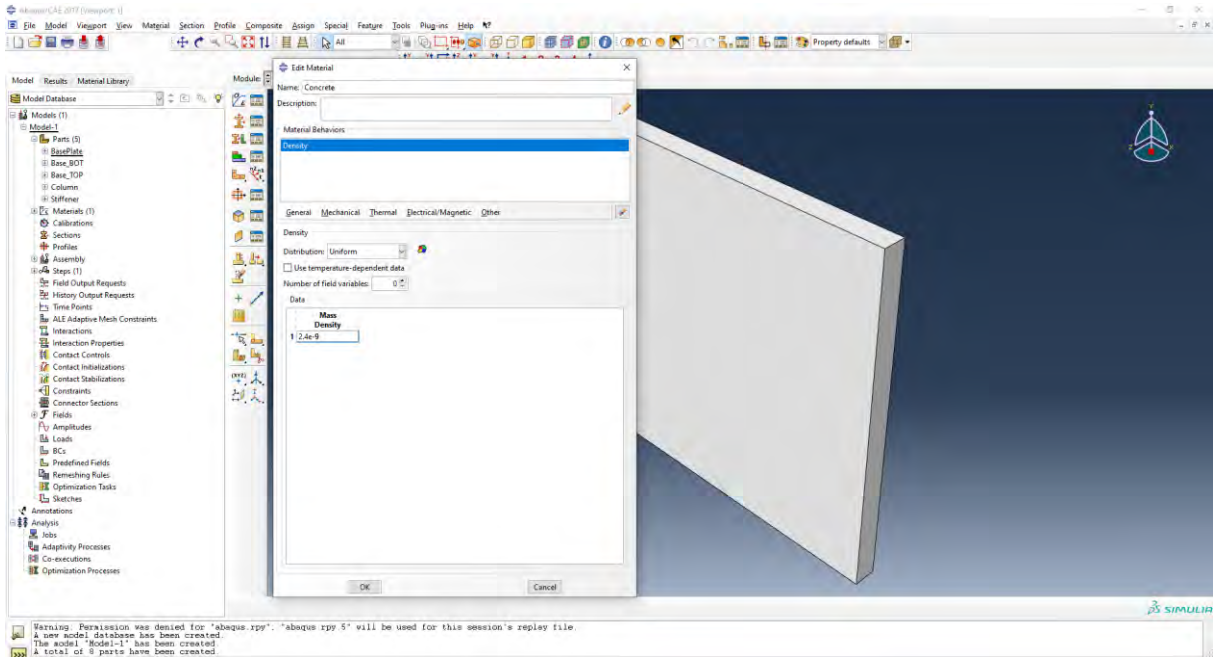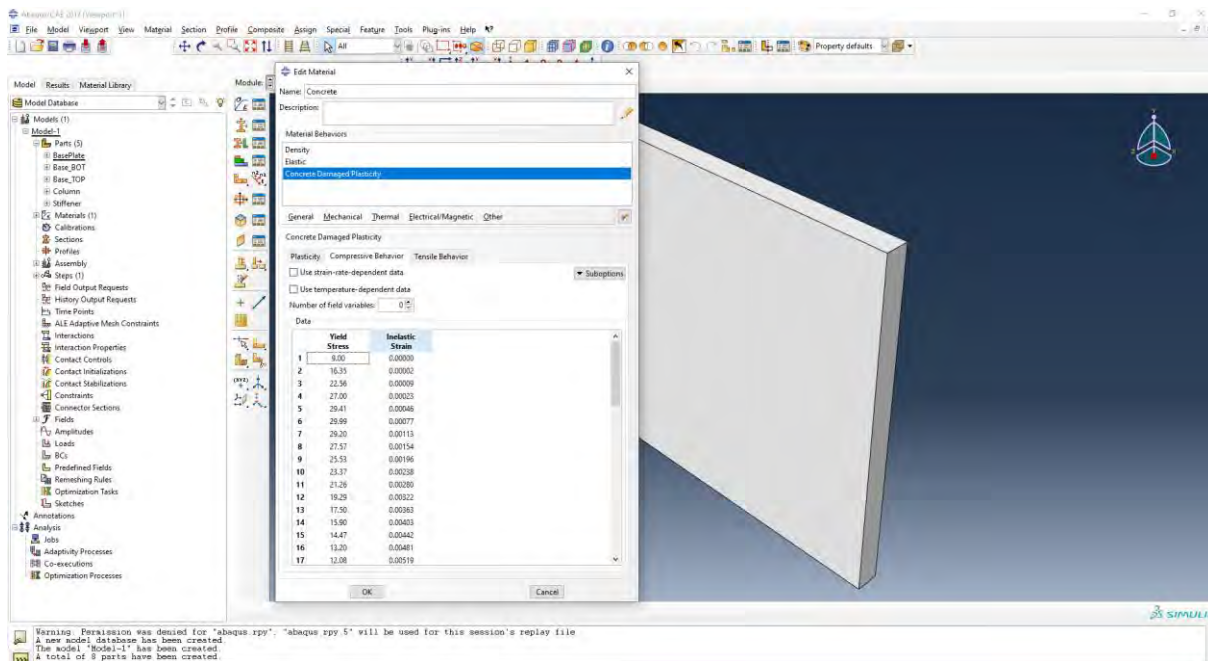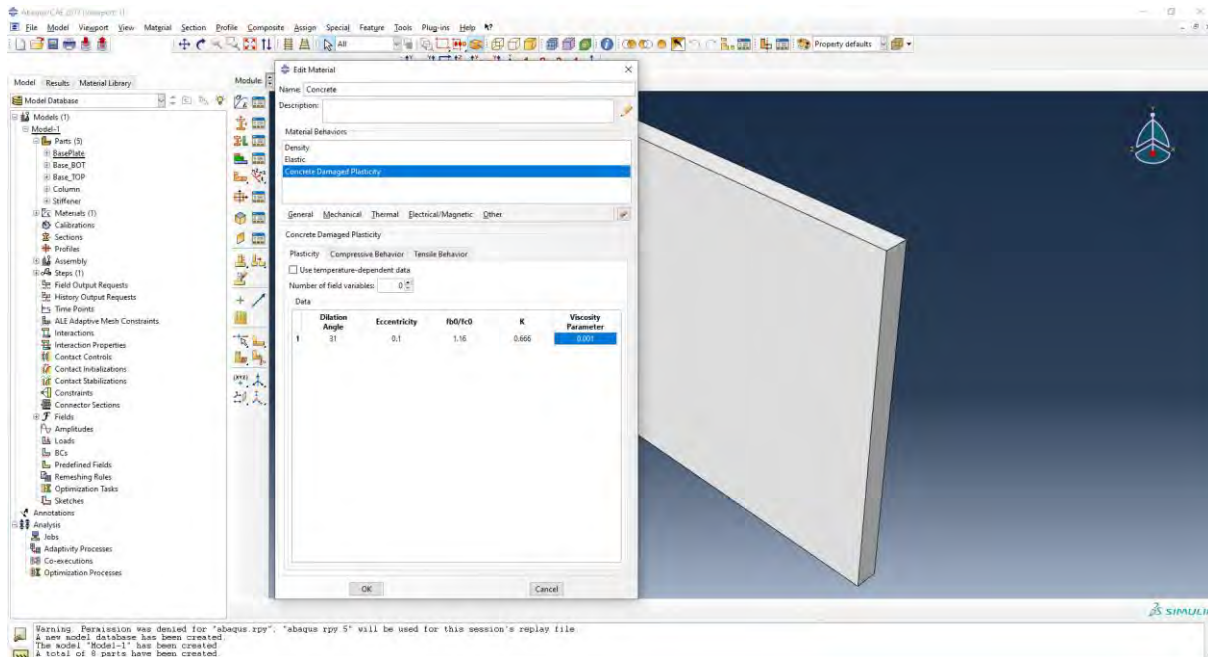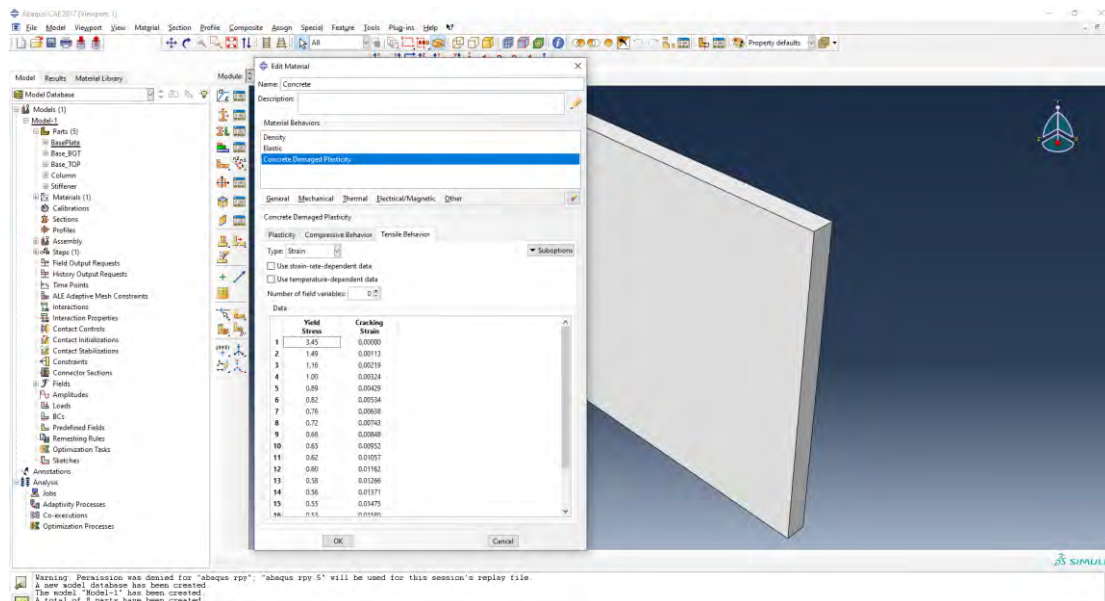
Figure 90: CDP Material

Any uniaxial constitutive model for concrete can be used. In this analysis the Popovics model was employ.

ABAQUS requires that the yield stress and inelastic strains be imputed as the material model. The first yield stress corresponds to the elastic part of the concrete constitutive model, approximately 30% of the maximum compressive stress and the maximum tensile stress. Inelastic strains correspond to the total strain in the constitutive model minus the elastic recoverable portion of the strain.
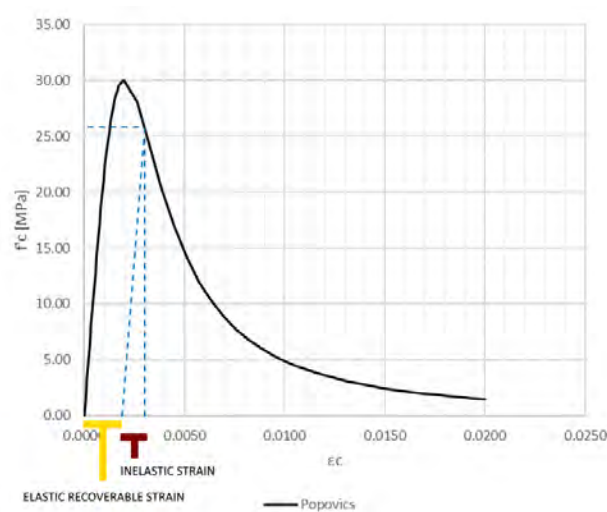
Figure 91:CDP Yield Stress vs Strain

Sections are the created. For this model Solid Homogeneous sections are used.
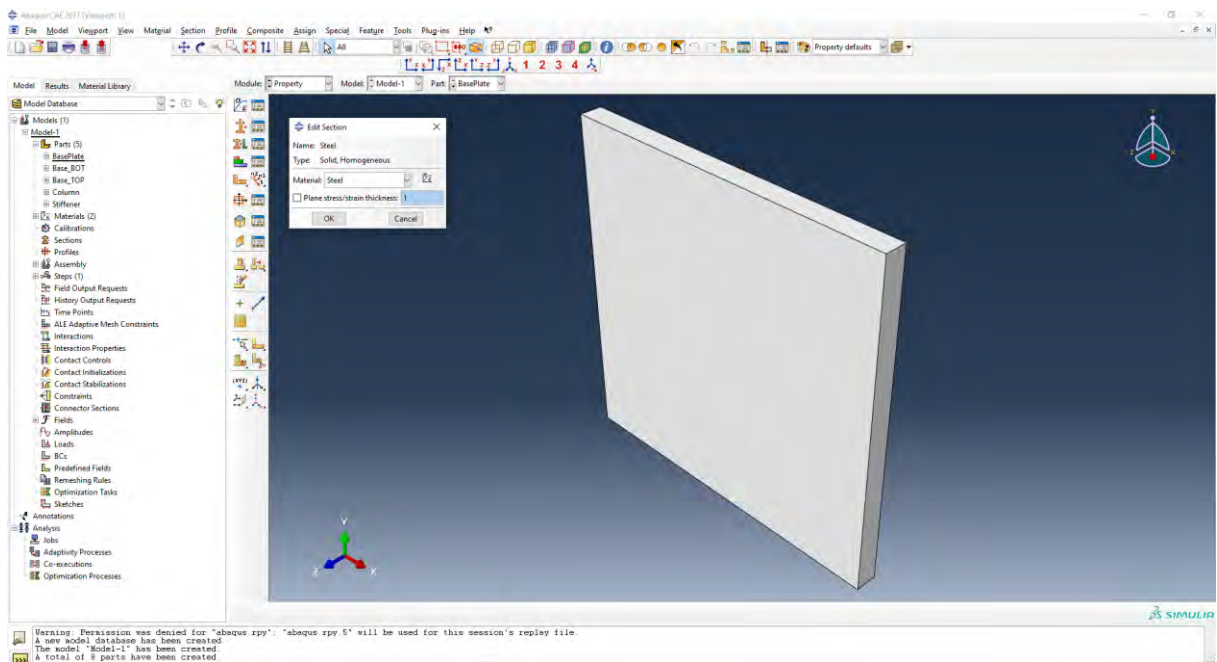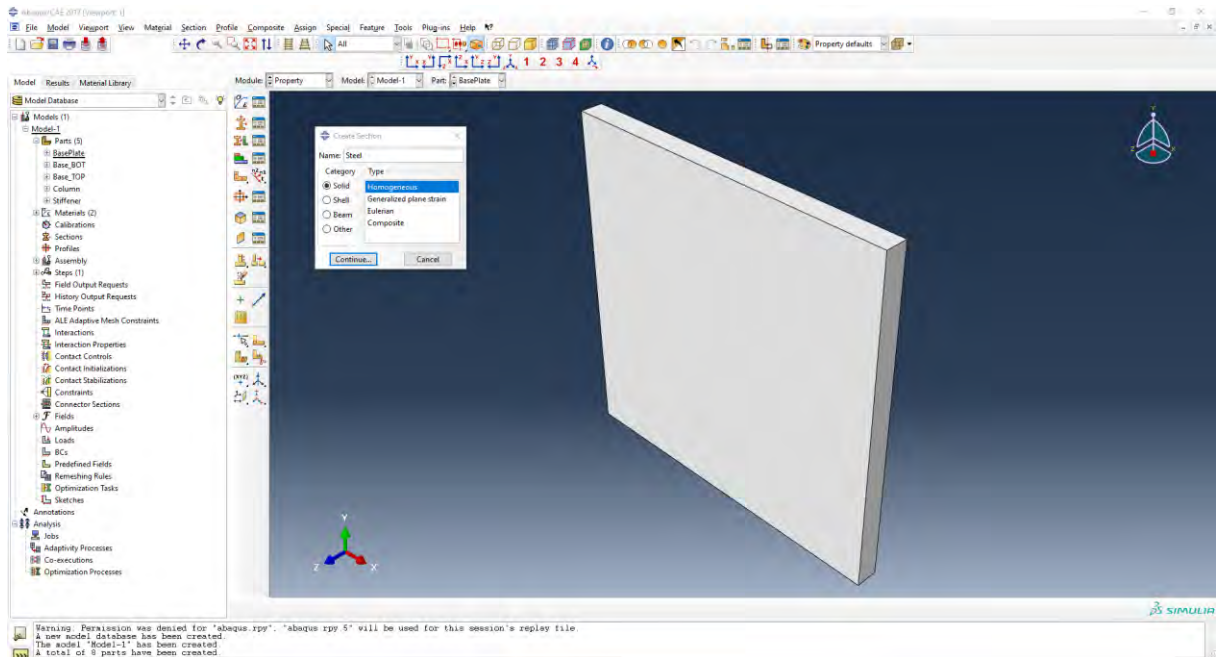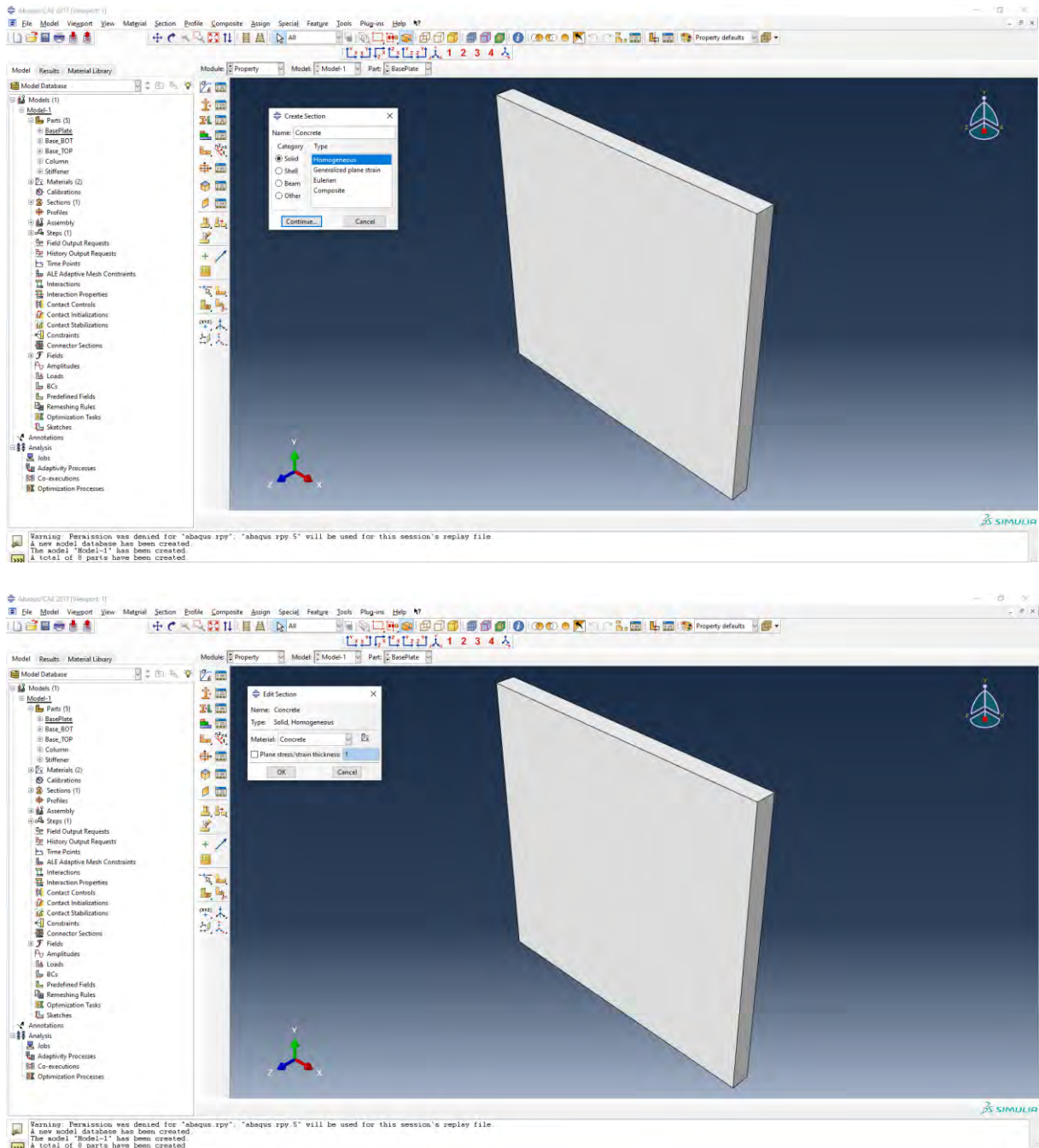
Figure 92: ABAQUS Properties Assigments

Then Sections are assigned to the different parts of the model. Only the procedure for one part

is shown in this document for brevity.
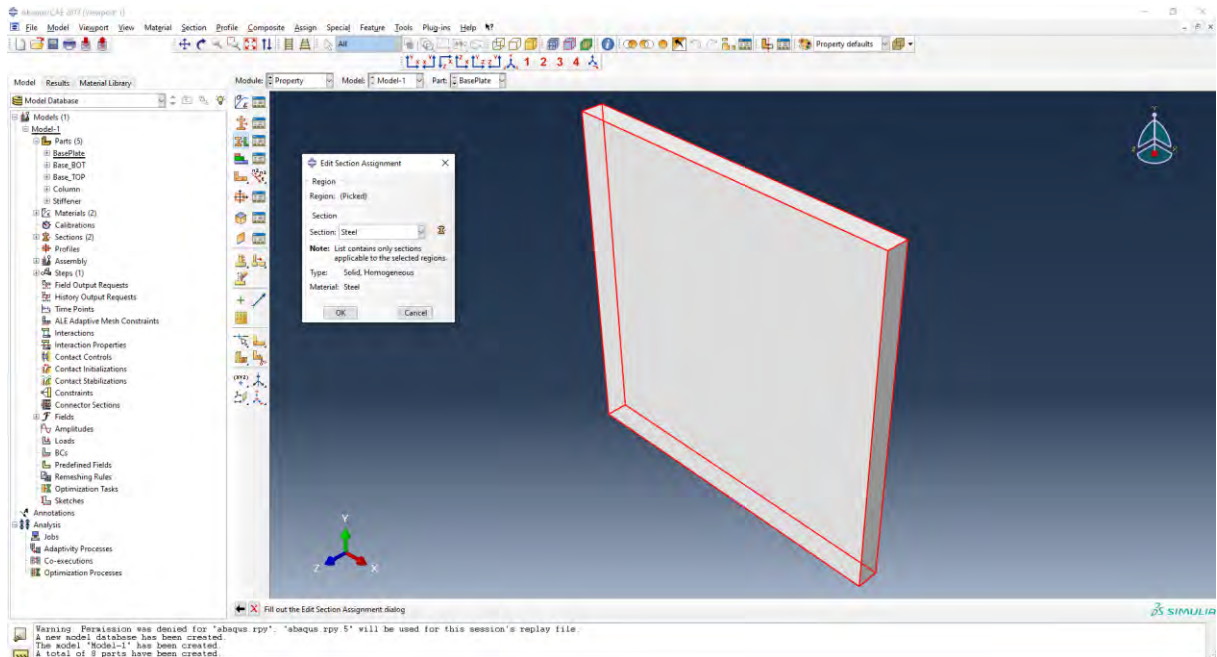
Then the model Assembly module is selected
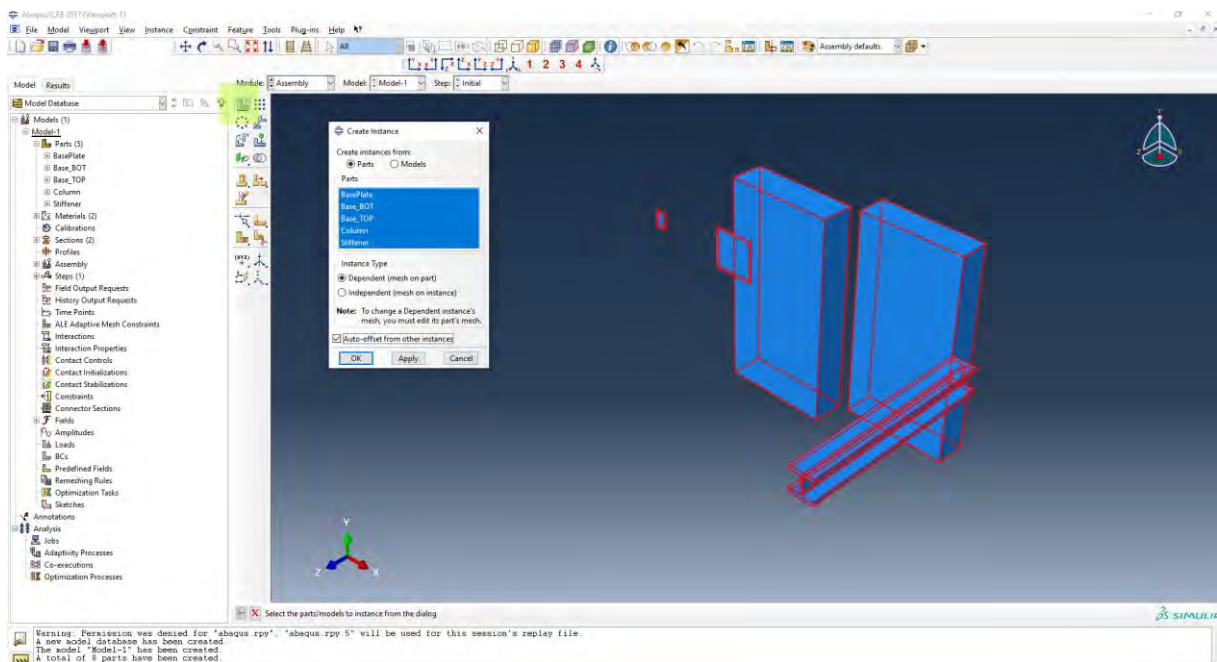
Figure 93: ABAQUS Assembly

Three additional stiffeners must be added to the assembly using the same module.

Using the translate instance the model is assemble. Datum points are created in the part module to aid the processes.
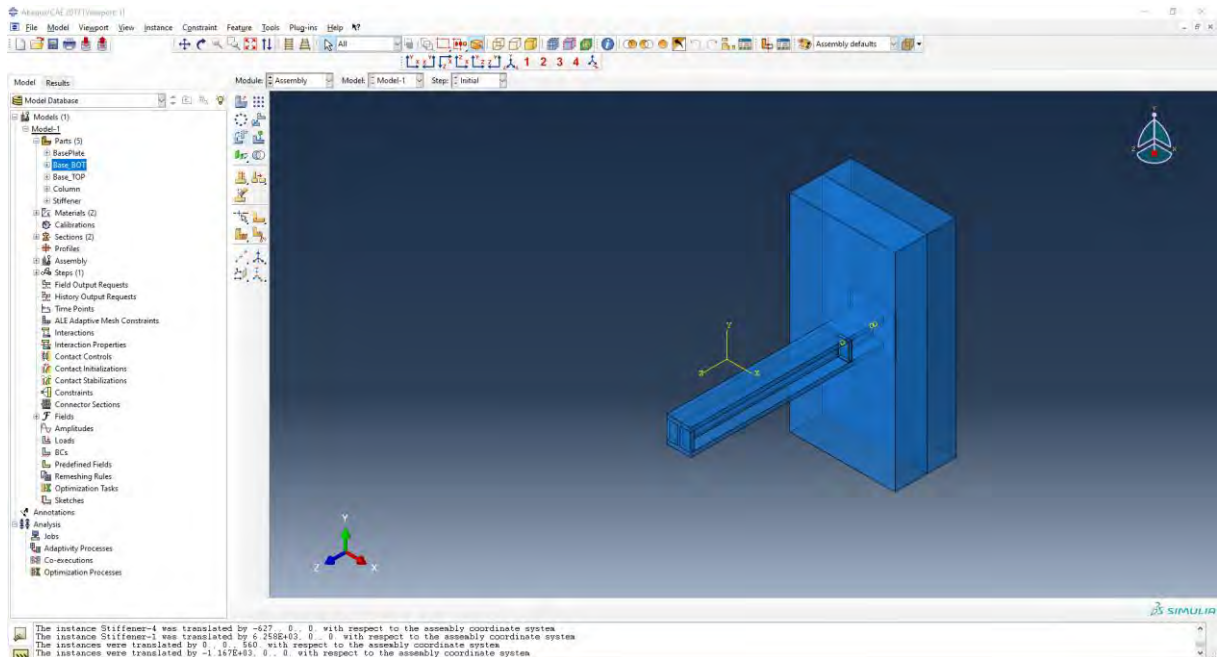
Figure 94: Assembly Formation

Once the assembly is created, the concrete parts are merged together.
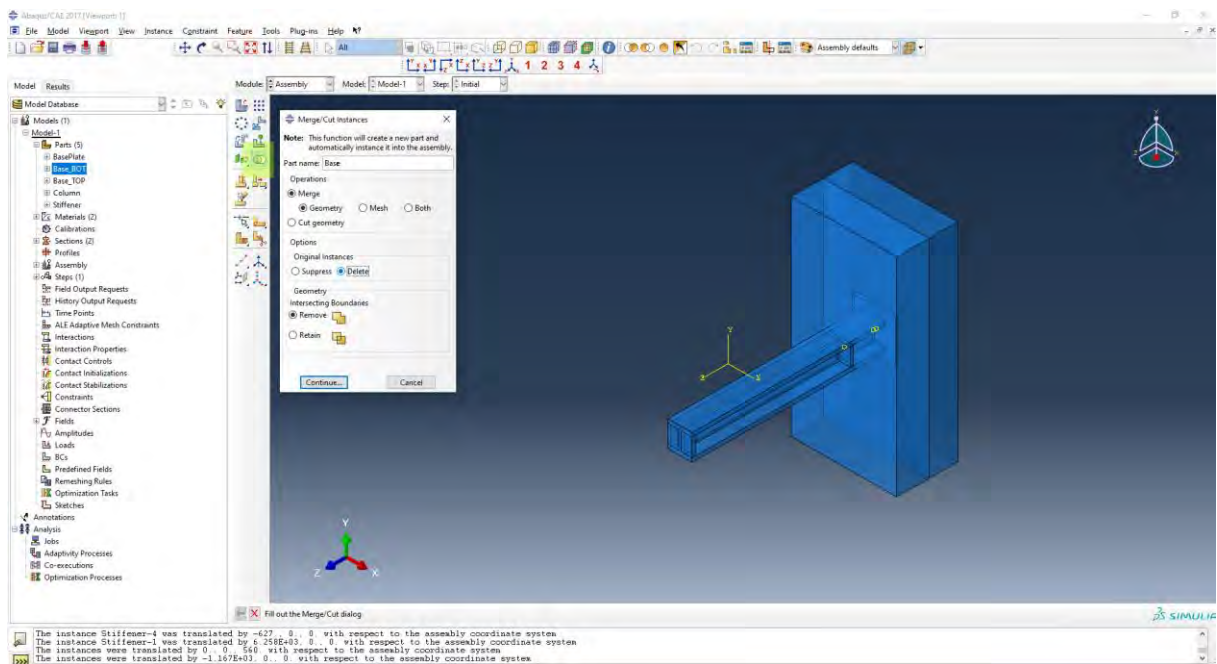
Then the void space in the concrete base is created
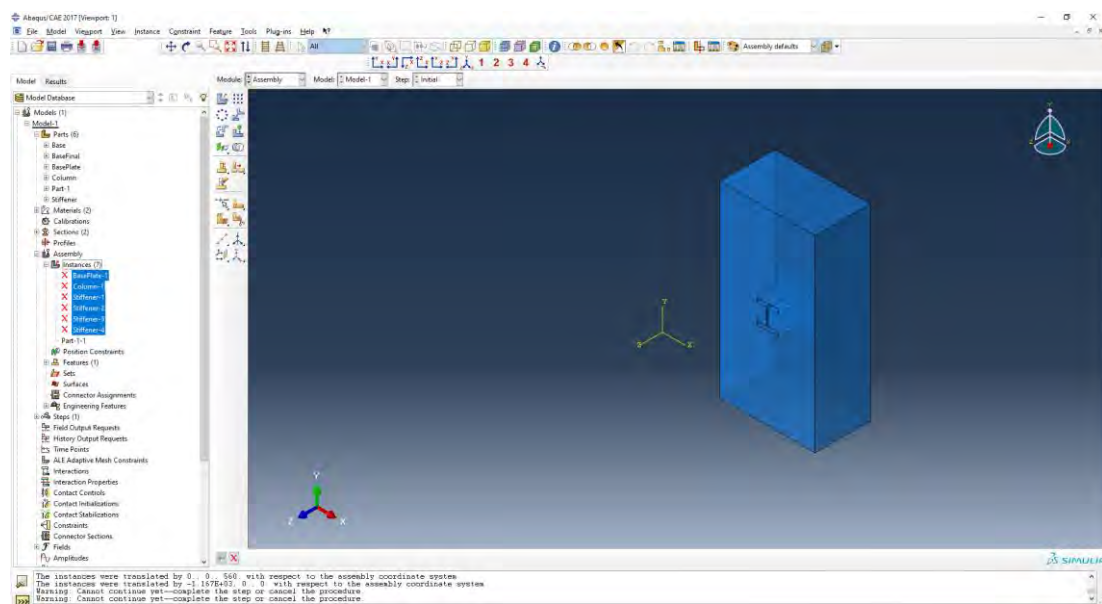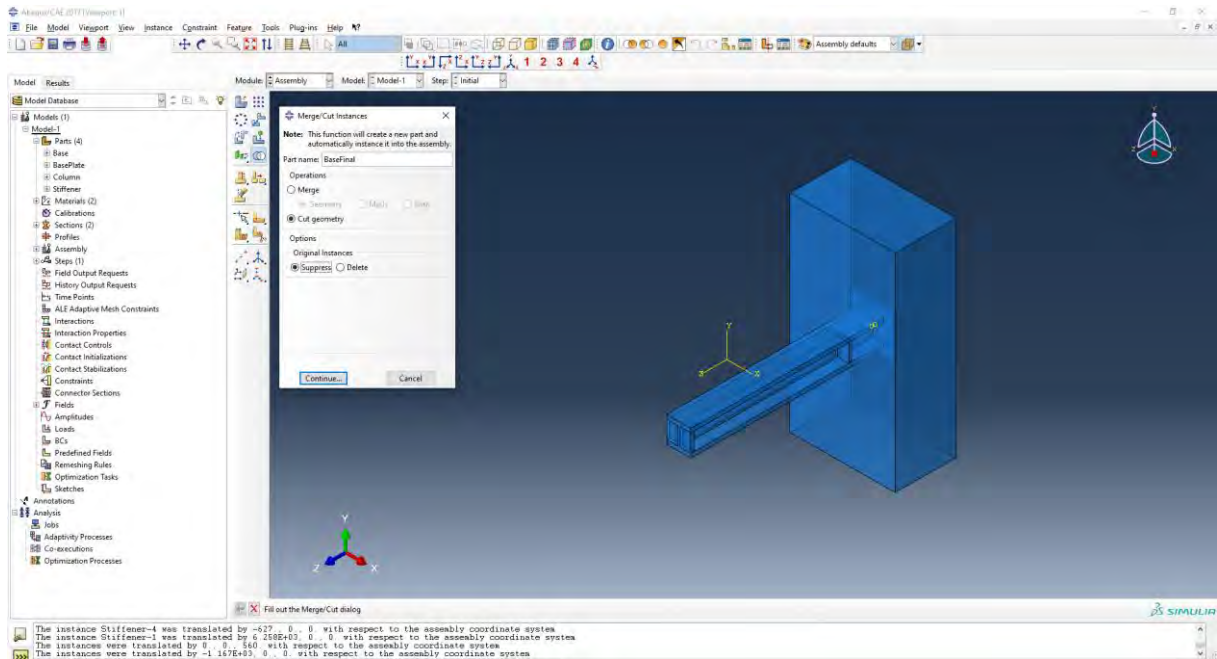
Figure 95: ABAQUS Void Creation

In the project browser the old parts are deleted and only the parts corresponding to the assemble remain.

In the Step module the analysis steps are then created: Gravity, Axial Load, and Lateral Loads.
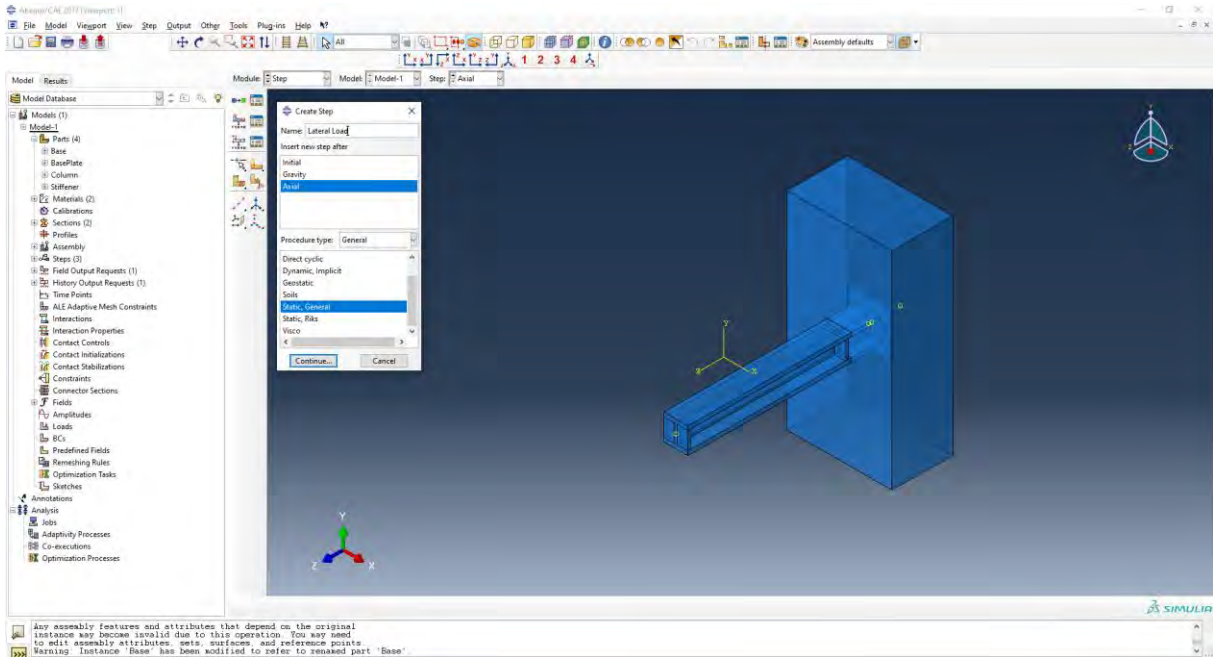
The procedure type is Static, General
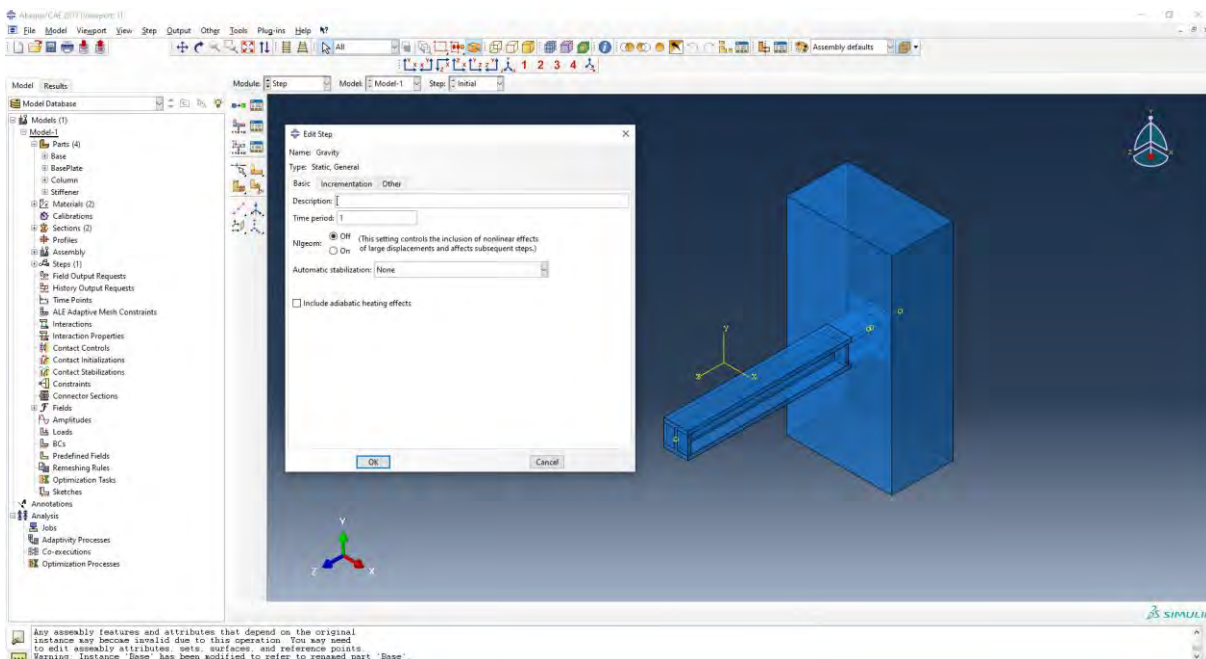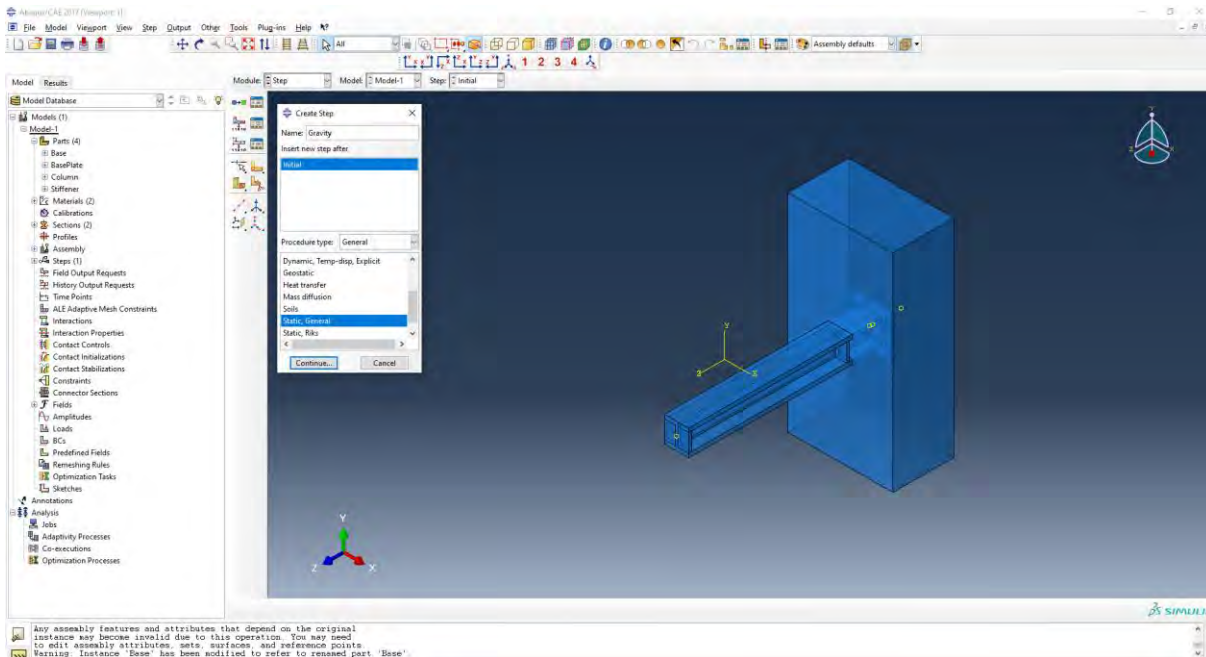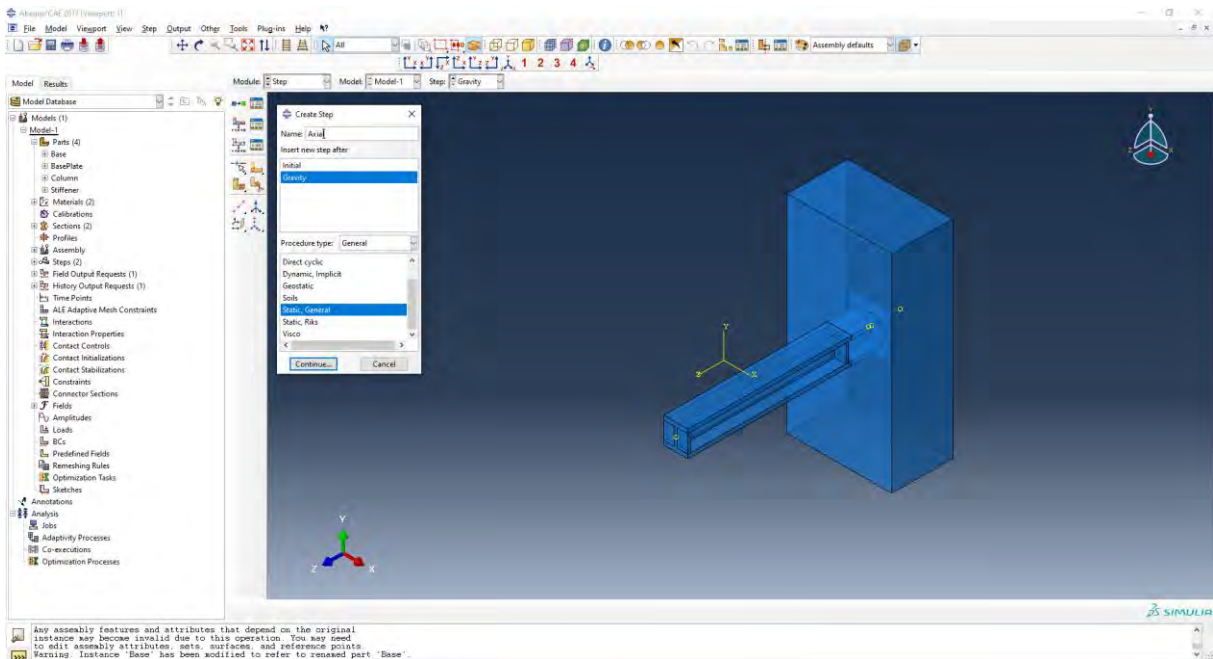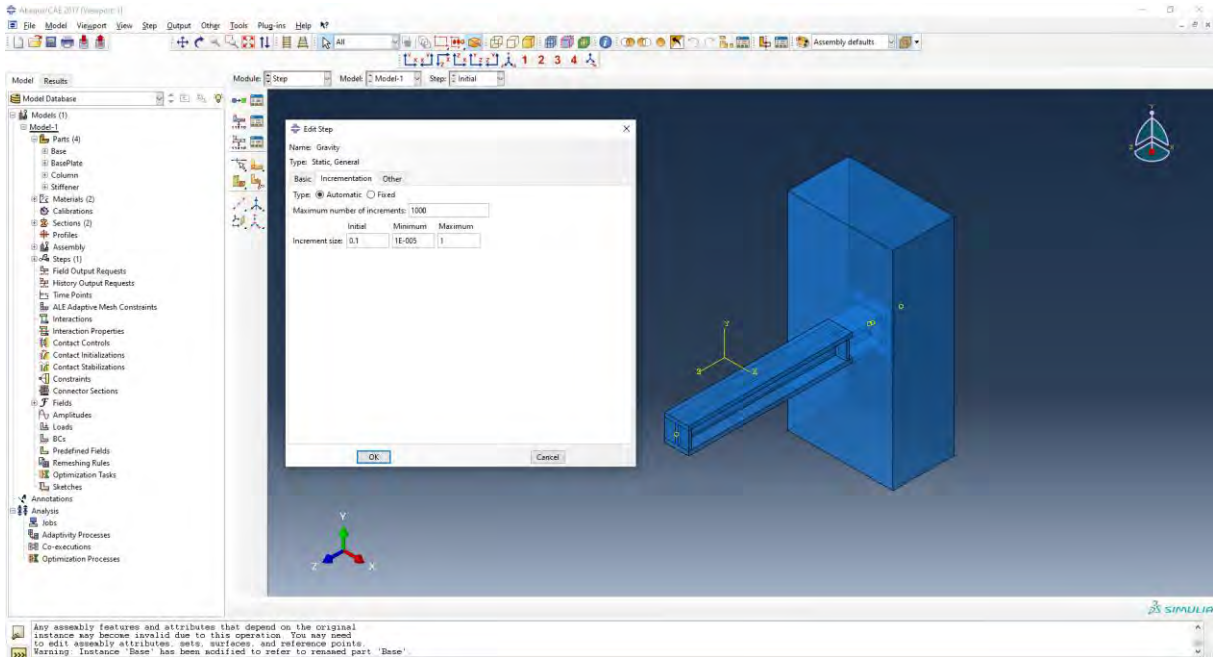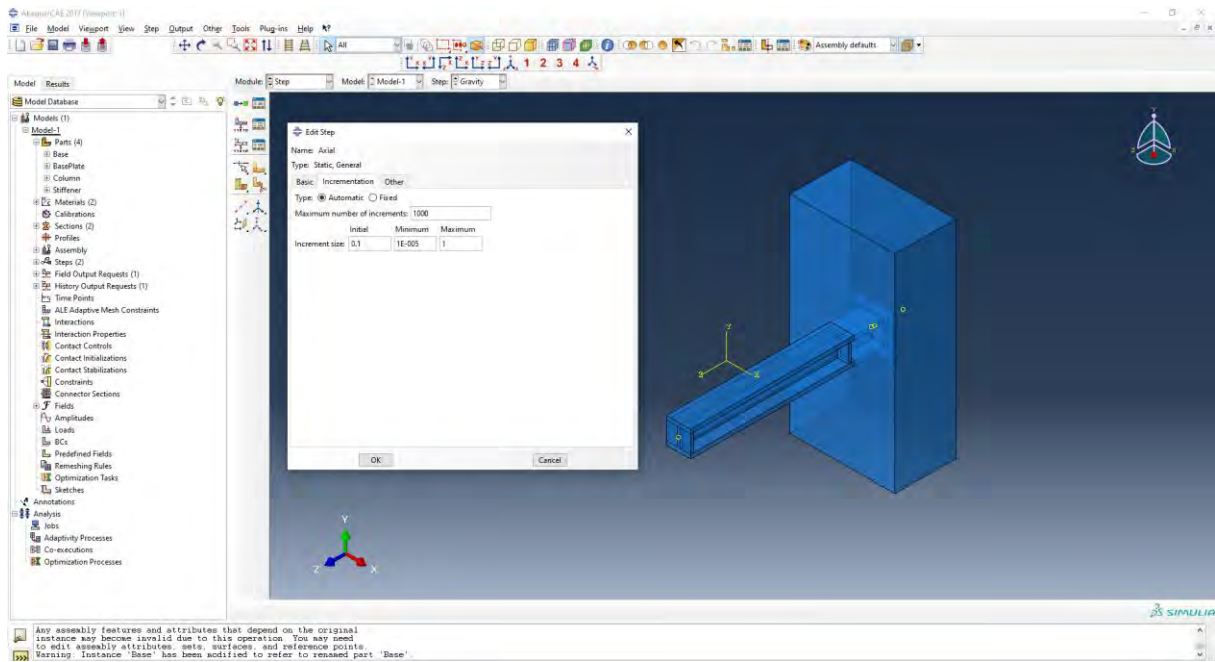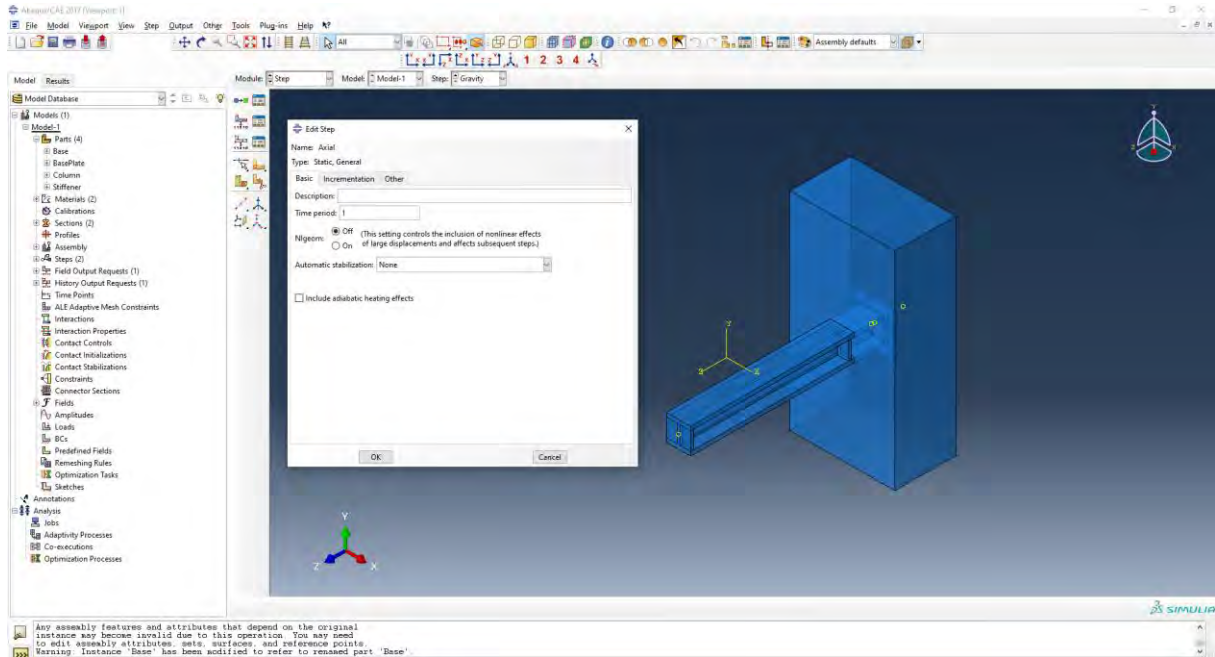
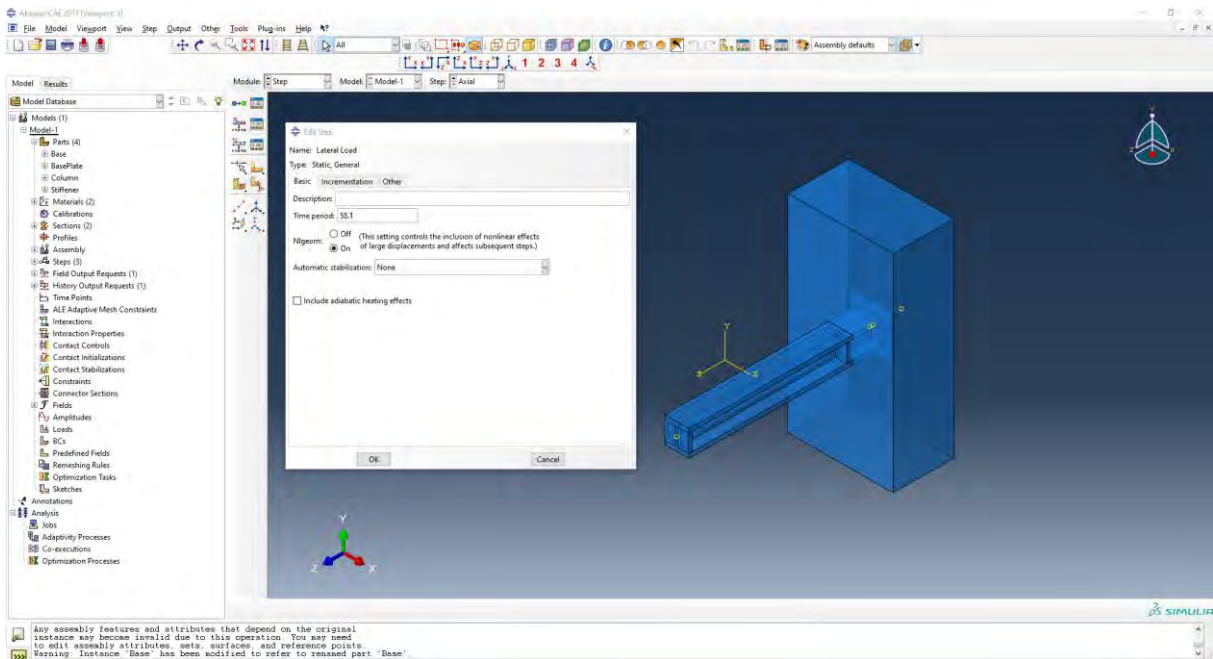In the lateral load step, the time correspond to the total time in the loading protocol.
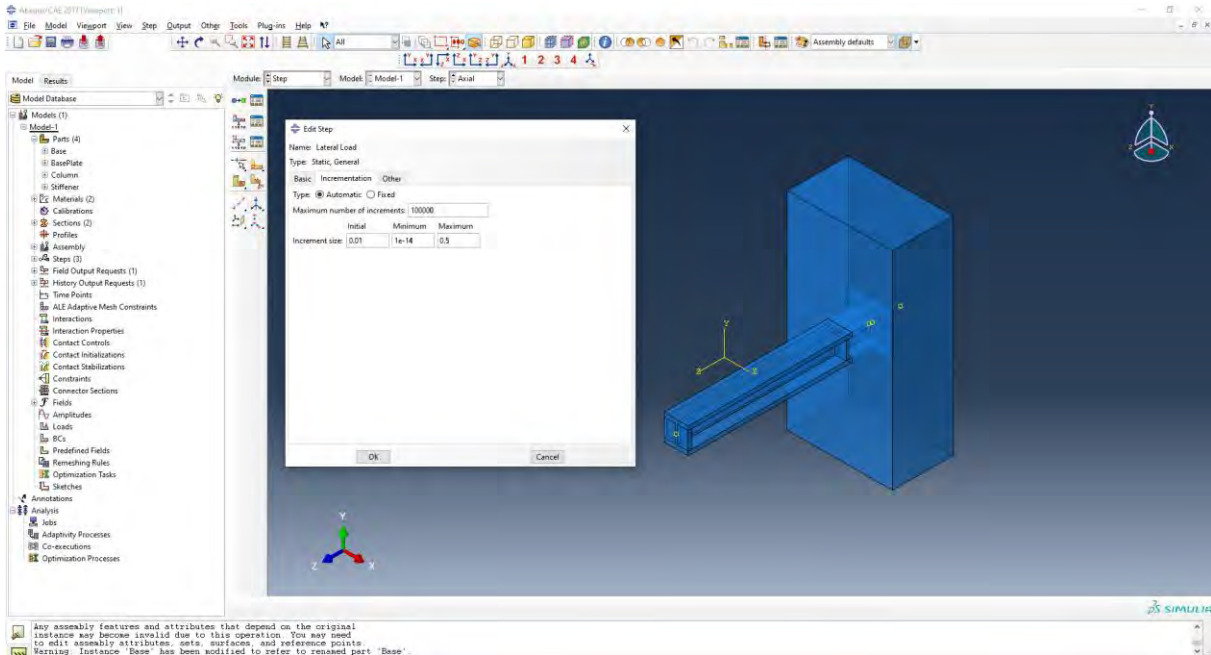

Figure 96: ABAQUS Step Creation

Automatic stabilization is not specified as it can introduce fictious forces to the model, care

must be given when using this parameter to increase the convergence of the model.

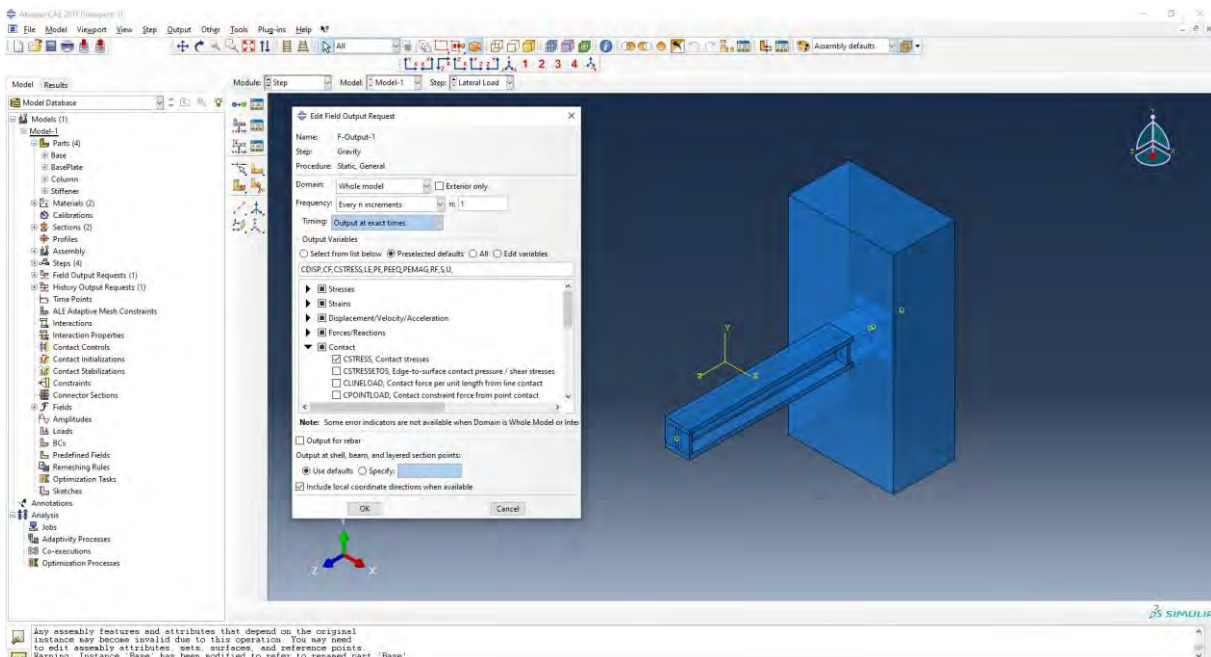Once the steps are created the Field output must be selected. This corresponds to all the saved results of the model.
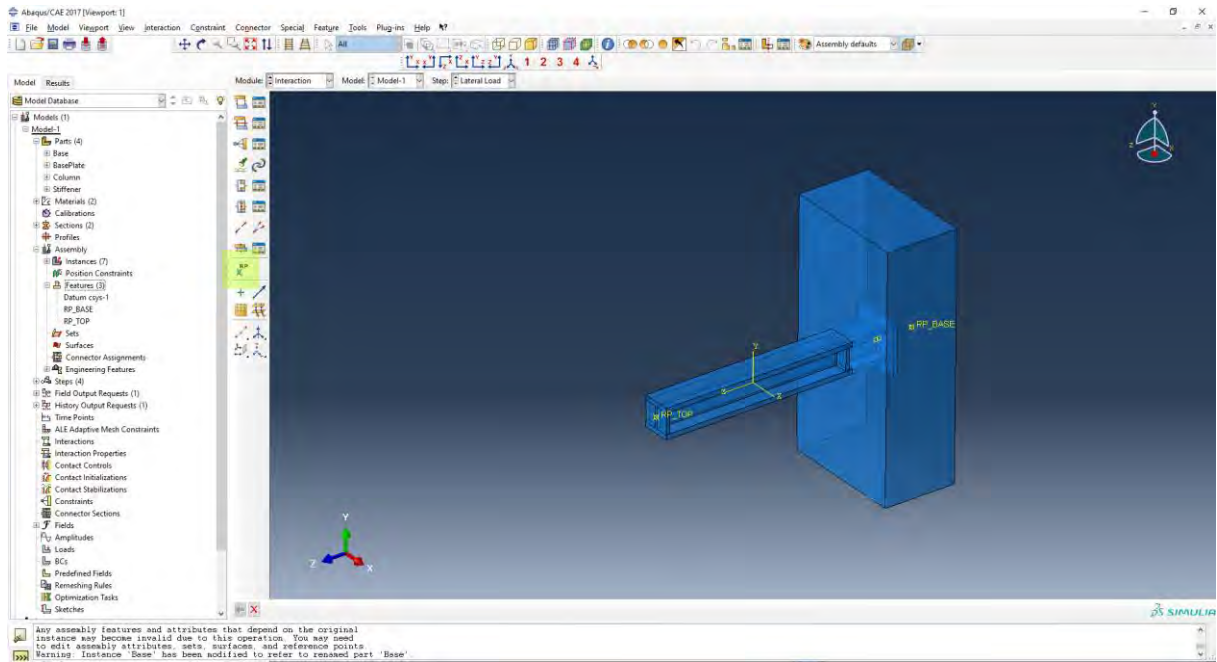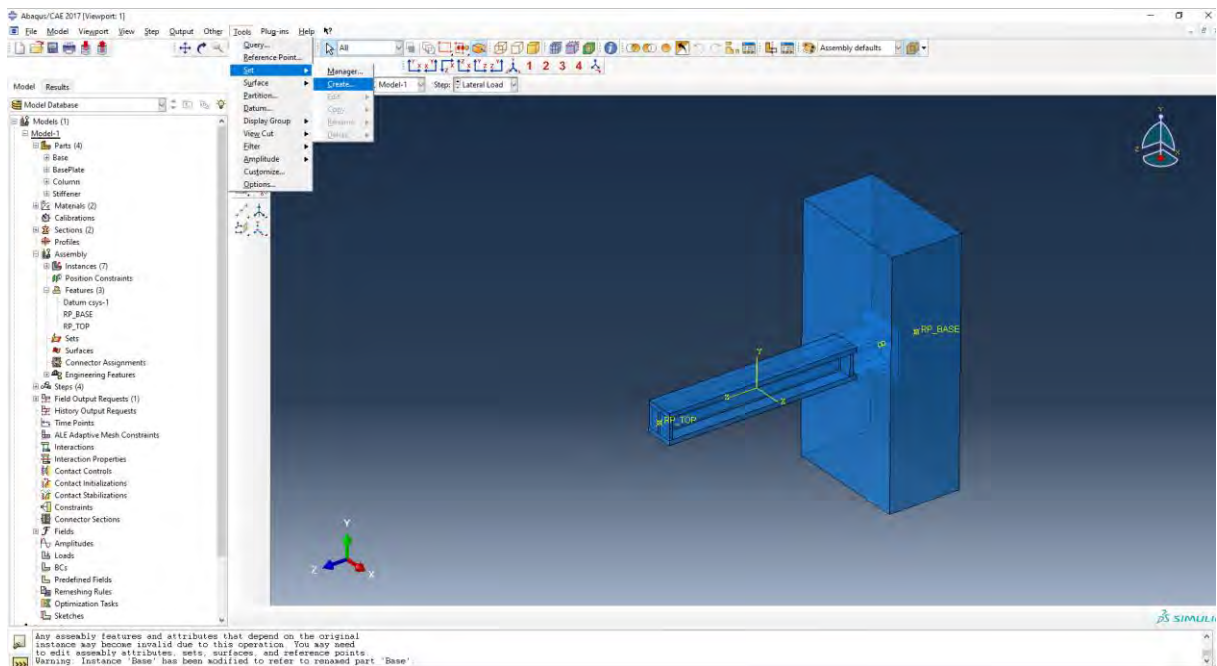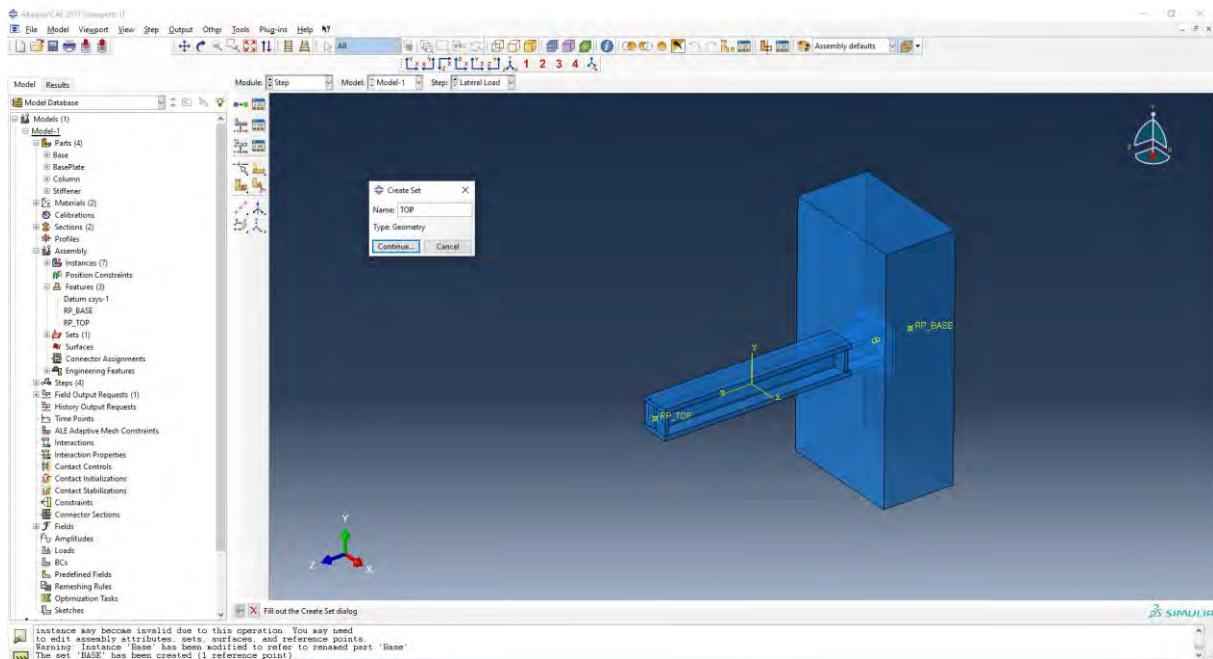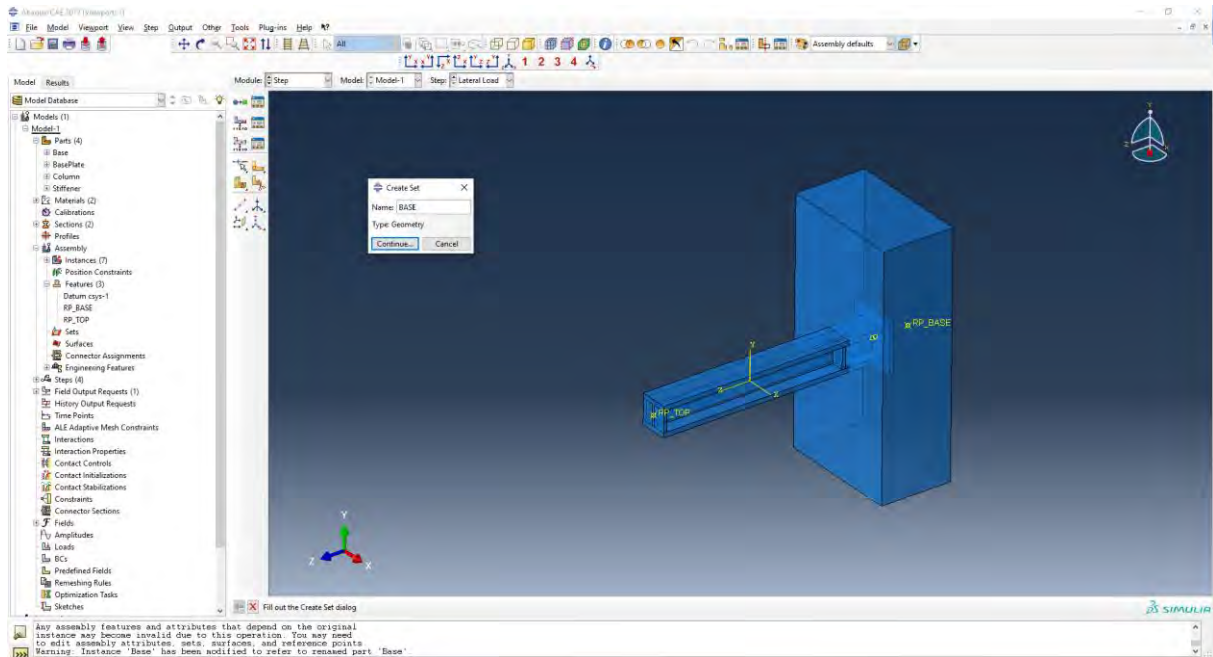

Figure 97: ABAQUS Field Output

In order to specify the history output of the model, first geometric sets must be created. O do this first Reference points must be created. This is done in the Interaction Module. Reference points are created in the Top and Base of the model.
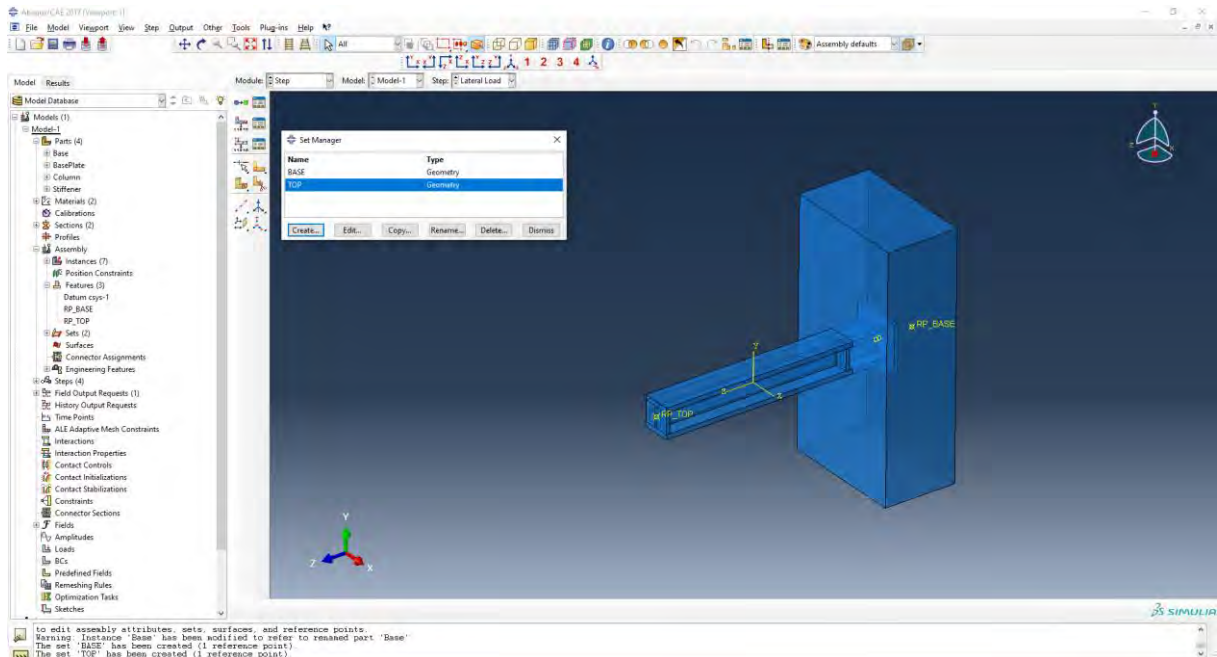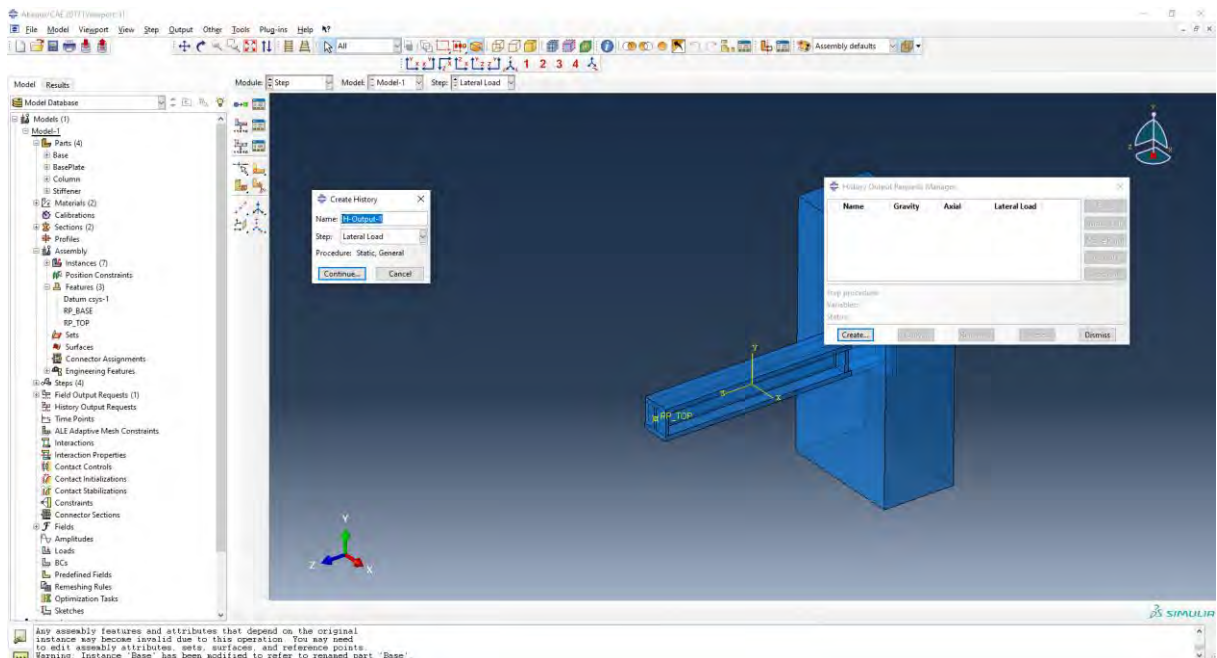
Then the geometry sets are created.

Figure 98: ABAQUS Geometric Sets

In the Step Module, now history output can be set. Two history output stances must be set, one for the Top reference point, and one for the Base reference point.
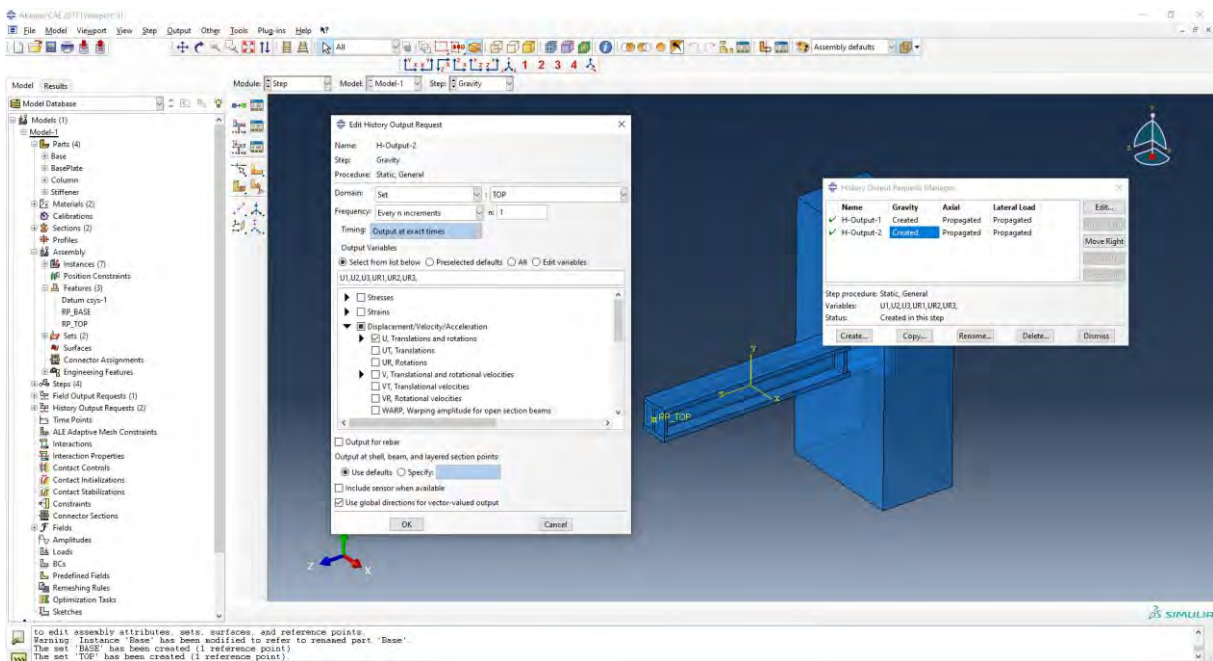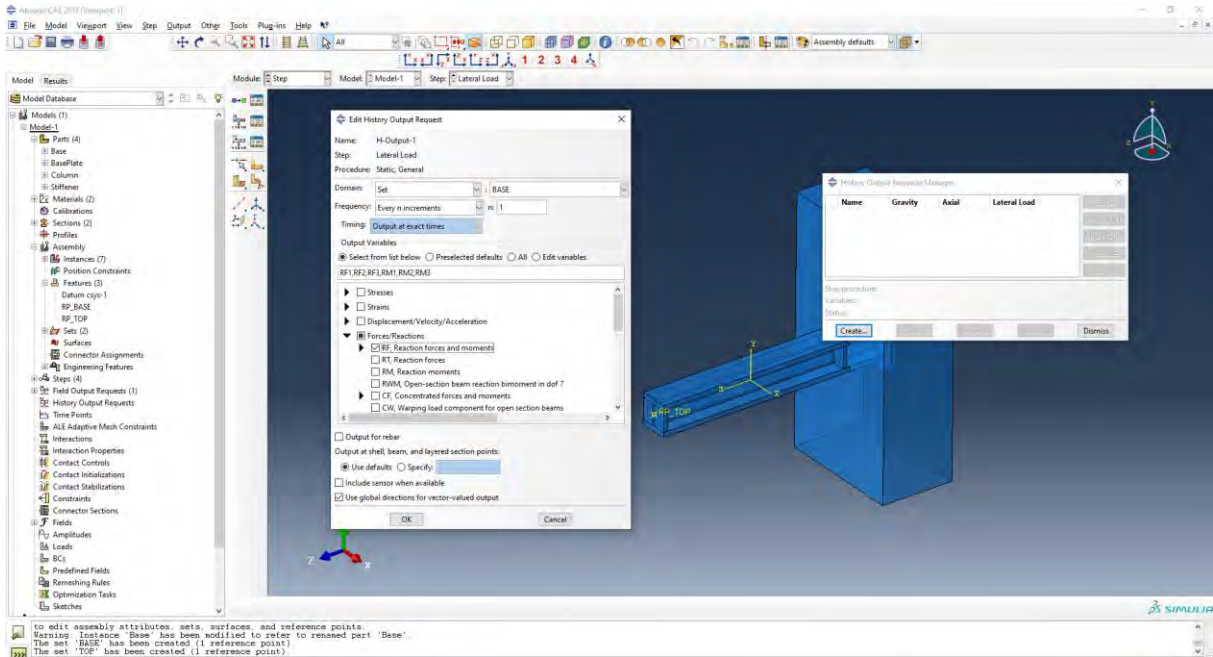
Figure 99:ABAQUS History Output

In order to apply loads and to aid the meshing process, datum planes are created in each part.

Once the datum planes are created the Partition cell is used to break the parts. The following

partitions were made.
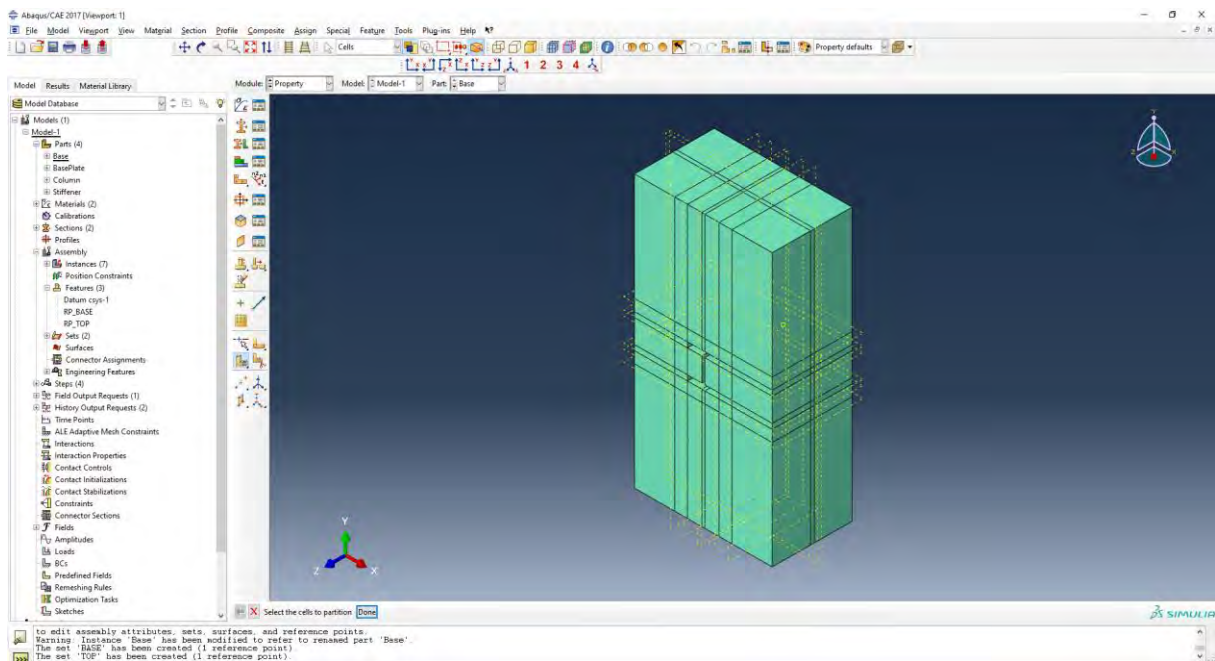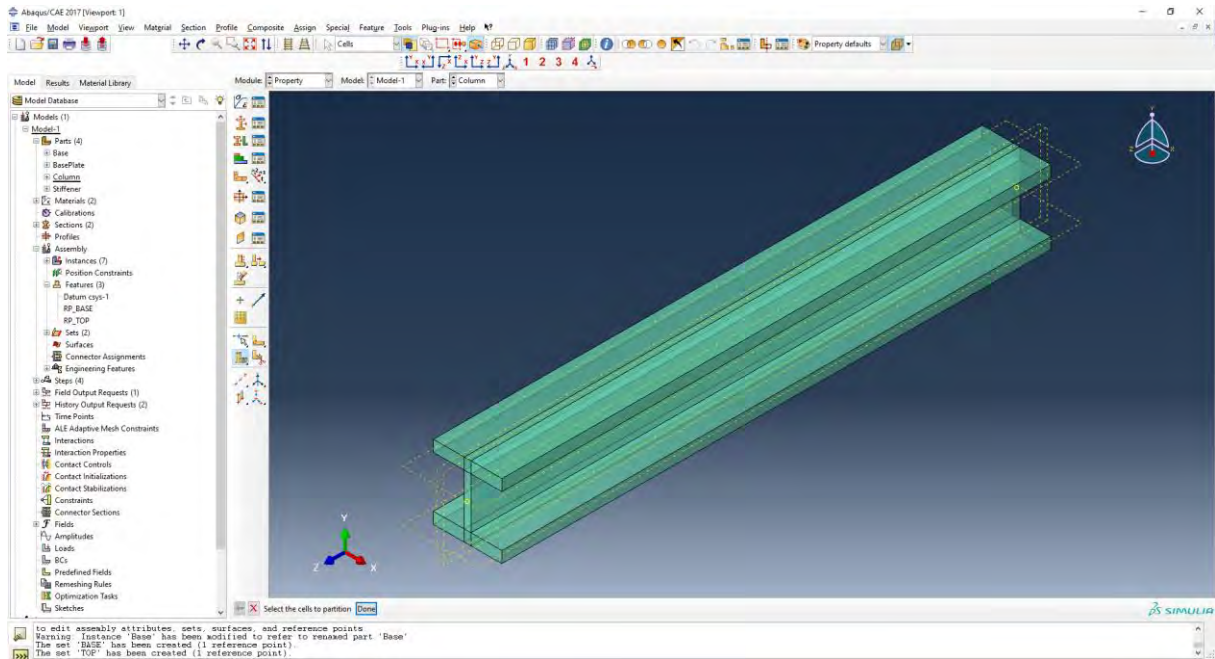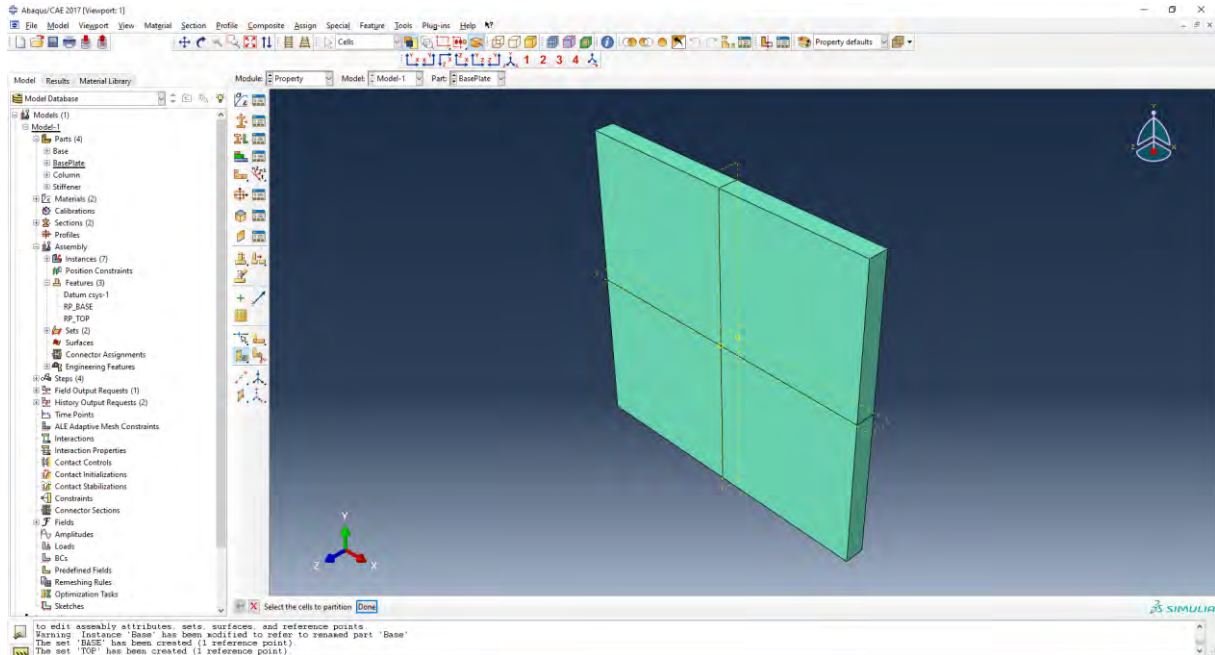
Figure 100:ABAQUS Datum Planes

The base plate datums were created in order to apply the axial load. The partition permits the creation of a central node in the part in which the load will be applied.

Once the partitions are made, in the Mesh module, the parts mesh are created.

Hex elements were selected for the mesh.
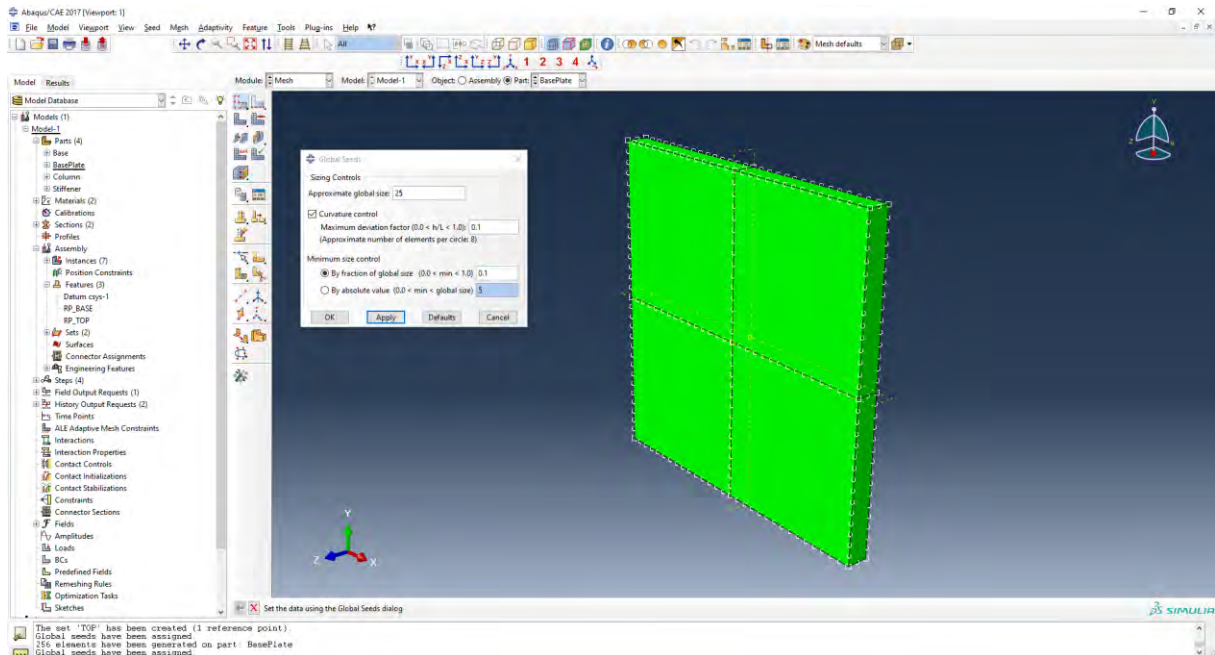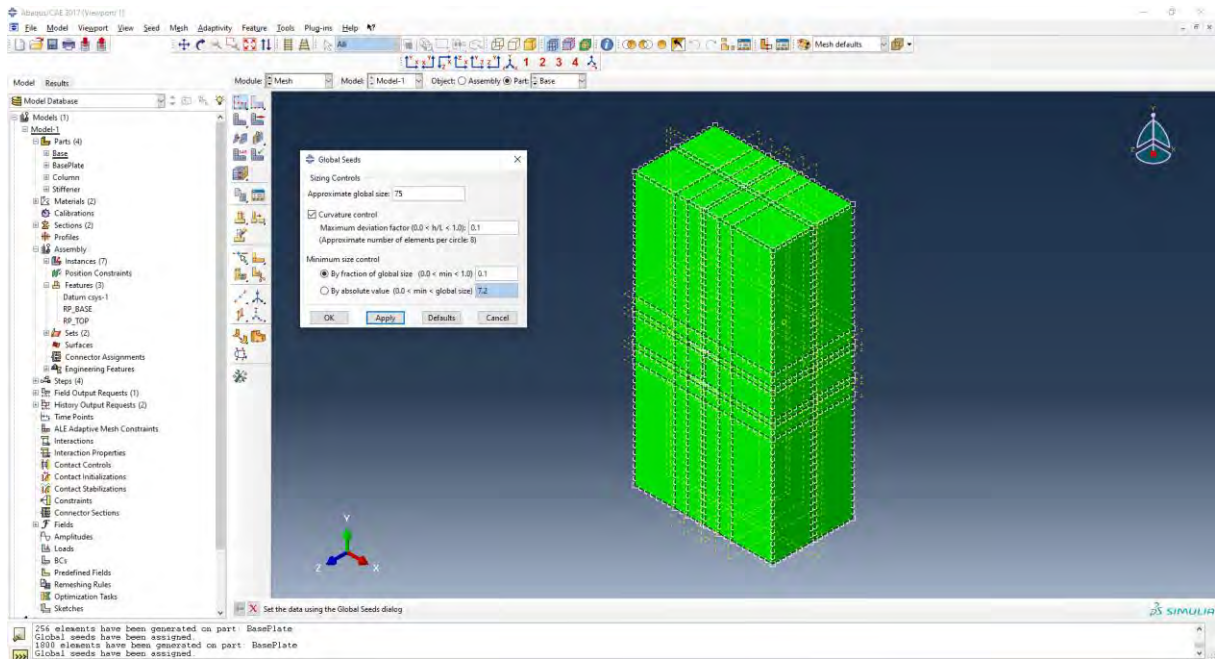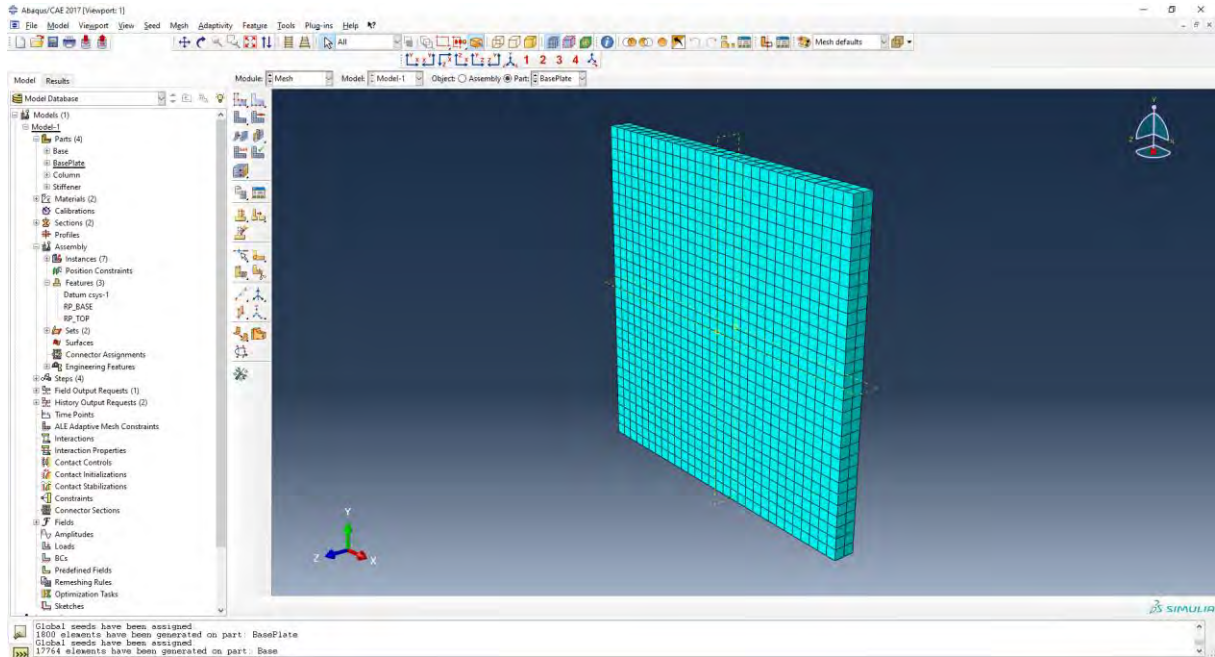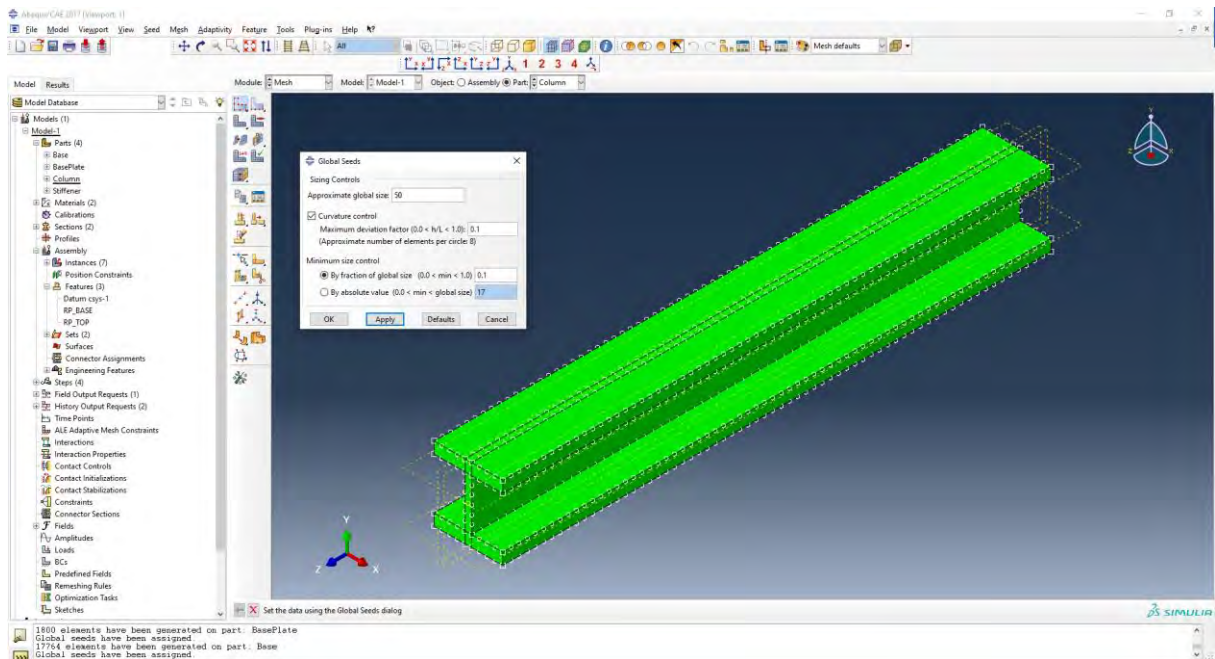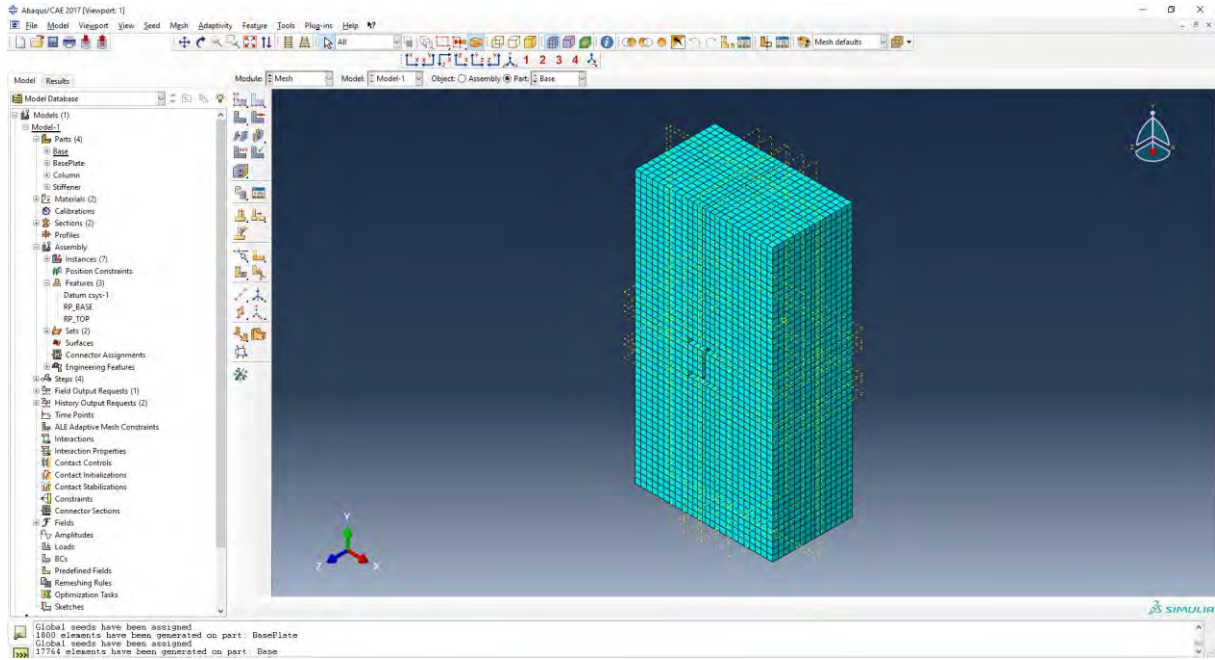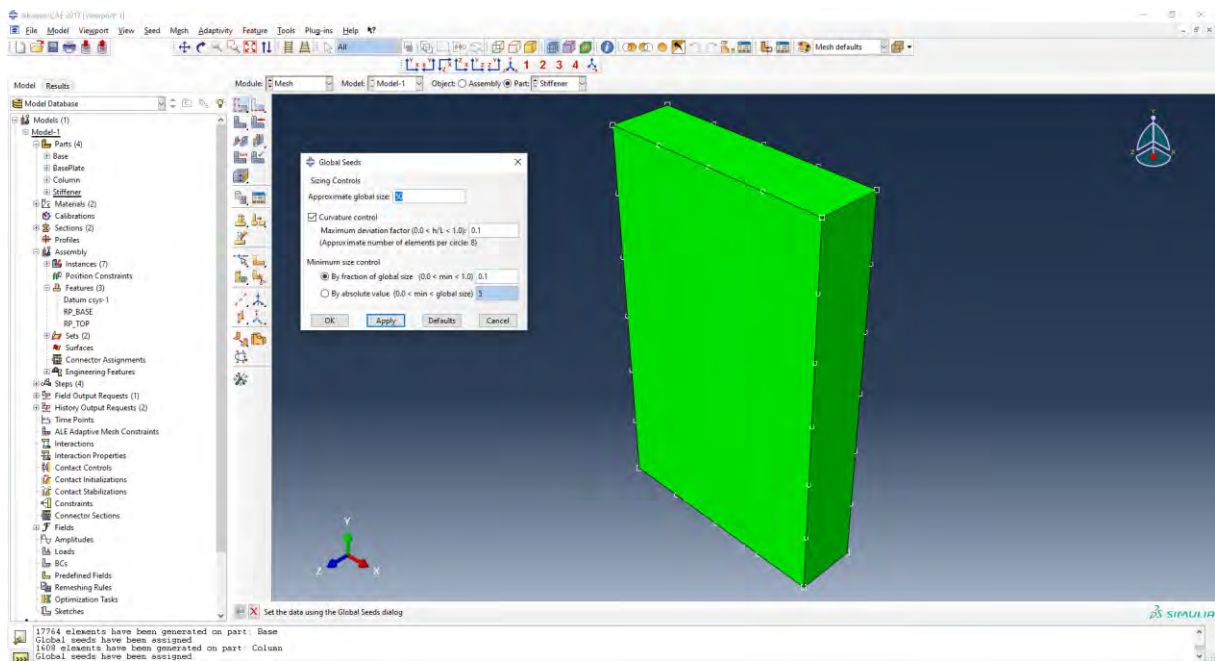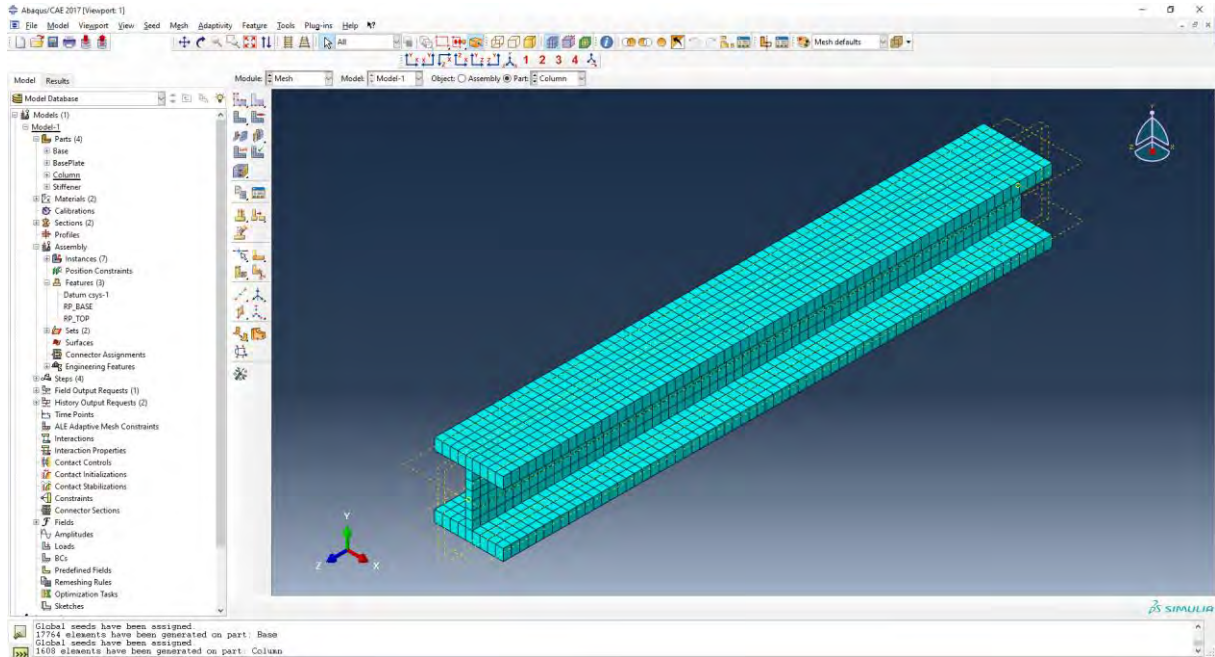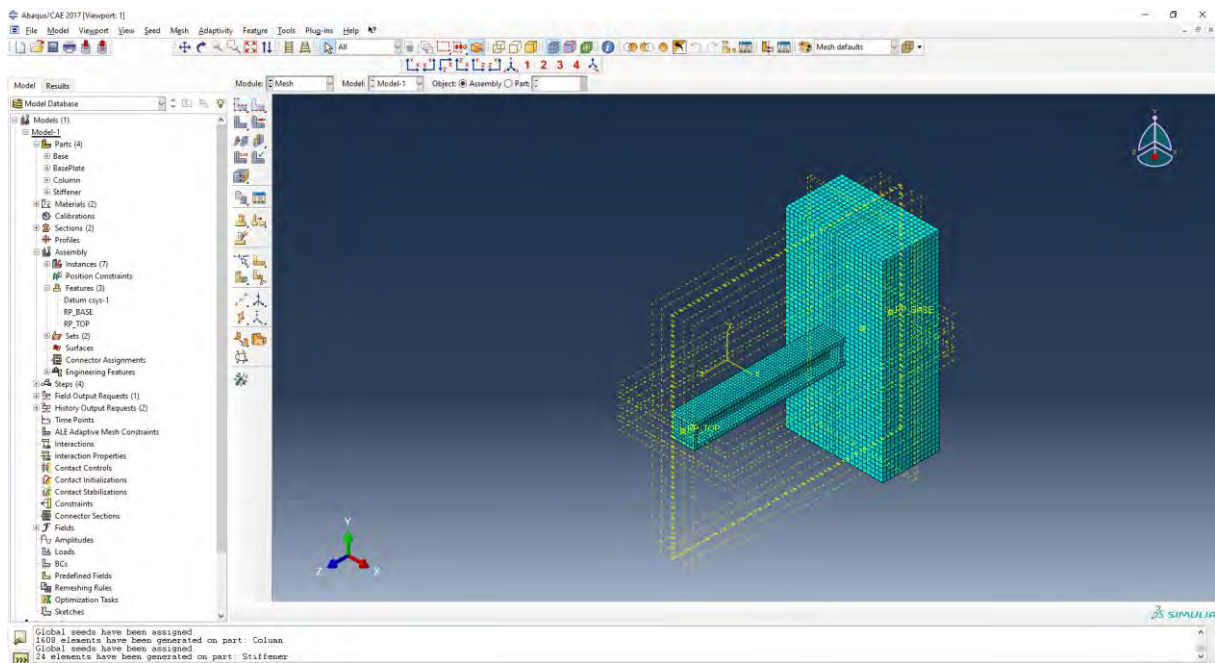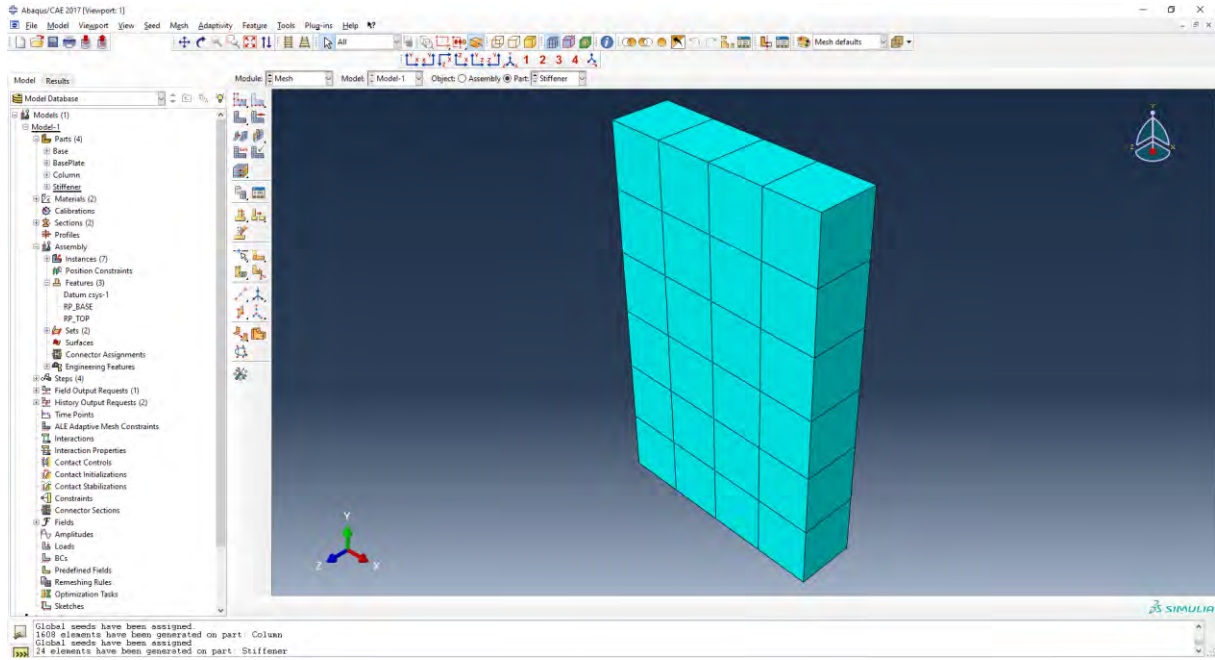
Figure 101:ABAQUS Mesh

In order to apply the Axial load to the model we create a Node Set, in the same manner as the

Geometry Set.
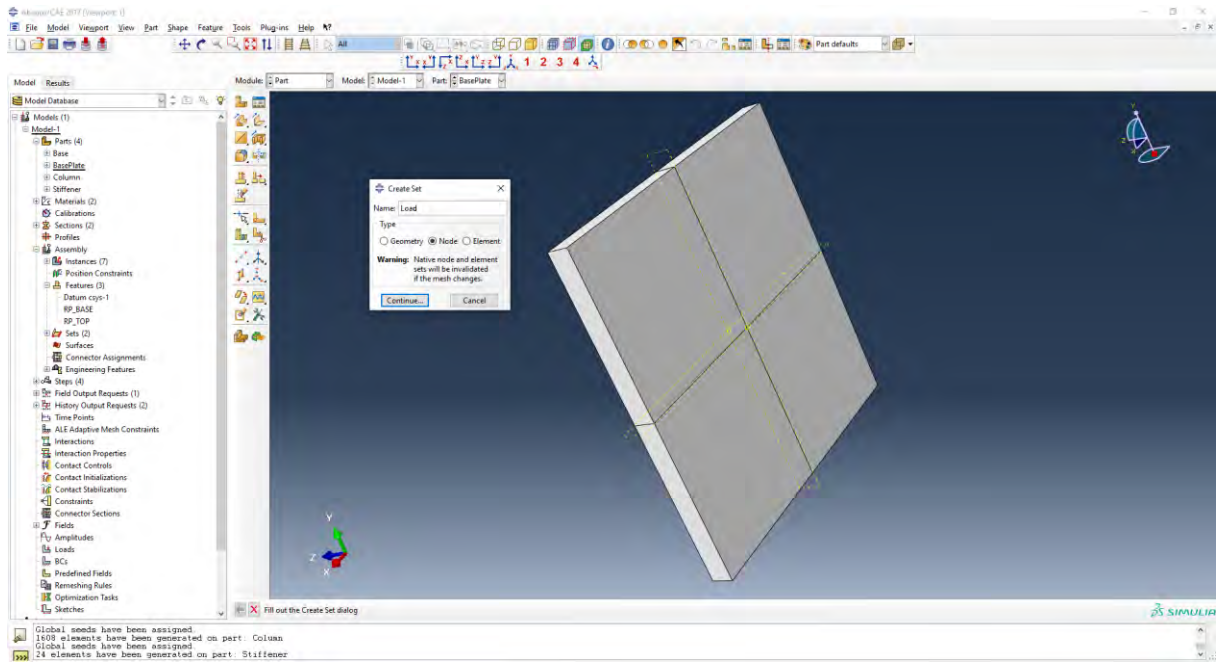
The in the Load Module load are then created.
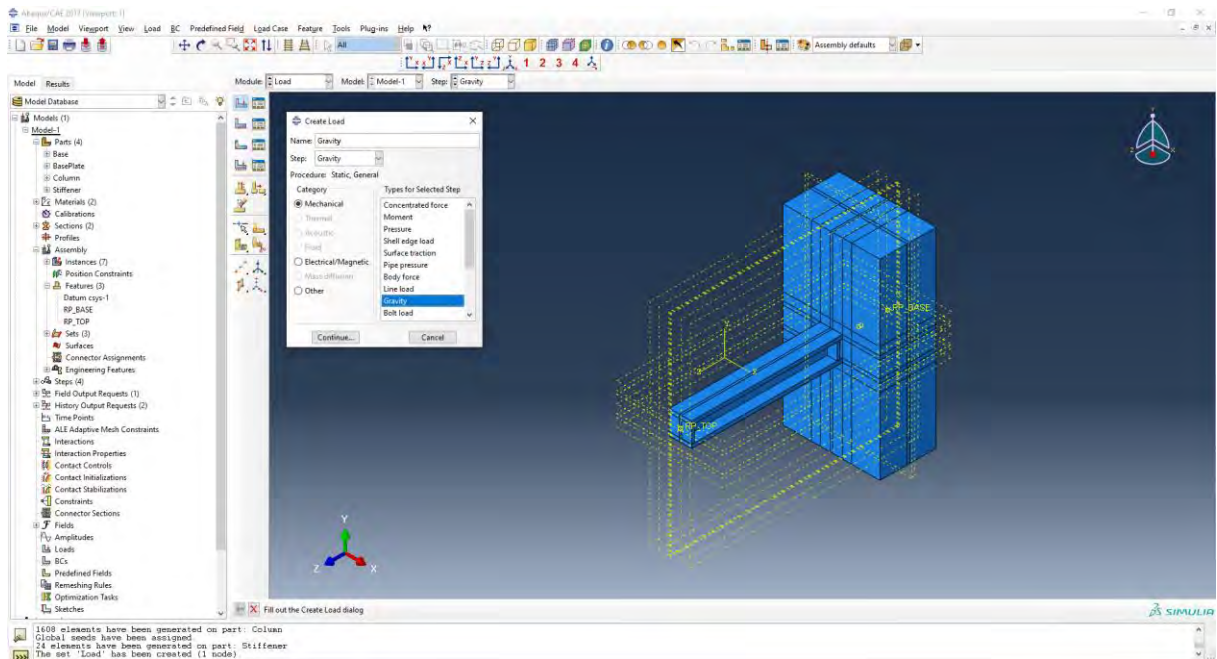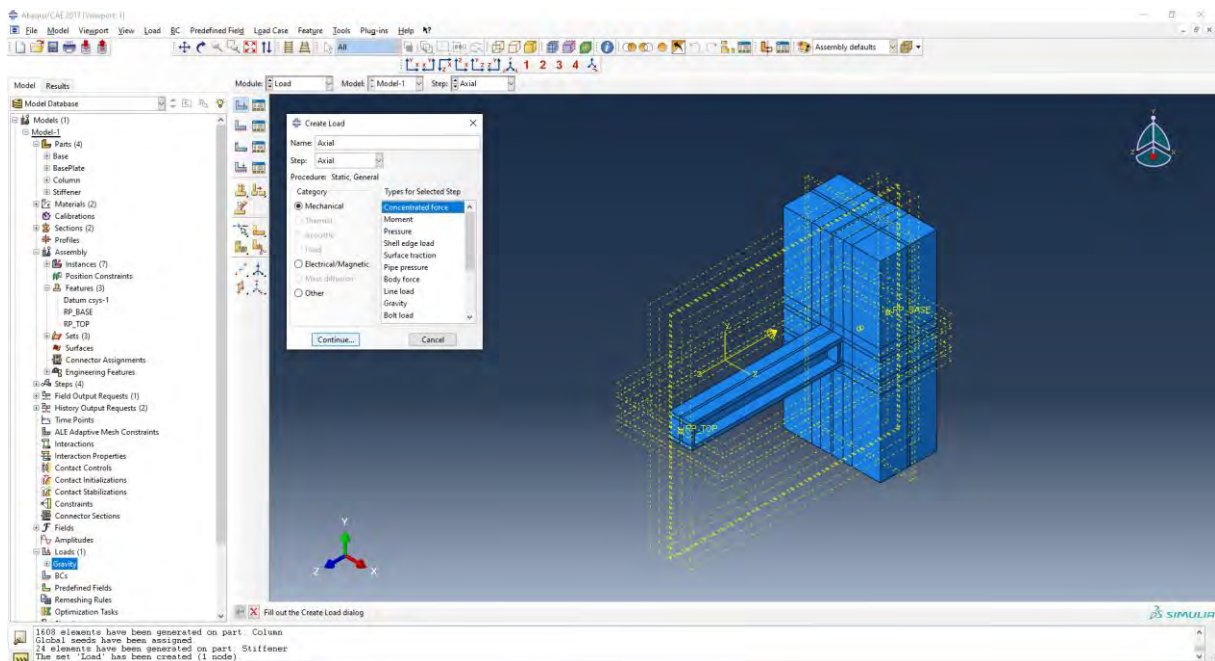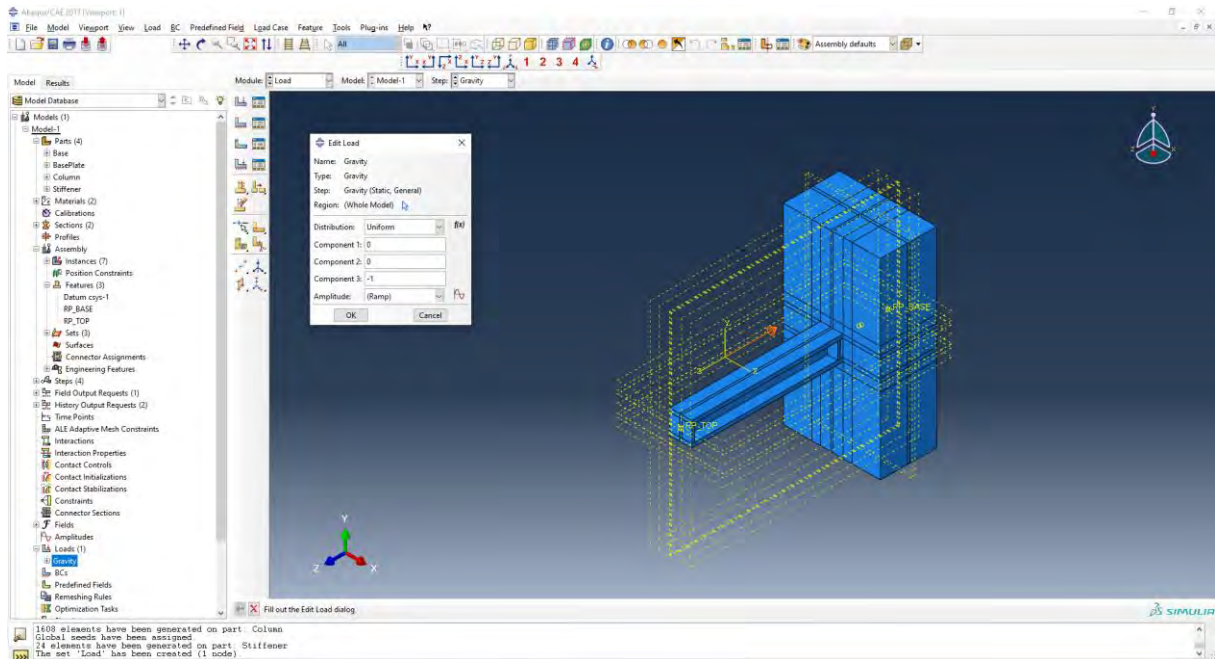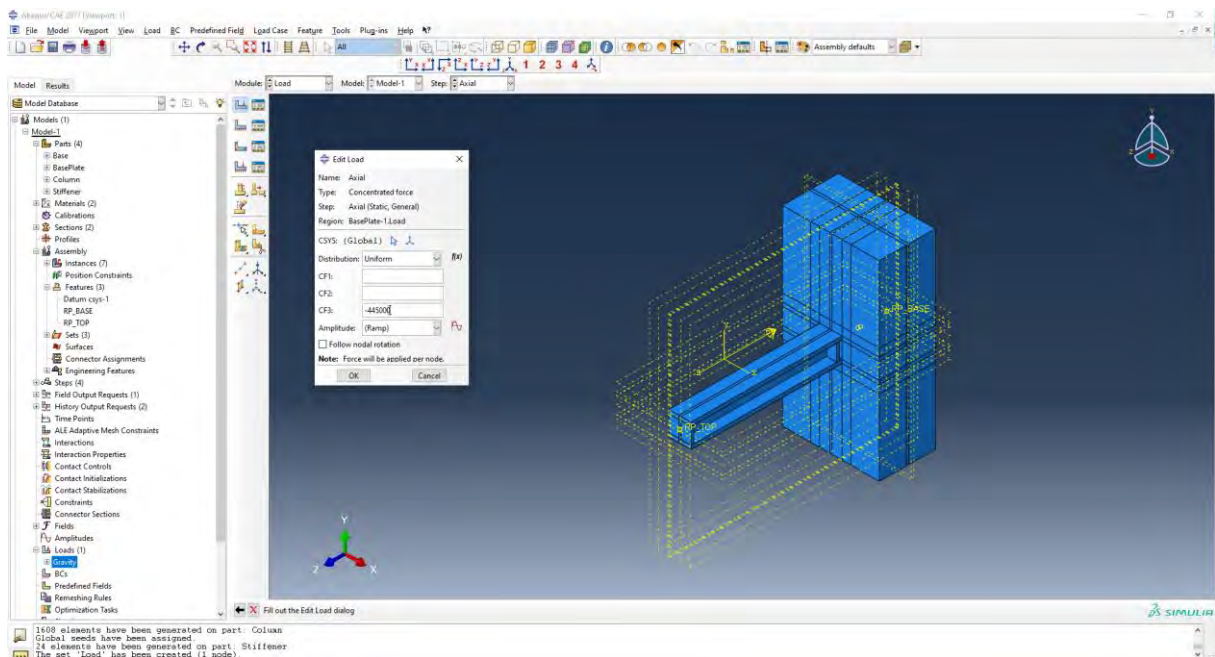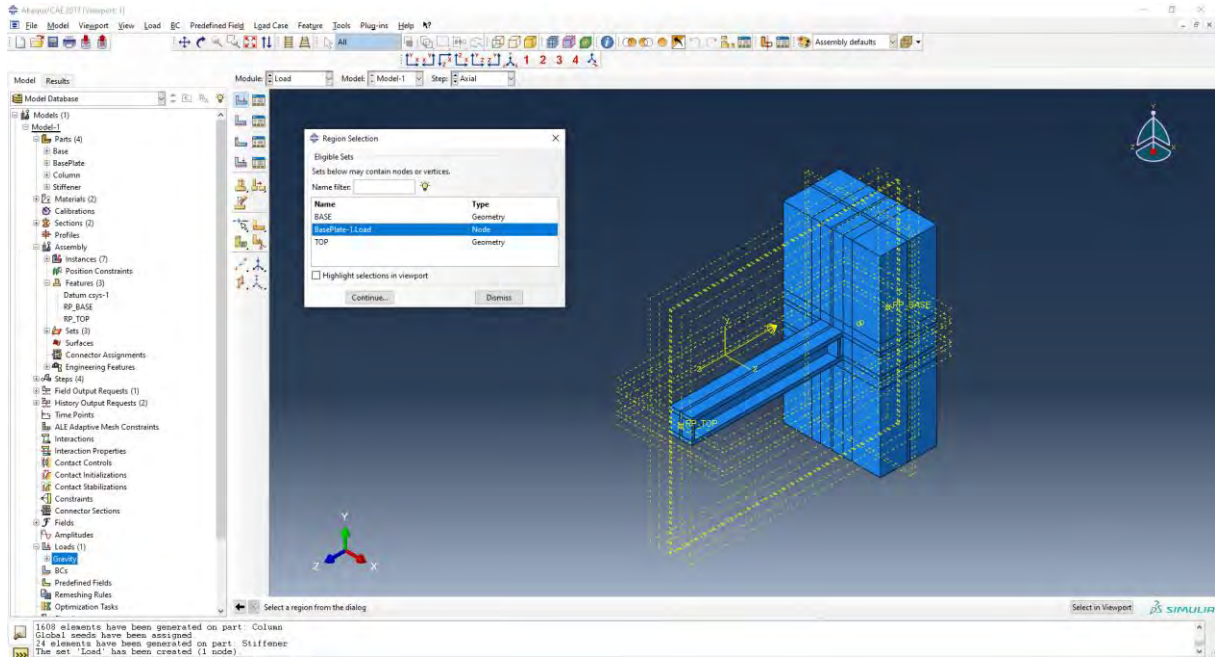
Figure 102:ABAQUS Loads

In order to apply the lateral displacement and the support conditions of the model, first tie

constrains must be applied to the model. For this we go to the Interaction Module.
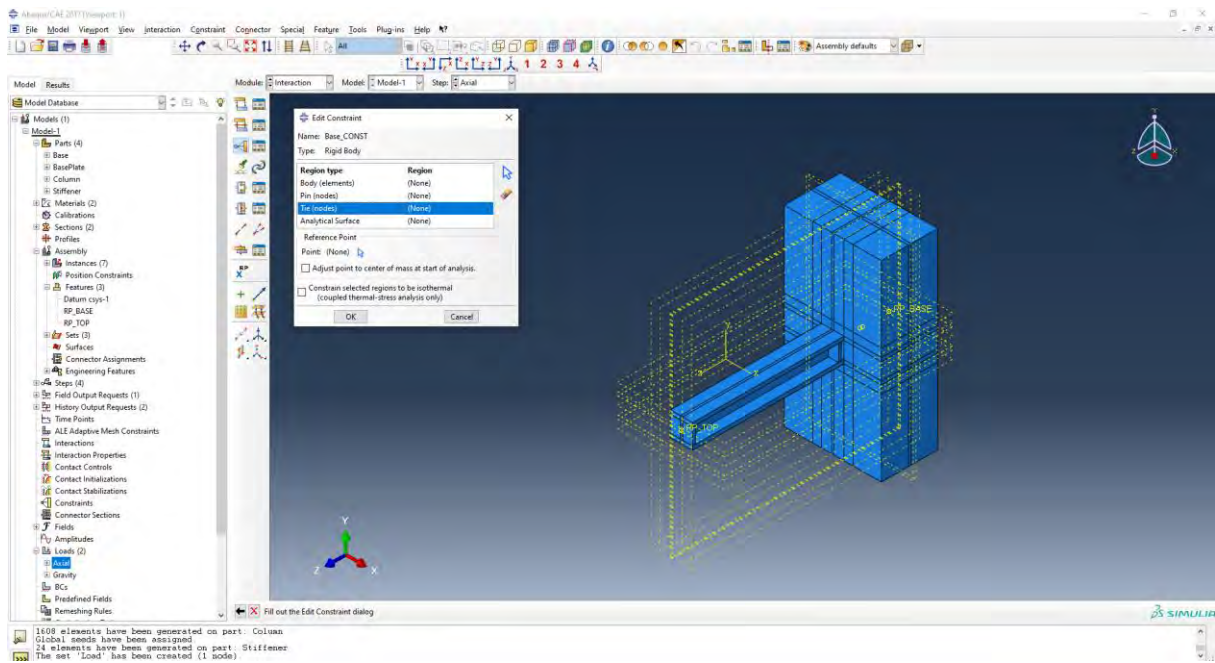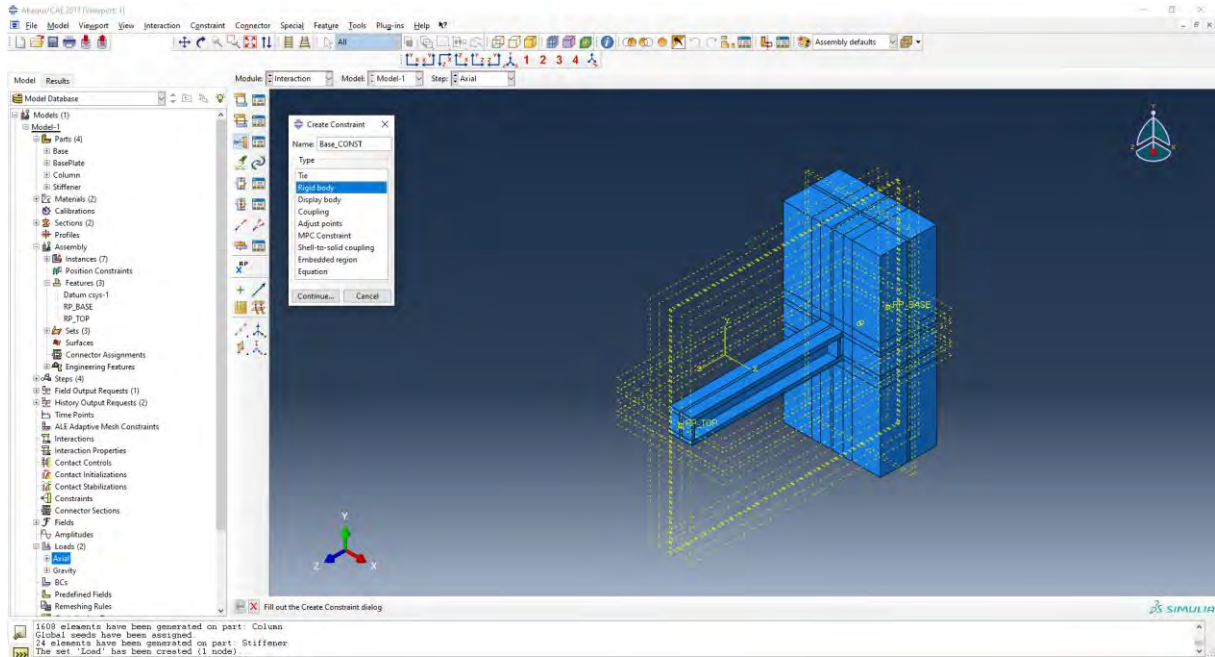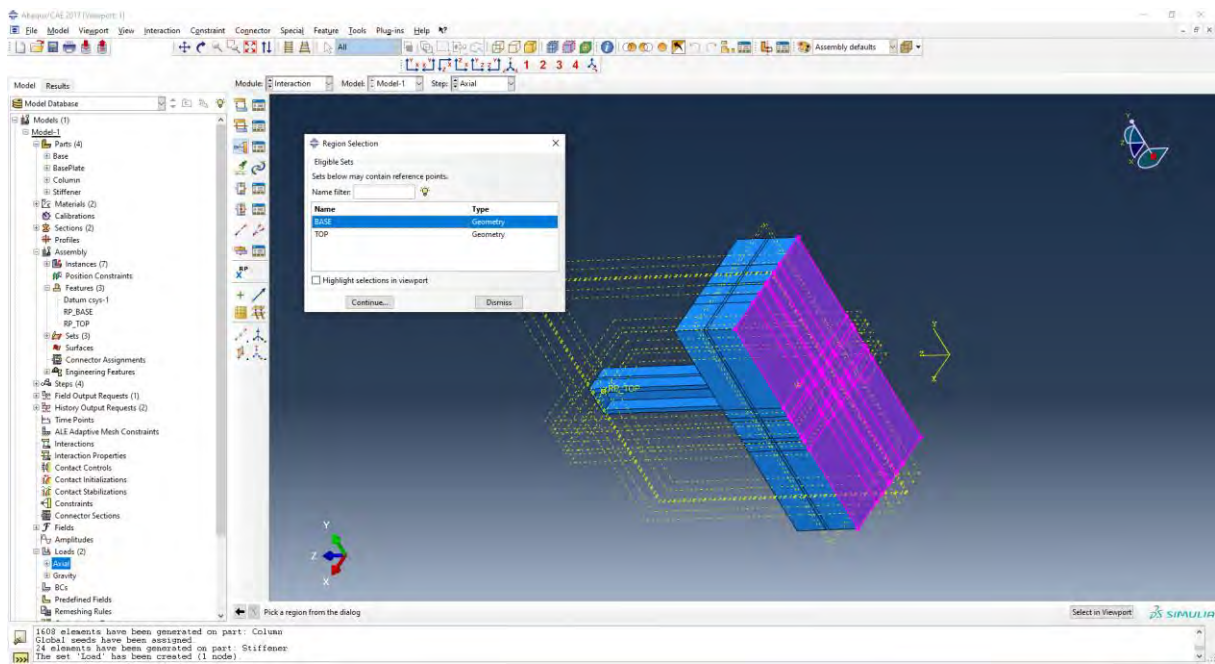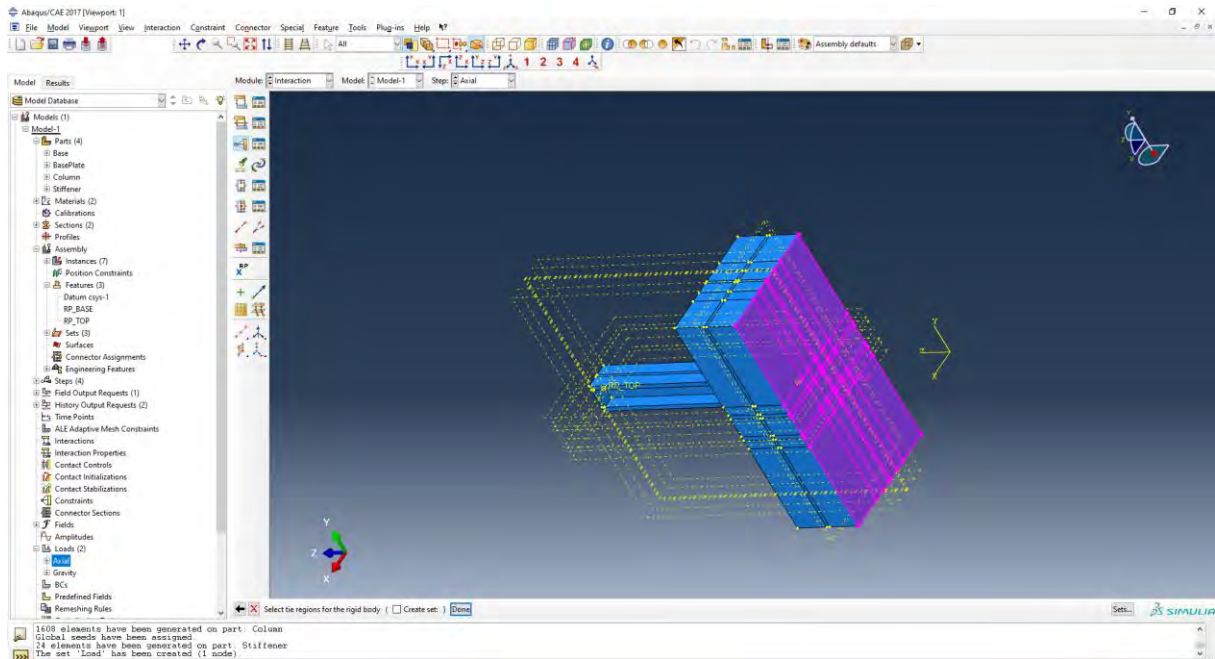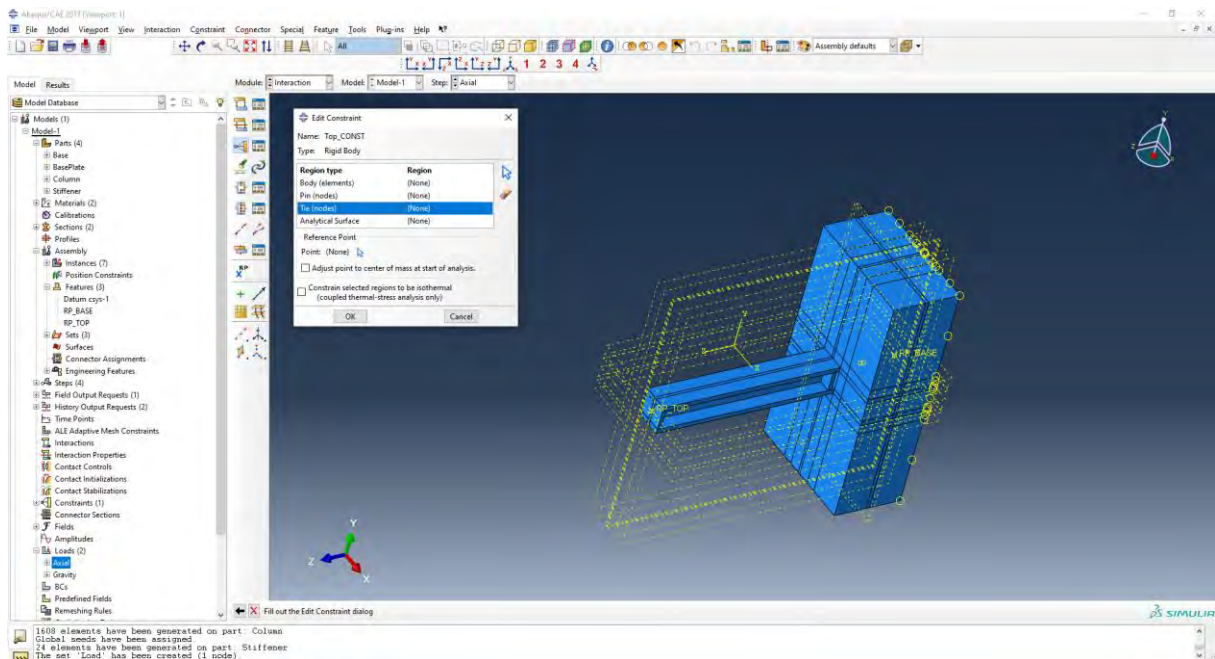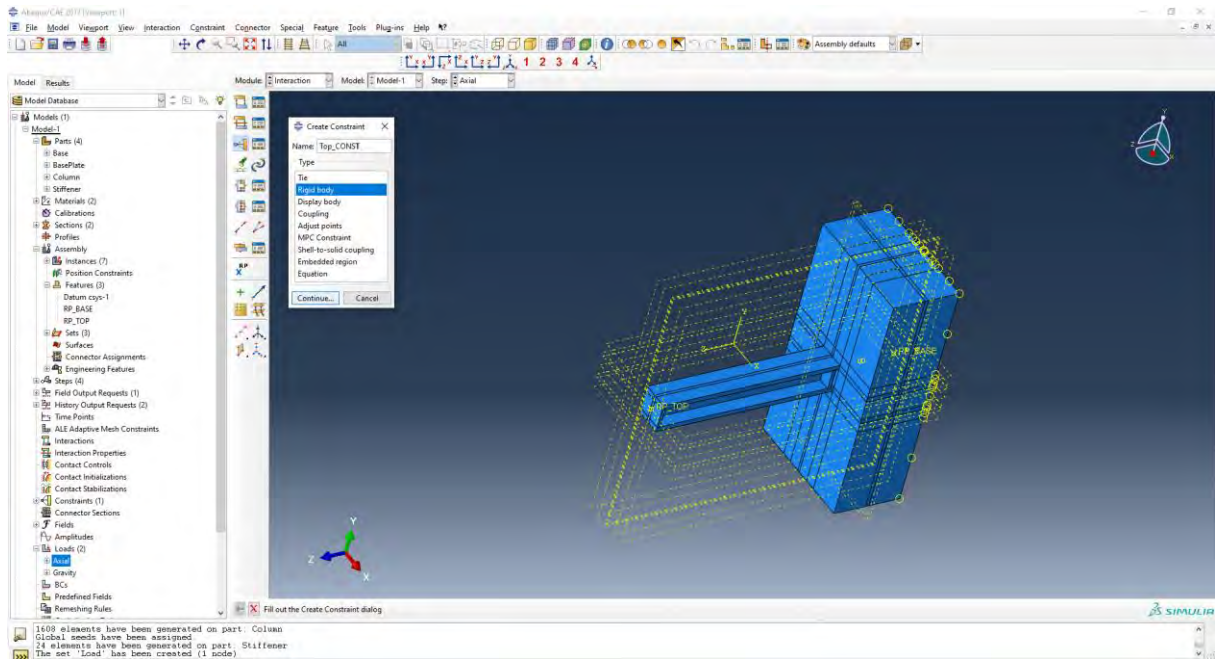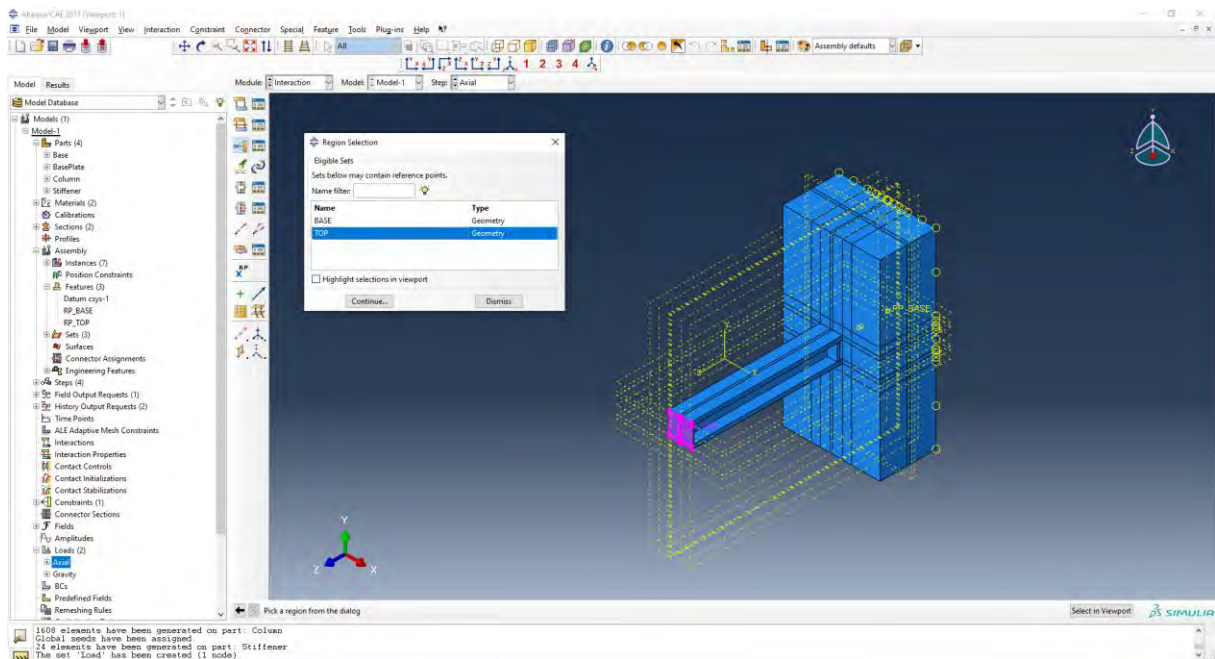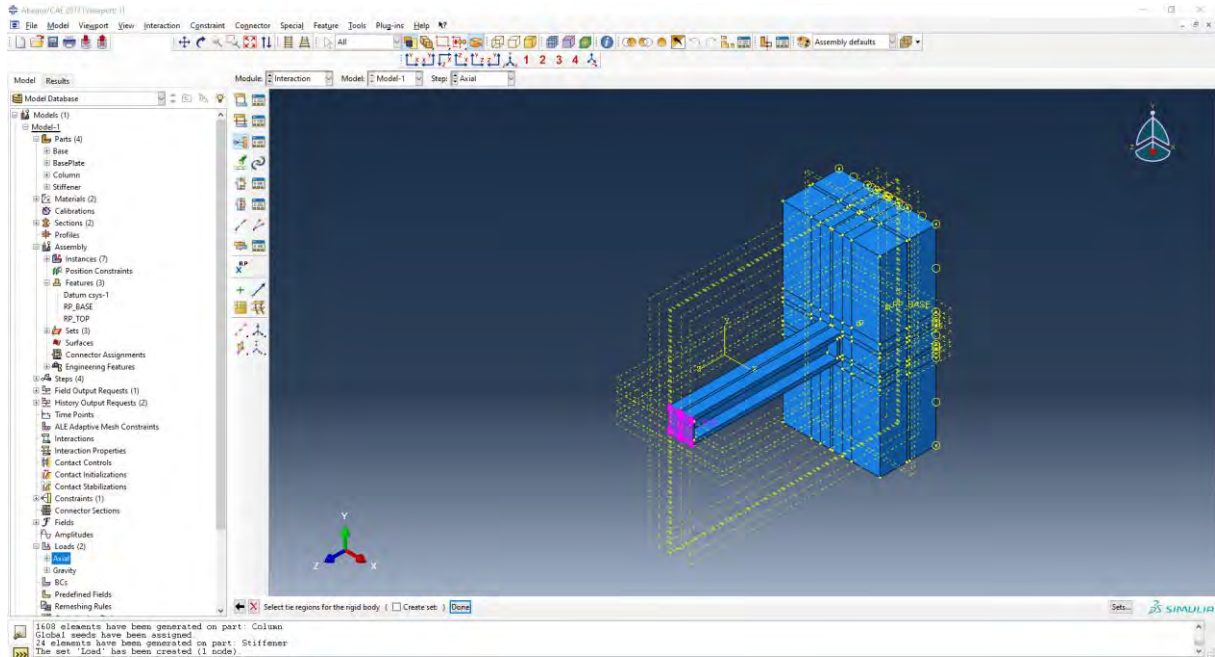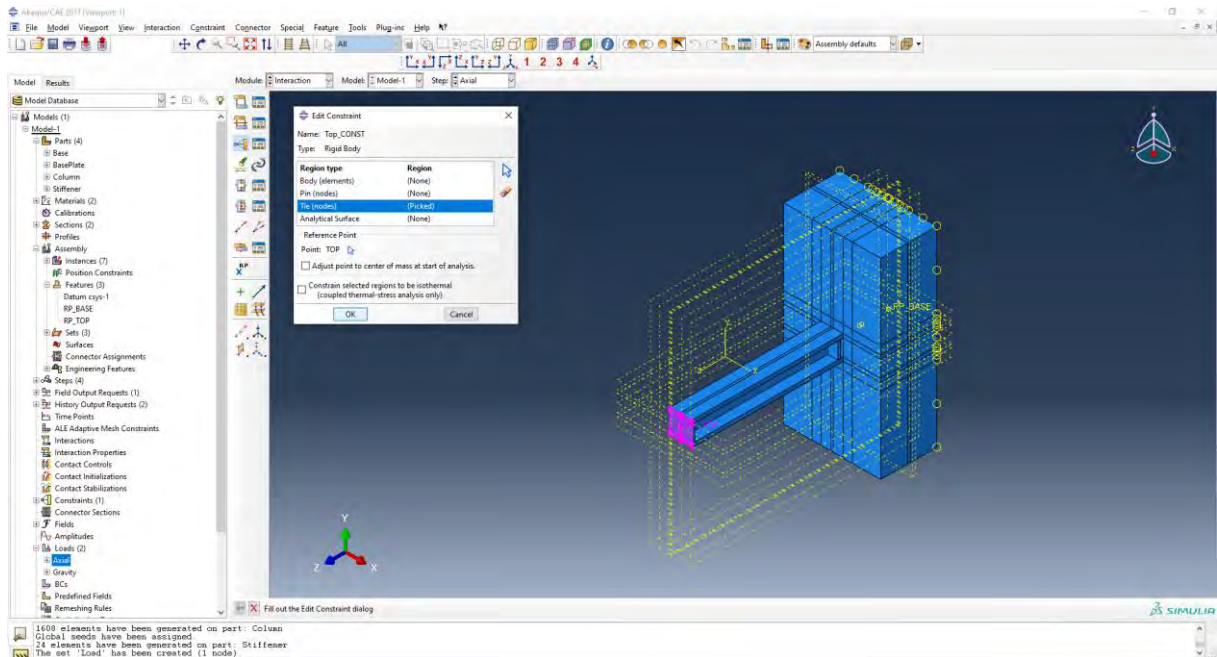
Figure 103:ABAQUS Tie Constrains

In the Load Module, the fix condition and the imposed displacement is applied.
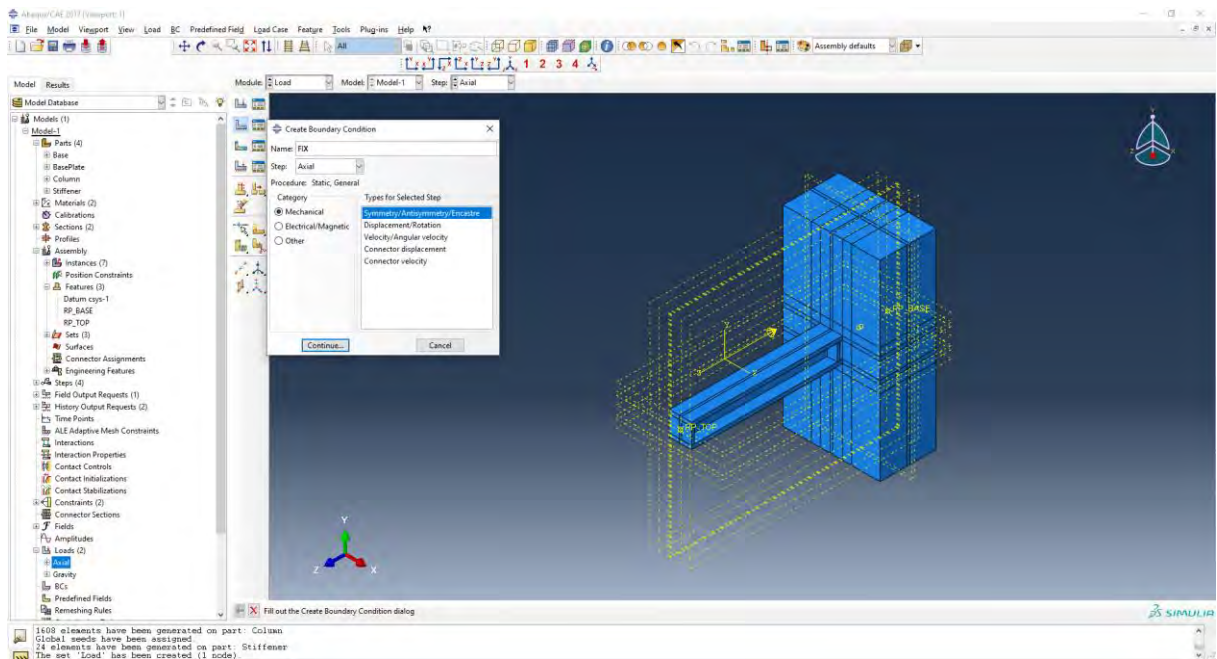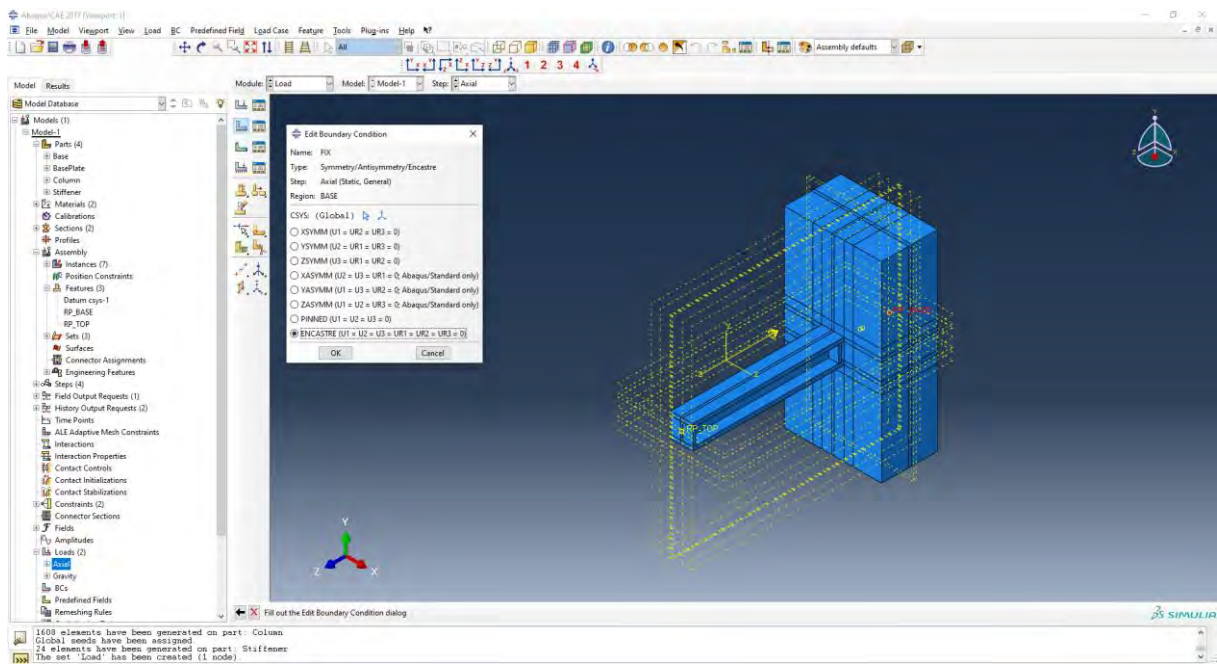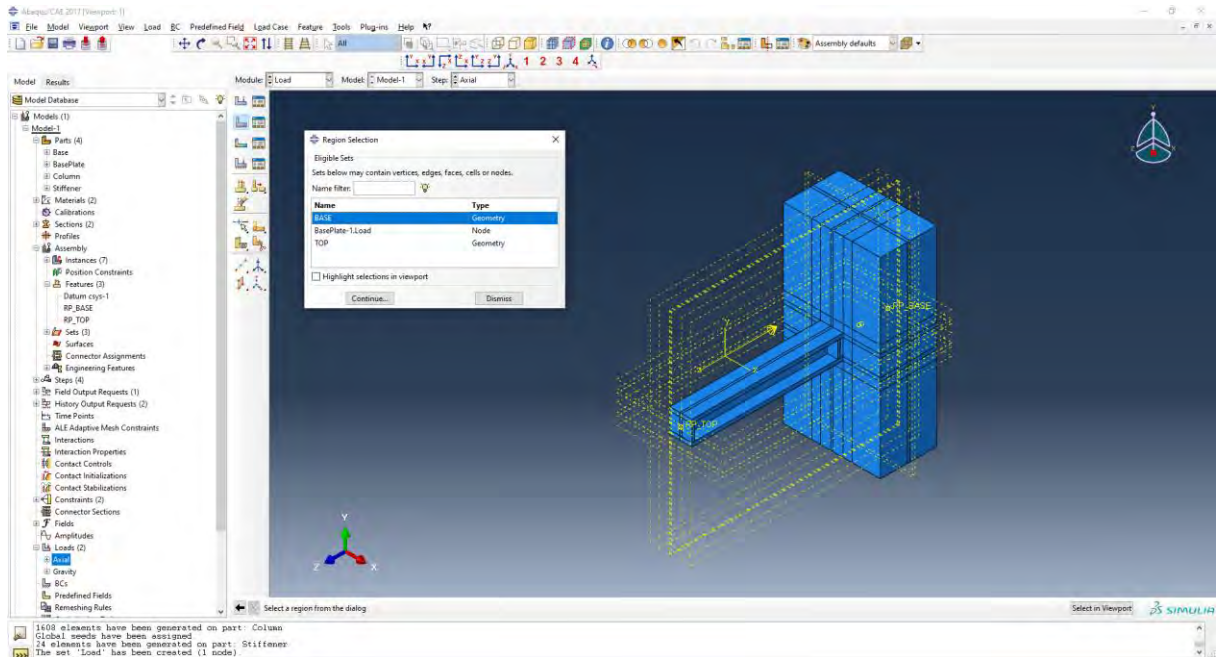
Figure 104:ABAQUS Boudary Conditions

In the project browser we look for amplitude and open it.
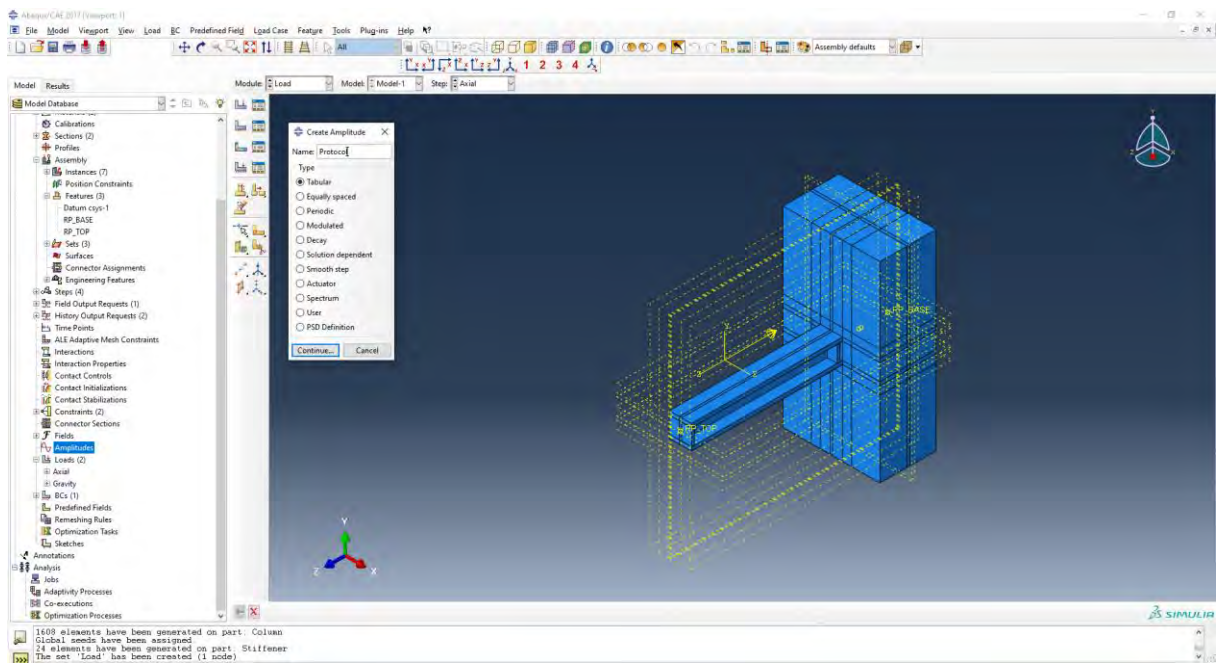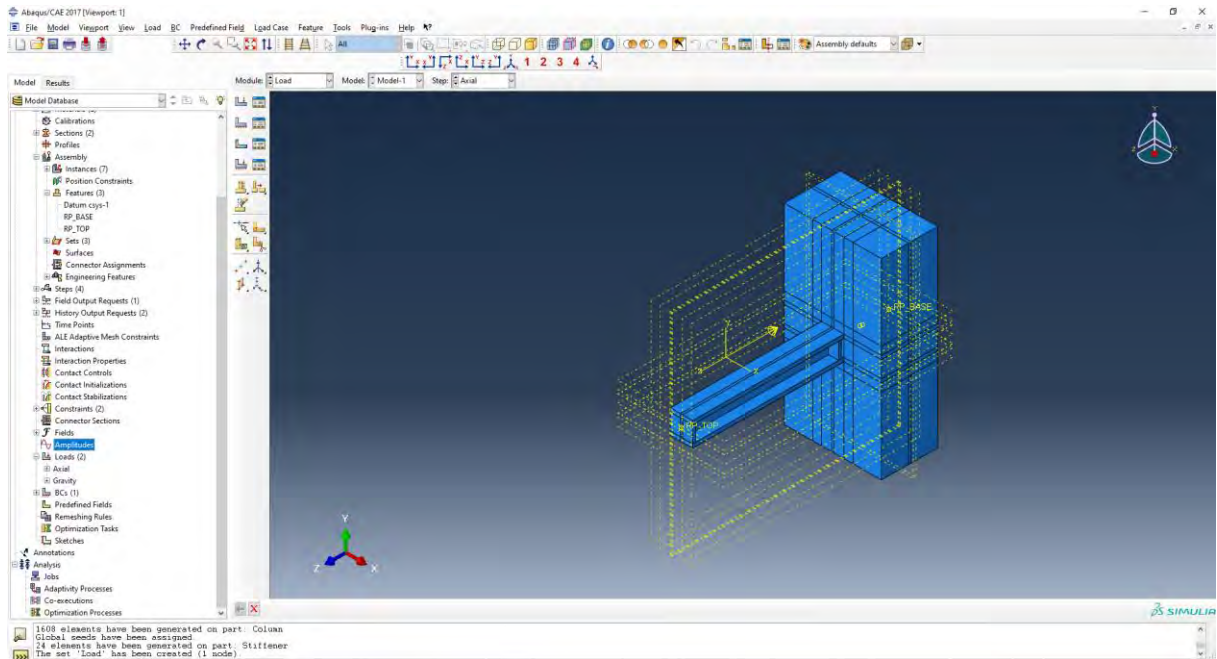
We paste the time versus displacement values from the test
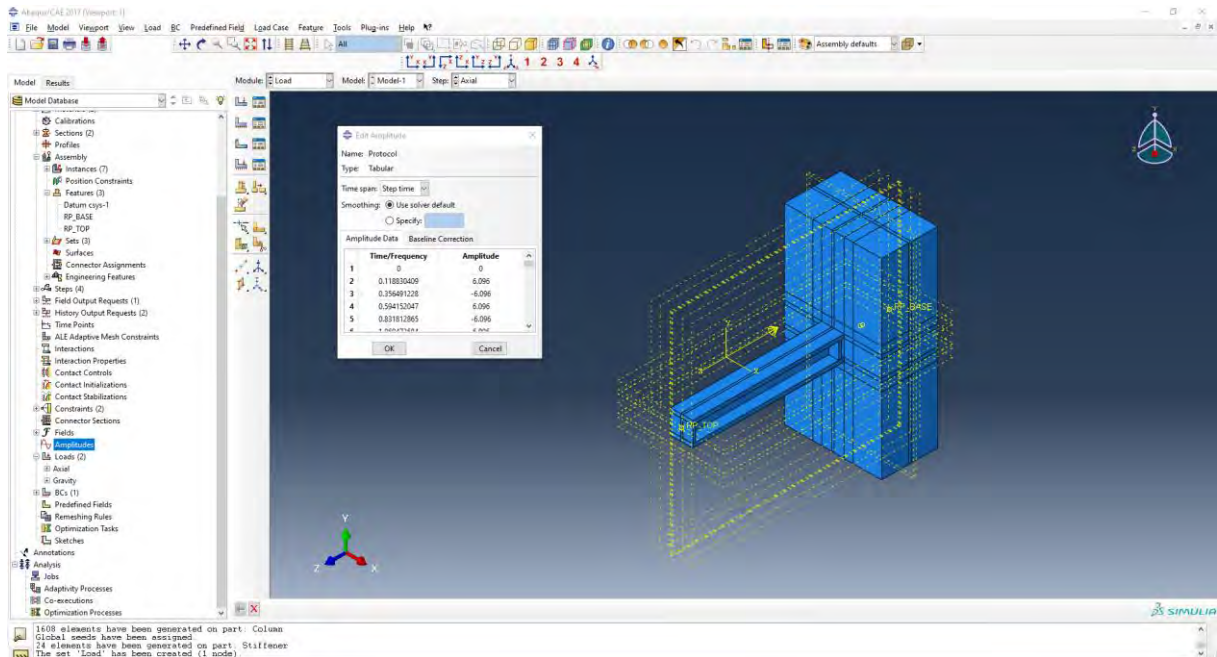
Figure 105:ABAQUS Loading Protocol

Then the force displacement is applied.
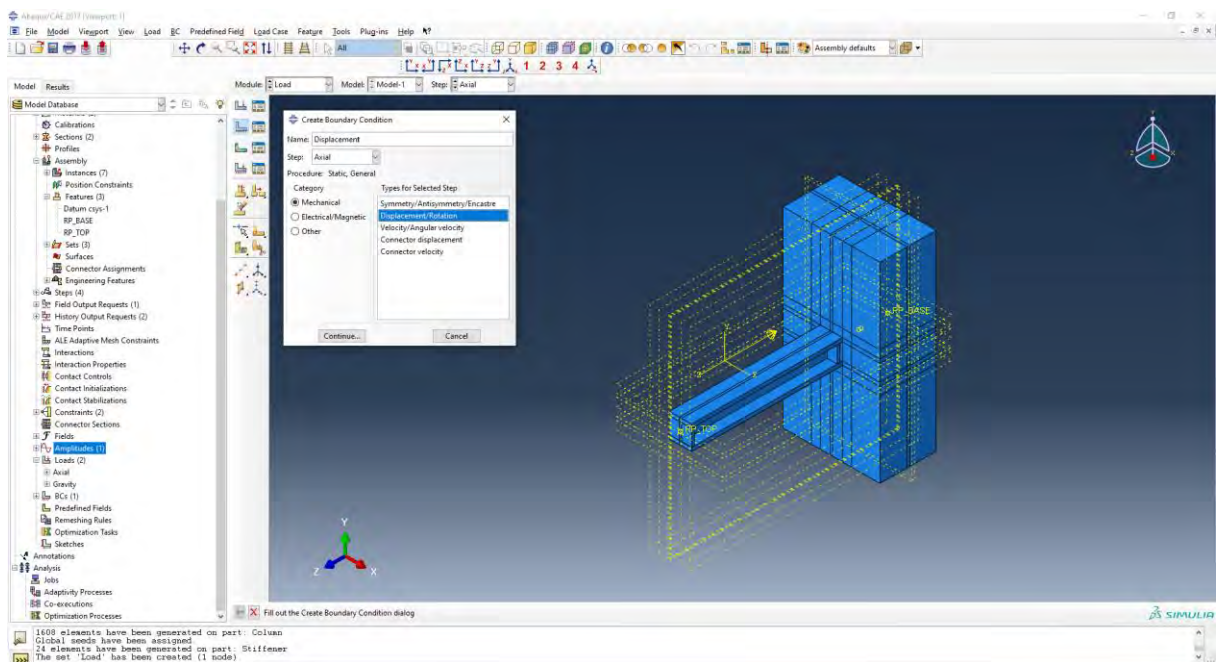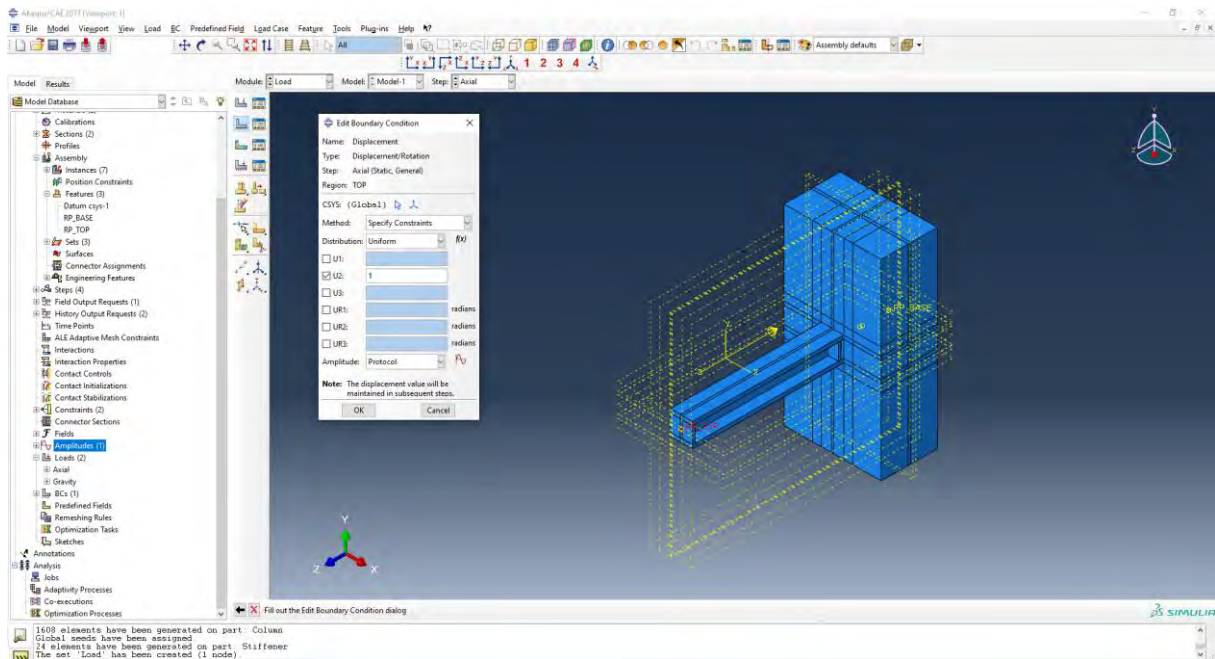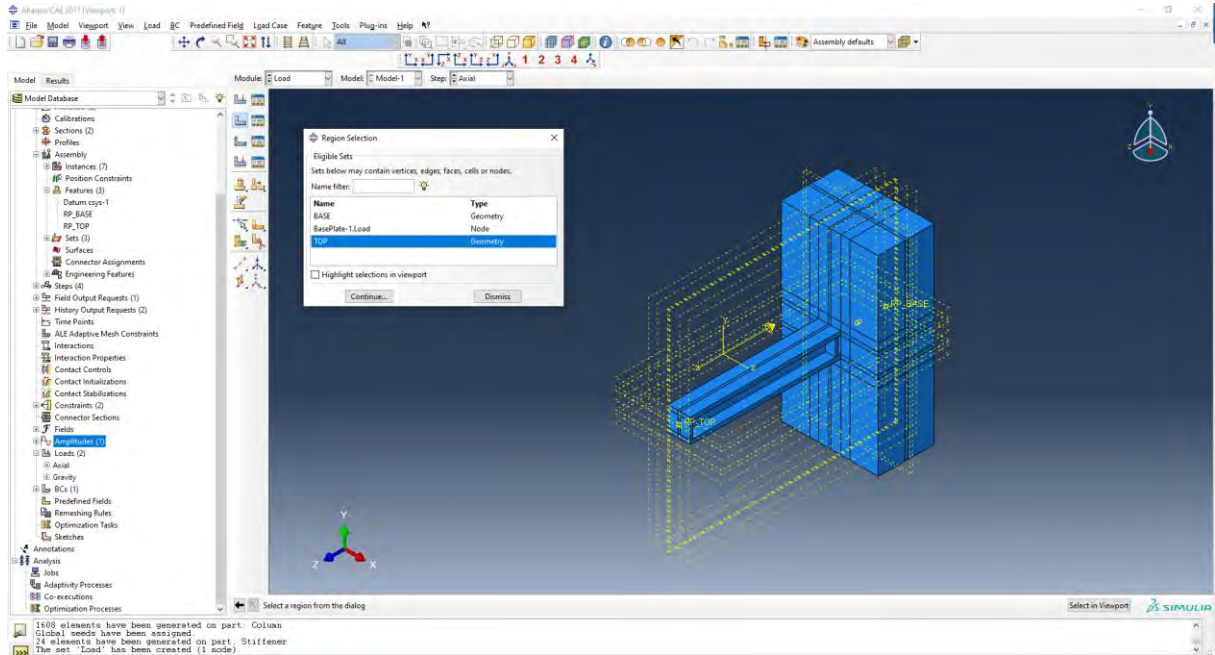
Figure 106:ABAQUS Displacement Assignment

The we verify that the boundary condition is applied at the beginning of the steps.
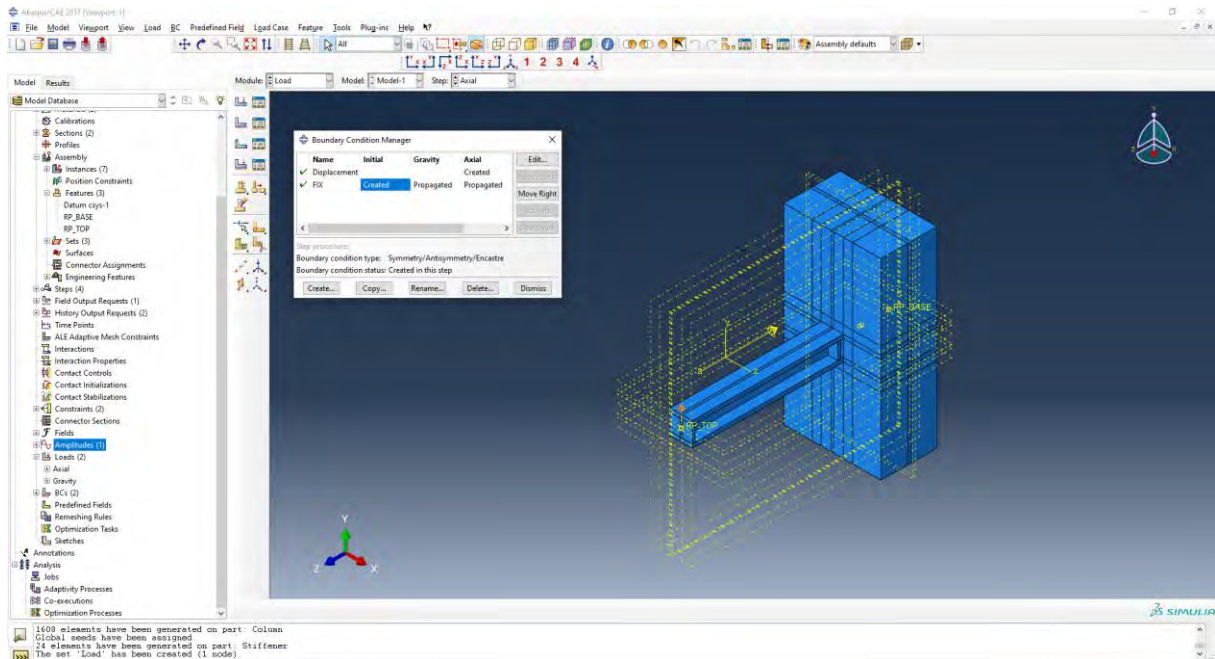
Then contact interactions must be applied to the model. For this we go to the Interaction

Module.
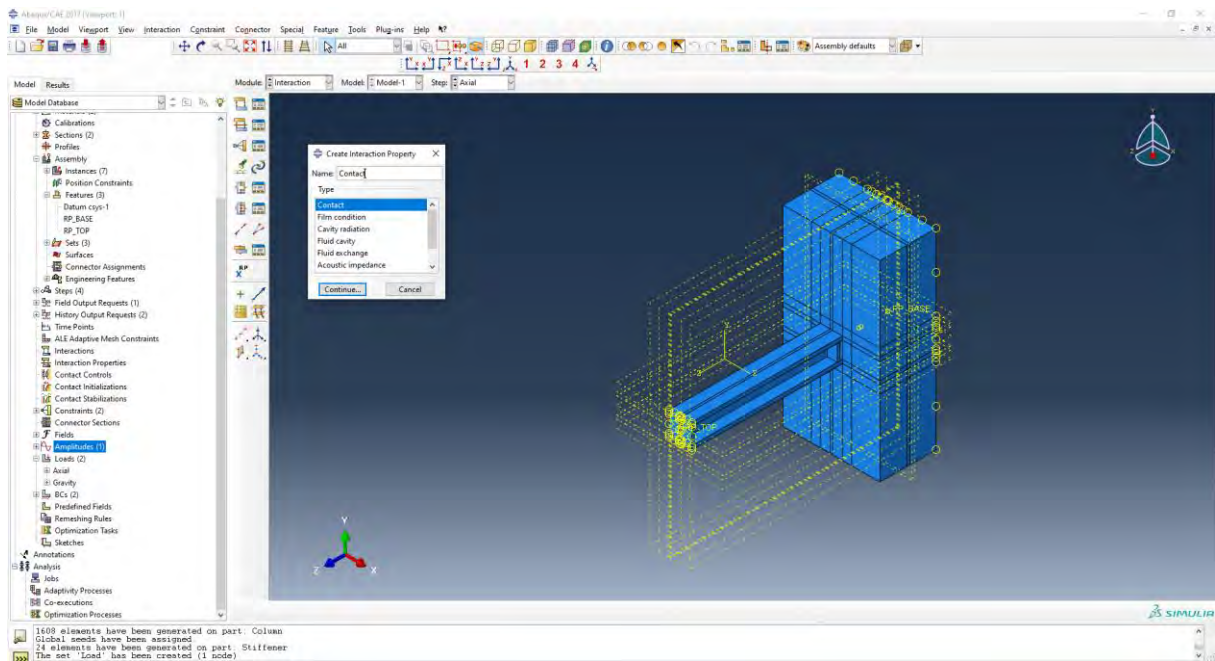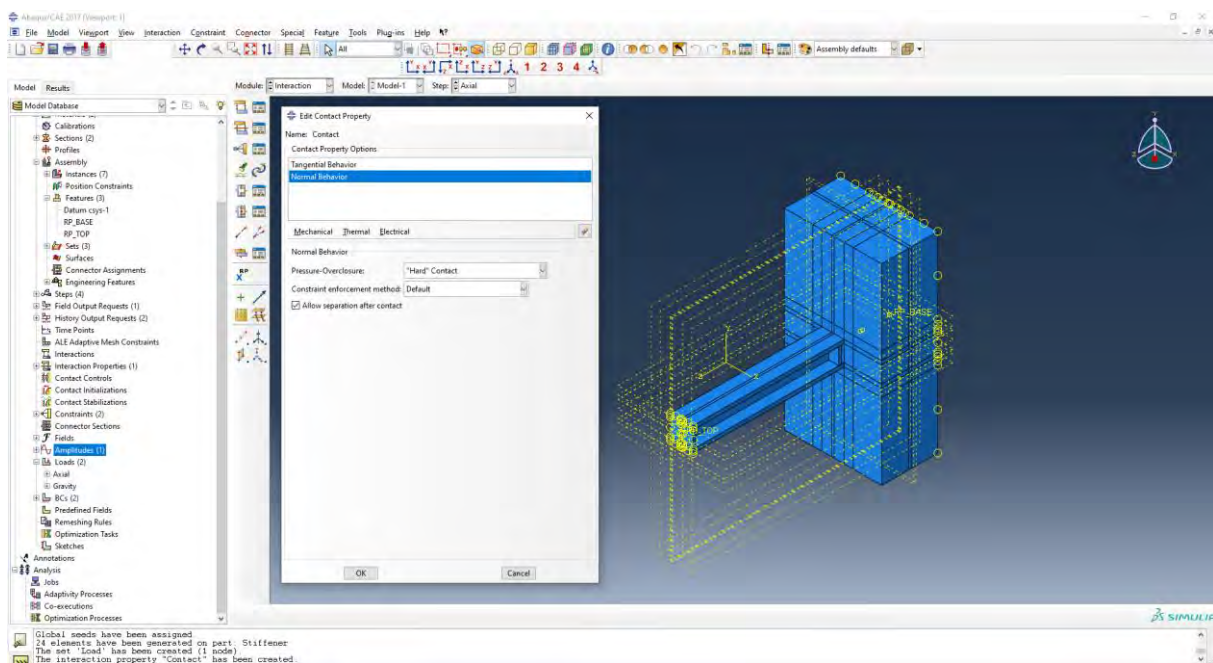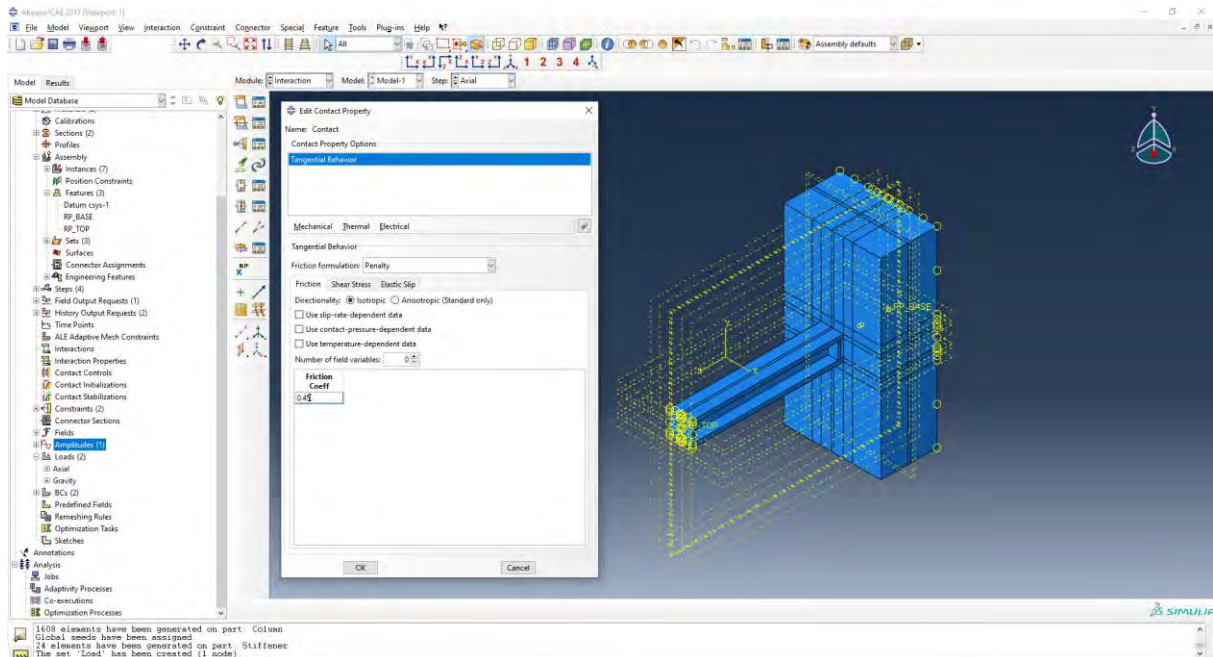
Figure 107:ABAQUS Contact Definition

With the find contact pairs tool we apply the contact interactions. Steel to steel contact is defined with a Tie constrain, while steel to Concrete is defined by de defined contact interaction.
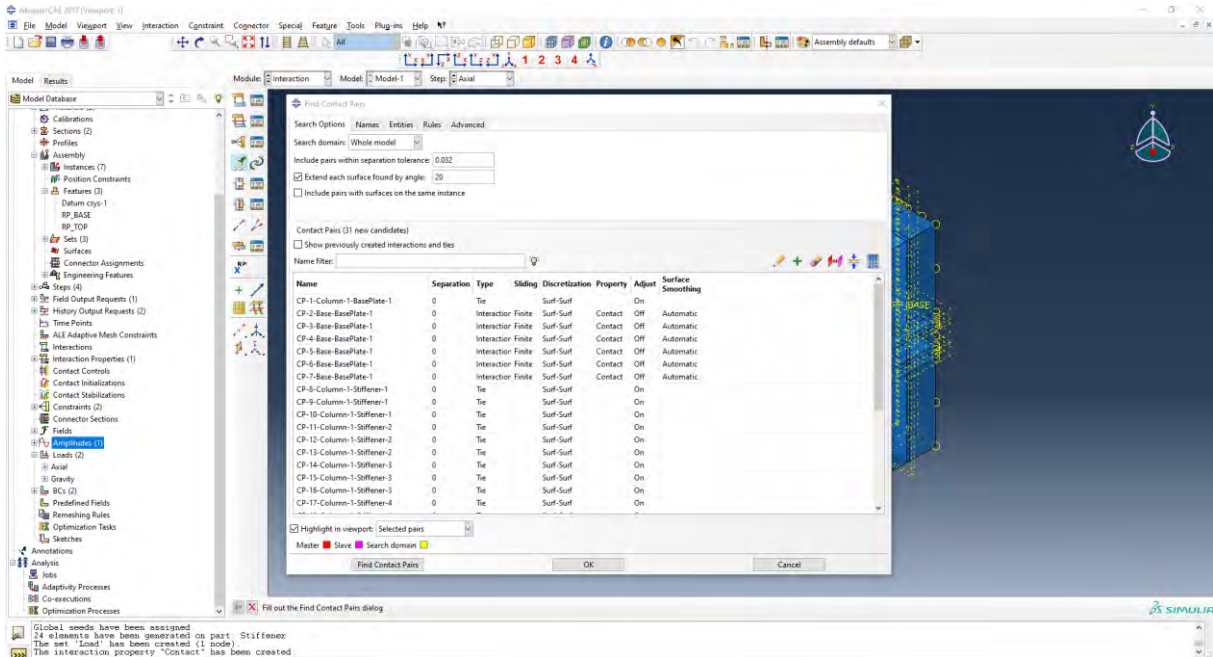
Figure 108:ABAQUS Contact Set-up

Finally, in the Job Module we set the Job, and run the model.
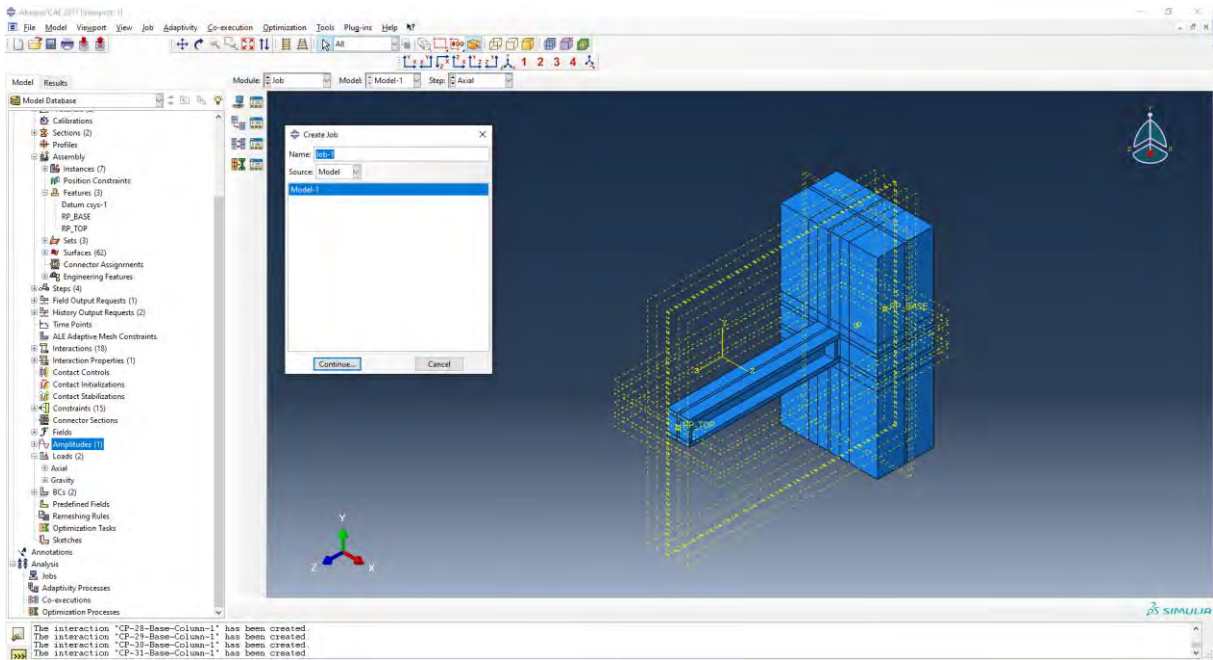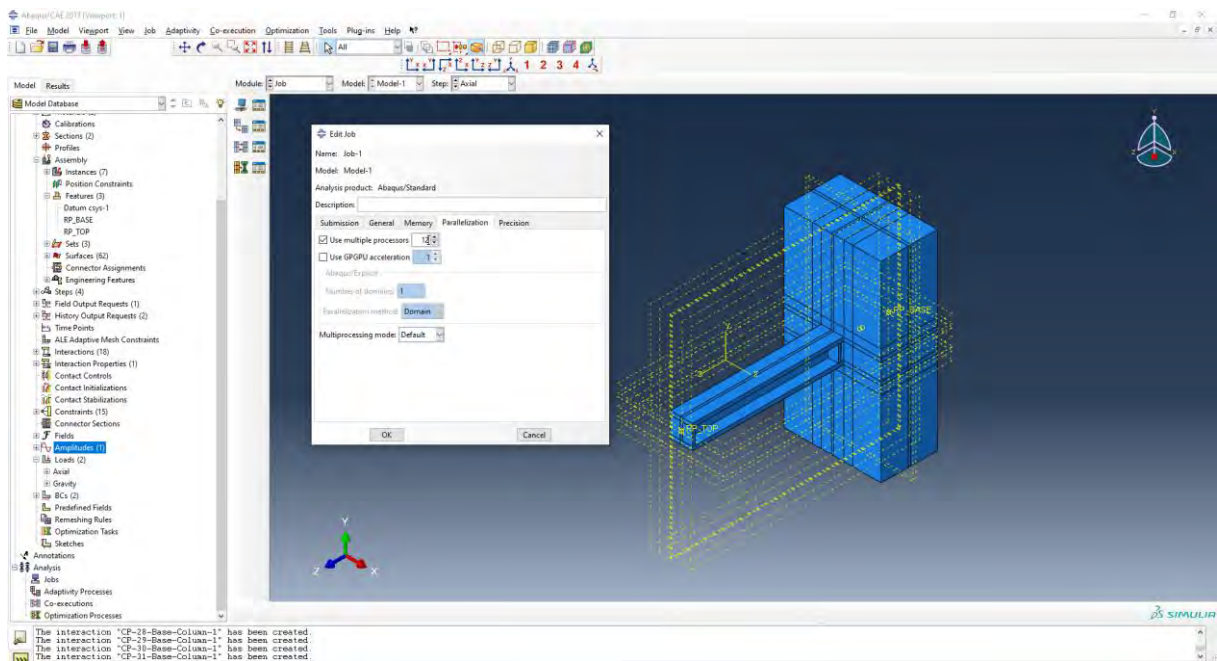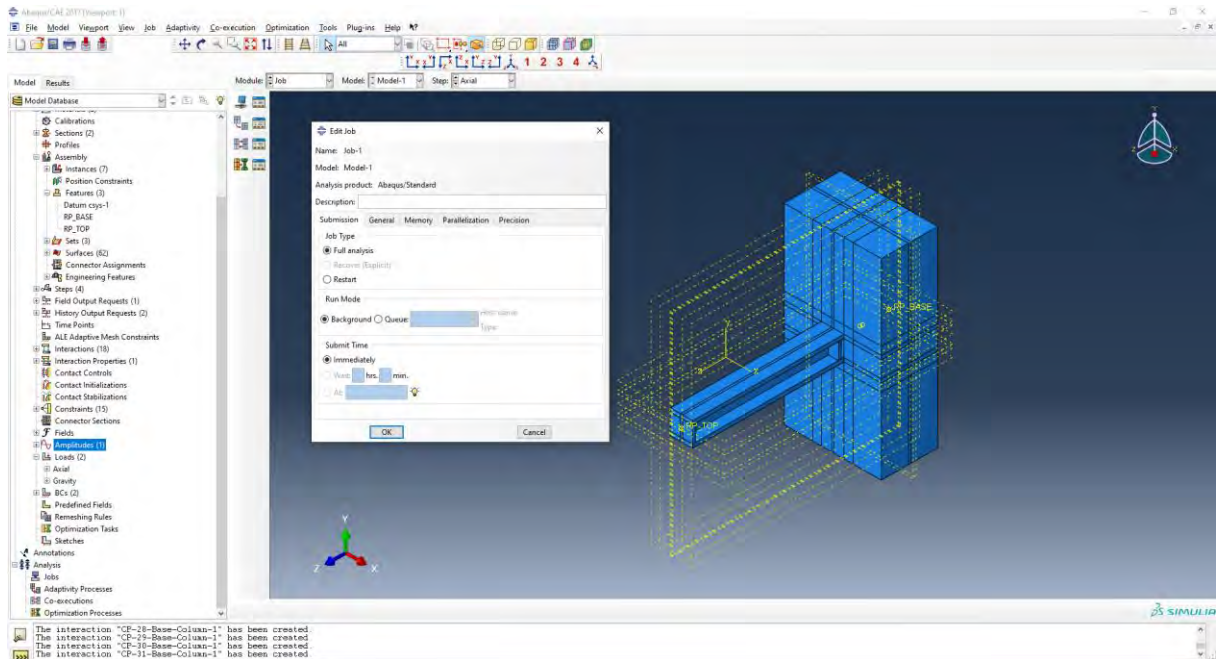
Figure 109:ABAQUS Job Creation

7. Appendix 2 – Modeling Sensitivity

For test #4 a sensitivity analysis was done to evaluate the Concrete Damage Plasticity input values.

For the initial run frictionless interaction was considered.
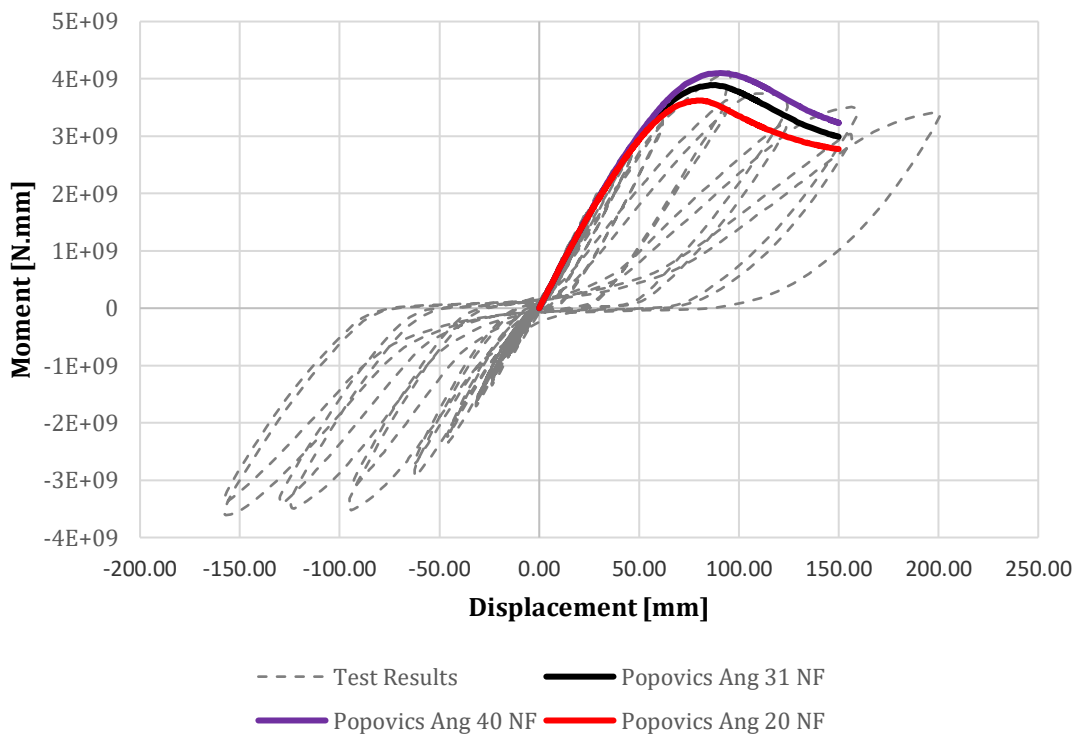
Figure 110: Test#4 - Dilatation Angle

Then friction was considered using a penalty formulation with a friction coefficient of 0.45.
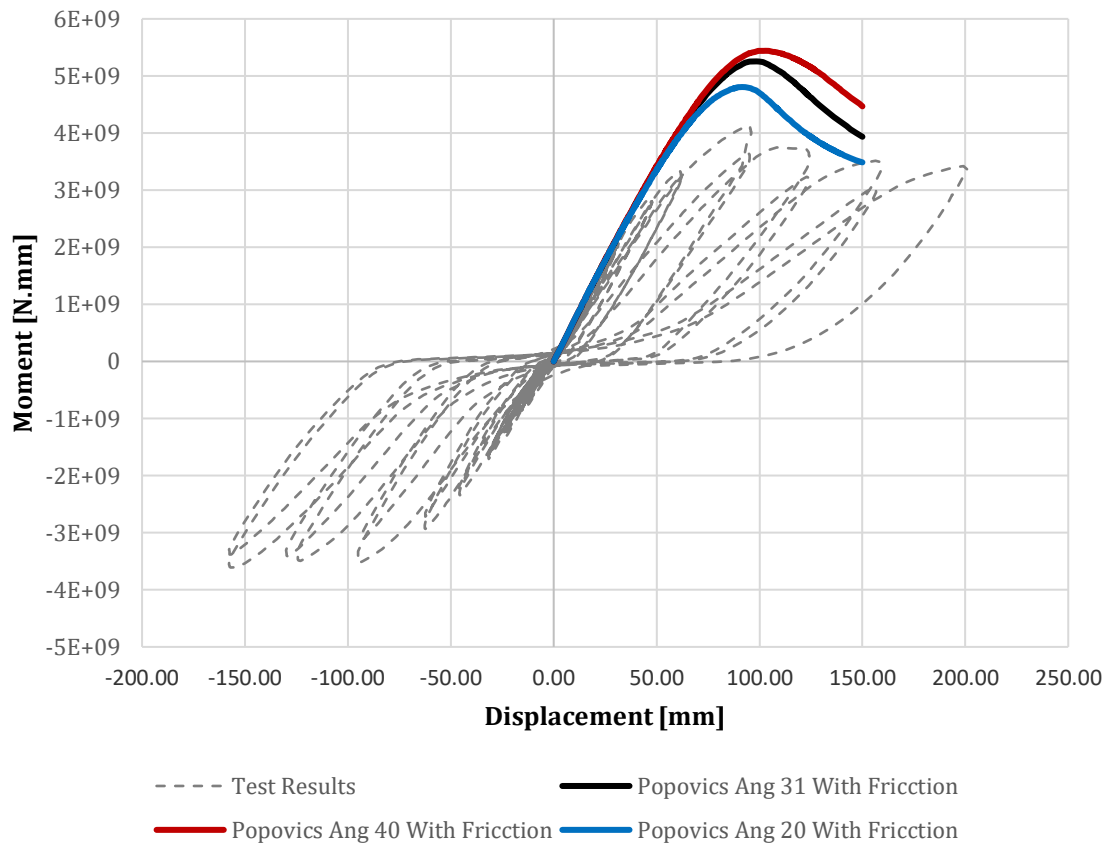
Figure 111: Test#4 NF Angle
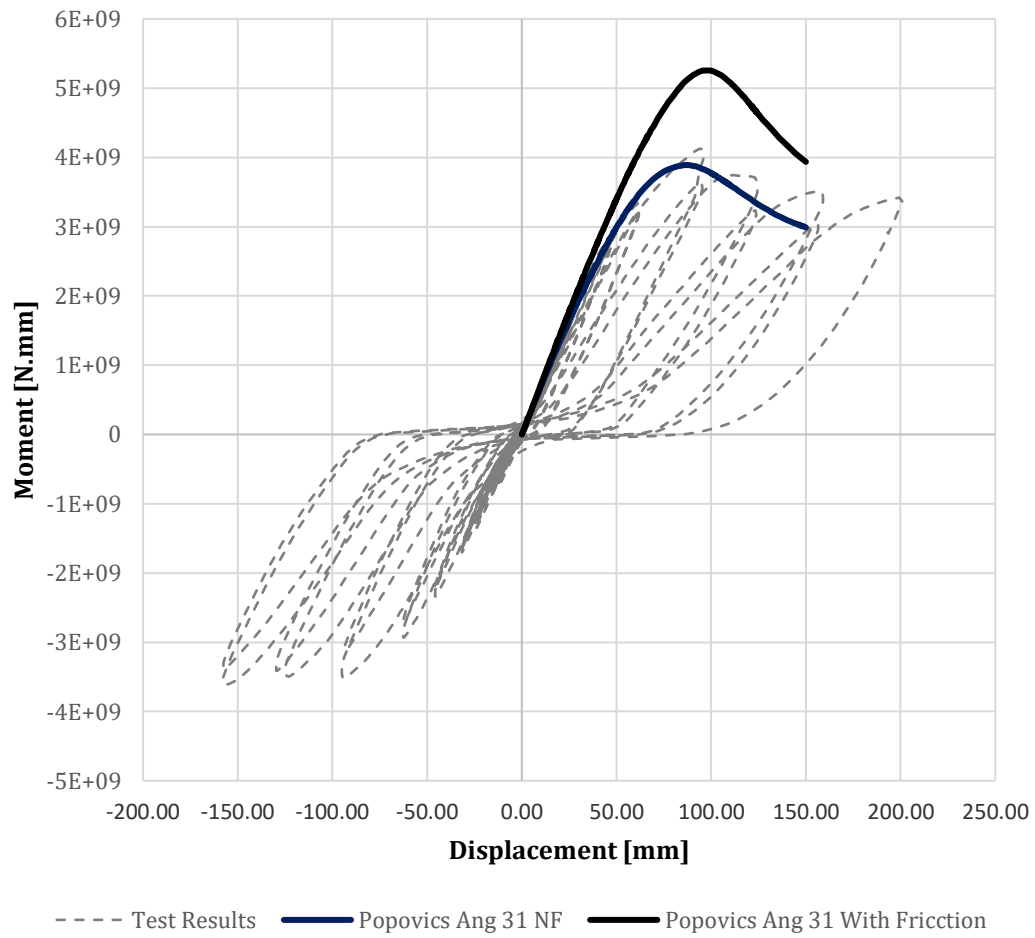
Figure 112:Test#4 Friction Comparison

Also, the SAC loading protocol was applied to both the model with and without friction

interaction.
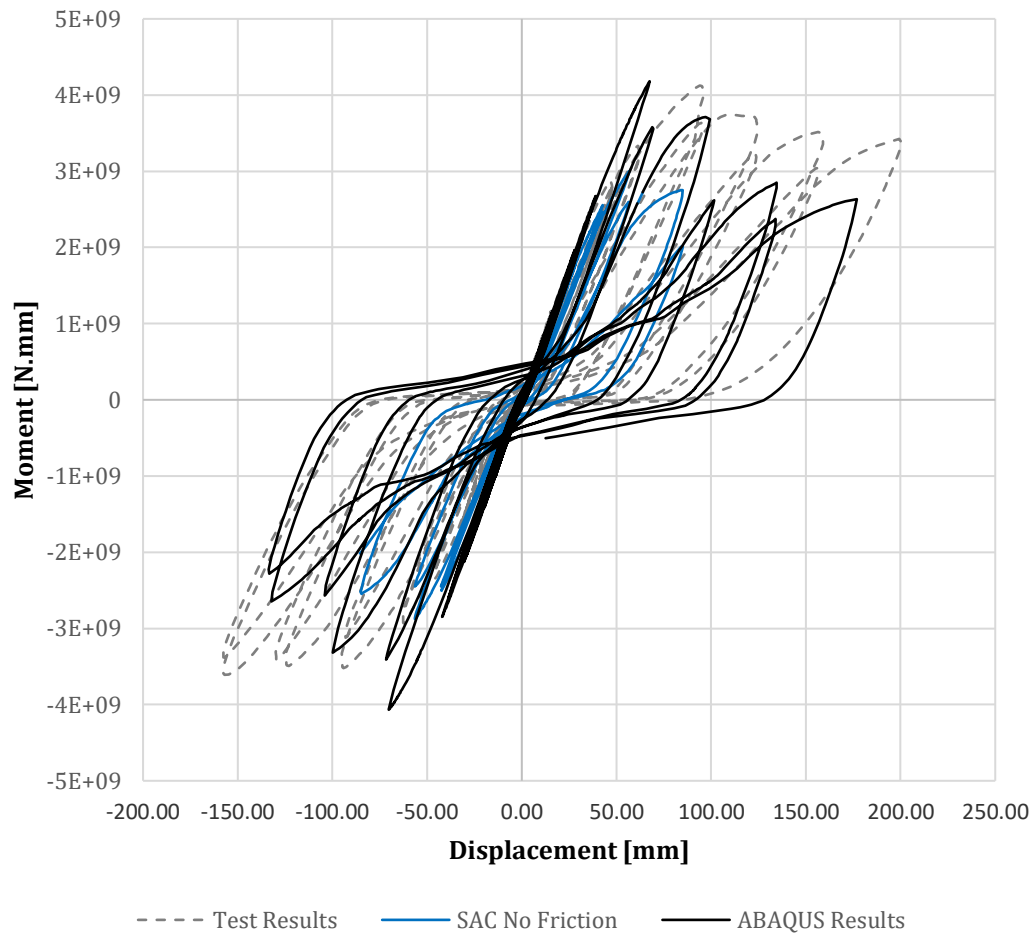
Figure 113:Test#4 Friction Comparison Cyclic

For Test#1 a sensitivity analysis was done to evaluate the effect of applying geometric

nonlinearity to the model.
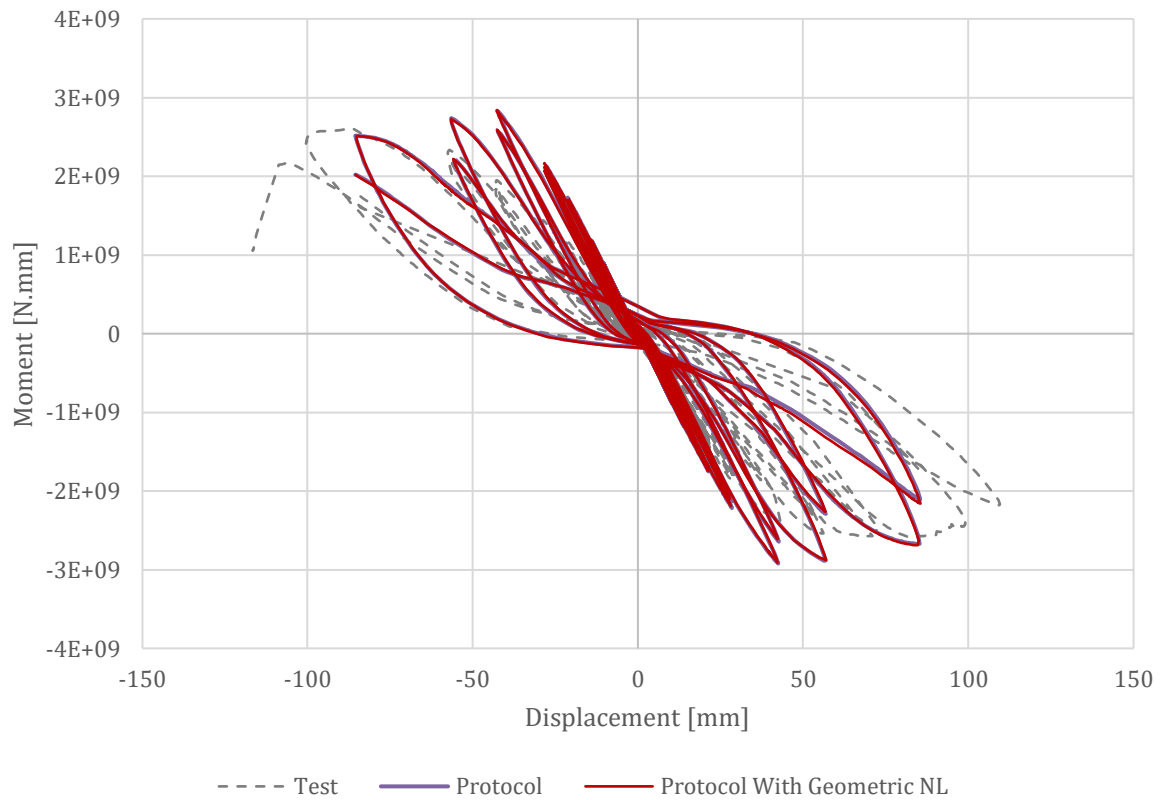
Figure 114:Test#1 Geometric Nonlinearity Comparison

For Test#1 a sensitivity analysis was done to evaluate the effect of varying the viscosity

parameter in the Concrete Damage Plasticity Model. The values used in the analysis were

0.01, and 0.005.
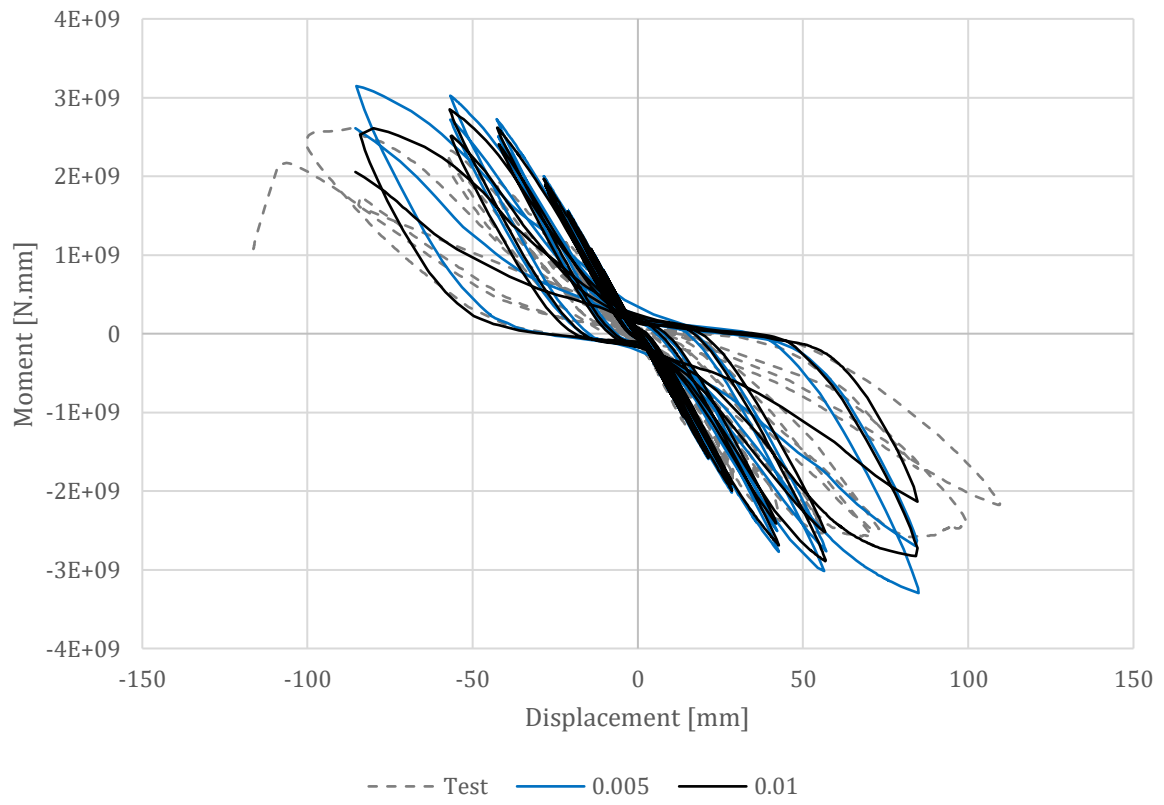
Figure 115:Test#1 Viscosity Comparison

8. Appendix 3 – COMPDYN 2021 - NONLINEAR FINITE ELEMENT MODELS FOR EMBEDDED BASE CONNECTIONS

NONLINEAR FINITE ELEMENT MODELS FOR EMBEDDED BASE CONNECTIONS

Nicolas Mora-Bowen[1], Pablo Torres-Rodas[2]

[1] Universidad San Francisco de Quito
Diego de Robles
e-mail: nmorabowen@estud.usfq.edu.ec

[2] Universidad San Francisco de Quito
Diego de Robles
e-mail: patorresr@usfq.edu.ec

Abstract

Column base connections are one of the most critical components in Steel Moment Frames (SMFs) since these connections transfer the loads (i.e., gravity, seismic, wind) from the entire superstructure into the concrete-foundation, being an interface between them. Typically, exposed base plates are preferred for low-and mid-rise buildings, while embedded base connections are the norm for tall buildings. This latter base configuration response is controlled by complex interactions between the column flange and the bottom base plate with the concrete foundation, where the mechanisms to transfer internal forces are idealized to underpin the current strength design methods. These mechanisms include horizontal bearing stresses between the column flange and the surrounding concrete and vertical bearing stresses of the base plate and the concrete foundation. Current methods to estimate the strength of these connections are validated against a limited number of experimental tests complicating their generalization for the different configurations that have not been tested. Although the results from these methods show good agreement with test data, the assumptions that underpin these methods have not been verified through sophisticated nonlinear finite element models. Motivated by this issue, this paper presents a series of nonlinear finite element models developed to provide insights into the behavior of embedded base connections for SMFs. These models incorporate the essential aspects that control the connection behavior, including constitutive material modeling and contacts among the connection components. Possible design implications are discussed, while the limitations of the current work and future lines of research are outlined.

Keywords: Column Base Connections, Embedded Base Connections, Finite Element Models.

1   INTRODUCTION

Column Base Connections are one of the most important components of Steel Moment Frames (SMFs). Several researchers [1-6] have demonstrated their significant influence on the seismic performance of SMFs systems. Because of this, these connections have been extensively studied over the last decade in different programs [7-11]. Typically, base connections can be broadly classified as exposed base plates (EBPs) and embedded base connections (EmBCs). The former type is the preferred detail for low to mid-rise buildings, while the latter is the norm for tall buildings.

EmBCs consist of a column welded to a bottom base plate (Refer to Fig. 1) and embedded into a concrete foundation. The applied forces, i.e., Axial Load, Bending Moment, and Shear, are resisted by a combination of the bearing stresses developed by the contact between the column flange and the foundation and by the vertical stresses at the bottom base plate. Grilli and Kanvinde [7] conducted a large-scale experimental program to study the seismic response of EmBCs. This program's focus was the flexural capacity of these connections and the development of a strength method based on the insights gained from the tests. A total of five tests were evaluated. The difference among them was the embedded length (510 and 760mm), column size, and axial load level.

Grilli and Kanvinde [7] postulated an internal stress distribution to idealize the mechanism that resists the applied loads. Figure 1 illustrates this mechanism which consists of horizontal bearing stresses accompanied by joint shear in the panel zone and vertical stresses at the bottom base plate. However, this idealized mechanism relies on pre-defined stress distribution (rectangular) on the bottom base plate as well as in the column flange against the foundation. It is well-known that the real stress distribution might differ from the assumed one due to the complex interactions between the components.

The behavior of EmBCs has been studied in the past from different perspectives. Grilli and Kanvinde [7] suggested a strength method to estimate their flexural strength. Torres-Rodas [12] proposed a procedure to estimate their rotational stiffness by aggregating the deformations within the components. The hysteretic characteristics of these connections were explored by Torres-Rodas [13] through a hinged model, which was validated experimentally and capture the force transfer mechanisms observed at [7]. Recently, Inamasu et al., [14] developed Finite Element (FE) models to explore the behavior of EmBCs further and suggest design recommendations. These models consist of shell elements with two rotational springs. Results indicate that current methods for the design of EmBCs are nonconservative.

Motivated by the preceding discussion, this paper presents a study with 3D sophisticated FE models to investigate further the seismic behavior of EmBCs. These models provide insights into the internal stress distribution and patterns of deformation of these connections. The models intend to capture phenomena such as the multi-axial constitutive response of the materials (steel and concrete), large deformations, and the contact between the column flange and the foundation. The paper starts by describing the models developed herein, and then the main findings are presented. Finally, the limitations of the study are discussed, and recommendations for future research are presented.
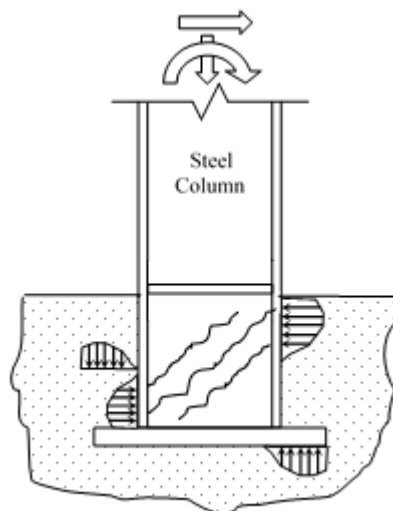
Figure 1: EmBC detail and internal force mechanism (from [7,12])

2   EXPERIMENTAL DATA

In this study, for the purposes of model validation, the experimental program conducted by Grilli and Kanvinde [7] at the University of California Davis was used. Thus, in this section of the paper, the details of the experimental program are briefly summarized. All tests consist of a steel column welded to a bottom base plate. The column height was about 3m, and it was embedded into a concrete foundation. All the specimens were subjected to the cyclic loading protocol ATC-SAC (Krawinkler et al. 2000 [15]). The parameters that changed among the tests are the embedded depth, the level of Axial Load (Tensile forces were used in one test), and the column size. Table 1 shows a summary of the test parameters, while Figure 2 a schematic representation of the test setup at UC Davis.

Based on the insights obtained from the mentioned experimental program, Grilli and Kanvinde [7] presented a strength method to characterize the flexural capacity of EmBCs. Key aspects of this method are detailed here. The applied Moment is resisted by a combination of horizontal bearing stresses developed by the contact between the column flange and the concrete foundation and vertical bearing stresses at the bottom base plate. Shear forces in the panel zone complement the horizontal bearing stresses. Thus, the Moment is resisted by these two mechanisms, i.e., horizontal and vertical stresses, with the implication that a fraction of the total applied Moment is distributed to each mechanism. This idealization entails an indeterminate problem, which is solved by the introduction of an empirically calibrated equation that considers the relative stiffness of the embedded column and the surrounding media.

In this manner, the connection strength may be calculated based on the associated limit states to each force transfer mechanism. For the horizontal bearing stresses, two limit states can take place 1) concrete bearing failure and 2) joint shear failure. On the other hand, in the vertical bearing mechanisms, four possible modes of failure are identified 1) base plate yielding, 2) concrete breakout under the base plate, 3) concrete breakout above the base plate, and 4) bearing failure of the concrete around the base plate. The connection strength is calculated by

combining the Moment capacity associated with both mechanisms ($M_{HB}^{capacity}$ and $M_{VB}^{capacity}$). Grilli and Kanvinde [7] concluded that the capacity estimated with the preceding procedure must be reduced by 30% for design purposes.
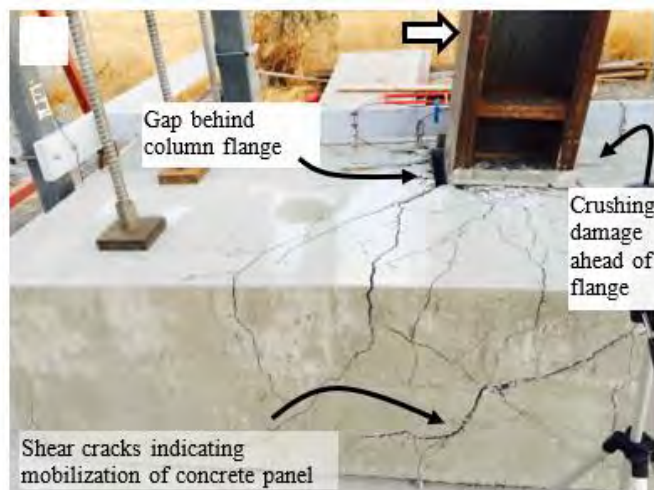
Figure 2: UC Davis experimental test (from [7,12])

3 FINITE ELEMENT MODELS

A total of four FE models have been developed to study the seismic behavior of EmBCs using the ABAQUS [16] simulation platform. Figure 3 illustrates a representative model built in this investigation. The models are composed of 3D Hex-structured elements. The meshes were refined in places where concentrations of stress are anticipated. As described in the previous section, the strength of the connection may be explained due to the contacts between the column flange and the base plate with the concrete foundation. Thus, the contacts are an essential feature of these models. These contacts are simulated with a finite sliding formulation with Normal and Tangential interaction properties. The former property was defined as hard contact, while the latter with a frictional formulation following the penalty method. A friction coefficient of 0.45 is adopted as recommended by Gomez et al. [11]. In contrast, welded elements inside the connection are assigned the tie constraint (i.e., steel column and base plate, steel column, and stiffeners) since welds are detailed to resist fracture even at large deformations.

Geometric nonlinearities, including large deformations formulations, are included in the models. The steel column and base plate are modeled with the Von-Misses surface with isotropic hardening. On the other hand, for concrete modeling, it is common to assume that this material behaves as an elastoplastic material in compression and brittle in tension. In this investigation, the concrete damaged constitutive plasticity (CDP) model was employed since it provides a general capability for modeling concrete and other quasi-brittle materials. Some of the details of this constitutive model provided by [16] are discussed. The CDP model uses concepts of isotropic damaged elasticity in combination with isotropic tensile and compressive plasticity to represent the inelastic behavior of concrete. It assumes that the main two failure mechanisms are tensile cracking and compressive crushing of the concrete material. Two hardening parameters control the evolution of the yield surface, ϵ_t^{-pl} and ϵ_c^{-pl} associated to

failure mechanisms under tension and compression loading, respectively [16]. The material properties are obtained from the ancillary tests from [7], and true stresses and strains were assumed in the material formulation.

The FE models were subjected to the SAC load protocol [15] in the Axial Load presence. In order to avoid the interference of P-delta effects in the connection response, the Axial Load was applied strategically at the bottom of the base plate. Thus, the Moment-Rotation response was recorded from the simulations and compared to validate the models with the associate experimental test. Figure 4 illustrates the results of the simulations and the corresponding validation against the experimental data. As per this Figure, the essential aspects of the hysteretic response are capture by the numerical results. Specifically, the simulations are able to capture the pinching behavior observed in the tests. Cyclic deterioration of the strength and the unloading stiffness are identified in these connections and well-represented in the simulations. The parameters that define the response's backbone curve are the Moment at First Yield, the Initial Rotational Stiffness, the Peak Moment Strength, and the Rotation Associate to the Peak Strength. A visual inspection of Figure 4 indicates that the differences between the simulations' parameters to the experimental tests' corresponding values are neglectable. Consequently, in the authors' opinion, the FE models are able to capture the key features of the connection response and are appropriate to investigate the behavior of EmBCs.
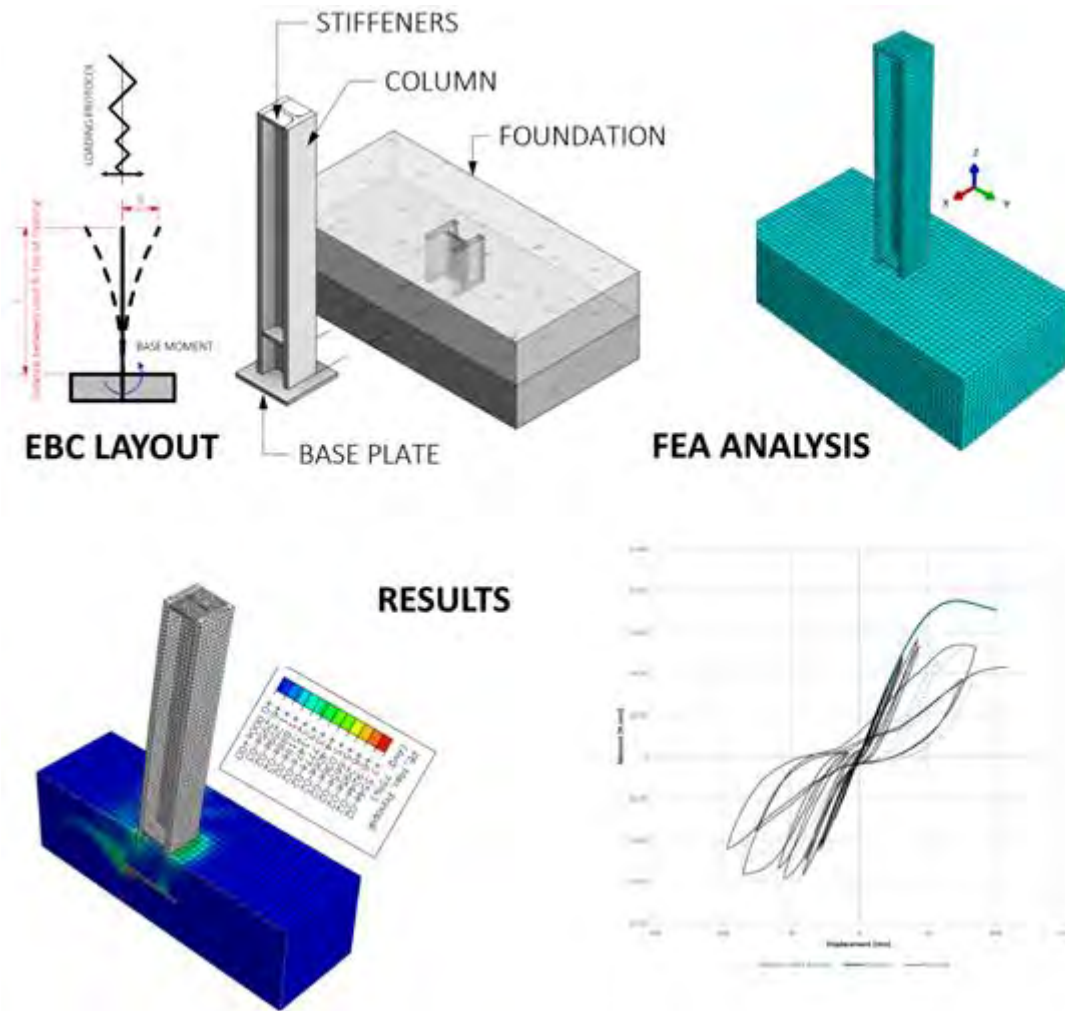
Figure 3: a) EmBC layaout, b) representative 3D FE model, c) example of the distribution of Stresses of a simulation, d) example of a hysteretic response

Test #	Column Size	P	$e_{mbedded}$	Base Plate			
				t_p	N	B	Z
		[kN]	[mm]	[mm]	[mm]	[mm]	[mm]
1	W14x370	445 [C]	510	50	760	760	2850
2	W18x311	445 [C]	510	50	865	710	2850
3	W14x370	0	760	50	760	760	3100
4	W14x370	445 [C]	760	50	760	760	3100

Table 11: Test Matrix Geometry and applied Axial Loads

4   DISCUSSION OF THE RESULTS

This section discusses the key findings from the FE simulations. Referring to Figure 4, all simulations show a well-defined linear-elastic branch up to the point where nonlinear behavior

starts, which corresponds to rotations close to 0.005rad. This observation is consistent with the experimental evidence reported by [7] that indicates that after 0.005rads, small cracks on the tension column flange start to open, entailing a gradual nonlinear response. These small cracks are accompanied by diagonal cracks, which start to grow near the steel column corners. Figure 5 shows a schematic representation of the crack propagation obtained from the simulation of test 1 once the deformation progresses.

As deformation progresses in all simulations, an appreciable loss of stiffness is observed because the concrete reaches its peak strength. At this point, the gap formed in the foundation in the tension flange side grows, which is consistent with the experimental tests [7]. This gap entails the pinching behavior observed in all the tests since it causes a relatively unconstrained rotation of the steel column as it moves back to the vertical position and goes in the reverse direction (following the cyclic loading protocol). A closer inspection of Figure 4 reveals that tests with higher embedment depths (760mm) present a more gradual stiffness decrease. This phenomenon may be attributed to the fact that higher embedment lengths imply a great fraction of the total Moment carried by the horizontal bearing stresses. Thus, when this latter mechanism starts to deteriorate, the force transfer to the vertical stresses seems to be more gradual.

Finally, in this section, the distribution of the horizontal bearing stresses is discussed. Figure 6 shows the stress distribution along the steel column flange of test 1 in two stages of the response, i.e., at the Moment associated with the First Yield and Peak Strength. As per Figure 6, for the first condition (i.e., My), the "real" stress distribution is closer to a triangular shape. This observation is not surprising since at this level of deformation, the connection starts to incursion in the nonlinear regime, and a triangular shape is consistent with an elastic behavior. In contrast, once the connection has reached its peak, it is observed in the simulations a more uniform stress distribution along a certain length of the flange. This finding is consistent with the rectangular stress block assumed by Grilli and Kanvinde [7] in their strength method. Although these findings may be used in the future to refine the strength, this topic deserves further scrutiny.
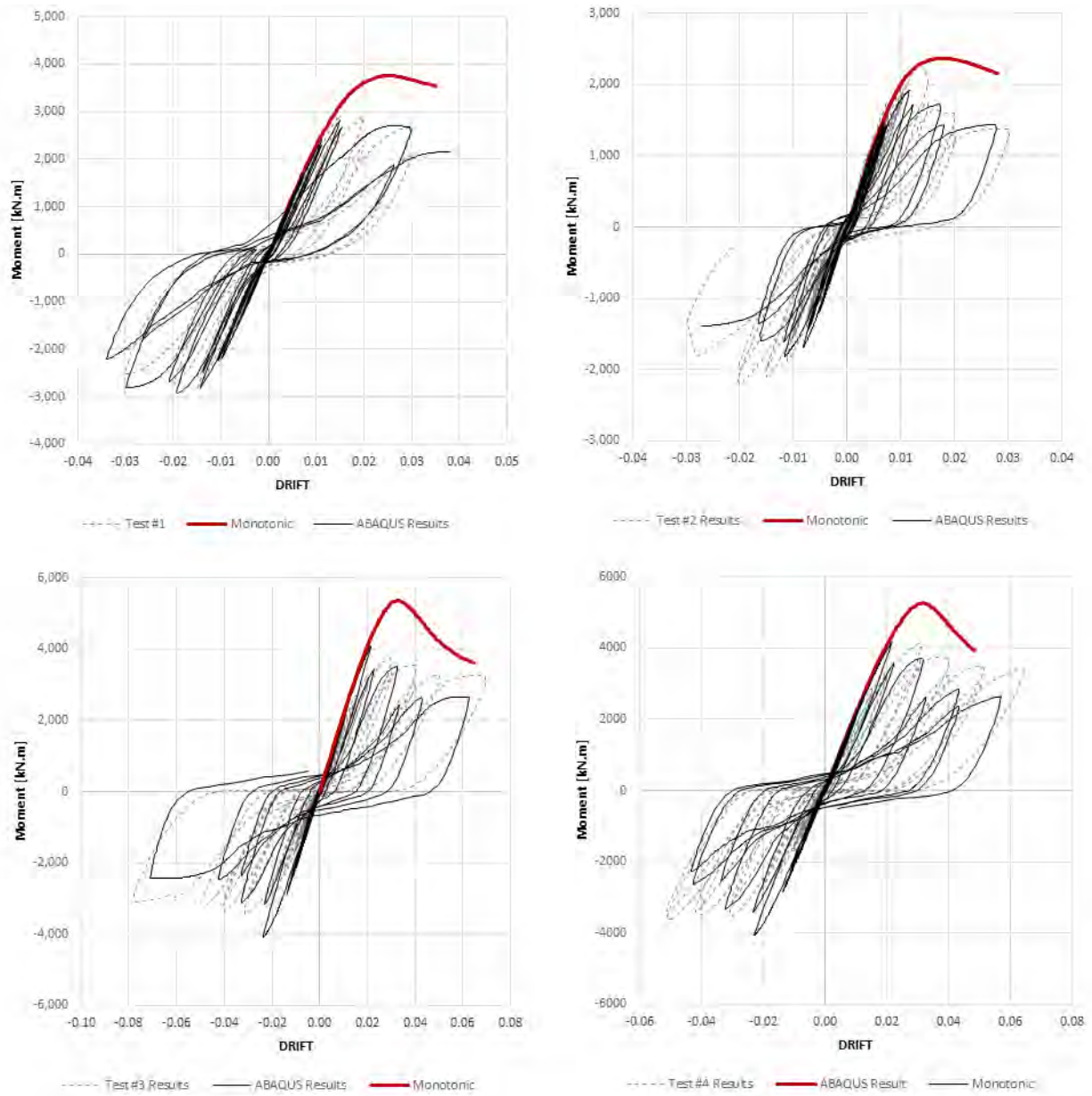
Figure 4: Hysteretic response of all FE simulations vs. Experimental data from [7]
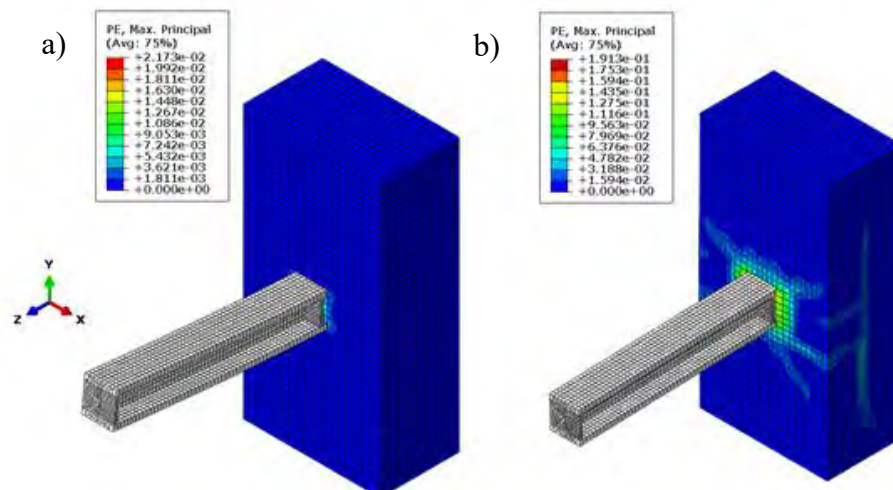
Figure 5: plastic strain distribution on the concrete at a) first yield, b) peak strength
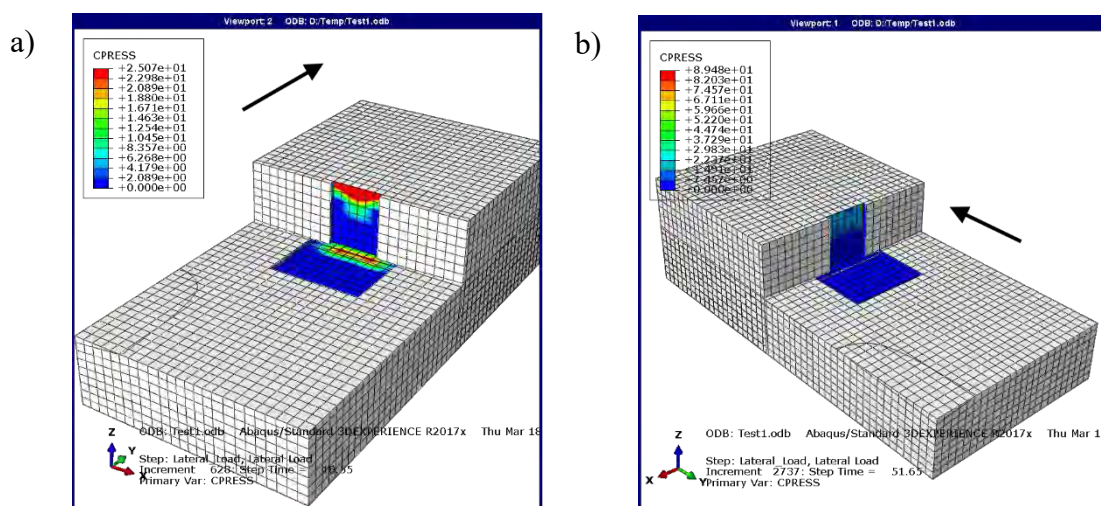
Figure 6: stress distribution on the concrete foundation due to column flange contact at rotations associated with a) first yield, b) peak strength

5 SUMMARY, LIMITATIONS, AND RECOMMENDATIONS

This paper presents a numerical study conducted on a critical component of SMFs such as EmBCs. A total of four FE models were developed in the ABAQUS platform [16] to explore the seismic behavior of these connections. Specifically, in this study, the internal force distribution and the patterns of deformation were identified from the simulations with the intention to gain insights aimed to improve the current design methods (e.g., [7]). All the models were validated against the experimental program conducted by Grilli and Kanvinde [7]. The goodness of the fit (i.e., the difference between the experimental and the numerical results) was considered an indicator of the reliability of the models.

The simulations indicate that at rotation levels close to the "first" yield of the connection, the stresses are not uniform along the column flange; instead, a triangular shape can be assumed. In contrast, at higher rotations, the stresses tend to become relatively uniform. Thus, when the

connection reaches its peak strength, it seems that the rectangular block assumption is appropriate. However, this issue deserves a further look.

The paper has several limitations that should be addressed in a new study in order to generalize the conclusions. For example, the number of simulations (four in total) is limited. Moreover, the experimental program by [7] is the only testbed used. It is recommended to build more FE models from other experimental programs available to assess different configurations' behavior (e.g., column size, embedment length, the influence of shear studs). Besides, this study does not address issues related to the seismic demands on the EmBCs, or a reliability analysis to assess if the strength resistance factors adopted are adequate or not. These topics have been addressed for exposed-based plates by [17,18,19] and should be conducted for EmBCs.

9. References

[1] Torres-Rodas, P., Flores, F., & Zareian, F. (2018). Seismic response of steel moment frame considering gravity system and column base flexibility. In Proc. 11th US Natl. Conf. Earthq. Eng., June 25–29, Los Angeles, USA.

[2] Falborski, T., Torres-Rodas, P., Zareian, F., & Kanvinde, A. (2020). Effect of base-connection strength and ductility on the seismic performance of steel moment-resisting frames. Journal of Structural Engineering, 146(5), 04020054.

[3] Torres-Rodas, P., Flores, F., Astudillo, B.X., Pozo, S. (2020). Sensitivity of special steel moment frames to the influence of column-base hysteretic behavior including gravity framing system. Proceedings of the International Conference on Structural Dynamic , EURODYN, 2020, 2, pp. 3629–3642

[4] Inamasu, H., de Castro e Sousa, A., Güell, G., & Lignos, D. G. (2020). Anchor-yield exposed column bases for minimizing residual deformations in seismic-resistant steel moment frames. Earthquake Engineering & Structural Dynamics.

[5] Y. Cui, F. Wang, S. Yamada, Effect of Column Base Behavior on Seismic Performance of Multi-Story Steel Moment Resisting Frames, International Journal of Structural Stability and Dynamics. 19 (2019) 1940007. https://doi.org/10.1142/S0219455419400078.

[6] Torres-Rodas, P., Flores, F., Pozo, S., & Astudillo, B. X. (2021). Seismic performance of steel moment frames considering the effects of column-base hysteretic behavior and gravity framing system. Soil Dynamics and Earthquake Engineering, 144, 106654.

[7] Grilli, D.A. and Kanvinde, A.M. (2015). "Embedded Column Based Connections subjected to Flexure and Axial loads," Report 3-11 submitted to the Charles Pankow Foundation.

[8] DeWolf J.T., and Sarisley, E.F. (1980), "Column Base Plates with Axial Loads and Moments," Journal of the Structural Division, ASCE, Vol. 106, No. 11, November 1980, pp. 2167-2184

[9] Astaneh, A., Bergsma, G., and Shen J.H. (1992). "Behavior and Design of Base Plates for Gravity, Wind and Seismic Loads," Proceedings of the National Steel Construction Conference, Las Vegas, Nevada, AISC, Chicago, Illinois.

[10] Burda, J.J., and Itani, A.M. (1999). "Studies of Seismic Behavior of Steel Base Plates," Report No. CCEER 99-7, Reno (NV): Center of Civil Engineers Earthquake Research, Department of Civil and Environmental Engineering, University of Nevada, NV.

[11] Gomez I.R., Kanvinde A.M. and Deierlein G.G. (2010). "Exposed Column Base Connections Subjected to Axial Compression and Flexure," Report Submitted to the American Institute of Steel Construction (AISC), Chicago, IL.

[12] Rodas, P. T., Zareian, F., & Kanvinde, A. (2017). Rotational stiffness of deeply embedded column–base connections. Journal of structural engineering, 143(8), 04017064.

[13] Torres-Rodas, P., Zareian, F., & Kanvinde, A. (2018). A hysteretic model for the rotational response of embedded column base connections. Soil Dynamics and Earthquake Engineering, 115, 55-65.

[14] Inamasu, H., Kanvinde, A. M., & Lignos, D. G. (2021). Seismic design of non-dissipative embedded column base connections. Journal of Constructional Steel Research, 177, 106417.

[15] Gupta, A., & Krawinkler, H. (2002). Prediction of Seismic Demands for SMRF's with Ductile Connections and Elements. SAC Joint Venture.

[16] ABAQUS, ABAQUS Analysis User's Manual Version 6.14–1, Dassault Systems Simulia Corp, RI, USA, 2014.

[17]Torres-Rodas, P., Zareian, F., & Kanvinde, A. (2018). Seismic demands in column base connections of steel moment frames. Earthquake Spectra, 34(3), 1383-1403.

[18] Torres-Rodas, P., Fayaz, J., & Zareian, F. (2020). Strength resistance factors for seismic design of exposed based plate connections in special steel moment resisting frames. Earthquake Spectra, 36(2), 537-553.

[19] Song, B., Galasso, C., & Kanvinde, A. (2021). Reliability Analysis and Design Considerations for Exposed Column Base Plate Connections Subjected to Flexure and Axial Compression. Journal of Structural Engineering, 147(2), 04020328.